Multi-layer metasurfaces for manipulating the propagation of microwaves along surfaces and edges

Julia de Pineda Gutierrez

Department of Physics and Astronomy
University of Exeter

A thesis submitted for the degree of
Doctor of Philosophy

November 2020

Declaration

Submitted by Julia de Pineda Gutierrez to the University of Exeter as a thesis for the degree of Doctor of Philosophy in Physics.

This thesis is available for Library use on the understanding that it is copyright material and that no quotation from the thesis may be published without proper acknowledgement.

I certify that all material in this thesis which is not my own work has been identified and that no material has previously been submitted and approved for the award of a degree by this or any other University.

Julia de Pineda Gutierrez
November 2020

I would like to dedicate this thesis to my family and friends, both in the UK and back in Spain, who have all been incredibly supportive with me throughout my Ph.D. studies.

Acknowledgements

My years as a Ph.D. student have been, to the least, an emotional roller-coaster. I have been very close to quitting more times than I can remember. However, in the end submission time has finally come. At this point, I need to thank many people that I have found along these years and that in one way or another have contributed to this personal achievement of mine.

Starting with my supervisors, Roy and Alastair, who have always been there to help me and point me in the right direction even when I felt like my research was not getting anywhere. I also need to thank many professors and researchers that I have met in conferences and courses who have given me different inspiring visions and interesting ideas.

I could never leave out my friends Joaquin and David, who have been an incredible support throughout these four years. We started this race together and we are finishing it together. I would like to thank them for putting up with my moaning and complaining and yet still stay my friends.

I also would like to thank all the people that have surrounded me during these years, my friends, in Exeter and Spain, all the girls I have lived with during these four years, and my fellow researchers and colleagues. You have all taught me so much, even without realising it.

And lastly, but the most important of all, my family: my mom, dad and brother who are always there to help me and listen to me, even when they don't understand what I am talking about.

From these years as a Ph.D student I take so many good experiences with me, especially all the travelling involved. I will never forget the amazing places I have been able to discover. However, I cannot wait for it to be over and I am very much looking forward to an exciting new adventure, whatever that is. In any case, I am sure I will take with me everything I have learnt these years, both personally and professionally. I can definitely say that I am a better version of myself than I was four years ago, and to me, that's the greatest achievement.

Abstract

This thesis comprises original experimental studies on surface waves propagating on metasurfaces at microwave frequencies. These studies are supported by matching simulation data, obtained by means of Finite Element Method modelling. The structures studied throughout this thesis are comprised of more than one layer of sub-wavelength elements arranged in different periodic lattices. However, these layers are very thin compared to the size of the elements comprising the arrays, resulting in structures that are extremely sub-wavelength in the (out-of-plane) dimension.

The work carried out as part of this thesis is divided in three main blocks, each of them looking at different features of metasurfaces, aiming to maximise different properties.

The first type of structure presented in this thesis are designed and engineered to maximise three main properties. These are the mode index of the modes bound to the structures, its in-plane isotropy and the bandwidth of operation of prospective devices based on such metasurfaces.

Whereas previous work in this field has considered single layers, the novelty here is the introduction of additional layers in order to increase the effective mode index of the modes supported by the structures. These extra layers create a capacitive effect between the overlapping areas of metal, therefore increasing the confinement of the waves. This is increased even further by minimising the separation between such layers. The second main goal in the design of the metasurfaces was to create a frequency independent mode index, aiming for the prospective development of broadband devices. For this, higher symmetries between the layers comprising the structures were introduced.

Following the studies of the infinitely periodic metasurfaces and its properties, the suitability for their implementation as graded index devices is proven.

Such devices are based on a graded mode index or surface impedance profile across the structure, which modifies the propagation of the wave. In the case of metasurfaces, the grading of the mode index is achieved by gradually varying the size or shape of the elements comprising the structure. This technique is used to design and manufacture two working planar Luneburg lenses, which are characterised experimentally and their performance compared with simulation data. The Luneburg lenses designed and manufactured as part

of the work contained in this thesis have the novelty of a higher fractional bandwidth of operation compared to similar metasurface devices, reaching 73%.

Another piece of work contained in this thesis involves a structure that guides microwaves with very high phase and group indices compared to similar metasurfaces. Its design is a simple two-layer discontinuous crossed metal-strip array. However, the novelty of this structure resides in the length of the metal strips, which extend to several unit cells. This work focuses on the isotropic wave dispersion shown at the lower frequencies. However, in addition to this, two of the higher frequency bands give rise to very strong negative dispersion, and also strong beaming occurs, which can be tailored easily by modifying the relative orientation of the layers.

The third piece of work included in this thesis focuses on the propagation of edge modes along the termination of a particular metasurface structure with hexagonal symmetry. Our metasurface is comprised of two layers of hexagonal arrays of circular metal patches. This structure, in addition to supporting a bound wave that propagates isotropically across the two-dimensional structure, also supports an edge mode that propagates only along its termination. Here, the propagation of the mentioned edge mode has been extensively studied. Firstly, its propagation along finite strips is considered, followed by its use to guide the electromagnetic field around different shapes. Finally, the coupling of two of these edge modes across small gaps between two terminated structures is explored, with different symmetries between them. In all cases, samples are designed, fabricated and experiments have been carried out and the original results obtained have been compared with simulation data calculated with a finite element method modelling software.

Table of contents

List of figures

Nomenclature

α	Attenuation constant
β	Propagation constant
δ	Amplitude decay length
ε	Relative Permittivity
η	Impedance of free space
λ	Wavelength
μ	Relative Permeability
ω	Angular Frequency
ψ	Wave Function
σ	Conductivity
c	Speed of light
k	Wavevector
k_0	Total Wavevector
n	Mode index
$tan\delta$	Loss Tangent
v_g	Group velocity
v_p	Phase velocity
Z_s	Surface Impedance

Acronyms / Abbreviations

FEM Finite Element Method

FFT Fast Fourier Transform

FSS Frequency Selective Surface

GRIN Graded Index

PCB Printed Circuit Board

PEC Perfect Electric Conductor

PhC Photonic Crystal

PMC Perfect Magnetic Conductor

RF Radio Frequency

SMRS Sinusoidally Modulated Reactance Surface

SPP Surface Plasmon Polariton

TE Transverse electric

TM Transverse Magnetic

TO Transfomation Optics

VNA Vector Network analyser

Chapter 1

Introduction

1.1 Aim of research

Electrical conductors support the propagation of electromagnetic waves localized at their interface with an insulator. For visible frequencies these modes are known as surface plasmons and have been widely studied since the 1950s [1]. Perfect conductors, which metals are often treated as at microwave frequencies, are unable to support bound surface modes since the fields are completely excluded from the substrate, however patterning of surfaces on a scale-length similar or smaller than the excitation wavelength recovers a similar 'plasmonic' phenomena. This concept was familiar to radar engineers of the mid-twentieth century [2, 3], and was readdressed theoretically and experimentally [4, 5] six decades later. It was shown that the dispersion of the modes supported on perfect conductors perforated with an array of subwavelength holes is governed by an effective permittivity of the same form as the plasmonic analogy. This behaviour is not only limited to holey structures but can also be extended to a wide range of surface textures. The size and spacing of the texturing elements can readily be controlled on all relevant length scales, which allows the creation of designer surface waves with almost arbitrary dispersion in frequency and space. These sub-wavelength textured structures, which normally exhibit a resonant behaviour, are known as metasurfaces.

Since the development of radar in the middle of the 20^{th} century, the design of structured metallic surfaces to manipulate the propagation of long-wavelength radiation has been of importance to the defence and telecommunications industries. These technologies range from filters, which can be configured to transmit or reflect specific frequency bands (known as frequency-selective-surfaces), to absorbing materials and polarisation converters. Over the years, many studies have been carried out to optimise these designs. However, many

challenges remain in this area of research, where more compact, flexible and broadband structures are always desirable.

The emergence of the field of two-dimensional metasurfaces, which fits within the broader field of three-dimensional metamaterials, has flourished in the microwave regime (frequencies between 1 GHz and 100 GHz), where sub-wavelength structures can be easily fabricated and manufactured. Metasurfaces have an added end-user interest due to their low profile and low cost. Their applications to guide surface waves [6] and to transform them into different wave-field configurations with desirable properties [7] is of particular commercial potential. The electromagnetic properties of metasurfaces (i.e. surface impedance, mode shape) can easily be controlled across the structure by simply varying the size or the shape of its elements [7], making them ideal for the manufacture of graded index devices such as lenses and leaky wave antennas [8–10].

The work presented in this thesis focuses on the investigation of some of these properties and applications, specially concerning metasurfaces which exhibit a high mode index. Throughout this thesis, different ways of achieving this property will be studied, looking also at maximising the isotropy of the metasurfaces and to increase the bandwidth of operation of the prospective devices.

1.2 Thesis outline

The research carried out throughout this thesis is aimed at designing new metasurfaces, looking to maximise the refractive index of the modes that they support and ensuring isotropy, whilst also reducing their dependence on frequency. Different metasurfaces are presented and characterised computationally and experimentally and some devices are proposed, manufactured and tested.

Chapter 2 is a historical and theoretical introduction. In this chapter, the physics behind the properties of metasurfaces are introduced, focusing the interest in the surface waves that they support, while making some analogies to surface-plasmon-polaritons confined to the interface between two media. The second important concept that is introduced in this first theoretical chapter is the role that periodicity plays in the dispersion of these microwave surface-waves.

Following the theoretical introduction, the experimental and numerical methods utilised throughout this thesis are presented in chapter 3. These include a lithographic fabrication procedure, by means of which the different samples were fabricated; the experimental measurements and further processing and analysis of the measured data, and the simulation techniques employed during the research conducted.

After these introductory chapters, the results obtained from the investigations carried out as part of this thesis are presented. They are summarised in four different chapters, each of which corresponds to a complete piece of work. The results presented here have also been published as four different peer-reviewed articles [9, 11–13] and have been presented in four international conferences.

In chapters 4 and 5, two different metasurfaces with low frequency dependence of the mode index are investigated. In chapter 4 a bi-layer design with glide symmetry is presented, comprised of two square arrays of circular patches with glide symmetry. This symmetry was chosen as it reduces the dispersion of the structure, resulting in a more broadband behaviour. The performance of this metasurface was tested by manufacturing a Luneburg lens whose performance is optimal in the range of frequencies between 6.5 GHz and 11 GHz, translating into a fractional bandwidth of 53%.

In chapter 5 a different metasurface design is presented, whose characteristics in terms of bandwidth and isotropy are improved with respect to those of the structure presented in chapter 4. In this case, a three-layer metasurface with hexagonal symmetry is designed and characterised. The surface waves here present some of the characteristic features given by structures with hexagonal symmetry, such as a straight Dirac-like dispersion and a Dirac crossing at the K-point of the Brillouin zone boundary. This structure, as the previous one, is also very thin and lightweight. Again the structure is tested by designing and characterising a Luneburg lens, which in this case presents an improved fractional bandwidth of 73%.

The goal in chapter 6 is to find a metasurface design that maximises the mode index of the modes it supports. For this purpose, a novel metasurface design consisting of an array of elements with a length up to three times bigger than the size of the metasurface unit cell is proposed. The main consequence of this design is an increase in the mode index presented by the structure. This is due to the decrease in frequency of the resonance of the elements as its size increases, together with any effects caused by the band gaps introduced by the periodicity of the structure occurring at much higher in-plane wave vector than the one corresponding to half wave resonances of the long strips. Also, this design ensures that the frequency of operation is far away from the resonant frequency of the constituent metallic elements, hence minimizing the the propagation losses. Three different metasurface designs featuring the same array of long elements is studied throughout chapter 6: a mono-layer and two bi-layer structures. The mono-layer shows a very anisotropic behaviour due to the intrinsic anisotropy of the elements comprising the array. This anisotropy, can be reduced by adding a second layer with a 90° rotation with respect to the first one. The addition of this second layer also increases the mode index even further as it introduces capacitive effects between the overlapping regions of the patches. Finally, in this chapter, a third design is

presented, where a displacement of half the periodicity of the structure is introduced in both x and y directions. This structure is found to have a very similar behaviour to the previously described.

In chapter 7, the propagation of localised edge modes along the termination of a double layered hexagonal metal-patch structure is modelled, fabricated and experimentally characterized. Two different terminations of the lattice are studied, one of them presenting an edge mode at much lower frequency than the other. This edge mode will then be used to guide the electromagnetic fields around both a triangular and a hexagonal shape.

To conclude chapter 7, the coupling of two microwave edge modes supported by a pair of these metasurfaces is studied experimentally and the results compared with the predictions from a numerical model. Further, the effect of glide symmetry on the pair of coupled edge modes is investigated. The glide symmetry closes the gap between the coupled edge modes at the Brillouin zone boundary and hence yields a more linear dispersion of the lowest order mode.

Finally, in chapter 8 a summary of the results obtained as part of this thesis together with some ideas for future works are presented.

Chapter 2

Theoretical Background

2.1 Introduction and historical background

Over the past several years, metamaterials and metasurfaces have become one of the fastest developing areas in theoretical and applied electromagnetism [14–17]. Their ability to provide full control of the reflected and transmitted fields and the freedom of manipulation that they offer, by simply changing the structure and specific features of the sub-wavelength elements that comprise them have contributed to the growing proliferation of metamaterials and metasurfaces devices as an alternative to those based on traditional optics and photonics.

Metamaterials are artificial structures, generally formed by periodic arrangements of sub-wavelength resonant elements [18–20]. At microwave frequencies those elements are usually metallic inclusions in a dielectric host environment. The resulting structure exhibits macroscopic electromagnetic or optical properties such as permittivity and permeability that can be engineered at the point of design and can even introduce properties and behaviours that are beyond those found in nature.

Metasurfaces are metamaterial layers whose thickness is also sub-wavelength. They are characterized by unusual reflection properties of plane waves or dispersion properties of guided surface waves. Many of the functionalities of metasurfaces can also be realized with layers of bulk metamaterials, however, metasurfaces present some practical advantages. Bulk periodic arrays are harder and more expensive to implement, especially when the size of the elements is reduced. Secondly, the operation of metamaterial devices require the fields to propagate for several wavelengths inside the material and, therefore, it is constrained by the high losses that accompany resonant elements. In addition, due to their lower absorption and losses, metasurfaces demonstrate better ability to manipulate the flow of electromagnetic energy than bulk metamaterials [21]. Finally, metasurfaces are extremely thin and light weight, and can therefore be integrated easily in many devices, providing a

novel approach to antenna design and other microwave components, specially for space and military applications [10, 22–24].

Metasurfaces are usually divided into two big groups: metasurfaces that provide interesting transmission and reflection properties, including the capability of changing the polarization of the fields, and metasurfaces for surface waves, that either prevent or support the propagation of electromagnetic modes bound to the surface. The use of artificial two-dimensional periodic structures to manipulate electromagnetic waves has been studied for both optical and microwave frequencies since the second half of the past century, however, over the past decades its development and proliferation has experienced a boost, and the metasurface term was coined.

Historically, the first studies on metasurfaces contemplate structures that exhibited resonant transmission and/or reflection. Those structures were traditionally known as frequency selective surfaces (FSSs) [25–28]. FSSs are usually based on periodically arranged metal elements on a dielectric substrate but can be also be achieved by creating voids on a continuous metal sheet. Conventional FSSs are usually resonant structures, with a periodicity and element size that is comparable to the wavelength. FSSs have been used as filters for microwave frequencies since the 1960s [29–31]. Researchers in optics have also studied metasurface-like structures since the early 1970s without introducing the term. In this case the structures were called nanoisland metal films and were used for sensing applications. Silver or gold nanoislands on a dielectric substrate possess localized plasmon resonances, enhancing the local electric field in the resonance frequency range [32].

The work carried out in this thesis focuses on metasurfaces that support the propagation of surface waves and therefore can be used to tailor their propagation.

The way in which metasurfaces are constructed, formed by the arrangement of many small elements, enables one to change the properties of the metasurface across the space very easily by just changing the geometry of the individual elements. This allows one to define different paths for the propagation of the electromagnetic fields bending the rays in a way that was traditionally achieved only with bulky components.

Surface waves and modes bound to an interface have also been studied since around the start of the 20^{th} century [33–35]. In 1907 Zenneck [36] found a solution to Maxwell equations for a wave propagating at the interface between air and salt (which is a material with finite conductivity). In 1909 Sommerfeld [37] studied the guiding of radio waves around the Earth and this was followed with many studies throughout the 20^{th} century as the use of radio waves extended for military and communications applications.

Bound surface waves, associated with resonant elements, are generally dispersive [2]. This means that the relationship between its energy and momentum is not linear. Usually, there is a sumit value of the frequency (energy) above which the energy of the mode does not increase anymore when the momentum of the mode keeps increasing and the dispersion approaches this frequency, known as the asymptotic resonance frequency (ω_0). As the mode approaches ω_0 the propagation of the wave is slowed down and the mode becomes more tightly bound to the surface. At optical frequencies, the resonance frequency is the natural frequency of oscillation of the electrons in the metallic surface and is known as the surface plasma frequency. At microwave frequencies the conductivity of metals is very high and modes on a planar surface are very loosely bound. However, the confinement of the electromagnetic fields can be increased by adding a subwavelength pattern to the metallic sheet. For these structured surfaces the asymptotic frequency of the surface wave's dispersion is related to the structural resonance frequency of the individual elements that comprise it. However, in spite of the different nature of the resonances, the behaviour of the surface wave dispersion at microwave frequencies is surface-plasmon polariton-like. This is the reason why the term 'spoof surface plasmons' is sometimes used to describe surface waves on such periodic structures [4, 5, 38].

The relationship between frequency (ω) and momentum (k) of an electromagnetic plane wave in free space is given by $\omega = ck$ and represents the dispersion relation of the mode. When the mode is bound to a particular structure, the dispersion relation loses this linear form. The momentum associated with a propagating mode, 'k' is referred to as the wavevector which can be separated into contributions in each dimension:

$$k_0^2 = k_\mathrm{x}^2 + k_\mathrm{y}^2 + k_\mathrm{z}^2, \tag{2.1}$$

where $k_0 = 2\pi/\lambda_0$ and λ_0 is the wavelength of the incident wave. The three components of k_0 are complex numbers with a real and an imaginary part, which determine the propagation and attenuation (or loss) suffered by that mode respectively.

A typical surface wave dispersion curve is illustrated in Fig. 2.1. In particular, the figure represents the dispersion of the mode (real part, as losses are not considered) supported by an array of square patches over a ground plane in the x (horizontal) direction. As the mode is bound to the surface, the dispersion is plotted as a function of k_x. In the figure, the blue line represents the dispersion of the mode and the red line represents the light line. The resonance frequency of the mode towards which it bends asymptotically (ω_0) is represented with a green dashed line. At low frequencies the dispersion curve follows the light line and the surface wave is loosely bound to the interface, as it propagates with a similar speed to that of a grazing photon propagating in free space. This corresponds to the area shaded in blue in

the figure. For this range of frequencies, surface modes are best described as a simple surface current that propagates on a good conductor. As the frequency increases and the mode bends away from the light line, approaching the asymptotic frequency, the wave is slowed down and the confinement of its electromagnetic fields increases.

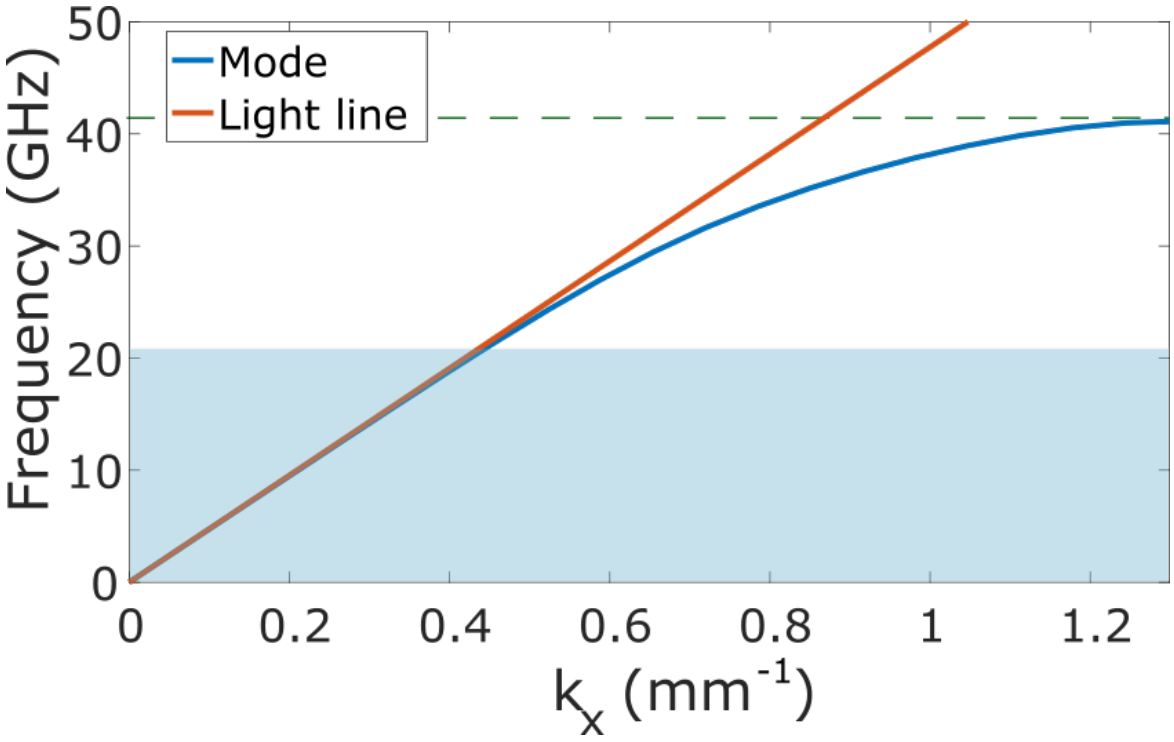

Fig. 2.1 Dispersion diagram of a typical surface wave at microwave frequencies. In this case, it corresponds to the mode supported by an array of square patches over a ground plane. As it represents a surface wave, the dispersion is plotted in the x (horizontal) direction. The blue line represents the dispersion of the mode and the red line represents the light line. The dashed green line represents the asymptotic frequency, towards which the mode bends. At low frequencies the dispersion curve follows the light line, whereas at higher frequencies it asymptotically approaches the resonance frequency adopting a surface plasmon-like behaviour. The range of frequencies for which the mode is practically indistinguishable from the light line is shaded in blue.

In summary, surface waves are a widespread phenomenon that occurs at different frequency ranges in the electromagnetic domain. With difference and similarities, they can be illustrated in different ways. In optics, surface waves are called surface plasmons [17], which are highly dispersive and can become strongly localized to the interface between a metal and a dielectric. Meanwhile, at microwave frequencies, the electromagnetic fields extend for many wavelengths into the surrounding space and are more appropriately described as surface currents. It is only when a resonant surface texture is added that the modes become

localised. Despite this, many analogies can be made between between both cases, and different phenomena can be extrapolated from one case to the other as will be shown later on in this thesis.

2.2 Metasurfaces for surface waves at microwave frequencies

Surface wave metasurfaces support the propagation of bound modes, with an electromagnetic field profile that decays in both directions away from the structure. In the limit where the period of the surface texture is much smaller than the wavelength of operation, the structure can be described using an effective medium model, and its properties can be summarized into a single parameter, the complex surface impedance [39]. This is defined as the ratio between the tangential electric field and the tangential magnetic field at the surface. A smooth conducting sheet will have low surface impedance while a textured surface, comprised of many small elements can be designed to have a high surface impedance. Depending on the way in which metasurfaces are designed, they can support either Transverse Electric (TE) or Transverse Magnetic (TM) modes or a combination of both.

For TE surface waves, the electric field is tangential to the surface and to the propagation direction, while the magnetic field extends out of the sheet in loops whereas for TM modes the magnetic field is tangential to the surface and the electric field jumps out in loops.

One way to derive the properties of surface waves is to solve for waves that decay exponentially away from a dielectric interface [40]. It is found that such waves exist on materials with a non-positive dielectric permittivity (or permeability), like metals. A second way of describing the same waves is by starting from the point of view of a material which has been assigned an effective complex surface impedance [39].

Throughout this thesis, the effective surface impedance of the material will be used repeatedly so it is convenient that we use this second approach as the way to define propagation of surface waves across the metasurface.

We will start by assuming a wave bound to a surface in the xy plane. The wave is propagating in the +x direction, with fields decaying in the +z direction. A sketch of the geometry of the problem is represented in Fig. 2.2.

We will assume a TE mode, since all the structures considered in this thesis are comprised of disconnected metallic elements and therefore support TE waves. In these kind of structures, the electric field stays in the plane of the surface, between the metallic elements, while the

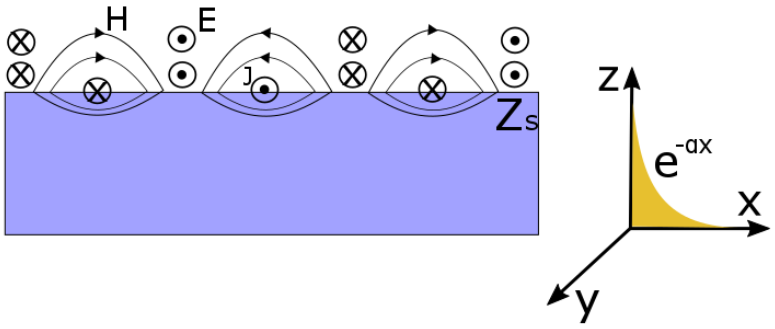

Fig. 2.2 Representation of a TE mode propagating in the x direction on an arbitrary impedance surface Z_S. The electric field is tangential to the surface while the magnetic fields loops in the out-of-plane direction. The fields decay in the z direction (away from the surface) with decay constant α.

magnetic field creates out-of-plane loops connecting those same metallic elements. This is shown in Fig. 2.2. However, in any case, the procedure is analogous for TM waves.

For TE surface waves, the electric field is parallel to the surface and perpendicular to the propagation direction, so $E_X = E_Z = H_Y = 0$. In addition, the field decays in the +z direction with decay constant α and propagates in the +x direction with complex propagation constant k.

The electric and magnetic field have the following expressions:

$$E = [0, E_Y, 0]e^{ikx}e^{-\alpha z}e^{-i\omega t}, \text{ and} \tag{2.2}$$

$$H = [H_X, 0, H_Z]e^{ikx}e^{-\alpha z}e^{-i\omega t}. \tag{2.3}$$

From Faraday's law

$$\nabla \times \vec{E} = -\mu \frac{\partial \vec{H}}{\partial t} \quad \Rightarrow \quad -\frac{\partial E_Y}{\partial z}\hat{x} + \frac{\partial E_Y}{\partial x}\hat{z} = -\mu \frac{\partial \vec{H}}{\partial t}, \tag{2.4}$$

and Ampere's law

$$\nabla \times \vec{H} = \varepsilon \frac{\partial \vec{E}}{\partial t} \quad \Rightarrow \quad \left[\frac{\partial H_X}{\partial z} - \frac{\partial H_Z}{\partial x}\right]\hat{y} = \varepsilon \frac{\partial \vec{E}}{\partial t}, \tag{2.5}$$

substituting equations 2.2 and 2.3 into equations 2.4 and 2.5, we obtain

$$-ikE_y = -i\omega\mu H_z, \tag{2.6}$$

$$\alpha E_y = -i\omega\mu H_x, \text{ and} \tag{2.7}$$

$$-\alpha H_x + ikH_z = i\omega\varepsilon E_y. \tag{2.8}$$

Finally, combining these three equations and cancelling, we get the dispersion relation for the surface waves:

$$k^2 - \alpha^2 = \varepsilon\mu\omega^2. \tag{2.9}$$

The same expression can be obtained for TM waves following an analogous procedure but exchanging the roles of the electric and magnetic fields according to the principle of duality [41].

This expression can be written in term of the surface impedance of the material. To compute the surface impedance we consider a rectangular surface area of the studied metasurface [39]. This geometry is shown in figure 2.3.

Fig. 2.3 Rectangular area used for computing the surface impedance.

As mentioned earlier, the impedance is defined as the ratio of the tangential electric field to the tangential magnetic field at the surface, similar to the impedance given by Ohm's law (the ratio of the voltage to the current along a sheet current),

$$Z_{\mathrm{S}} = \frac{E_{\mathrm{t}}}{H_{\mathrm{t}}}. \tag{2.10}$$

TE surface waves have a single electric field component that is tangential to the surface, oriented along the y direction. The magnetic field forms loops that emerge from the surface in the XZ plane and therefore has two components, one which is tangential to the surface and another one normal to the surface. For the surface impedance calculation we just need to consider the component tangential to the surface.

Let's start with the tangential component of the magnetic field:

$$H_{\mathrm{t}} = H_{\mathrm{X}} = Ce^{ikx-\alpha z}e^{-i\omega t}. \tag{2.11}$$

Using Faraday's law the transverse component of the Electric field can be obtained:

$$\nabla \times \vec{E} = -\mu \frac{\partial \vec{H}}{\partial t} \quad \Rightarrow \quad \frac{\partial E_{\mathrm{y}}}{\partial z} = -i\omega\mu H_{\mathrm{X}}. \tag{2.12}$$

Substituting equation (2.11) in this expression and integrating with respect to z we solve for E_{y},

$$E_{\mathrm{y}} = \frac{i\omega\mu}{\alpha} Ce^{ikx-\alpha z}e^{-i\omega t}. \tag{2.13}$$

To obtain the surface impedance we calculate the ratio between the calculated electric and magnetic fields. However, to obtain the correct sign of the impedance the vector nature of the fields needs to be taken into account. The surface impedance is defined for a wave approaching the surface from the outside. This convention ensures that an absorbing surface will have positive resistance while a reflective surface will have negative resistance. Considering this, the surface impedance can be calculated as

$$Z_{\mathrm{S}} = -\frac{E_{\mathrm{y}}}{H_{\mathrm{Z}}}. \tag{2.14}$$

Inserting equations (2.10) and (2.12) the surface impedance for TE waves is given by

$$Z_{\mathrm{S}}(TE) = -\frac{i\omega\mu}{\alpha}. \tag{2.15}$$

This expression corresponds to a negative reactance, therefore, a capacitive surface impedance is required to support a TE surface mode.

To calculate the surface impedance for TM surface waves we again assume a surface in the xy plane with impedance Z_{S} and a surface wave that propagates in the positive direction

of the x axis with decaying fields in the positive direction of the z axis.

For TM surface waves $H_{\mathrm{x}} = H_{\mathrm{z}} = E_{\mathrm{y}} = 0$. As for the previous case, we assume a decay constant α and a propagation constant k. However, in this case we start with the tangential component of the electric field,

$$E_{\mathrm{t}} = E_{\mathrm{x}} = Ce^{ikx-\alpha z}. \tag{2.16}$$

Making use of Ampere's law we obtain the y component of the magnetic field

$$\nabla \times \vec{H} = \varepsilon \frac{\partial \vec{E}}{\partial t} \quad \Rightarrow \quad \frac{\partial H_{\mathrm{y}}}{\partial z} = i\omega\varepsilon E_{\mathrm{x}}. \tag{2.17}$$

Finally substituting equation (2.16) in equation (2.17) and integrating, the tangential magnetic field is obtained,

$$H_{\mathrm{y}} = \frac{-i\omega\varepsilon}{\alpha} Ce^{ikx-\alpha z}. \tag{2.18}$$

In this case the surface impedance is

$$Z_{\mathrm{S}} = \frac{E_{\mathrm{x}}}{H_{\mathrm{y}}}. \tag{2.19}$$

Inserting in equation (2.19) equations (2.16) and (2.18) the surface impedance for TM surface waves is

$$Z_{\mathrm{S}}(TM) = \frac{i\alpha}{\omega\varepsilon}. \tag{2.20}$$

For TM surface waves a positive reactance is obtained and therefore, an inductive surface is required for the propagation of transverse magnetic modes.

In equation (2.9) we obtained the dispersion relation of surface waves in the context of the effective surface impedance model. The wave vector k is given in terms of the decay constant α but for practical applications it is more useful to express it in terms of the surface impedance that we just obtained.

For TE waves we can combine equations (2.9) and (2.15) and we obtain,

$$k^2 = \omega^2 \left[\mu\varepsilon + \frac{\mu^2}{Z_{\mathrm{S}}(TE)} \right]. \tag{2.21}$$

If we substitute in this expression the speed of light in vacuum $c = \frac{1}{\sqrt{\mu_0 \varepsilon_0}}$ and the impedance of free space $\eta = \sqrt{\frac{\mu_0}{\varepsilon_0}}$, (where μ_0 and ε_0 are the permittivity and permeability of free space), we obtain the dispersion relation for TE waves as a function of the surface impedance,

$$k_{\mathrm{TE}} = \frac{\omega}{c}\sqrt{1 - \frac{\eta^2}{Z_{\mathrm{S}}(TE)^2}}. \tag{2.22}$$

An analogous expression can be found for TM waves by combining equations (2.9) and (2.20)

$$k_{\mathrm{TM}} = \frac{\omega}{c}\sqrt{1 - \frac{Z_{\mathrm{S}}(TM)^2}{\eta^2}}. \tag{2.23}$$

Another important and very useful quantity used to describe surface waves propagating across a metasurface is the mode index. The mode index is defined as the ratio between the wave vector in the mode supported by the metasurface and that for a plane wave propagating in free space at the same frequency. It is related to the phase velocity and describes how much the surface waves propagating across a metasurface are slowed down. As the mode index increases, the velocity of propagation of the surface wave is reduced.

$$n_{\mathrm{SW}} = \frac{k_{\mathrm{SW}}}{k_0}. \tag{2.24}$$

Using the definition of mode index and the values of the wave vector previously obtained, an expression for the mode index can be obtained, for TE surface waves,

$$n_{\mathrm{TE}} = \sqrt{1 - \frac{\eta^2}{Z_{\mathrm{S}}(TE)^2}}, \tag{2.25}$$

and for TM surface waves,

$$n_{\mathrm{TM}} = \sqrt{1 - \frac{Z_{\mathrm{S}}(TM)^2}{\eta^2}}. \tag{2.26}$$

2.3 Infinitely periodic structures

When electromagnetic waves propagate along the interface between a metal and a dielectric, the mode is very loosely bound. To increase the confinement of the mode to the structure a periodic sub-wavelength patterning needs to be added. Those periodically patterned structures

provide artificial boundary conditions that allow surface waves to be tightly bound even at microwave frequencies.

Concepts of solid state physics [42] are useful in describing metamaterials as two dimensional periodic structures. We will consider a two-dimensional Bravais lattice in the xy plane. This specifies the periodic array in which the repeated units of the structure are arranged. In 2D, a Bravais lattice is defined by two vectors: $\vec{a_1}, \vec{a_2}$. All points that comprise the Bravais lattice can be written as a linear combination of the lattice vectors.

$$\vec{R} = n_1\vec{a_1} + n_2\vec{a_2}, \tag{2.27}$$

where n_1, n_2 are integer numbers. A second lattice known as the reciprocal lattice is also defined. If we consider a plane wave $e^{i\vec{k}\vec{r}}$, the reciprocal lattice is defined as the set of wavevectors $\vec{k}$ that yield plane waves with the periodicity of the Bravais lattice. Therefore, a wave vector $\vec{k}$ belongs to the reciprocal lattice of a Bravais lattice of points $\vec{R}$ if it satisfies the condition,

$$e^{i\vec{k}(\vec{r}+\vec{R})} = e^{\vec{k}\vec{r}} \quad \Rightarrow \quad e^{i\vec{k}\vec{R}} = 1. \tag{2.28}$$

As for the real-space lattice, any vector in the reciprocal lattice can be written as a linear combination of the reciprocal lattice vectors: $\vec{b_1}, \vec{b_2}$.

$$\vec{k} = \alpha_1\vec{b_1} + \alpha_2\vec{b_2}, \tag{2.29}$$

The reciprocal lattice vectors can be obtained from the real-space lattice vectors by calculating the cross product with the perpendicular direction;

$$\vec{b_1} = 2\pi\frac{\vec{a_2}\wedge\vec{z}}{|\,\vec{a_2}\wedge\vec{a_1}\,|}, \text{and} \tag{2.30}$$

$$\vec{b_2} = 2\pi\frac{\vec{z}\wedge\vec{a_1}}{|\,\vec{a_2}\wedge\vec{a_1}\,|}. \tag{2.31}$$

This is a two-way relation as the reciprocal lattice of a reciprocal lattice is the original Bravais lattice.

The metasurfaces studied in this work are assumed to be periodic in both directions of space, i.e. x and y. That reduces the study of the whole structure to just one primitive unit cell with the appropriate boundary conditions. A primitive unit cell is a region that may be tessellated to fill the space without either overlapping or leaving voids when translated through the vectors of the Bravais lattice. A primitive unit cell contains only one lattice point.

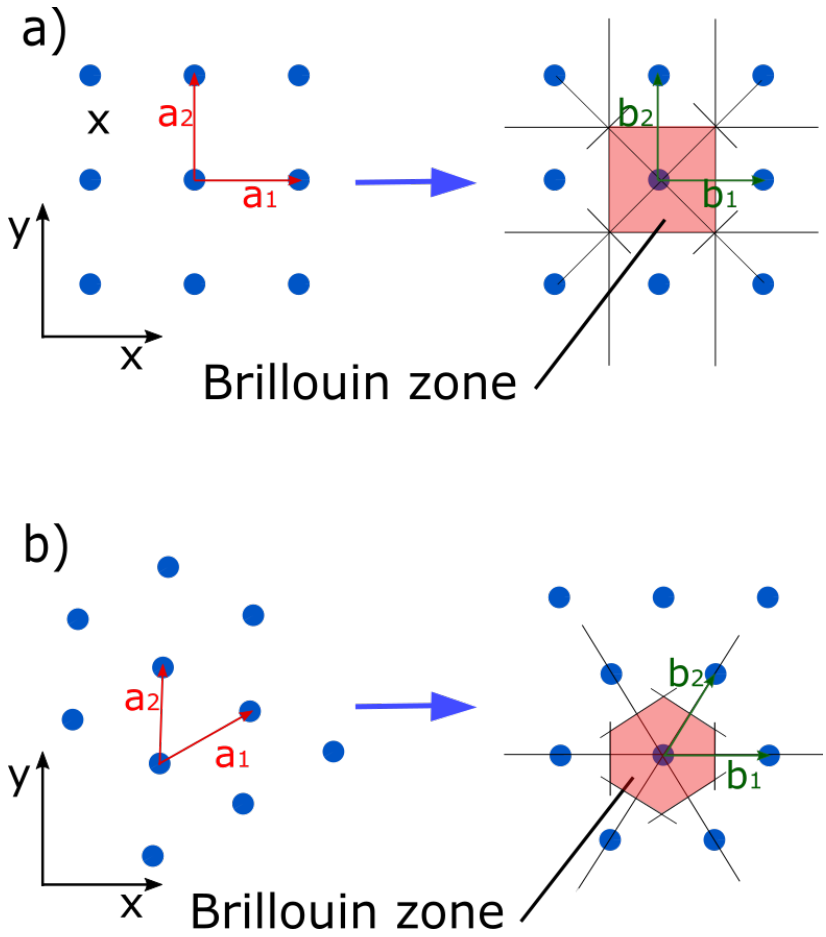

Fig. 2.4 Direct and reciprocal lattices for a square array of elements a) and for a hexagonal array of elements b) The lattice vectors $\vec{a}_n$ are shown in red and the reciprocal lattice vectors $\vec{b}_n$ are shown in green. The blue dots represent the lattice/reciprocal lattice points and the area shaded in red on the reciprocal lattice represents the Brillouin zone.

In the same way, all the relevant information about the structure in reciprocal space is contained in the first Brillouin zone [43]. The first Brillouin zone is the Wigner-Seitz cell of the reciprocal lattice, this is, the group of points that are closer to a given lattice point than to any other lattice point. In Fig. 2.4 the direct and reciprocal lattices for two structures, one with square symmetry and a the second with hexagonal symmetry are represented as well as their correspondent Brillouin zones.

Throughout this thesis, different structures with these two geometries will be studied and the modes they support will be represented in the first Brillouin zone.

2.3.1 Periodic potential and band structure

In a periodic metasurface, the potential $U(\vec{r})$ will also have the periodicity of the Bravais lattice:

$$U(\vec{r}+\vec{R}) = U(\vec{r}), \tag{2.32}$$

According to Bloch's Theorem the eigenstates of the potential can be written as a plane wave weighted by a function with the periodicity of the Bravais lattice [42].

$$\Psi_{n,k}(\vec{r}) = e^{i\vec{k}\vec{r}} f_{n,k}(\vec{r}), \tag{2.33}$$

where

$$f_{n,k}(\vec{r}+\vec{R}) = f_{n,k}(\vec{r}). \tag{2.34}$$

This implies that

$$\Psi_{n,k}(\vec{r}+\vec{R}) = e^{i\vec{k}\vec{R}} \Psi_{n,k}(\vec{r}). \tag{2.35}$$

The wave vector appearing in Bloch's theorem can always be confined to the first Brillouin zone. This is because any $\vec{k'}$ not in the first Brillouin zone can be written as $\vec{k'} = \vec{k} + \vec{K}$ where $\vec{K}$ is a reciprocal lattice vector and $\vec{k}$ lays in the first Brillouin zone.

For electromagnetic fields, the equivalent description is given by Floquet's principle, which implies that when an infinite, planar, periodic structure is illuminated by an infinite plane wave, then every unit cell in the periodic plane must contain exactly the same currents and fields, except for a phase shift, corresponding to the incident field phase. This principle allows all currents, fields and potentials to be written in terms of a modified Fourier series, which consists of an ordinary Fourier series multiplied by the incident field phase [44].

First Brillouin zone

The first Brillouin zone of a structure periodic in the x-direction with a period p is represented in Fig. 2.5. The Brillouin zone extends between $\frac{-\pi}{\mathrm{p}}$ and $\frac{\pi}{\mathrm{p}}$, where p is the period of the lattice, and it is symmetric with respect to the origin. The modes propagating in such periodic structures extend to different Brillouin zones, these are labelled as bands. However, in the reduced Brillouin zone scheme, the different bands are translated into the first Brillouin Zone, where the different regions or bands are delimited by the diffracted and non-diffracted light lines.

In the figure, the first Brillouin zone is delimited by the blue dashed lines. The red lines represent the light lines and the black lines are the modes supported by the structure. The zone shaded blue (below the light lines) is the non-radiative zone while the green zone

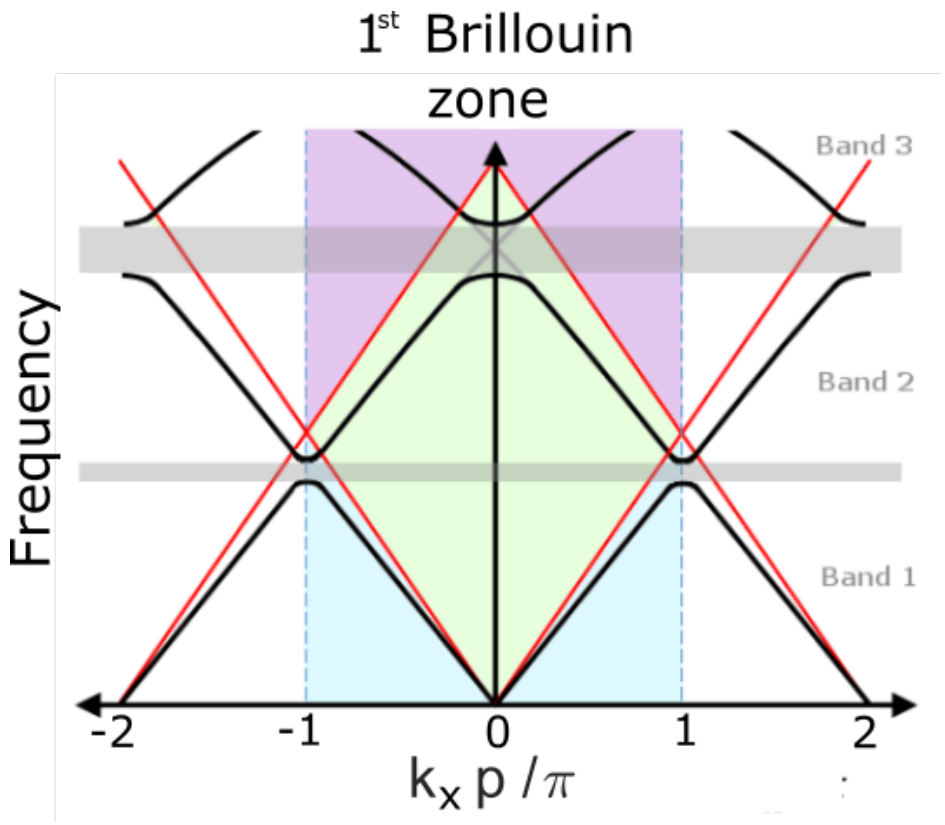

Fig. 2.5 Extended band diagram of a periodic structure in the x direction, the periodicity of the structure is p. The first Brillouin zone is delimited by the blue dashed lines. The red lines represent the light lines and the black lines are the modes supported by the structure. The zone shaded blue is the non-radiative zone while the green one is the radiative zone with only radiation providing from specular reflection and the purple one is also radiative but includes first order diffracted modes. The grey regions mark the ranges of frequency where no modes are supported by the structure (band gaps).

corresponds to the radiative zone with only specular radiation and the area shaded purple is also radiative but also includes first order diffracted modes. The grey regions mark the ranges of frequency where no modes are supported by the structure, known as band gaps.

The modes propagating in the non-radiative region are bound to the surface and cannot radiate as its momentum is mostly in-plane. The velocity at which these modes propagate is slower than the velocity of propagation in free space. On the contrary, in the radiative region, an incident plane wave can couple to the surface mode and these modes can also re-radiate by diffraction. Finally, the purple region corresponds to modes above the onset of diffraction, where specular radiation that transmits through or reflects off the surface is accompanied by diffracted radiation due to the periodicity of the lattice.

Band Gaps

Typical periodically structured metasurfaces present dispersion diagrams with modes that instead of simply crossing at the Brillouin zone boundary split creating band gaps. A band gap is a certain range of frequency at which no propagating modes are supported by the structure.

In a periodic structure with a periodicity p, this splitting is repeated for $k_{\mathrm{X}} = \pm N\frac{\pi}{p}$ and it is due to the existence of two modes in the radiative region corresponding to $k_{\mathrm{X}} = \pm(k_{sw} - k_p)$, one is scattered by $+k_p$ and the other one by $-k_p$. At $k_x = 0$ both modes have a wavelength $\lambda_{sw} = \frac{2\pi}{k_{sw}} = \mathrm{p}$, and they are counter-propagating. This results in two standing waves with the same wavelength but different energy, both with zero group velocity. The result of this splitting is a gap in frequency between the two modes. This situation is repeated every time the wavelength is a multiple of the periodicity of the structure (equivalent to $k_x = N\frac{\pi}{p}$). The difference in energy between the two modes is due to a difference in the charge distribution and in the field configuration, in a similar way to the band structure found in solids [42].

For instance, in a sinusoidal grating, the lower energy solution, corresponds to the situation where the charges are positioned at mid-height of the sinusoidal corrugations while for the higher energy mode, the charges are positioned in the peaks and valleys of the surface.

The energy stored in the system depends on both the charge and field configurations. The standing wave with charges at the peaks and valleys has a greater separation of charges and therefore represents the higher energy state, as the field lines are more distorted. The size of the energy gap depends on the surface geometry and the parameters of the materials forming the structure.

The mentioned band gaps are expected in all structures where the underlying symmetry of the surface is represented by a translation operator, this is, in any periodic structure. However, it will be shown in a later section that under certain symmetry conditions band gaps can be absent.

Phase and group velocities

As previously discussed, the dispersion curve describes the relationship between the energy and momentum of a surface wave. The way in which both quantities are related defines the velocity of the mode. For a wave propagating through a dispersive medium two velocities are defined. The first quantity is defined as the ratio of the angular frequency ω to the in-plane wave vector k and it is known as phase velocity (v_{p}),

$$\vec{v_{\mathrm{p}}} = \frac{\omega}{|\vec{k}|}\hat{k}. \tag{2.36}$$

This is the speed at which the wave fronts advance and it is related to the mode index. $n = \frac{c}{|\vec{v_p}|}$. The group velocity is defined as the first order derivative of ω with respect the in-plane wave vector $(\vec{k})$ and given by the gradient of the dispersion curve.

$$\vec{v_g} = \nabla_{\vec{k}}\omega \tag{2.37}$$

The group velocity is the speed at which a wave can transmit information and hence it is always smaller than the speed of light in vacuum (c). The direction of the group velocity indicates the direction of the power flow and the direction in which energy is being transferred.

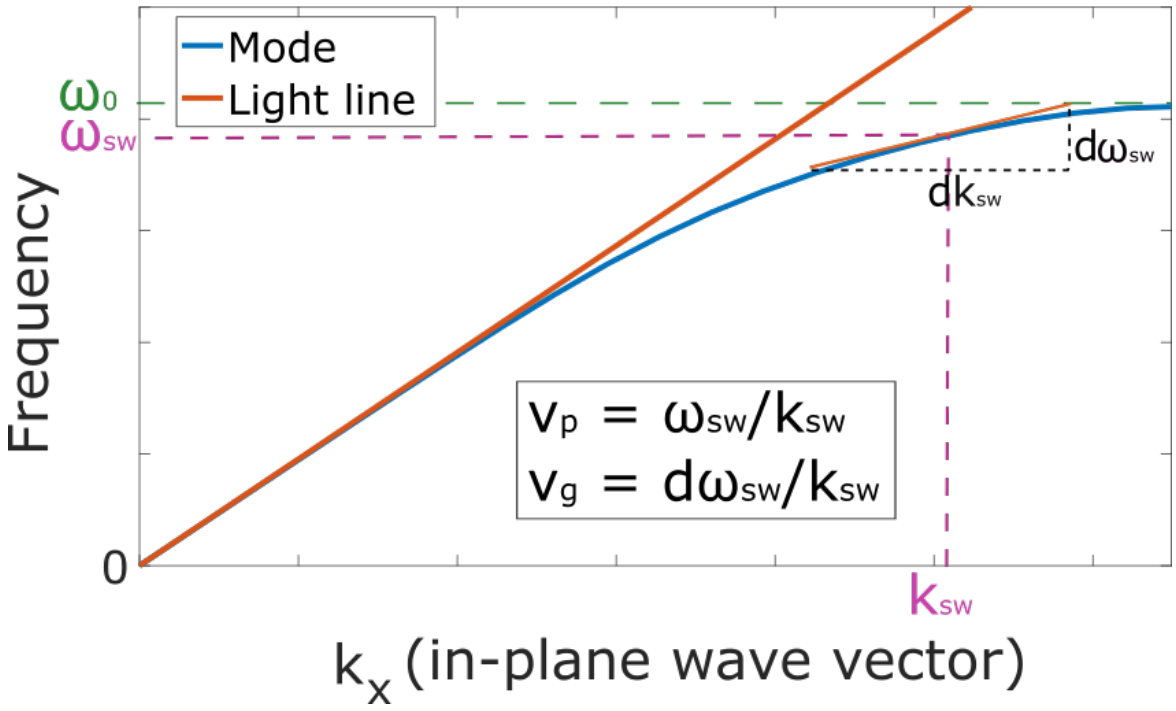

Fig. 2.6 Dispersion diagram of a surface mode propagating in the x direction. The red line represents the light line while the blue line represents the dispersion of the surface wave. The phase velocity and the group velocity of the mode are also illustrated: The phase velocity is given by the ratio of ω to k_x and defines the mode index. The group velocity is the gradient of the dispersion and tends to zero as the wave approaches the Brillouin zone boundary. For the light line, both the phase and group velocity have the constant value c (speed of light in free space).

The phase velocity and the group velocity do not need to have the same direction. For example, this situation is found in metamaterials with negative refractive index [45], or in anisotropic materials exhibiting beaming, [46] where the momentum propagates in all directions (phase velocity) while the energy (group velocity) is channeled in a particular direction or set of directions.

Group velocity and phase velocity are vector quantities, however, it is very common to find a scalar magnitude that represents the component in a particular direction of interest. For instance in the x direction, they would have the form,

$$v_{\mathrm{p}} = \frac{\omega}{k_{\mathrm{x}}} \quad \text{and } v_{\mathrm{g}} = \frac{d\omega}{dx}. \tag{2.38}$$

In Fig. 2.6, the dispersion diagram of a periodic structure (in the x direction) is represented, together with references to the phase and group velocity at a specific point in the dispersion. In the figure, the red line represents the light line while the blue line represents the dispersion of the surface wave, which tends asymptotically to the resonant frequency ω_0. The phase velocity is given by the ratio of ω to k_x while the group velocity is the gradient of the dispersion and tends to zero as the wave approaches the Brillouin zone boundary.

Symmetry

All the metasurfaces considered in this thesis are periodic structures, obtained by applying different symmetry operations. These symmetry operations define the lattice in which the resonant elements are arranged. However, the lattice only defines the primary structure of the metasurface. The different individual resonant elements that sit on the points defined by the lattice may have a different symmetry to that of the lattice. The resonant elements can have a second set of intrinsic symmetry operations, which also plays an important role in the overall behaviour of the modes supported by the structure, giving rise to some properties such as anisotropy and chirality.

According to Neumann's principle [47], the symmetry of a physical phenomenon is at least as high as the crystallographic symmetry [48], this is, the symmetry that is common to the lattice and the individual elements. This can be illustrated by performing some vectorial analysis [49].

Let's consider any vectorial magnitude such as the Poynting vector or the group velocity. If we take any vector originating on the Brillouin zone boundary, we can obtain equivalent vectors by applying the symmetry operations defined by the structure. Those would represent the different vectors arising from the scattering of the surface mode. For example if we consider the black arrow in Fig. 2.7, through reflectional symmetry, one can deduce the red arrows and subsequently though translational symmetry the blue arrows can be obtained. In all three cases, corresponding to different geometries, there is no net magnitude normal to the Brillouin zone boundary. Furthermore, if we were to place the vector at a corner on any of the Brillouin zones, there will not be any net magnitude at all. Those points are known as high symmetry points.

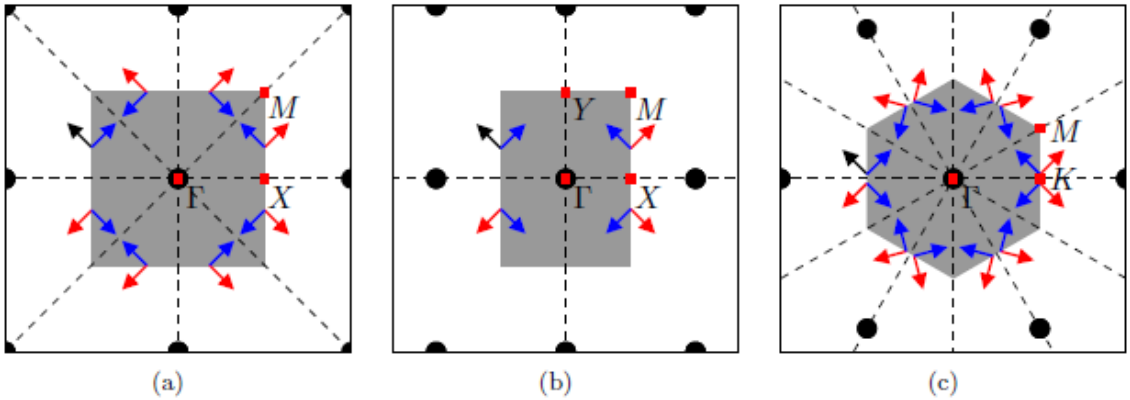

Fig. 2.7 Reciprocal lattices for structures with a) square, b) rectangular and c) hexagonal direct lattices. The dashed black lines represent the symmetry planes of each structure and the grey shadowed area corresponds to the first Brillouin zone. Any vector quantity located on the Brillouin zone boundary (black arrows) can be replicated by symmetry operations: reflection (red), translation (blue) and rotation [50]. In all three cases, once all the symmetry operations have been applied, the vector quantity ends up having no net magnitude in the direction perpendicular to the Brillouin zone boundary.

The results of this analysis show that there will be standing waves associated with these vector quantities in the normal direction to the Brillouin zone boundaries. Therefore, for systems with equal or higher symmetry to that of the lattice, standing waves associated with Bragg scattering form in the Brillouin zone boundaries. In the context of surface waves supported by a periodic structure, this means that the group velocity must tend to zero as the surface mode approaches Brillouin zone boundary for systems possessing such symmetry.

However, in some cases, the symmetry of the lattice does not match the symmetry of the elements that comprise it. An example of this is a 60° rhombic tiling [51].

In this case, the Bravais lattice is hexagonal and therefore the Brillouin zone is the same one as in Fig. 2.7 c). However, the symmetry of the overall system is given by the symmetry lines that are common to the lattice and the structural elements, so in this case only two lines of symmetry are present. The reciprocal lattice and symmetry lines are shown in Fig. 2.8. Following the same procedure as in the previous case, the black arrow, representing any arbitrary vector lying on the boundary of the unit cell, can be reflected and translated into the red and blue arrows respectively. It can clearly be seen that there is no net magnitude normal to the boundary defined by X and M. However as shown in Fig. 2.8, a vector originating at the face defined by M and N will always have a non-zero net component normal to this boundary, since the symmetry of the system does not lead to a cancellation. In particular, this vector can correspond to entities such as the group velocity or the Poynting vector and

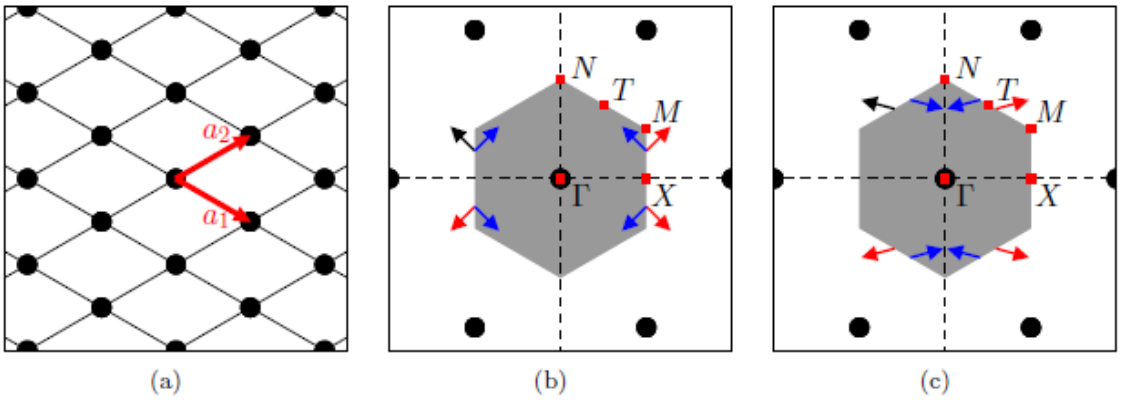

Fig. 2.8 Example of a case, where the symmetry of the lattice and the structure do not match. It consists of an array of 60° rhombuses (a)). The Bravais lattice is hexagonal and therefore the Brillouin zone is the same one as in Fig. 2.7 c). The symmetry of the overall system is given by the symmetry lines that are common to the lattice and the structural elements, so in this case only two lines are seen. Performing the same vectorial analysis as in the previous case, the red and blue arrows are found but in this case the vectorial quantity has net magnitude normal to the Brillouin zone boundary.

therefore, for this system, it is possible to find a nonzero group velocity at the Brillouin zone boundary.

As a result, we can conclude that it is the planes of symmetry common to both the lattice and the elements that dictate the symmetry of the system [43] and hence whether the dispersion of a mode must approach a Brillouin zone boundary with zero group velocity.

2.4 Metasurfaces for wavefront shaping

Traditionally, wavefront shaping elements such as lenses and reflectors have been a key element in optical and microwave devices. The performance of these devices is based on a spatially variable phase delay, acquired by the beam when it propagates through a bulky body. With the proliferation and development of radio communications the requirements for those devices regarding precision and size have increased dramatically. The need to solve these problems encouraged the development of flat and optically thin structures as a tool for wavefront manipulation.

So far, in this chapter, we have only considered periodically repeated metasurfaces, however, in order to introduce a spatially varying phase velocity and to be able to redirect the ray trajectory, aperiodicity needs to be introduced. This aperiodicity may be obtained by gradually changing the geometry of the elements in contiguous cells. In 2012 the term

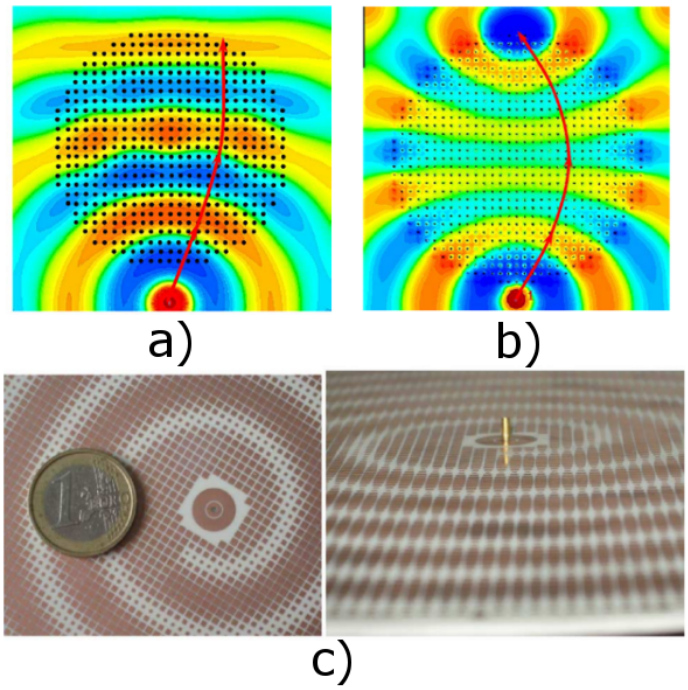

Fig. 2.9 Different flat microwave devices, based on single layer metasurfaces where the geometry of the constitutive elements has been gradually varied. a) represents a Luneburg lens, capable of transforming the cylindrical wave fronts of a point source into plane waves. In b) a Maxwell fisheye is depicted, translating a point source placed at the perimeter of the lens to the opposite side and in c) two pictures of leaky wave antennas built with modulated surface impedance metasurfaces are presented. Depending on the periodicity of the metasurface, the angle of radiation can be chosen [7].

'metasurfing' was introduced by Maci et. al. [7] to refer to a metasurface-driven wavefield configuration transformation. In that study, the use of variable-impedance metasurfaces was proposed for transforming surface or guided waves into different wavefield configurations with desirable properties of various kinds.

The proposed metasurfaces are characterized by inhomogeneous constitutive parameters (impedance, mode index), which impose surface impedance boundary conditions in terms of the ratio of the tangential electric and magnetic fields. It is important to note that often the periodicity of the structure is kept constant while the geometry and the size of the constitutive elements are varied to achieve the desired properties. The effective parameters for each unit cell are obtained under the assumption that each constitutive element of the metasurface is embedded in a locally uniform periodic structure. That is, identifying the local texture and the relevant associated properties (i.e. mode index) with those of a periodic structure that locally matches the geometry.

Different devices have been developed with this technique such as Luneburg lenses [8], Maxwell fisheye lenses [7] or leaky wave antennas [52].

A similar effect can be obtained without the need to know the trajectory of the rays by using transformation optics (TO), developed by J. Pendry in 2006 [53]. However, TO presents some technical difficulties regarding the control of the variation of the homogenized constitutive tensor of three-dimensional metamaterials, together with anisotropy and extreme parameters (such as relative permittivity under unity [54]). These issues complicate its implementation in practical devices, however, in recent years more and more transformation optics devices have been investigated.

2.5 Conclusions

In this chapter, the theoretical basis behind the work carried out in this thesis was presented. This includes the properties of surface modes supported by planar and periodically structured interfaces. The dispersion of modes supported by these structures was discussed as well as important concepts such as band gaps and propagation velocities, which will be of importance in the following chapters. In addition, the concept of graded, non periodic metasurfaces, which will be explored in depth in the following chapters and leads to different metasurface devices was introduced.

In the next chapter, the experimental and numerical tools used throughout the thesis are presented. These include a lithographic technique used to manufacture the samples, the measurement procedure by means of which the surface waves are studied as well as the numerical analysis and simulation tools employed.

Chapter 3

Methods

3.1 Introduction

In this chapter, the experimental and numerical methods, including the fabrication techniques used to produce the different metasurfaces under study in this thesis and the characterization and analysis of the modes they support are presented.

To fabricate the samples, a very simple lithographic technique, presented in section 3.2, is employed. This technique allows the samples to be fabricated in-house in a very short time, providing a cheap way to test and optimize different designs quickly.

To characterize the structures, the surface modes they support need to be excited and measured. The experimental characterization, which requires a Vector Network Analyser (VNA) is discussed in section 3.3. With the VNA the amplitude and phase of the electromagnetic field is recorded but further processing is necessary to obtain the iso-frequency curves and the dispersion diagrams. To do so, a spatial Fourier analysis method, presented in section 3.4 is employed. In this section, the way in which the field profiles of the waves propagating bound to the surfaces are obtained is also discussed.

Finally, in section 3.5, the numerical method used to complement the experimental results as well as to provide a theoretical comparison is presented. All the numerical calculations presented in this work have been obtained using a Finite Element Method (FEM) modelling software, which produces the dispersion diagrams and iso-frequency contours of the modes supported by different structures as well as their instantaneous field plots.

3.2 Sample fabrication: Lithographic technique

The lithographic technique used to fabricate the samples and devices studied in this thesis is a very simple print-and-etch technique. The fabrication procedure is depicted in Fig 3.1. It is a very fast and cheap technique, which allows samples to be fabricated in-house in less than an hour. This procedure uses a Xerox ColorQube printer to print a mask over a copper-coated dielectric sheet (Fig. 3.1 a). This means that the dimensions of the samples are limited to 410 mm by 295 mm (A3 paper) and the resolution of the features is limited by the resolution of the printer, which is no better than 100 µm.

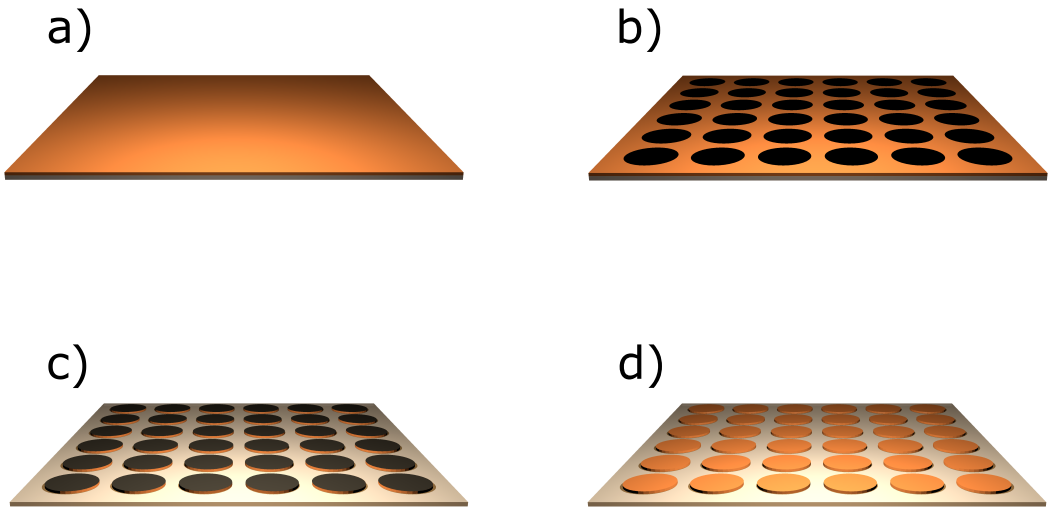

Fig. 3.1 Different stages of the lithographic process used to fabricate the samples. a) represents a sheet of copper laminate on which the mask is printed (b). The exposed copper is then etched (c) and the ink removed (d). The black regions denote the presence of ink while the dielectric is represented as a light grey sheet.

The technique consists on directly printing the desired pattern onto a copper laminated dielectric (Fig. 3.1 a). The Xerox ColorQube uses wax-like solid ink that bonds well to the metallic surface (Fig. 3.1 b). This is used to cover the areas that do not need etching. Following the printing, the sample is submerged in a Ferric Chloride solution (40% vol.), widely used for printed circuit board (PCB) manufacturing. This solution dissolves the unwanted exposed copper (Fig. 3.1 c). Finally, the sample is cleaned using a hydrocarbon based solvent (WD-40), which dissolves the ink, followed by isopropyl alcohol (IPA) to remove all possible residues of oil and dust. The final result is a continuous dielectric sheet

with the desired copper pattern on top (Fig. 3.1 d). All the structures presented in this thesis have been manufactured using GTS 5510. This copper laminate consists of an 18 µm layer of copper on a 25 µm thick dielectric with a permittiviy $\varepsilon = 2.8$, resulting in very thin and flexible structures. However, this technique can be employed for the manufacturing of samples with a dielectric thickness of at least up to 50 µm with different permittivities.

The structures under study in this thesis are generally comprised of more than one layer of copper patches. Due to limitations of the printing method, only single-sided sheets can be manufactured precisely. Double sided copper coated sheets can be used but the alignment of double-sided printing is not accurate enough for the requirements of the structures presented here. Therefore, different single-layered structures need to be aligned and stacked together to make multilayer structures. For that purpose, alignment marks are included in the mask to ensure the different layers can be stacked up precisely. The alignment marks used consist of a triple cross pattern place at each of the four corners of the sample, to show if the layers are misaligned or twisted. Once the sheets are aligned, they are secured in place using duct tape. Finally, to keep the sheets bound together, a thin oil layer is placed between them, taking special care in ensuring that there are no air bubbles inside this oil layer. The oil used for this purpose is 3 in 1 oil, which is cheap and readily available. Due to the high surface tension of the oil, the metasurface sheets (copper and dielectric) are kept together, even when the sample is held vertically. This oil layer acts as a second dielectric layer which increases slightly the separation between the patches and therefore needs to be taken into account as well as its dielectric constant and loss tangent.

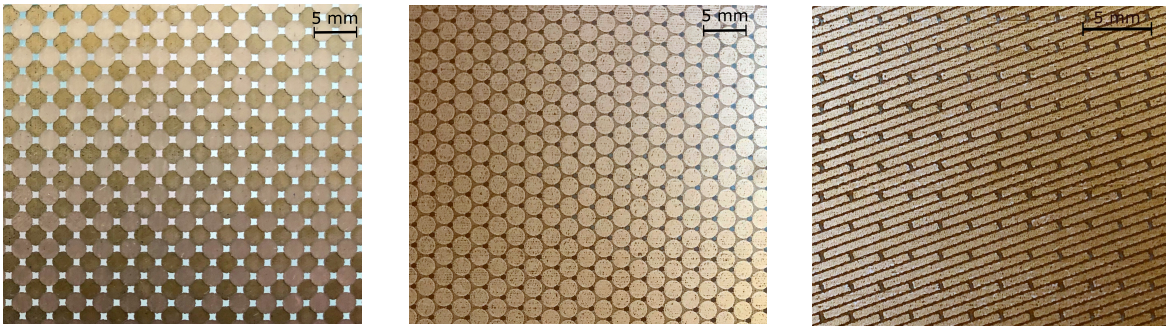

Fig. 3.2 Different samples fabricated using the described lithographic technique. From left to right: bi-layer of circular patches on a square array with glide symmetry (presented in chapter 4), triple-layer of circular patches on a hexagonal (ABC) lattice (studied in chapter 5) and a bi-layer of rotated rectangular strips on a square lattice (studied in chapter 7).

If a higher resolution or a longer durability of the samples was required, this manufacturing process could be replaced by usual printed circuit boards (PCB) purchased from an external manufacturer.

3.3 Measurement of surface waves

The experimental characterization of microwave modes bound to a surface is a key element throughout this thesis. By means of the experimental techniques described in this section, the instantaneous field plots of the modes are obtained as well as their behaviour in reciprocal space (isofrequency contours and dispersion diagrams). For this, further processing in the form of Fourier analysis is required, which will be presented in section 3.4.

The experimental setup used to characterise all the structures in this thesis comprises of a Vector Network Analiser (VNA) and a translational XYZ stage.

3.3.1 Vector Network Analiser

A VNA can, among other things, indirectly measure both the amplitude and phase information of an electric field associated with a surface wave. When an antenna is placed in the proximity of a metasurface, the loops of electric or magnetic field associated with the supported surface wave, induce a current in the antenna. This antenna is used as a probe, which is connected to the VNA. The mentioned current generates a voltage which is assumed to be linear with the strength of the field and is then measured by the VNA.

The measurement of the voltage is processed digitally, resulting in real (I) and imaginary (Q) parts of the original signal. The time-averaged electric field, also known as the amplitude of the electric field (**A**), can be expressed via the I and Q values according to expression 3.1:

$$\mathbf{A} = I^2 + Q^2 \tag{3.1}$$

A VNA internally generates a voltage resulting in a radio frequency (RF) signal that is sampled, transmitted and compared to the signal from the detected voltage. A detailed explanation of the functionality of the VNA can be found in the technical documents provided by the VNA manufacturers [55].

A VNA measures scattering parameters (S-parameters) on a two port system. A ‘port’ is the adaptor from which the RF signal internally generated by a VNA is converted into a mode that can then propagate on a coaxial cable which transports the RF signal for its use on some other device (i.e. an antenna).

The term ‘scattering parameters’ comes from transmission line terminology and describes the results of an electromagnetic wave propagating through free space and experiencing a region of space which can no longer be considered a vacuum. These parameters, which comprise the elements of a matrix known as S-matrix, are used to describe reflection and transmission measurements.

The VNA used to take the measurements in this thesis is a two-port instrument, however, there are VNAs with more than two ports. In the two-port case, the VNA simultaneously measures the ratio of incoming to outgoing radiation for the four possible combinations of the two ports between which, the device under test is placed. These four ratios are the S-parameters and are denoted as S_{mn} where m and n are the receiving and emitting ports respectively. In the cases studied in this thesis, the parameter of interest is the S_{21} parameter, as we are interested in the radiation that couples into modes that propagate towards the detecting probe, across the surface. An schematic of the different S-parameters, showing how they relate to the different transmission and reflection measurements in a two-port VNA system is shown in Fig. 3.3.

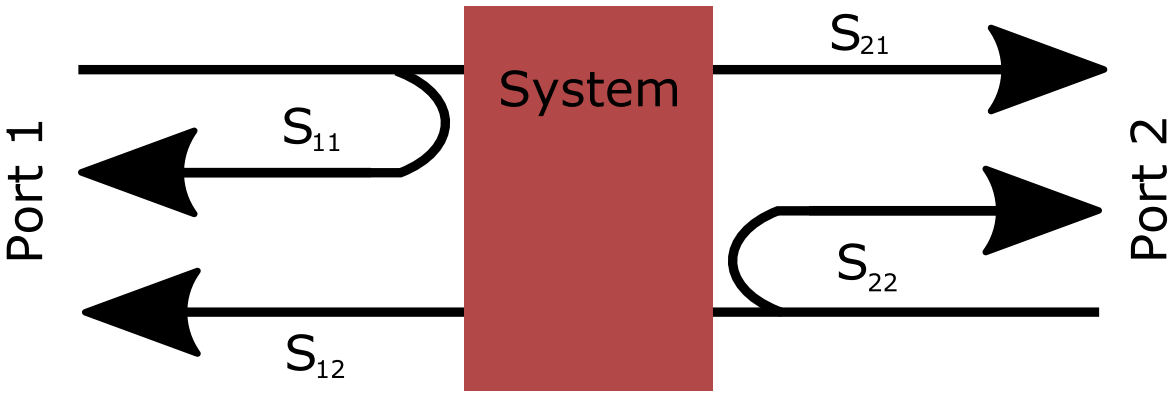

Fig. 3.3 Schematic of the different S-parameters, showing how they relate to the transmission and reflection measurements of a system between the two VNA ports.

The VNA used in this thesis is a two port continuous wave (CW) device which measures reflection at each port and transmission between ports. Due to the CW nature of the device, transmission and reflection can be measured simultaneously as long as the port emitting the signal is the same for both measurements.

3.3.2 Experimental setup

To measure the electromagnetic fields that propagate across the different samples studied in this thesis, a two-port vector network analyzer (VNA) connected to a motorised XYZ stage has been used. The experimental setup is optimized to measure near-field, however, some free space radiation is also detected and needs to be removed from the raw data. In all the experiments performed throughout this thesis, only the value of the transmission between port 1 and 2 is required (S_{21} parameter). This parameter is given in the form of amplitude and phase normalised to an internally referenced signal.

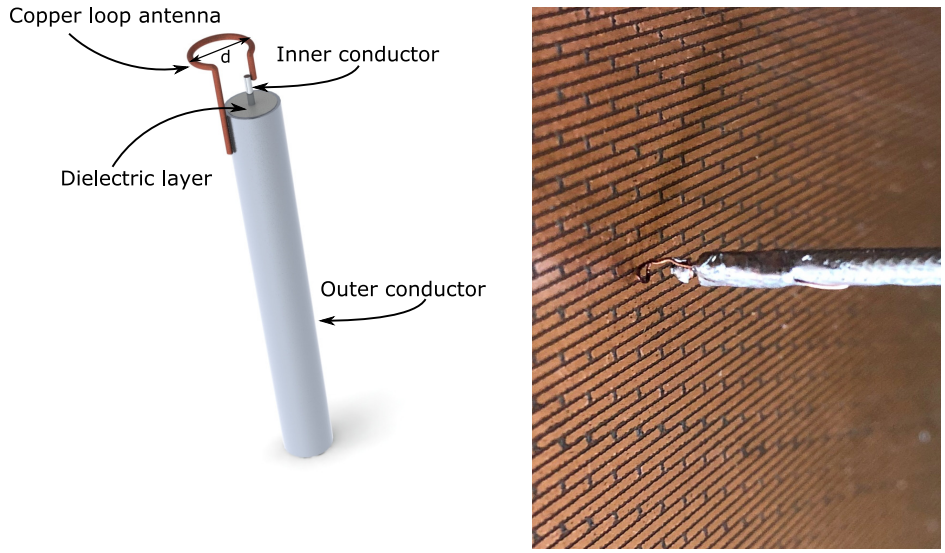

Fig. 3.4 (Left) Sketch of one of the coaxial cables terminated with a loop antenna used to measure the out-of-plane magnetic field of surface waves. The loop antenna is made out of enamelled copper wire and soldered into the outer and inner conductors of the coaxial cable. The diameter of the loop antenna is approximately $d = 1\,\text{mm}$. (Right) Photograph of a sample being measured with a loop antenna attached to a coaxial cable.

To measure the fields propagating along the structure, the supported electromagnetic modes need to be excited with an antenna, acting as a point source on one side of the sample. Meanwhile, to detect the fields a similar antenna is required on the opposite side of the sample. For that purpose, two near-field probes are used.

The two ports of the VNA are connected to two coaxial cables terminated in two very small antennas (near-field probes), which can be treated as point sources. The size of the antennas is important for two reasons, firstly, because they must be used at frequencies below their first resonance and secondly, to minimise the perturbation of the fields that are been measured.

Both antennas are placed very close to the metasurface, within 0.5 mm, in a way that the overlap and subsequent coupling of the fields of the eigenmodes and that of the antenna are maximised. A photograph showing the antenna attached to a coaxial cable is shown in Fig. 3.4 (right). The picture was taken after performing a surface scan of a periodic array of rectangular patches. It can be seen in the picture that the size of the antenna is small compared with the dimensions of the sample and that it is placed very close to the surface.

All the metasurfaces studied in this thesis are multilayer structures, comprised of layers of metallic patches separated by dielectric slabs. These kind of structures possess a field profile where the electric field is strongly confined to the dielectric spacing between the metal

patches making it very difficult to measure. However, the magnetic field extends out-of-plane in loops between the patches in a TE-like field configuration. In this way, two very small loop antennas ($d \approx 1\,\text{mm}$) may be used as source and probe. The antennas are oriented so that the loop is parallel to the plane of the surface, maximising the detection of the out-of-plane magnetic field. A schematic of the described near-field antenna is shown in Fig. 3.4 (Left). The measurement of the fields is possible as the out-of-plane magnetic field of the modes drives an alternating current around the metallic loop.

It is assumed that the presence of the antenna does not affect the field distribution of the modes supported by the metasurface as its scattering cross-section is very small. However, in reality, in the limit of zero perturbation there would be zero overlap of the field (no coupling) and therefore the probe would not detect the surface waves, making it unsuitable. In any case, the dimensions of the antenna (diameter of the loop and length of the vertical wire) are made as small as possible to minimise the effect of the antenna on the surface-waves fields.

The described experimental set up can also be used for the measurement of transverse magnetic (TM) surface waves if the loop antennas are changed for pin antennas, which act as electric dipoles. In contrast to TE surface waves which possess E_y, H_x and H_z components, TM surface waves possess E_x, E_z and H_y so the detection of the out-of-plane electric field needs to be maximised. In this case, it would be the out-of-plane electric field that induces an oscillating current in the central pin of the coaxial cable.

The studies performed throughout this thesis, require the measurement of field maps. For that purpose, the amplitude and phase of the electromagnetic fields need to be recorded for a large number of points (on the order of 10^4) across the sample. This is very time consuming if performed without a motorised translation stage, which also increases the precision and accuracy of the measurements.

In this way, the field maps are recorded using a motorised three-axis translation stage. This stage has a range of motion of $1200\,\text{mm} \times 1200\,\text{mm} \times 1200\,\text{mm}$ with a positional accuracy of $100\,\mu\text{m}$. However, due to the 2-dimensional nature of the structures under study, only displacement in two spacial directions is required, as the probe is kept always at the same distance from the surface.

For all the experimental measurements performed in this thesis, the samples are mounted vertically, attached to a perspex frame. This frame is attached to one of the sides of the structure containing the motorised arm, as shown in Fig. 3.5.

The antenna used as a source is placed on the outer side of the sample and is fixed during the whole measurement. This configuration is shown in Fig. 3.4 (right). The antenna used as a probe is attached to the motorised arm and moves in y and z directions scanning the whole surface of the sample. The scan is performed in a Cartesian grid, in steps of 1 mm,

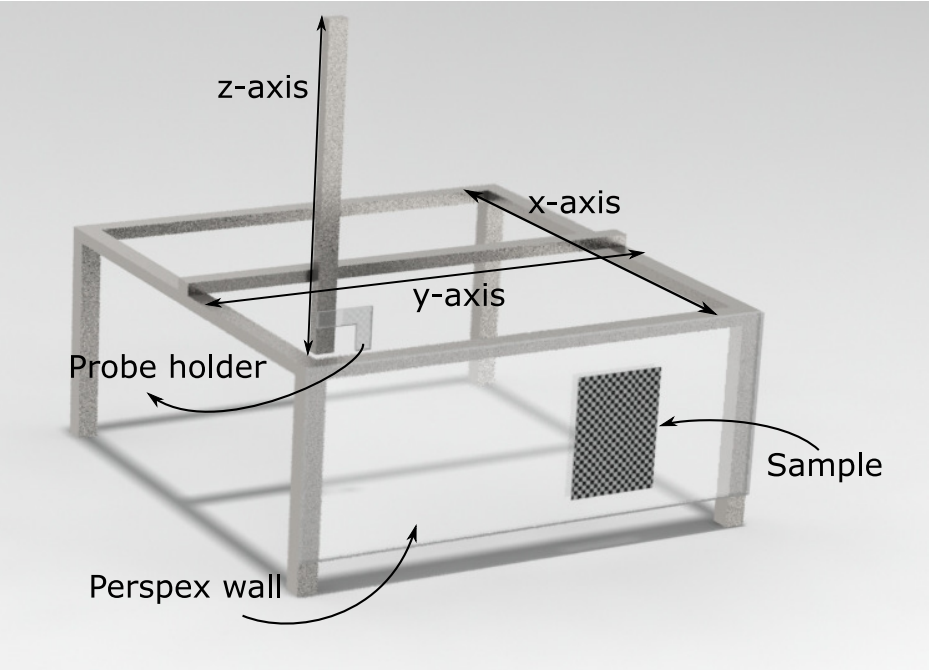

Fig. 3.5 Schematic of the XYZ motorized stage used to perform the field measurements. It consists of a metallic structure with a motorised arm that can move in a Cartesian coordinate grid. The sample is attached to a perpendicular perspex wall with a sample-size (A3) cutout. The probe (which has not been included on this schematic) is attached to the motorised arm via a perspex holder. The source is placed close to the sample on the outside of the structure using a separate retort stand.

leaving enough time between measurements to enable the arm to move and stop vibrating before recording the next measurement (this is usually of the order of 1 second between measurements).

The mount to which the near-field probe is held is also made of perspex, minimising the presence of metallic elements in the proximity of the sample and probes, and so minimising unwanted scattering.

As mentioned before, the antennas used as source and probe are attached to two coaxial cables, connected to two ports of a VNA (Anritsu VectorStar MS4644A).

Each S-parameter is a complex value representing the magnitude and phase of the incoming signal referenced to the outgoing signal. The mentioned VNA records the S-parameters for frequencies in the range between 100 MHz and 40 GHz in steps of 100 MHz. By measuring the phase and amplitude of the transmission coefficient (S_{21}) at points across the surface, the instantaneous field map of the radiation propagating across the surface is obtained. The electromagnetic field is an oscillating wave whose amplitude ($|E|$) and phase (ϕ) are directly measured with the VNA. By combining these two measurements, the

instantaneous field can be defined as:

$$\text{Field}_{\text{inst}} = Re(|E|e^{i\phi}) \tag{3.2}$$

Fig. 3.6, shows these three relevant magnitudes (amplitude, phase and instantaneous field map), measured for a metasurface placed in vertical position (as depicted in Fig. 3.5) using two loop antennas. The measurements correspond to a three-layer metasurface with circular patches in a hexagonal array (Structure studied in chapter 5). The structure has a periodicity of $p = 2.4\,\text{mm}$ and the patches have a diameter $d = 2.1\,\text{mm}$.

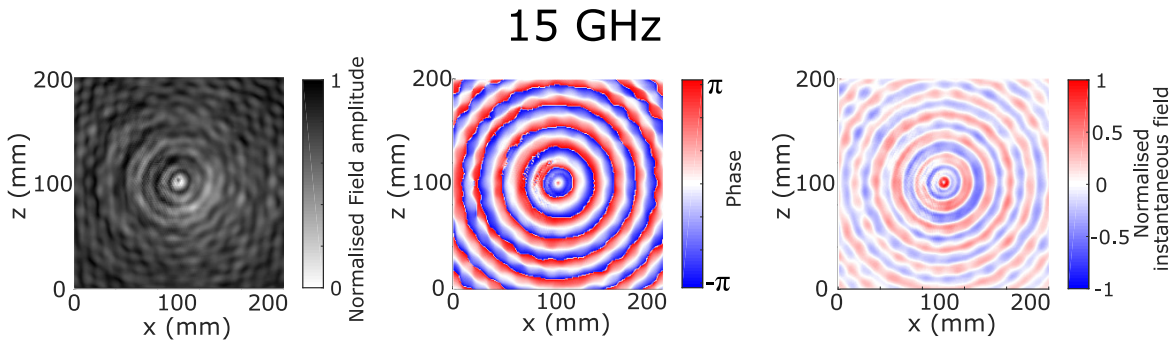

Fig. 3.6 Different magnitudes measured using the described experimental setup (VNA, near field probes and XYZ stage). From left to right, amplitude of the electric field ($|E|$), phase (ϕ) and finally, the instantaneous field map obtained as a combination of both. All the plots correspond to the scan of a three-layer metasurface with circular patches in a hexagonal array (Structure studied in chapter 5). The structure has a periodicity of $p = 2.4\,\text{mm}$ and the patches have a diameter $d = 2.1\,\text{mm}$.

Depending on the type of probe used, the predominant field would be E_z, for an electric probe (pin antenna) or H_z if a magnetic probe (loop antenna) is used. However, the probes do inevitably pick up some of the other components as well. For all the structures studied in this thesis a magnetic probe has been used, so the fields measured would mostly correspond to H_z.

3.4 Reciprocal space and Fourier analysis

In this section, the method used to analyse the experimental data, taken as described in section 3.3 is presented. With this method, the iso-frequency contours and dispersion diagrams of the modes supported by different metasurfaces are obtained.

The instantaneous field plots obtained from the VNA measurements are a combination of contributions from the different modes supported by the structure at a determined frequency plus reflections from the edges and any kind of radiation present in the surrounding space that interferes with the modes. This complicates the extraction of useful information from the measured data. To have a better understanding of the measured data, a spatial Fourier transform is performed. This retrieves the information regarding the periodicity of the fields (i.e. the wave vectors), allowing one to differentiate the different modes propagating in the structure and separating them from the unwanted reflections and interference.

The data taken with the VNA is well defined in frequency (to the degree of accuracy limited by the VNA) and measured in space. A spatial Fourier transformation reveals the wave vector composition of the signal.

Throughout this thesis, both one-dimensional and two-dimensional field measurements have been performed. In all cases, this is followed by Fourier analysis of the measured data, which, as described below, can vary slightly depending on the nature of the measurement and the device being studied.

3.4.1 1D Measurements

In some cases, for instance when the wave propagates only in one dimension, or to shorten the measurement time, a one-dimensional analysis of the structure is sufficient to determine the dispersion diagram of the modes.

For this type of measurement, only one line of data is taken using the experimental setup described in section 3.3. As it was described, the source is placed on one side of the sample but only one line of points is scanned on the opposite side. A diagram showing this experimental set up is shown in Fig. 3.7. Once the instantaneous field plot is obtained using equation 3.2, a one-dimensional Fast Fourier Transform (FFT) algorithm is performed.

To calculate the Fourier Transform of the measured field maps, the built-in FFT function in MATLAB (‘fft’) is employed. This function provides the complex Fourier amplitudes present in the measured signal, given the wavevectors to which they correspond as input arguments. To obtain the experimental dispersion diagram, the normalised amplitude of the Fourier coefficients is plotted as a function of frequency and wave vector. The maxima of this two-dimensional plot corresponds to the dispersion diagram of the modes.

The wave vectors required as input arguments for the ‘fft’ function are determined straight forwardly as the size of the step between measurement points and the total length scanned are well known.

The maximum accessible wave vector is determined by the step-size (separation between measurement points) as shown in equation 3.3 where Δx is the step-size. This wave vector

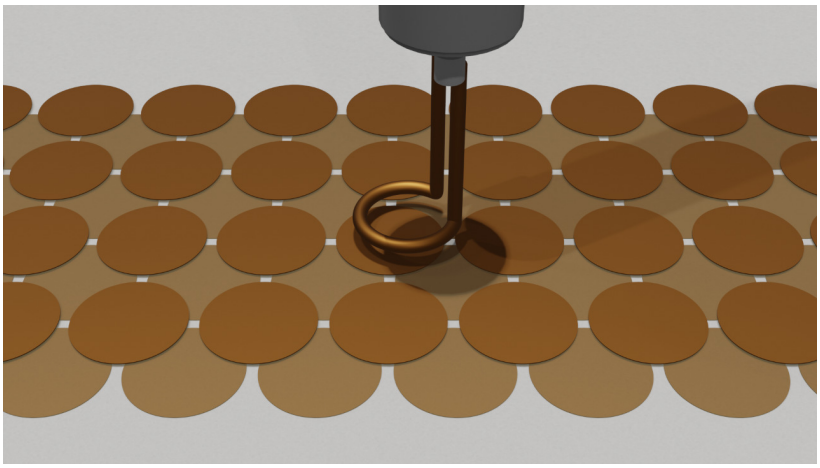

Fig. 3.7 Diagram showing the set up used to perform one-dimensional measurements. In the figure, the sample is a strip constituted of two layers of a metasurface with circular patches in a square array. The strip is four patches wide and can be considered infinitely long. The top layer is displaced by half of the period with respect to the first one in both horizontal directions. To take the measurement, a loop antenna attached to a coaxial cable is used. The antenna is oriented so that the plane of the loop is parallel to the sample.

corresponds to the point at which a half wavelength can fit in this increment and therefore, to the smallest wavelength that can be resolved.

The resolution achieved in reciprocal space (Δk) is determined by the total length of the scanned region (L), as shown in equation 3.4. Hence, in order to maximise the resolution within the first Brillouin zone of the dispersion, the scan should cover as many unit cells as possible. In terms of step size, being able to obtain two measurement points per unit cell, such that $k_{\max} = \frac{2\pi}{p}$ where p is the periodicity, ensures that the resulting dispersion covers both the first and second Brillouin zones.

$$k_{\max} = \frac{\pi}{\Delta x} \tag{3.3}$$

$$\Delta k = \frac{2\pi}{L + \Delta x} \tag{3.4}$$

Depending on whether the data set consists of an even or odd number of points (n), the wavevectors that are sampled within the spectrum are determined according to equation 3.5:

$$\begin{aligned} &k \in \{-k_{\max}, -k_{\max} + \Delta k, \ldots, k_{\max}\} \quad \text{even n} \\ &k \in \{-(k_{\max} - \frac{\Delta k}{2}), -(k_{\max} - \frac{\Delta k}{2} + \Delta k), \ldots, (k_{\max} - \frac{\Delta k}{2})\} \quad \text{odd n} \end{aligned} \tag{3.5}$$

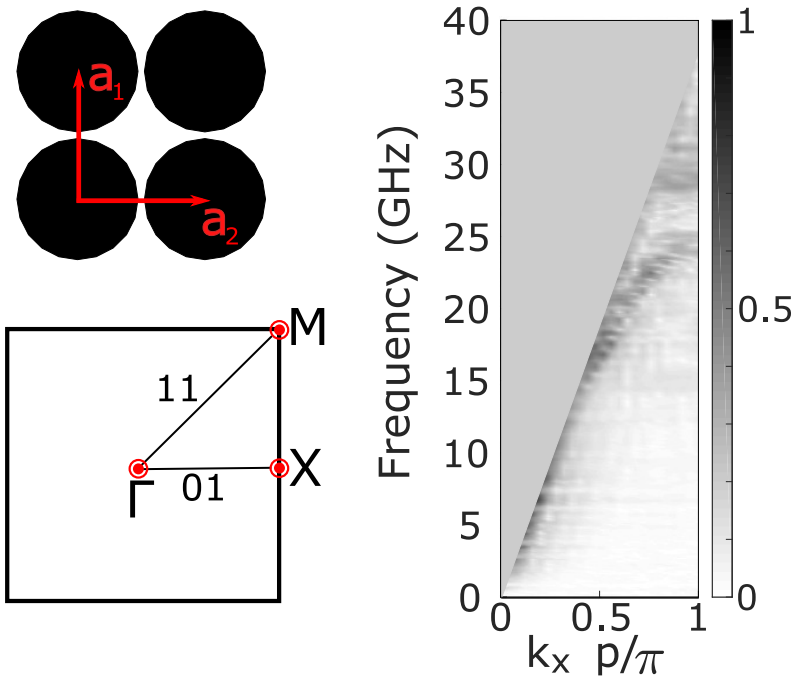

Fig. 3.8 Normalised Fourier amplitude, obtained after performing a 1D Fourier transform to a line of scanned data. It represents the one-dimensional experimental dispersion diagram of the modes supported by a single layer of circular patches in a square array. The dispersion diagram represents only the propagation in the horizontal direction, as only one line of data has been analysed. The shaded area corresponds to the radiative domain which lacks of interest in this case. On the left hand side, a diagram of the structure and a sketch of the first Brillouin zone are also included.

This kind of one-dimensional measurements can be performed when the propagation of the waves across the structure is isotropic or when the mode is known to propagate in just one dimension (as in the case of an edge mode, see chapter 8). However, generally, the propagation of wave modes across a metasurface is subject to some kind of anisotropy and therefore, a two dimensional analysis of its Fourier components is required.

In fig 3.8 the dispersion diagram obtained from the one-dimensional Fourier analysis of a metasurface is presented. In this case, it corresponds to the dispersion diagram of the modes supported by an infinite array of circular patches arranged in a square lattice. Only one line of data has been measured to illustrate that a quick measurement is enough to obtain sufficient data to determine the dispersion of the modes supported by the structure in the horizontal direction.

However, as it will be shown in the next section, the quality of the dispersion plots is improved when a two-dimensional scan is performed for which the information is also not only limited to a single direction.

3.4.2 2D Measurements

The main aim of this thesis is to study the propagation of waves across two dimensional structures. The propagation characteristics of the modes are determined by the collective resonances of the elements comprising the structures, which give rise to effective media properties. However, neither the elements nor their arrangement in space are perfectly isotropic. This means that the propagation characteristics vary for the different directions of propagation.

In order to capture all the components of the wave vector of the propagating wave, a 2D scan followed by a 2D Fourier analysis needs to be performed. The procedure is very similar to that described before for a 1D Fourier analysis. However, in the two-dimensional case a surface area of the sample is scanned, recording the amplitude and phase of the electromagnetic field for every point of a Cartesian grid as shown in section 3.3 and obtaining an instantaneous field map equivalent to that shown in Fig 3.6.

Following the measurement, the data is processed performing a two dimensional Fast Fourier Transform. In this case, applying the built-in MATLAB function 'fft2'. The function requires the two dimensional grid with the sample values for the wavevectors, which, as in the previous case, is calculated manually.

The wavevectors (k_{X} and k_{Y}) are calculated in the same way as per the 1D case. Again, the resolution of the measurement in reciprocal space is determined by the size of the scanned surface and the maximum accessible wave vector by the step-size of the measurement.

$$\begin{aligned} k_{\mathrm{Xmax}} &= \frac{\pi}{\Delta x} \qquad & \Delta k_{\mathrm{X}} &= \frac{2\pi}{L_x + \Delta_x} \\ k_{\mathrm{Ymax}} &= \frac{\pi}{\Delta y} \qquad & \Delta k_{\mathrm{Y}} &= \frac{2\pi}{L_y + \Delta_y} \end{aligned} \tag{3.6}$$

The 2D fast Fourier is performed on the real part of the instantaneous field map at every measured frequency. It returns a 2D matrix containing the complex Fourier amplitudes of the two-dimensional wavevector spectrum. The surface plot of the absolute value of this gives the isofrequency contours, associated with the modes, at that particular frequency.

The geometry and symmetry of these plots is determined by the periodic lattice of the structure. Their features form a periodic array according to the reciprocal lattice vectors where the different Brillouin zones can be defined. In the isofrequency contour plots, we can distinguish two sets of features. In the first place, we find a dark circle, corresponding to grazing radiation propagating in free space, known as the light circle, everything inside this light circle is free radiation. Secondly, we find bound surface modes, these are the

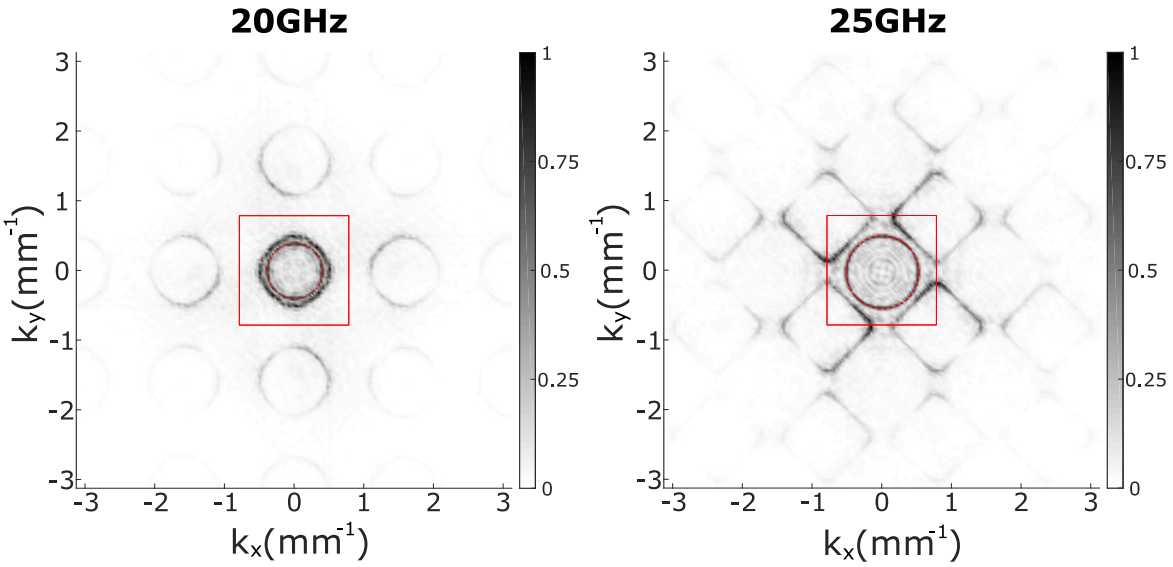

Fig. 3.9 Normalised Fourier amplitude, illustrating the isofrequency contours at 20 GHz and 25 GHz for an array of circular patches in a square lattice. In real space, the period of the structure is $p = 4$ mm and the diameter of the patches $d = 3.6$ mm. The light line is represented as a dotted red circle and the first Brillouin zone is represented by a red square.

features of interest for the research conducted in this thesis and appear outside of the circle, corresponding to radiation with a higher in-plane momentum. As we are only interested in modes that propagate bound to the surface, the information that appears inside the light line can be discarded.

The isofrequency contours plots obtained at two different frequencies (20 GHz and 25 GHz) for a periodic array of circular patches in a square lattice is presented in Fig. 3.9. In real space, the period of the structure is $p = 4$ mm and the diameter of the patches $d = 3.6$ mm. In these plots, the light circle is represented as a dotted red line and the first Brillouin Zone is denoted by a red square. It can be seen how the features are repeated with the periodicity of the reciprocal lattice and how the square lattice affects the geometry and shape of the features.

Finally, the dispersion diagrams are obtained by repeating this procedure for all the measured range of frequencies. Subsequently, the dispersion diagram is a three-dimensional plot, where the z-axis is frequency. This can be simplified by taking cuts in the different directions of interest in k-space. The chosen directions usually coincide with the directions of high symmetry of the structure and are therefore determined by the symmetry of the reciprocal space lattice. The final result is a surface plot containing the Fourier amplitude as a function of the frequency and the in-plane wave vector. This data is normalised so that the contrast of the different features is maximised.

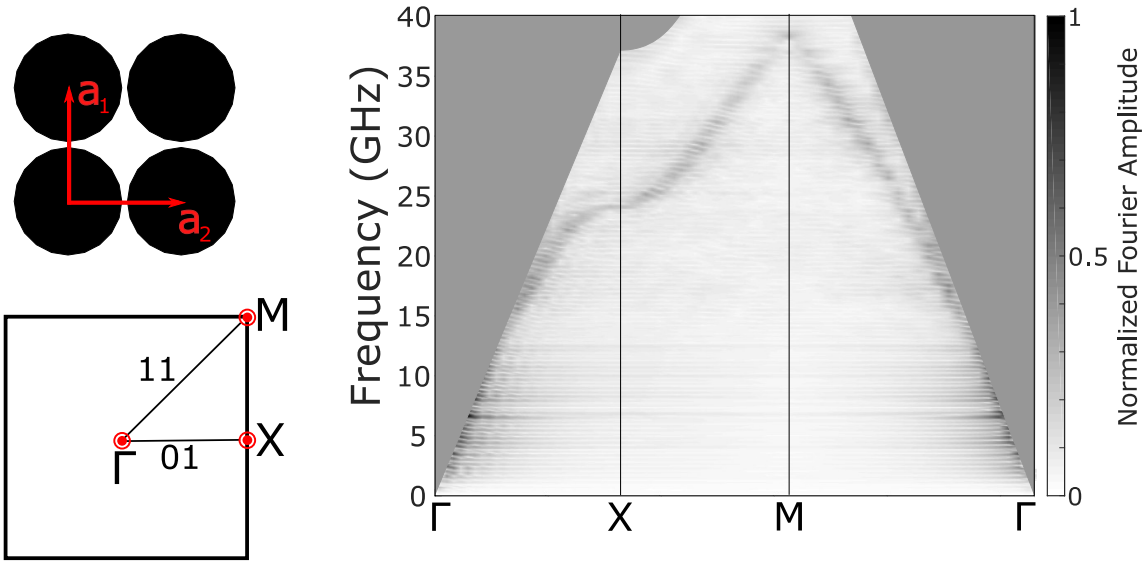

Fig. 3.10 Normalised Fourier amplitude, obtained after performing a 2-D Fourier transform of the fields scanned over a surface. It represents the dispersion diagram of the mode supported by a single layer of circular patches in a square array. The dispersion diagram is represented for three high-symmetry directions of the structure. On the left hand side, diagrams of the structure in real-space and of the Brillouin zone, highlighting the three directions of interest, have also been included.

In Fig. 3.10 the Fourier amplitude data, illustrating the dispersion diagram of the modes supported by the same two dimensional square lattice of circular patches that was mentioned before is presented. On the left, a sketch of the lattice and the first Brillouin Zone are also included. In this dispersion diagram only three directions have been considered. The area corresponding to the radiative modes has been shaded as it is of no interest for this work.

3.4.3 Analysis of field measurements

Throughout this thesis, different metasurfaces will be used to tailor the propagation of surface waves. To check the performance of the such devices, the profile of the electromagnetic fields propagating across the structure will have to be measured. However, as was mentioned before, since our samples are finite in size, surface waves are reflected from the edges. These reflected waves in addition to some free space radiation are also detected by the near field probe, masking the wanted surface wave fields.

However, this can be solved by performing a Fourier analysis which allows one to differentiate the unwanted radiation from the studied surface modes. In this way, the unwanted radiation can be removed from the raw data, resulting in a clearer plot of the surface modes bound to the structure.

To do so, firstly, the instantaneous field map is obtained, as described in section 3.3; then, a fast Fourier transform is performed to the instantaneous field, obtaining the isofrequency contours (see section 3.4.2). In the isofrequency contour plots, it is easy to differentiate between the radiative modes and the bound surface modes as the latter have higher in-plane wave vector. By removing a circular shape of points from the isofrequency contour data, covering the light circle, we make sure that all the remaining data is non-radiative.

Zero-padding, together with a Hamming window must also be applied to the measured data in order to minimize artefacts introduced by the Fourier transform. Finally, an inverse Fourier transform is performed to go back to real space, where the instantaneous field plots of only the modes bound to the surface are now represented. Generally, the resulting field profile is normalised to the highest value of the amplitude and presented as a color-plot, ranging between -1 and 1.

3.5 Numerical modelling

Numerical simulations are an essential part of the work undertaken during this PhD. Firstly, they are a fast and inexpensive way of predicting future experimental results. They are also a good way to optimise designs, as the different parameters can be easily modified and finally, they also provide a better understanding of the physical behaviour of the structures as the electromagnetic fields inside them, otherwise inaccessible, can be visualised.

Throughout this thesis, the commercial software COMSOL multiphysics has been widely used. The simulations performed can be divided in two main categories: 'eigenmode simulations' and 'frequency domain simulations'. The eigenmode simulations are used to obtain the field profile and the dispersion diagram of the modes supported by different infinitely periodic structures, where all the elements are identical. The second type of simulation is used to obtain an approximation of the behaviour of a bigger structure, where the size of the elements is tailored to give a particular effective permittivity profile. In both cases, the numerical method used is a Finite Element Method modelling, where the structure is meshed and the problem solved for each of the small mesh elements.

3.5.1 Finite Element Method

The finite element numerical method tackles the problem of solving the electromagnetic field for a complex geometry, big in comparison to the wavelength of operation, by dividing it into small elements and solving Maxwell's equations at the boundaries between the elements. The small finite elements are usually tetrahedral and are collectively called a mesh. The

choice of the mesh plays an important role in the simulation, as it will determine how well and how quickly the software converges to a solution.

In Fig. 3.11 a meshed structure and a close-up of one of the tetrahedral mesh elements is shown. It can be seen that the mesh elements are smaller in the areas close to the metasurface, where the electromagnetic fields are stronger and its variation is more pronounced. In general terms, the resolution required is in the order of ten mesh elements per wavelength. It is important to find a trade-off in terms of the element size and computation speed. The mesh elements must be small enough to converge to an accurate solution while ensuring the computation time is optimized.

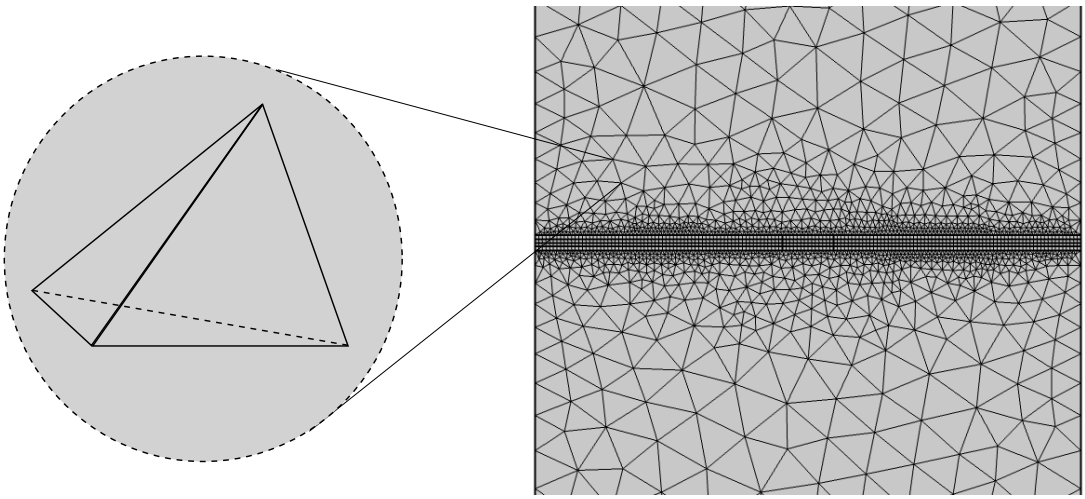

Fig. 3.11 Meshed surface with a close up of a typical tetrahedral mesh element. This mesh contains two types of elements. The majority are tetrahedral, however, the part corresponding to the dielectric spacing has been meshed using a sweep, resulting in polyhedral elements.

For thin periodic surfaces such as metasurfaces, the fields decay very quickly as we move away from the surface. In particular, for the structures studied in this thesis, this decay distance is of the order of the hundreds of microns. For this reason, the mesh can be made coarser for the rest of the space surrounding the structure.

Throughout this thesis, several multilayer structures are modelled. The most effective way of meshing these structures is by ensuring all the different layers have identical mesh elements. This is achieved by a 'sweep', where only the top layer is meshed and then the mesh is extended to the layers below. An example of an structure meshed in this way is shown in Fig. 3.11.

Typically, Maxwell's equations are solved for the electric field ($\vec{E}$), as given in equation 3.7. The relative permittivity and permeability ($\underline{\underline{\varepsilon}}$ and $\underline{\underline{\mu}}$) are given as input parameters to the model and can be defined as completely generalised anisotropic matrices,

$$\vec{\nabla} \times \underline{\underline{\frac{1}{\mu}}}(\vec{\nabla} \times \vec{E}) - k_0^2 \underline{\underline{\varepsilon}} \vec{E} = 0. \tag{3.7}$$

Once the equation has been solved for the full mesh, a scattering matrix is derived and the eigenvalues λ_{ef} of the system are obtained. The calculated electric field can be the expressed as,

$$\vec{E}(\vec{r},t) \; = \; Re(\tilde{\vec{E}}(\vec{r})e^{-\lambda_{ef}t}), \tag{3.8}$$

where $\tilde{\vec{E}}(\vec{r})$ is a phase vector representing the complex time-invariant electric field.

This is applicable to the two types of simulation that have been carried out throughout this thesis. In the next sections, the particular details of each of these are explained.

3.5.2 Eigenmode solver

Most of the structures studied throughout this thesis are two-dimensional infinitely periodic arrays. This means that they can be modelled as a single unit cell with periodic boundary conditions, which simulate the response of a periodic array. This reduces the size of the structure that needs to be modelled, in consequence reducing the solve time. In the commercial software COMSOL multiphysics, periodic faces are defined as boundary conditions in the Radio Frequency (RF) module. To define a Floquet periodicity between two opposite faces of the structure, the reciprocal wavevectors need to be defined as an input parameter, corresponding to the lattice vectors of the reciprocal lattice. When periodic boundary conditions are defined between two faces, the field is forced to be identical at every pair of points on the periodic faces. This means that the faces need to be meshed in the same way so that equivalent points can be found on both faces.

The eigenfrequency solver calculates the resonances of the structures associated with a given phase difference between the Floquet boundaries, which defines an in-plane wave vector. In this way, if the process is repeated for different in-plane wave vectors, the dispersion diagram of the modes supported by the structure can be determined. It is also possible to make changes in the solver to calculate the resonances of the structure for a particular given frequency and in that way, a plot of the isofrequency contours can be obtained.

An example illustrating the use of the eigenmode solver is presented in Fig. 3.12. It shows the different boundary conditions required by the COMSOL's eigenvalue solver to calculate the modes supported by an array of patches in a square lattice. Firstly, periodic boundary conditions are defined on the vertical walls (a) and b) in the figure). The central area corresponds to the metasurface: c) and d) represent the areas corresponding to the

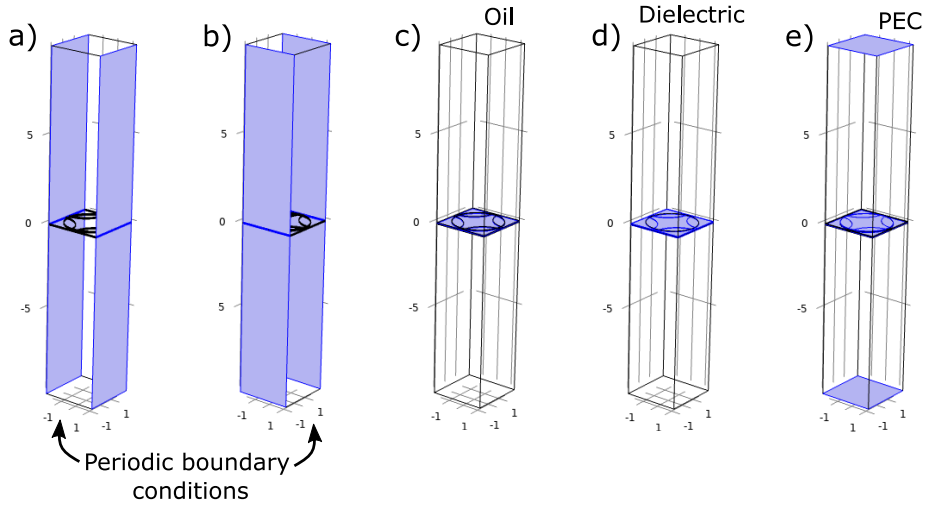

Fig. 3.12 Different boundary conditions defined in a COMSOL model to obtain the eigemodes supported by a periodic structure. Periodic boundary conditions are defined on the vertical walls (a) and b)). c) and d) represent the areas corresponding to the dielectric and the oil layers respectively, where the appropriate permittivity, permeability and conductivity are defined. Finally, a perfect electric conductor (PEC) boundary condition is defined on the top and bottom layers and in the area corresponding to the metal patches.

dielectric and the oil layers respectively, where the appropriate permittivity, permeability and conductivity are defined. Finally, a perfect electric conductor (PEC) boundary condition is defined on the top and bottom layers and in the area corresponding to the metal patches. The function of the top and bottom PEC layers is no other than to delimit the area over which the electric field is calculated. They are placed far enough from the metasurface to ensure that the electromagnetic field has a zero net value and they do not interfere with the modes supported by the metasurface.

3.5.3 Frequency domain (driven) models

The second group of simulations performed in this thesis, are those used to investigate the response of a system when it is excited at a given frequency. In this case the S-parameters are calculated, obtaining equivalent data to that measured with the VNA.

This type of simulation, for instance, can provide a model of the performance of graded index devices, which comprise large areas of metamaterial elements. In this case, a simplification of the model is needed as including all the different metamaterial elements results in a model that would be too computationally heavy.

The simplification performed consists in substituting the metamaterial layer by a surface with a given impedance. An impedance-sheet provides a non-dispersive boundary condition,

which defines the effective index of the mode supported by the structure for each point. The mode index is directly related to the surface impedance and can be fed into the model as a function of position. Therefore, this is a straightforward way of modelling graded index devices. The impedance is given as $Z = R + i\chi$, where χ is the reactance and R is the resistance, which acts simply as damping and is negligible for low-loss systems.

The way in which the mode index is related to the surface impedance is derived directly from Maxwell's equations and is slightly different for TE and TM waves as shown in equations 3.9 and 3.10. To define an impedance boundary condition, the effective permittivity (ε), permeability (μ) and conductivity (σ) of the effective surface need to be provided. Here, we assume that the magnetic response of the structures is negligible and therefore $\mu = 1$. In the case of the permittivity, it is obtained from the impedance and therefore directly related to the mode index of the metasurface (see equations 3.9 and 3.10).

$$Z_{TE} = \frac{1}{\sqrt{\varepsilon_{TE}}} = \frac{\eta}{\sqrt{1 - n_{TE}^2}} \tag{3.9}$$

$$Z_{TM} = \frac{1}{\sqrt{\varepsilon_{TM}}} = \eta\sqrt{1 - n_{TE}^2} \tag{3.10}$$

where η is the impedance of free space.

The conductivity of the effective medium also needs to be included in the model, in this case a small value is chosen ($\sigma = 1\text{e}^{-10}$ S/m). It is important to highlight that the values of permittivity, permeability and conductivity are not characteristics of the metasurface but quantities that are obtained from the impedance and are needed as input arguments of the model.

An example of a model representing a Luneburg lens modelled as an impedance sheet is shown in Fig. 3.13. The impedance sheet (bottom layer) is divided into two sections and encapsulated inside a box.

To model the impedance profile of a metasurface layer containing a Luneburg Lens (or a graded device of any kind), two regions with different impedance profiles need to be defined: the background and the device (in this case the Luneburg lens). As a Luneburg lens is a circular device, the model includes a circular region where the impedance varies radially, according to the profile of a Luneburg lens. For the rest of the structure, a continuous impedance, corresponding to the background mode index is defined.

For this kind of model, an excitation source is required. For planar surface devices, the excitation chosen is a point source. In particular, a point magnetic dipole was chosen in this case in order to excite a TE surface-wave, similar to the one supported by our metasurface.

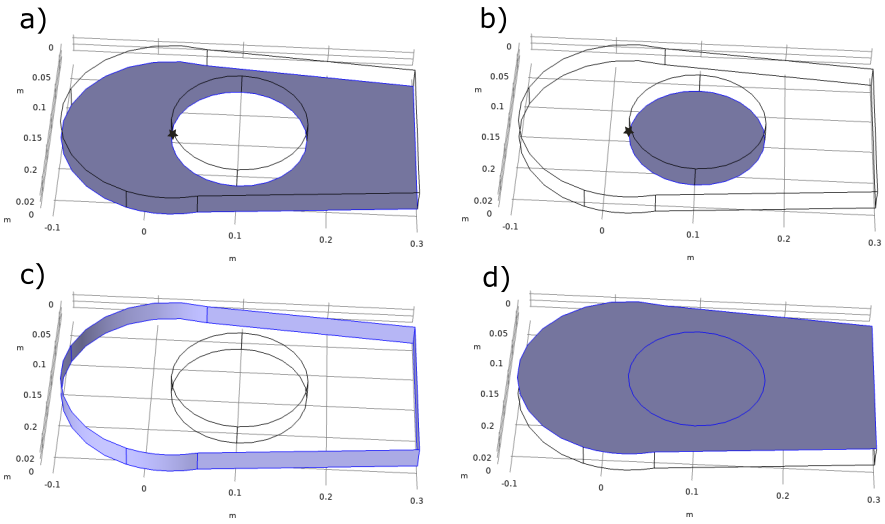

Fig. 3.13 Different boundary conditions used to model a Luneburg lens as an impedance sheet. Two different impedance boundary conditions have been defined: a constant impedance for the background (a)) and a radially varying impedance to represent the lens (b)). On the lateral walls, shaped in a way that reduces reflections, a scattering boundary condition is defined (c)) and finally, the top layer is modelled as a perfect electric conductor. The source, marked with a star, was modelled as a magnetic dipole and placed on the perimeter of the lens.

On the vertical walls of the model, scattering boundary conditions tailored to the chosen excitation source are defined. These boundary conditions minimise the reflections coming from the walls which bound the surface.

Finally, the whole model is encapsulated inside a box with a Perfect electric conductor (PEC) boundary condition on the top face. The function of this PEC layer is only to close the space where the equations are solved. It only needs to be a couple of centimeters away from the impedance surface as the surface waves are very confined to the surface.

3.5.4 Mesh and convergence

To compute a solution, the solver follows an iterative process, whose ultimate goal is to converge to an accurate enough solution. This process starts by computing the field for a particular mesh, once this is calculated, it refines the mesh in the regions of large gradient of the field. The software then compares the second result with the first one and keeps repeating the process until the difference in successive steps is below an user-defined threshold. At this point, it is assumed that the model has converged to an accurate solution, where the field at the different mesh elements is a good enough approximation to the continuous field distribution in the physical system.

An appropriate choice of the mesh, where the elements are smaller close to the regions of higher concentration of fields and where the gradient is stronger, is very important to reach a rapid convergence and reduce the computation time. An example of this is shown in Fig. 3.11. For the structure represented, the unit cell of a metasurface, a finer mesh was defined in the proximity of the metasurface, where the gradient of the electric field is strongest. The elements are then made progressively bigger as they move further away from the surface.

3.6 Conclusion

In this chapter, the experimental and numerical techniques used to fabricate and characterise the structures that will be presented in the following chapters have been introduced. All the samples studied in this work have been fabricated in-house, using the lithographic technique described in section 3.2 and characterized following the procedures explained in sections 3.3 and 3.4. Some examples, including some very basic experimental results, have been provided to illustrate the described measurement and analysis techniques.

In the following chapters, all the techniques explained in this chapter will be applied for the manufacturing, measurement and analysis of different metasurfaces.

Chapter 4

Glide-Symmetric bilayer metasurface for graded-index surface-wave structures

4.1 Introduction

In this chapter, a metasurface structure comprised of two layers of circular copper patches is presented. It has the peculiarity that the layers comprising the structure are shifted with respect to each other so that they have 'glide symmetry', which will be defined in section 4.2. The resulting structure presents a broadband behaviour compared to most metasurfaces, in addition to being flexible and light weight, both very desirable characteristics in the field of microwave engineering.

Firstly, in section 4.3, the design process of the structure is explained. In this section, the effects of the addition of a second layer of patches are studied as well as how the properties of the metasurface change with the relative position of the two layers (separation and displacement). In section 4.4 the previously presented metasurface is characterized experimentally, and the results compared with modelling data obtained with a FEM software.

Following this characterization, an experimental device featuring the previously described metasurface is presented in section 4.5. This device is a Luneburg lens, which is part of the graded index devices family. This device was manufactured and its performance measured experimentally, showing an operational bandwidth of 53%. This is a much improved bandwidth compared to other similar metasurface lenses [8, 56, 57].

4.2 Background

The work presented in this chapter requires the introduction of two important concepts: 'glide symmetry' and 'graded index devices'. Glide symmetry is one of the symmetry transformations that lie under the scope of 'high symmetries'. It is the combination of a mirror symmetry operation and a translation. The concept of high symmetries in electromagnetic structures was introduced by Oliner and Hessel in the 1960s but it was not until the beginning of the 21^{st} century when it found numerous engineering applications.

Glide symmetry has proven to increase the bandwidth of operation of different microwave devices such as lenses or antennas [58–60].

4.2.1 Higher Symmetries

A periodic structure possesses a higher symmetry when the unit cell coincides with itself after more than one geometrical operation of a different kind. These geometrical transformations can be translations, rotations, mirroring, etc. The effect of these kind of symmetry operations in microwave devices such as wave guides was first studied by Crepeau et al. [61] in 1964. It was followed by different theoretical studies, where glide structures were used for the purpose of slowing wave propagation, for application in travelling-wave tubes [62–64], and leaky-wave antennas [65].

The combination of different types of symmetry in a periodic structure has a strong influence on the propagation properties. One of the most interesting consequences of higher symmetries is the possibility to reduce the dispersion of the lowest-order propagating modes. In addition, the electromagnetic band gap between the lowest order modes at the Brillouin Zone boundary can be reduced, or even completely removed. Under the scope of high symmetries we find glide and screw (also known as twist) symmetries.

Recent work on structures with higher symmetries (in both one and two dimensions) has demonstrated the previously mentioned effects. These high-symmetric structures have also been implemented on different microwave devices, improving their performance. Some examples are: ultra-wideband Luneburg lenses [66, 67], leaky-wave antennas with low frequency dependence [68], cost-efficient gap waveguides [69], contact-less flanges with low leakage [70], transmission lines with low-dispersive propagation [71, 72], and fully metallic reconfigurable filters and phase shifters [73]. Most times, the structures possessing higher symmetries are metallic, or a combination of metal and dielectric, however, the effect of high symmetries has also been reported for all-dielectric structures [74].

Screw (or twist) Symmetry

Screw symmetry, also known as twist symmetry, belongs to the family of high symmetries as it is a combination of an angular rotation and an axial translation. A structure possessing screw symmetry coincides with itself when these two operations are performed simultaneously. The screw symmetry operator, defined in equation 4.1, is determined by two parameters, the angle of rotation (ϕ) and the translation distance (δ),

$$\mathrm{F}(\mathrm{r}, \varphi + \phi, \mathrm{z} + \delta) = \mathrm{F}(\mathrm{r}, \varphi, \mathrm{z}) \tag{4.1}$$

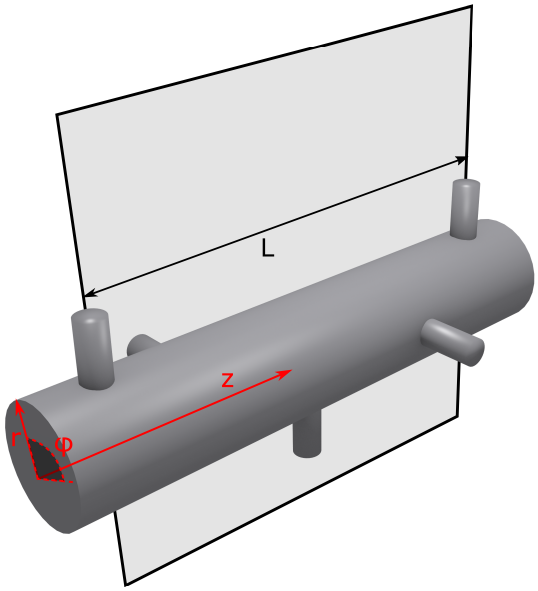

Fig. 4.1 Unit cell of a structure presenting screw symmetry. The structure consists of a circular tube which has cylindrical protuberances. For each iteration, the protuberances are displaced by $\frac{L}{4}$ and rotated a quarter of a turn ($\frac{\pi}{2}$ rotation).

For a one-dimensional system, which can be described in a cylindrical coordinate system, the operations which give it screw symmetry are:

$$\begin{gathered} z \to z + \delta \text{ with } \delta = \frac{L}{m} \\ \varphi \to \varphi + \phi \text{ with } \phi = \frac{2\pi}{m} \end{gathered} \tag{4.2}$$

where z is the direction in which the system is periodic (translation axis) and φ is the rotation around that axis. m is an integer number, and represents the number of symmetry operations which give a unit cell.

For each application of the symmetry operator (simultaneous rotation of ϕ and translation of δ), the structure will coincide with itself. This results in a structure that is periodic in both φ, with a periodicity of $2\pi = m\phi$ and z, with a periodicity $\mathrm{L} = \mathrm{m}\delta$.

A typical structure presenting screw symmetry is presented in Fig. 4.1. In this case, the symmetry operator performs a rotation of $\phi = \frac{\pi}{2}$ rad plus a translation of $\delta = 10\,\mathrm{mm}$ (a quarter of the period of the structure). In the example, the period of the structure is $\mathrm{L} = 4\delta$.

Glide Symmetry

A glide reflection is a symmetry operation in which a periodic structure, when reflected in an arbitrary plane and translated by half its period, will coincide with itself.

In the one-dimensional case, the operations that give a system glide symmetry are:

$$\begin{aligned} x &\to x + \tfrac{p}{2} \\ z &\to -z, \end{aligned} \tag{4.3}$$

where p is the period of the structure.

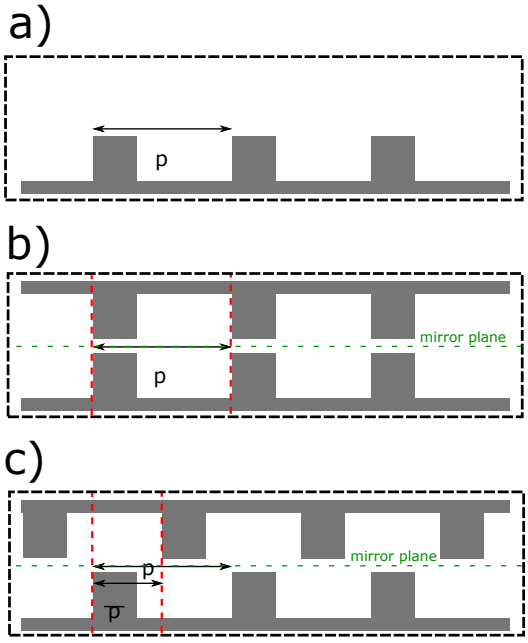

Fig. 4.2 Sketch of the process of construction of a 1D glide-symmetric structure. a) shows a one-dimensional structure with a period p. b) shows the same structure with an extra layer obtained by applying a mirror symmetry to structure a) and finally c) shows the glide-symmetric structure where the top structure has been displaced by p/2.

A very simple case of a one- dimensional structure presenting glide symmetry is shown in Fig. 4.2. In the figure, a) shows the original structure, b) shows the first step, where a

second layer is obtained by applying a mirror symmetry operation to the first one. Finally, c) shows the glide-symmetric structure, obtained by displacing the top layer by p/2.

This glide-symmetric system maintains the same periodicity as the original system (p) but presents two orthogonal standing wave solutions at the Brillouin zone boundary ($\lambda/2$=p) with equivalent energy [75].

For a system with a square lattice, which is periodic in both, x and y directions, with period p, the operations that give the system glide symmetry are;

$$\begin{aligned} x &\to x + \tfrac{p}{2} \\ y &\to y + \tfrac{p}{2} \\ z &\to -z \end{aligned} \tag{4.4}$$

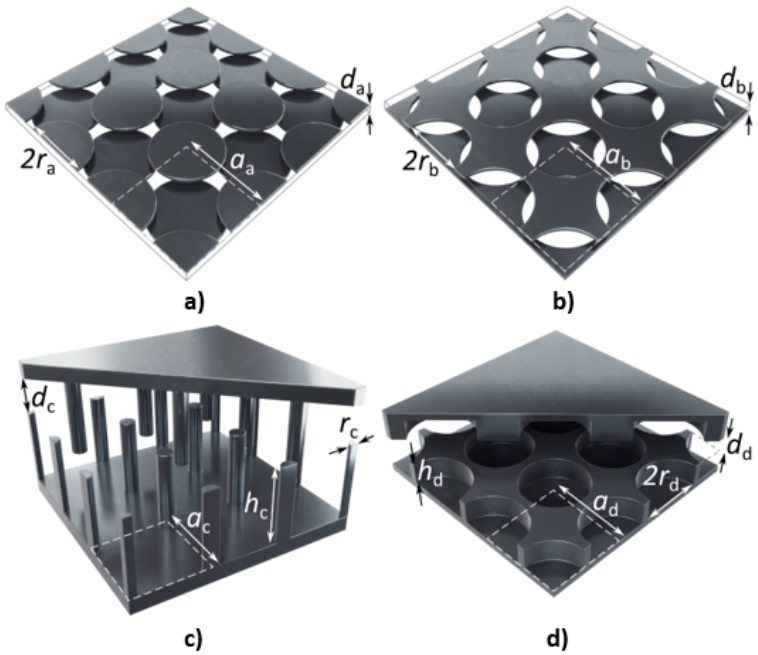

Fig. 4.3 Some examples of double-layer metasurfaces presenting glide symmetry: a) represents an array of circular patches and b) the complementary structure, an array of circular holes. c) is an array of pins in a parallel plate waveguide and d) is an array of holes also in a parallel plate waveguide. The cut in the third and fourth structures is just to show the internal structure.

To illustrate the effect of these symmetry operations, we have applied it to a variety of metasurfaces in the microwave range: an array of circular patches, an array of circular holes, an array of pins in a parallel plate waveguide and an array of holes in a parallel plate wave guide. The glide-symmetric version of these structures are represented in Fig. 4.3.

The dispersion curves for the two-lowest energy modes for each of the structures presented in Fig. 4.3 are represented in Fig. 4.4. To illustrate the changes in the dispersion characteristics caused by the introduction of glide symmetry (blue lines), these figures also include data for a metasurface exhibiting just reflection symmetry (red lines). For all these structures, it is shown that the dominating effect of the glide symmetry is to enforce a degeneracy of the first (solid) and second (dashed) modes between the X- and M-points in k-space. The diagram also shows that while the first mode for each structure has zero group velocity at the M-point (gradient goes to zero at the M-point), they have non-zero group velocity at the X-point (i.e. finite gradient).

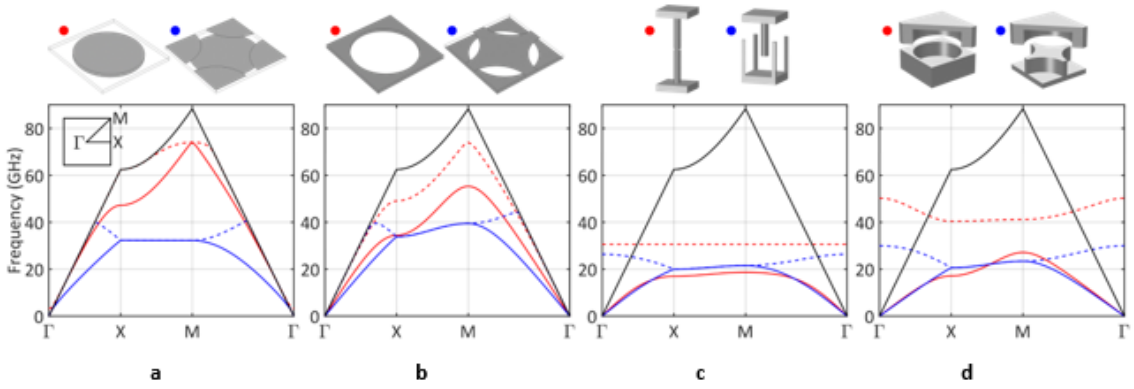

Fig. 4.4 Dispersion diagrams of the different metasurface structures with glide symmetry. Each dispersion diagram includes the modes for the structure with glide symmetry (blue lines) and the modes for an equivalent system with reflection symmetry (red lines), where the lowest-order mode is the solid line, and the second mode is the dashed line. The black lines represent the light line. The structures being modelled are shown above each plot, where the grey areas are metallic and all surrounding space is air. It can be seen that in all cases the presence of glide symmetry straightens the dispersion of the first mode and closes the band gap at the Brillouin zone boundary.

These symmetry-induced degenerate points and lines have been the topic of a number of works investigating topological states [76]. The usual band gap at the X-point due to the coupling of the two lower modes and the formation of two different energy standing waves is now absent. The full-band dispersion of the 2D periodic structures shows that this is also the case at the M-point. The crossing can be interpreted as a complete lack of coupling between these two modes as a result of the fields in each mode being orthonormal to one another at the Brillouin zone boundary. The behaviour of the double layer metasurfaces shown in Figure 4.4 corresponds to the situation where the interaction between the modes on the two individual layers is very strong (the separation between them, d, is small compared to the period, p). As the separation increases, the modes evolve into a degenerate pair with

dispersive behaviour identical to that of a single array. This effect is shown in section 4.3.2 for the bi-layer of circular patches studied in this chapter.

It could be inferred that the effect due to glide symmetry is simply accountable to the wrong choice of unit cell, where the correct one has the 'apparent' period of $\frac{p}{2}$ for 1D periodicity and $\frac{p}{\sqrt{2}}$ for 2D periodicity, and the mode is scattered back into the first Brillouin zone [62]. However, this is not the case. Even for a simple 1D waveguide with periodic corrugations, the modes of a system where the unit cell has two pins with glide symmetry (one pin protruding from the upper surface of the wave guide and one from the bottom), and that of a unit cell with two pins without glide symmetry (both pins on the bottom surface) are not equivalent [77].

The suppressed dispersion of the modes supported by all four of the glide-symmetric structures in Fig. 4.3 make them ideal candidates for graded index surface devices that control the propagation of wave fronts across the surface.

4.2.2 Graded index devices

Graded-index (GRIN) devices are a group of structures designed to achieve a specific wave field configuration by means of a graded refractive index, which translates into a graded mode speed. They work by curving the propagation path of electromagnetic fields by means of a gradual variation in the refractive index of the material [78].

When a plane-wave propagates in a homogeneous material, it travels in a straight line and its phase velocity is determined by the refractive index of the material. When such a plane wave travels from one material to another, with a different refractive index it experiences a refraction governed by Snell's law. The refraction will result in an abrupt change in the direction of propagation when the wave crosses the interface. However, if instead of having an interface between two different materials with a very different refractive index, the index is varied adiabatically in space, the trajectory of the wave will curve smoothly. The direction of the wave will curve until it reaches a direction of propagation that is parallel to that of a wave refracted by the step change.

For a mode that is confined to an interface, the ratio of its phase velocity (v_{p}) to that of a grazing photon (speed of light, c) is known as Mode index (n_{sw}), as shown in equation 4.5. In practice, this mode index can be treated in a similar way to the refractive index of a bulk material.

$$n_{\mathrm{sw}} = \frac{ck}{\omega} = \frac{c}{v_{\mathrm{p}}} \tag{4.5}$$

In theory, the refractive index should be graded in infinitesimally small steps, however, this is not achievable in practice. In that way, what we aim for is to reduce the steps as much as possible. For GRIN devices where the index variation was achieved by stacking layers of dielectric of different permittivities, the size of the variation step is clearly defined and given by the thickness of the different layers. However, when a metasurface is used to fabricate a GRIN device, the size of the step over which the index can be varied is not that clear. For a single layer metasurface with only one element per unit cell, the smallest step would corresponds to the size of the unit cell. This index grading results in a structure were a unit cell is surrounded by slightly different unit cells. Here, to estimate the mode index of a single unit cell an approximation needs to be made. It is assumed that the unit cell behaves in the same way, and therefore presents the same local mode index, when it is surrounded by slightly different unit cells as it does when it is part of an infinitely periodic structure [79, 80].

The case of the metasurfaces studied in this thesis is slightly more complicated as it contemplates structures with more than one layer, shifted with respect to each other. As a consequence, they present more than one element per unit cell, some of which are shared between more than one unit cell. This means that the approximation needs to be taken a step further as it is assumed that a single element gives a particular mode index, even when there are elements of a slightly different size withing the same unit cell.

A straightforward example of a GRIN device can be found in nature. In the human eye, the lens is a thin layer of transparent, flexible tissue, located directly behind the iris and the pupil. Its function is to help focus the light on the retina. It has a small grading of the refractive index, which increases towards its centre to minimise optical aberration and maximise resolution [81].

Traditionally, GRIN devices were fabricated using dielectric layers with different permittivity. This resulted in bulky structures, often difficult to fabricate. However, with the introduction of metamaterials and metasurfaces, where the index can easily be varied across the structure by simply changing the size or shape of its elements, the design and fabrication procedure of these devices became much easier. Metasurfaces also contribute to reducing the profile of GRIN devices as they can be very thin structures, and to an improvement in its performance as the mode index can be varied in smaller steps (as small as the unit cell of the structure). However, they are two-dimensional devices, so they work on a plane rather than in space.

The first artificial graded index device ever proposed is attributed to James Clerk Maxwell, and it is known as Maxwell's Fisheye lens. It is important to note that this lens is not in any shape or form related to the so called 'fisheye' lens in photography; which was developed much later with the purpose of creating an extreme wide-angle image, almost hemispherical in coverage.

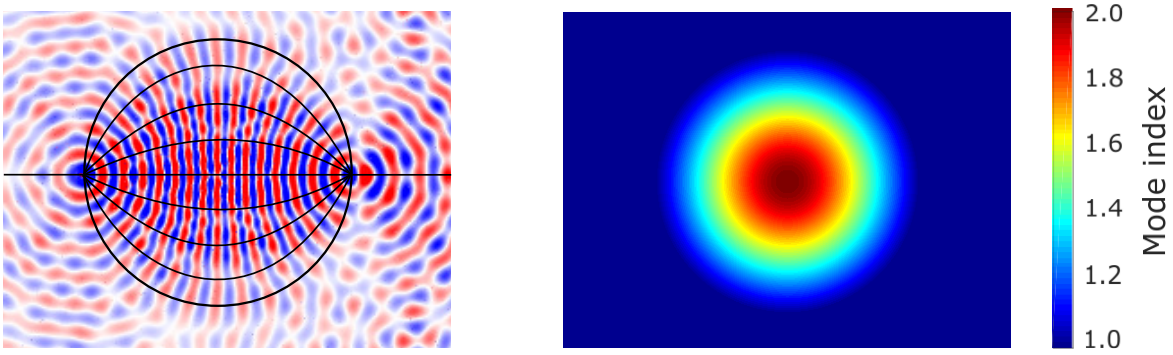

Fig. 4.5 Field profile and ray tracing of a Maxwell's Fisheye lens when a point source is placed on its perimeter. The wave fronts are compressed as they move towards the centre of the lens due to an increase in the mode index. After passing through the lens, the wave fronts are refocused into a secondary point source that is a mirror image of the original one.

The Maxwell Fisheye lens was not proposed with the purpose of inventing some useful device but merely for curiosity. The properties of this lens were described in one of a number of set problems of puzzles in the 1853 Cambridge and Dublin Mathematical Journal [82]. The challenge was to find the refractive index as a function of radius, given that a ray describes a circular path, and further to prove the focusing properties of the lens. The solution is given in the 1854 edition of the same journal [83]. The problems and solutions were originally published anonymously, but it was later attributed to J.C. Maxwell. The solution consisted of about 3 pages of subtle geometry as the solution to a mathematical problem relating to the passage of rays through a sphere of variable refractive index. At the end he added a note: 'The possibility of the existence of a medium of this kind possessing remarkable optical properties, was suggested by the contemplation of the structure of the crystalline lens in fish'. The field plot and corresponding ray tracing of a Maxwell's Fisheye lens is presented in Fig. 4.5.

However, Maxwell's discussion did not lead to new a technology in his day. It was not until the 20^{th} century when R. Luneburg and others discussed the application of Graded Index Devices for imaging purposes.

Some examples of graded index devices are the Luneburg lens [84], which allows one to perfectly focus a plane wave and it has found many applications in radar engineering technology; the Maxwell fisheye lens [85], which allows one to perfectly focus a point source

and has some applications in the field of antennas [86]; the Eaton lens, a device that changes the direction of a plane wave [87] and the perfect cloak [88, 89].

Luneburg Lens

The Luneburg lens was first designed and described theoretically in the 1940s by R. Luneburg [90]. Such a lens was originally presented as a spherical device, but it can be made circular for the case of surface waves in a plane. It focuses the radiation of a point source placed on its perimeter to create a plane wave on the opposite side of the lens or vice versa. This effect is achieved by a graded mode index profile that decreases radially from the center of the lens. The field profile and ray tracing produced by a Luneburg lens is shown in Fig. 4.6. It is shown how the cylindrical wave fronts of a source placed in the perimeter of the lens are compressed as they penetrate the lens and their curvature is reduced to the point where they are transformed intro plane waves after passing through the lens.

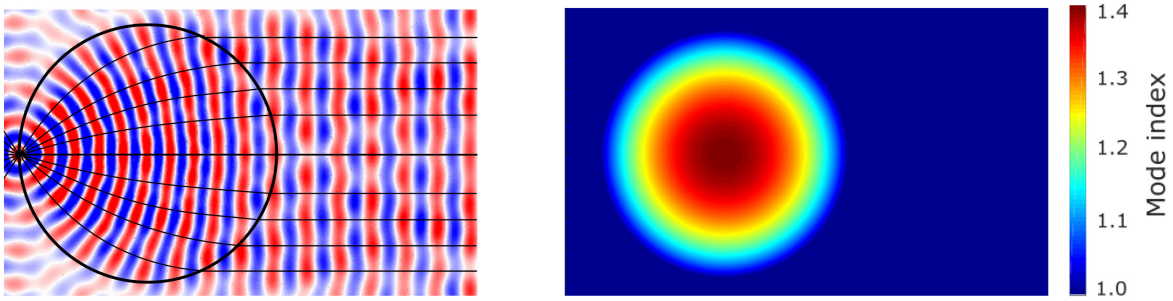

Fig. 4.6 Field profile and ray tracing of a Luneburg lens when a point source is placed on its perimeter. The wave fronts are compressed as the penetrate the lens due to an increase in the mode index. After passing through the lens, the wave fronts coming from the cylindrical source are transformed into planar wave fronts. The perimeter of the lens is highlighted in black and the ray tracing of the wave fronts has been superposed to the field profile.

These devices work under the assumption that the ray optics approximation can be applied, meaning that they need to be significantly bigger than the wavelength of operation. Usually, a size ten times bigger than the wavelength is a good enough approximation.

A Luneburg lens in free space has the mode index distribution presented in equation 4.6. Such devices have a permittivity of 2 in the center of the lens and this decays radially, matching the permittivity of free space as it reaches the edge of the lens:

$$n_m(r) = \begin{cases} 1 & \text{if } r > R_0 \\ \sqrt{2 - \left(\frac{r}{R_0}\right)^2} & \text{if } r \leq R_0; \end{cases} \tag{4.6}$$

where r is the distance to the centre of the lens and R_0 is the radius of the lens.

For planar metasurface devices, like the ones presented in this thesis, most frequently the lens would be contained in a metasurface sheet with a mode index different from that of free space. In that case the mode index at the edge of the lens needs to match the background mode index (n_0) and the range of mode index variation that needs to be achieved is ($n \subset \{n_0, 2n_0\}$). For this case, the profile as a function of the distance to the center of the Lens would be:

$$n_m(r) = \begin{cases} n_0 & \text{if } r > R_0 \\ n_0\sqrt{2 - \left(\frac{r}{R_0}\right)^2} & \text{if } r \leq R_0. \end{cases} \tag{4.7}$$

Luneburg lenses have been implemented in many ways over the past 50 years. A working device featuring a Luneburg lens for transverse magnetic (TM) surface-waves was first developed in 1960 [91]. The mode index profile was realized by tailoring the thickness of a polystyrene overlayer, and by arranging a series of cylindrical posts of varying height on a ground plane, resulting in bulky devices. In 2001, Park et al. [92, 93] developed a planar Luneburg lens for TM surface waves comprised of a square array of square posts of varying height in a parallel-plate waveguide. A surface wave Luneburg lens has also been proposed and characterized for transverse electric (TE) surface waves, [94]. In this device three concentric rings of circular holes of different sizes are etched in a square lattice on the top plate of a dielectric-filled parallel metal plate waveguide, providing the required mode index profile.

Since it was first proposed, Luneburg lenses have been studied for different ranges of frequencies, from infrared to microwaves [9, 8], were they have shown to have many applications, specially in the fields of antenna design [95–97] and radar engineering [98, 99]; to optical frequencies [100, 101] and even acoustics [102, 103].

In all cases, the graded index profile is achieved by varying the mode index in steps rather than as a continuous function of the radius, due to fabrication limitations. However, this approximation has proven to be valid, enabling a satisfactory performance of the device.

With the proliferation of metamaterials and metasurfaces, many new Luneburg lens devices have been presented [104–106], taking advantage of the versatility of metamaterials and metasurfaces. However, metasurfaces are usually dispersive, presenting a mode index which varies strongly with frequency. This results in narrowband devices, not suitable for some applications. Here, with the introduction of glide symmetry, we study how the bandwidth of operation of GRIN devices can be increased.

4.3 Metasurface Design

The metasurface under study in this chapter is a bi-layer of circular copper patches in a square array separated by a dielectric spacing. Both layers are identical but they are shifted with respect to each other by half of the period of the lattice, exhibiting Glide symmetry. Both layers are fabricated independently according to the procedure described in section 3.2. In that way, the separation between the layers of copper patches is given by the dielectric substrate plus an oil layer used to bind the sheets together. A schematic of the described structure is presented in Fig. 4.7.

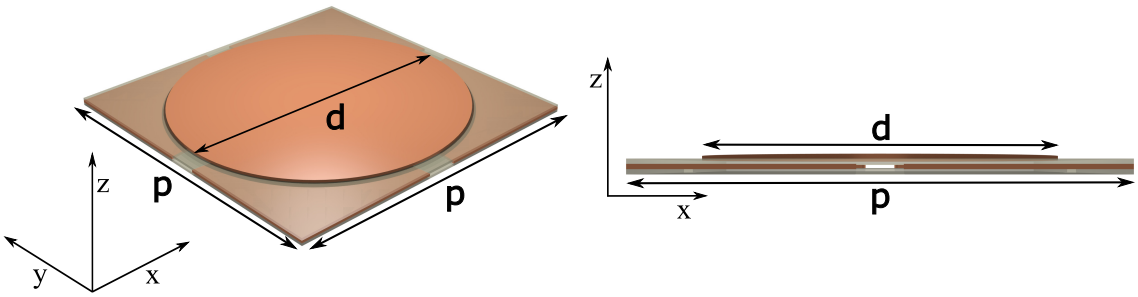

Fig. 4.7 Schematics of a unit cell of a bi-layer of copper circular patches in a square array presenting glide symmetry. The patches have a diameter d and the structure is periodic in both x and y directions with a periodicity p. Both layers of patches are printed over a dielectric substrate, which also acts as a spacing between the metal patches. A cross section of the structure is also included on the right hand side.

Due to fabrication limitations, the thickness of the dielectric slab cannot be any thinner than 25 µm and the oil layer necessary to keep the sheets together, increases the separation of the copper patches by an extra 25 µm. This sets a practical lower limit to the spacing between the copper patches. In theory, there are still four parameters that can be varied to tailor the behaviour of the metasurface. Those are the periodicity (p), the diameter of the patches (d), the separation between the layers (t) and the permittivity of the dielectric (ε) . However, as shown later on, practically, the only parameter that can be varied systematically across a device is the diameter of the patches.

In this section, by means of numerical eigenmode simulations, the effect of each of the mentioned parameters is investigated. These simulations also allow one to understand better the behaviour of the structure, as they produce the field maps inside the metasurface.

Firstly, a value for the periodicity of the structure (p) is chosen. This determines the length scale and the frequency of operation of the structures. In this case, a periodicity of $p = 3.2$ mm was chosen. The reasons for using this scale-length were mainly practical as the

motifs are small enough to support modes in the range of frequencies that can be measured experimentally with the equipment described in section 3.3 and big enough not to make the alignment of the layers extremely difficult. However, all dimensions can be scaled so that the operational frequency band matches any particular requirements. Although, smaller motifs and gaps would make the fabrication procedure more difficult, and can even require to move to more complicated fabrication techniques.

4.3.1 Multilayer structures

The metasurface presented here is comprised of two layers of metallic patches, separated by a dielectric spacing. The effect of having two layers of patches instead of one and the advantages of placing this second layer in a way that the structure presents glide symmetry are investigated in this section.

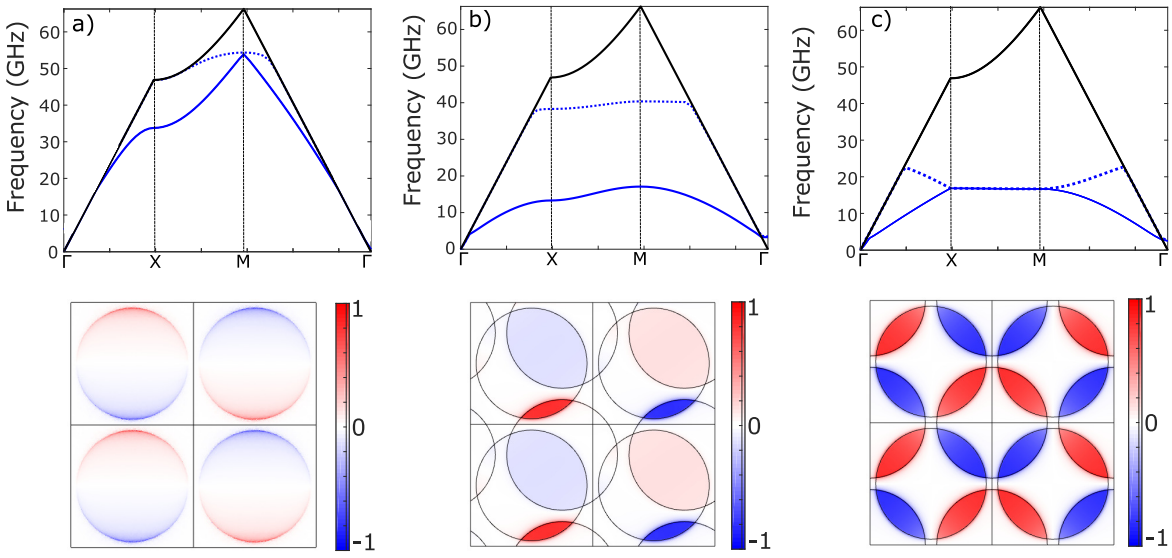

Fig. 4.8 Dispersion diagrams of three different structures featuring the same array of circular patches in a square lattice. The first one, a) is a mono-layer, the second one, b) is a bi-layer where the layers are shifted by a quarter of the period in both x and y directions and c) bi-layer with glide symmetry. All the structures have the same periodicity (p = 3.2 mm). The diameter of the patches is d = 2.9 mm and the metal thickness is $t_c = 18\,\mu$m. The dielectric slab between the layers of patches has a thickness of $t_d = 25\,\mu$m and a permittivity of $\varepsilon = 2.8$. The first order mode is represented with a solid line while the second order band is represented with a dashed line. Bottom: Normalised out-of-plane electric field (E_z) for the three described structures inside the dielectric spacing.

In Fig. 4.8 the dispersion diagrams and out-of-plane electric field (E_z) profiles of the proposed glide symmetric structure (c) are compared with that of a single layer of the

same square array of circular patches (a) and a third one, where the top layer has been displaced only by a quarter of the period (b). For all three structures, the lowest order mode is represented with a solid blue line and the second order mode is represented with a dashed line.

The first structure (mono-layer), presents a very dispersive lowest order mode. This mode follows the light line for small values of the wavevector and then deviates quickly to approach the Brillouin zone with zero group velocity. This is the classic surface plasmon-like behaviour of most periodic metasurfaces, which results in both a low index for low frequencies followed by a strong variation of the effective mode index at higher frequencies.

In the dispersion diagram of the second structure, as a consequence of adding a second layer, the lowest order mode is pushed down in frequency, away from the light line. This is due to an increased confinement of the fields, which now propagate inside the dielectric between the two layers. Consequently, the mode index increases. However, the structure still shows a resonant behaviour with a strong frequency dependence.

In the third graph, where the layers are displaced with respect to each other by half of the period (p), the effects of glide symmetry are clearly shown. In the first place, the lowest order mode is reduced in frequency and displaced away from the light line. This means that its effective mode index is increased with respect to that of the single layer. A second very noticeable feature is that the band gap between the first (solid) and second (dotted) modes at the Brillouin zone boundary is closed and the dispersion of the first mode straightened. This is a direct consequence of the glide symmetry of the structure.

The improved linearity of the dispersion of the lowest order mode is a very useful feature for microwave engineering. It means that, provided that the dispersion goes though the origin, the group and phase velocities have similar values which change rather slowly with frequency.

For both structures, b) and c), there is a big capacitive coupling effect between the overlapping patches. This results in an electric field that is normal to the plane and confined to the overlap regions. This makes the metasurface have a more wave-guide-like behaviour, presenting bound surface modes even at low frequencies, which results in an increase of the mode index.

4.3.2 Coupling and study of the effects of the separation between the layers of patches

In this section, we study how the separation between the layers of patches affects the behaviour of the modes supported by the structure. To this end, the dispersion diagrams of various structures with different values of the separation between the layers were calculated.

The size and shape of the copper patches and the lattice on which they are positioned are the main features of the presented structure and the novel properties it exhibits are related to the way in which both layers are positioned with respect to one another. In this way, for the sake of simplicity, it was chosen to study a structure where the arrays of copper patches are separated by a layer of air of varying thickness. Later, in the experiments, the air will be replaced by a dielectric substrate, which causes the modes to only move slightly in frequency, but their features remain the same.

The dispersion diagrams of a metasurface comprised of two layers of metallic circular patches in a square array with glide symmetry and separated by a layer or air with varying thickness are represented in Fig. 4.9. The periodicity of the array and the diameter of the patches have been fixed to p = 3.2 mm and d = 2.9 mm.

Using FEM software, the dispersion diagram of the modes supported by the metasurface has been calculated for different separations (t) between the layers ranging from 25 µm to 10 mm. Only the Γ to X dispersion is shown in the diagram. This is enough to understand much about the behaviour of the structure as the dispersion of the modes is isotropic for the considered range of frequencies. In the figure, the modes are represented in blue (solid line for the first mode and dotted line for the second) and the light line ($k = \omega/c$) is represented with a black line.

As it is shown in the dispersion diagrams, when the separation between the layers is big compared to the wavelength ($s = 10$ mm); the interaction between the layers is minimal and the dispersion of the modes supported by both sheets resembles that of a single sheet (as in Fig. 4.8 a)), thus the two modes are degenerate.

When the separation between the layers is reduced, the interaction between the modes supported by the two layers of patches increases. In all cases, the effect of glide symmetry is shown, resulting in a degeneracy (absence of band gap) at the Brillouin zone boundary. As the layers become closer together, this effect is enhanced and the lowest order mode straightens, resulting in an increase in the frequency at which the modes hit the Brillouin zone. As for the second mode, for lower values of the in-plane wave vector, it moves towards the light line.

It is shown that for separations of (300 µm) and smaller, the dispersion diagram maintains the same shape but is lowered in frequency as the separation between the layers is reduced.

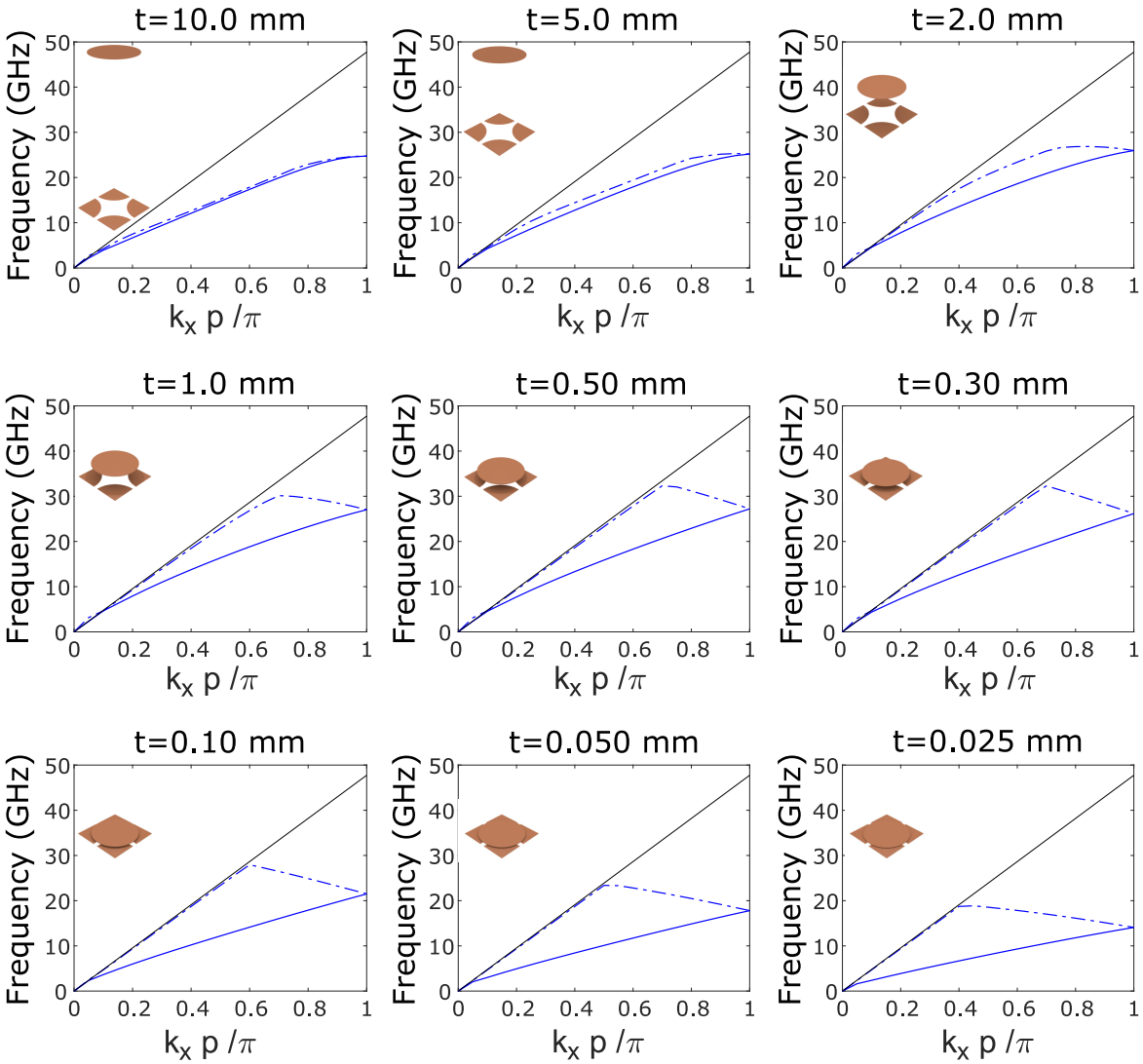

Fig. 4.9 Dispersion diagram of the two layer metasurface of circular patches with glide symmetry for different values of the separation between the layers. The dispersion is presented only in the horizontal direction (Γ to X). It has also been assumed that the layers of patches are separated by air. The first mode is represented with a solid line and the dotted line corresponds to the second mode. The light line is represented by a black line. A diagram representing a unit cell of the structure for the different values of the separation has also been included.

This is due to an increase in the confinement of the fields and the capacitive effect between the overlapping regions of the patches, similar to the effect shown in Fig. 4.8 b) and c). As a consequence, it can be concluded that the mode index increases as the separation between the layers is reduced, and therefore, ideally, the separation between the layers should be made as small as possible to maximise the mode index.

So far, the effects of the separation between the layers have been studied when they are separated by a layer of air, or in other words, as if the patches were in free space. However, when a physical device is made, the patches need to sit on some dielectric substrate. This dielectric layer has two functions, the first one, as mentioned before is to provide a support for the metal patches; and the second one is to act as a spacing between the layers of patches. This sets a lower limit to the separation between the layers as the smallest thickness copper-coated dielectric that is commercially available is 25 µm.

In addition, due to alignment issues, the fabrication procedure carried out in our lab is limited to single-sided printing, meaning that two single-layer metasurfaces need to be stacked together to result in the proposed bi-layer. To keep both surfaces together, a layer of oil is placed between them, increasing the separation between the copper patches another further 25 µm.

In this way, the final stacked multilayer structure that can be fabricated as described in section 3.2 consists of:

- One layer of 18 µm thick copper patches.
- A 25 µm dielectric (PET) layer (substrate) with a permittivity of 2.8, where the first layer of patches is supported.
- An oil layer with a thickness of 25 µm and a permittivity of 3.4 required to bind the dielectric/copper layers together.
- A second layer of copper patches, in this case displaced by half of the period with respect to the first one.
- A second dielectric layer, identical to the first one which supports the second layer of patches.

It needs to be mentioned that the thickness and permittivity of the oil layer are not exact values but estimations obtained from different FEM simulations. In these simulations, the parameters where varied in order to fit the experimental data obtained from numerous samples.

4.3.3 Mode index variation: Relation to the patch diameter

As it was introduced in the theoretical background, most structures with glide symmetry present a lowest order mode which has a very linear dispersion, with a finite group velocity at

the Brillouin zone boundary. These features result in a mode index with a reduced frequency dependence. The mode index is calculated from the dispersion diagram as the ratio between the wave vector at which the mode appears at a certain frequency and the correspondent wave vector for the light line at that same frequency.

In that way, the mode index for the structure illustrated in Fig. 4.7 is presented in Fig 4.10 (right) as well as its dispersion diagram (left). The difference in index across this frequency range for the Γ to X (horizontal) and Γ to M (diagonal) directions is negligible, confirming the isotropic nature of the supported surface wave dispersion for frequencies up to 12 GHz.

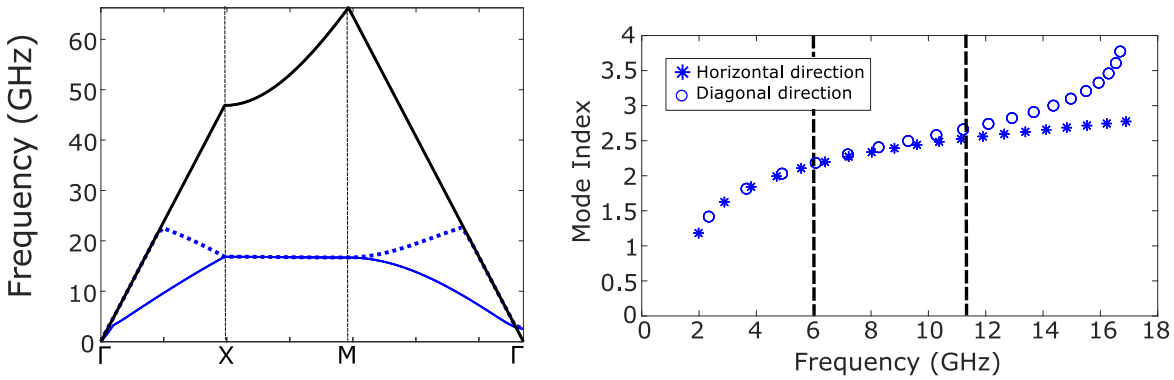

Fig. 4.10 (Left) Dispersion diagram of the two layer metasurface of circular patches with glide symmetry presented in Fig. 4.7. This structure has a patch diameter of 2.9 mm and a periodicity p = 3.2 mm. The space between the layers of patches is filled with a 25 µm thick dielectric with a permittivity of 2.8 and a 25 µm thick oil layer with a permittivity of 3.4. The first mode is represented with a straight line and the dotted line corresponds to the second mode. The light line has been represented in black. The dispersion diagram has been calculated for the three directions of interest of a square lattice (shown in Fig. 3.10), including the horizontal and the diagonal directions in the lattice. On the right hand side, the mode index correspondent to these two directions is presented. The horizontal direction (Γ to X) is represented with stars while the diagonal direction (Γ to M) is represented with circles.

This isotropic behaviour will also be shown later in the form of circular isofrequency contours. In the figure, it is also shown that the mode index varies only by 5% with frequency for the range between 5 GHz and 12 GHz. This is a clear improvement with respect to most single-layer metasurfaces, which will result in a much more broadband performance of any prospective microwave devices.

In this section, we also study the dependence of the effective mode index presented by the metasurface with the diameter of the patches that comprise it. As was discussed in the previous section, the only degree of freedom left after choosing the periodicity of the structure, which sets the range of operational frequency, is the diameter of the patches. In

this way, in order to grade the mode index of the structure, a diameter profile, which varies with the position of the patches needs to be defined.

To do this, an expression relating the diameter of the patches to the mode index they present needs to be obtained. For this purpose, the dispersion diagram, and from it the mode index, of infinitely periodic metasurfaces with varying patch diameter have been calculated using a FEM software. This study results in a function that relates the diameter of the patches and the effective mode index for a whole range of frequencies. When the frequency of operation of the prospective device is selected, a direct relation between the diameter and the mode index is well defined.

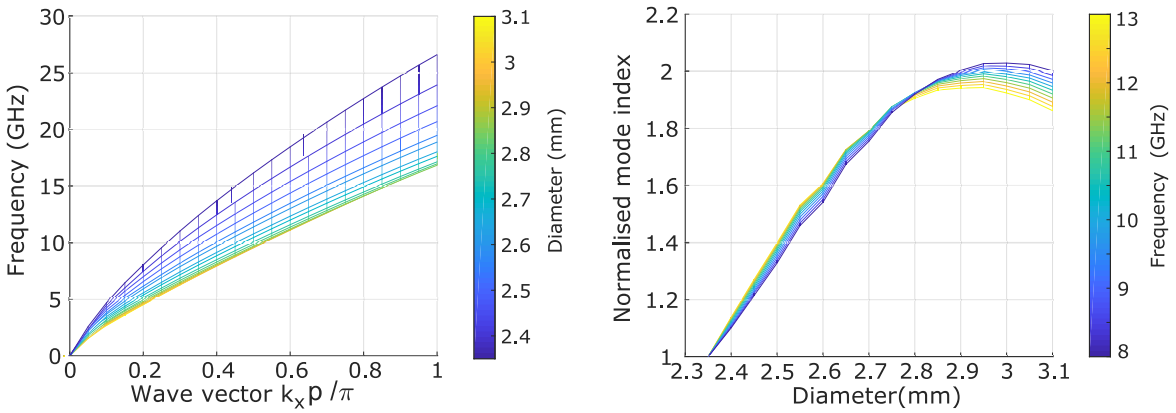

Fig. 4.11 (Left) Dispersion diagram of the double layer glide-symmetric array of circular patches for values of the diameter of the patches between 2.35 mm and 3.1 mm keeping the periodicity ($p = 3.2$ mm) constant. It is shown that as the patches get smaller the dispersion gets closer to the light line, as the confinement of the fields decrease and the capacitance reduces as the overlap region between the patches get smaller. (Right) Normalised mode index presented by the structure as a function of the diameter of the patches for different frequencies.

This kind of relation is a key element in the design of GRIN devices. It also shows the range of mode index that is achievable with this particular structure, which is a limiting factor in the design of GRIN devices.

If the mode index of the metasurface varies strongly with frequency, a graded index device will only work at the selected operational frequency, as the diameter of the patches required to obtain the desired mode profile would be very different at different frequencies. However, if the mode index is relatively constant over a wide range of frequencies, or has the same frequency dependence, the device will work over the whole range.

The effect of varying the patch radius of the structure presented in Fig. 4.7 is shown in Fig. 4.11. On the left hand side, the dispersion diagram of the structure is shown for different values of the diameter of the patches. In this case, only the dispersion diagram in

the horizontal direction (Γ to X) is presented. As the patches become smaller, the dispersion diagram moves up in frequency, towards the light line. This is due to a decrease in the capacitive effect in the metasurface caused by a reduction of the overlap regions between the patches, and a decrease in the confinement of the fields.

On the right hand side, the dependence of the mode index with the patch diameter, immediately obtained from the first plot, is presented. The mode index has been normalised to that presented by the metasurface with the smallest diameter, so that the achievable mode index contrast is highlighted. It is also shown how the mode index varies with frequency. This variation is stronger for larger patches.

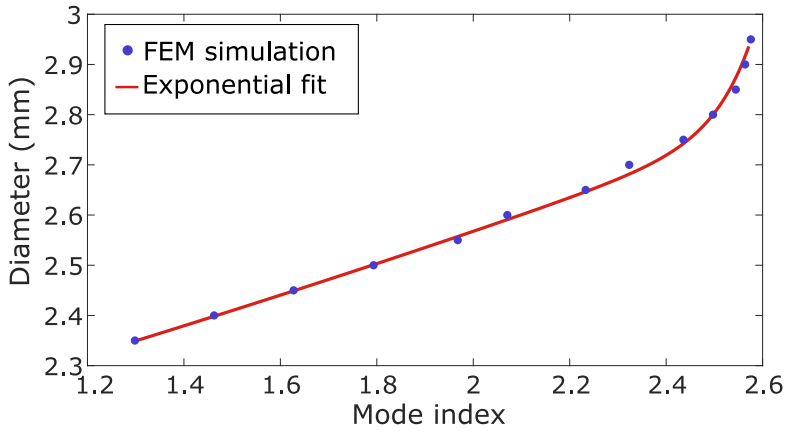

Fig. 4.12 Mode index presented by the metasurface at 10 GHz as the diameter of the patches that comprise it is varied. The blue dots correspond to the value of the mode index obtained with a Finite Element Method simulation and the red line represents an exponential fitting curve (Equation 4.8).

The next step is to choose the frequency of operation, for which the expression relating the mode index and the patch diameter will be calculated. In this case, it was chosen to be 10 GHz. This frequency is inside the range in which the variation of the mode index is below 5%, as shown in Fig. 4.10.

The relation that provides the diameter of the patches necessary to obtain a particular mode index is obtained by calculating the mode index shown by metasurfaces with different diameter sizes at the chosen frequency and then fitting the points obtained to an exponential curve. This relation is shown in Fig. 4.12. The blue dots represent the data obtained with the FEM software, while the red line is an exponential fit, with its general expression shown in equation 4.8.

$$d = ae^{bn} + ce^{dn} \tag{4.8}$$

4.4 Experimental characterization of an infinitely periodic metasurface.

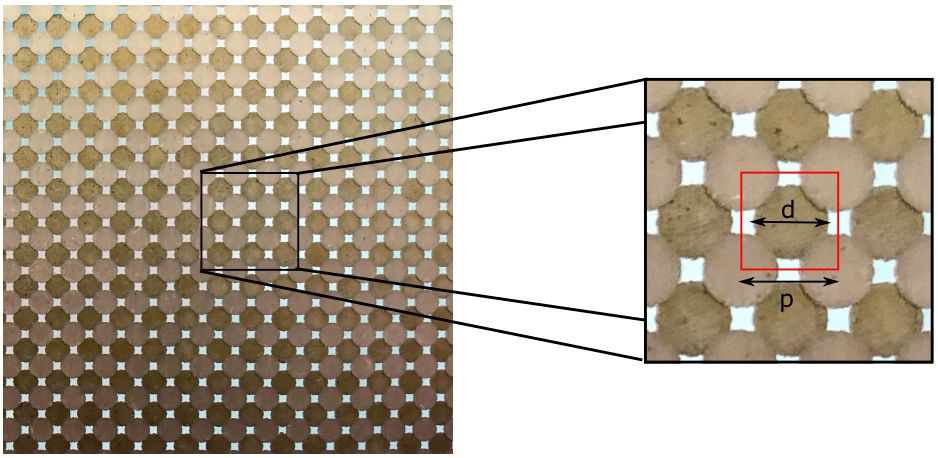

Fig. 4.13 Photograph of the sample used to characterize an infinitely periodic bi-layer metasurface of circular patches in a square array with glide symmetry. The structure has a periodicity of 2.4 mm and a diameter of 2.1 mm. On the right hand side a close-up of the structure is presented, where the unit cell is marked in red.

In this section, we present the experimental results (isofrequency contours and dispersion diagram), of the infinitely periodic (i.e. not graded) glide-symmetric metasurface presented in Fig. 4.7. To obtain them, a sample was fabricated following the procedure explained in section 3.2 and then measured as stated in section 3.3. The dimensions of the sample are the same as those described in section 4.3. A picture of this sample is shown in Fig. 4.13.

An area of 200 mm by 200 mm was scanned with a loop antenna positioned at a fixed distance of 0.5 mm from the metasurface. As explained in section 3.3, the plane of the loop antenna is oriented parallel to the sample, to maximise the detection of the out-of-plane magnetic field. Such scan measures the amplitude and phase of the electromagnetic surface fields. After this scan and the appropriate Fourier processing of the measured signal, the isofrequency contours for the different frequencies are obtained. These isofrequency contour plots are presented in Fig. 4.14 for 6 different frequencies between 10 GHz and 20 GHz.

In these isofrequency contours, different features can be distinguished. Firstly, in the center of the plot, we find the light circle, which bounds the area of k-space corresponding to the radiative modes. This light circle is represented with a red dotted line which corresponds to the wavevector of a grazing photon coming at 90° from the source right on the sample.

The modes propagating across the structure for the considered frequency are also evident in these plots. In the case of these bound modes, the in-plane wave vector is bigger than

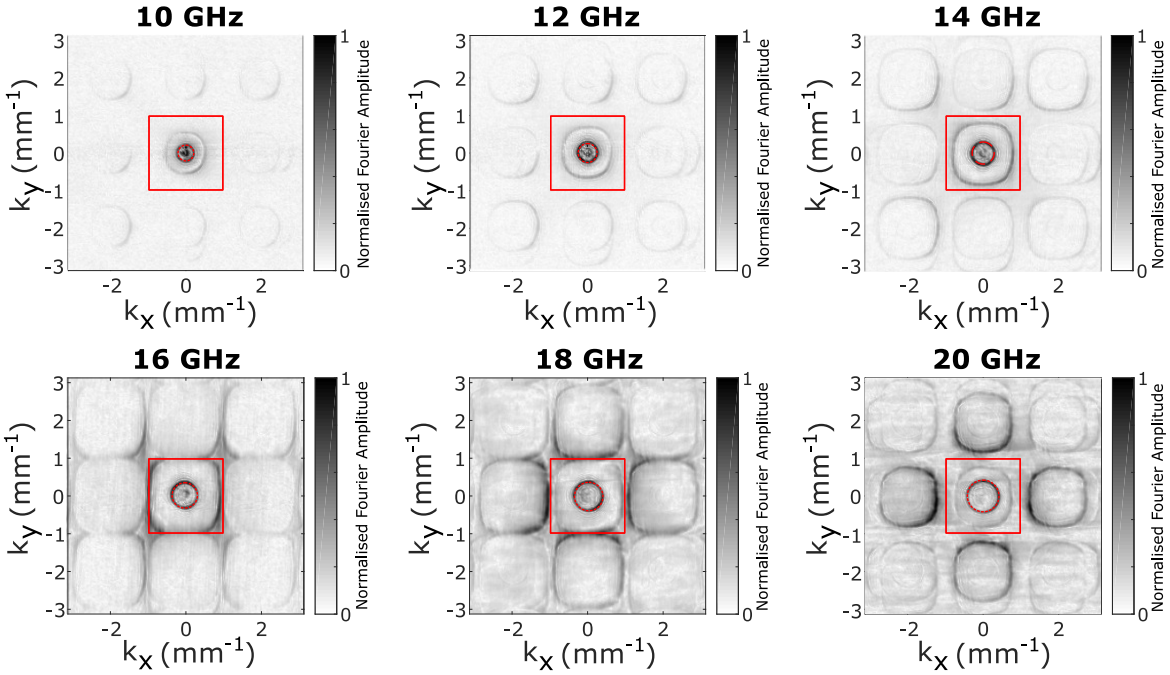

Fig. 4.14 Normalised Fourier amplitude, representing the isofrequency contours for the presented glide-symmetric structure at frequencies between 10 GHz and 20 GHz. The first Brillouin zone boundary is represented in red and the light line is also included as a red dotted circle.

that of the light circle ($k > k_0$) and therefore appear outside the dotted red line. Finally, the different modes are repeated with the periodicity of the reciprocal space. This means that all the relevant information corresponding to the eigen solutions is contained within the first Brillouin zone, which is delimited by a red square.

The isofrequency contours at low frequencies (up to 12 GHz) are circular, illustrating that the structure possesses an isotropic behaviour. However, this isotropy is lost as the frequency increases and the isofrequency contours adopt a square-like shape. This distortion is caused by the periodicity of the lattice and therefore presents four-fold symmetry.

Once the isofrequency contours are obtained for each frequency from the experimental field scan and interpreted; the dispersion diagram of the structure can be constructed by taking cuts in the directions of interest (high symmetry directions of the square lattice) and then stacking the lines of data obtained at each frequency.

In Fig. 4.15 the resulting dispersion diagram is represented as well as the mentioned directions of high symmetry and the unit cell of the structure.

In the dispersion diagram, the experimental measurement is represented as a grey scale with the FEM results superimposed as red dots. The first mode is represented with red dots and the second mode with red squares. A very good agreement between the experiment and

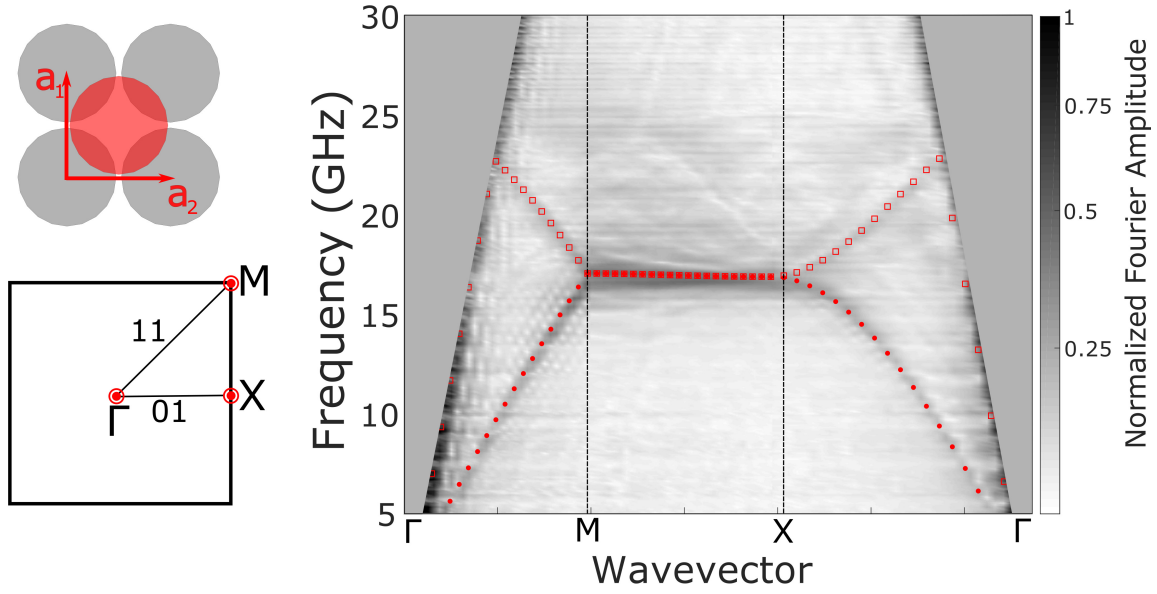

Fig. 4.15 Normalised Fourier amplitude, representing the dispersion diagram of the modes supported by the presented glide-symmetric structure for frequencies between 5 GHz and 30 GHz. The experimental data is represented as a grey-scale and the FEM data is superposed in red (dots for the lowest order mode and squares for the second mode). The area corresponding to the radiative modes ($k < K_0$) has been shaded in grey. A unit cell of the structure and a sketch of the first Brillouin zone are also included.

the simulation data is obtained. This agreement reinsures confidence in modelling so that the FEM simulations can be used as an accurate way of calculating the mode index shown by the structure and therefore the experiment does not need to be repeated for every diameter of the patches.

Also, the characteristic features that are expected of glide symmetry are clearly shown, i.e. the improved linearity of the lowest order mode and the absence of a band gap at the Brillouin zone boundary.

4.5 Experimental device: Luneburg lens

Once the expression relating the mode index and the patch diameter was obtained, and it was proven that the modelling results resemble accurately the experimental measurements, a graded index device was designed, manufactured and tested.

The chosen device is a planar Luneburg lens. The Luneburg lens is integrated in a metasurface with a background index of $n_0 = 1.7$. The mode index of the lens will then vary between $n_0 = 1.7$ and $\sqrt{2}n_0$ according to equation 4.7. This index profile is shown in Fig. 4.16.

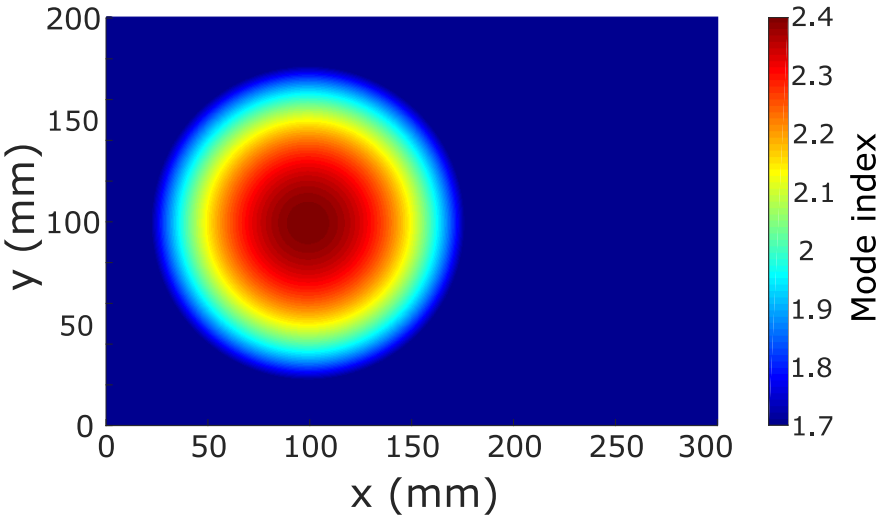

Fig. 4.16 Index profile of the experimental metasurface device containing a Luneburg lens. The background metasurface presents a mode index of $n_0 = 1.7$. Inside the lens, the mode index increases radially towards the centre of the lens, where it duplicates its background value.

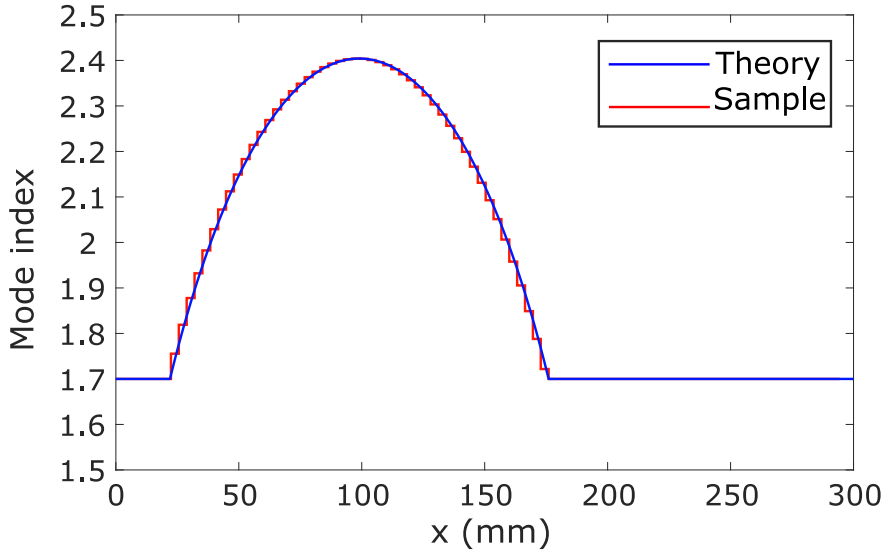

Fig. 4.17 Approximation of the index profile of the experimental metasurface device containing a Luneburg lens across a horizontal line crossing the lens by it centre (red) compared to the theoretical profile where the mode index varies in infinitesimal steps. The background metasurface presents a mode index of $n_0 = 1.7$. Inside the lens, the mode index increases radially towards the centre of the lens in steps of the size of the unit cell of the structure.

To obtain the index profile presented in 4.16, a patch size is assigned to every unit cell across the metasurface as a function of its position.

In theory, the mode index should vary in infinitesimally small steps and therefore it should be slightly different for each point in space. However, an experimental sample using a unit cell interpretation can only be an approximation. In practice, the position of the centre of the patch is taken as a reference to calculate its diameter. If the metasurface was a monolayer, the mode index would vary in steps of the size of the unit cell of the structure. However, the structure considered here is a bi-layer with more than one element per unit cell. This means that as the different patches comprising the unit cell are at different distances from the centre of the lens, their diameters vary. Also, some patches contribute to more than one unit cell and therefore, the step of the index variation cannot be clearly defined.

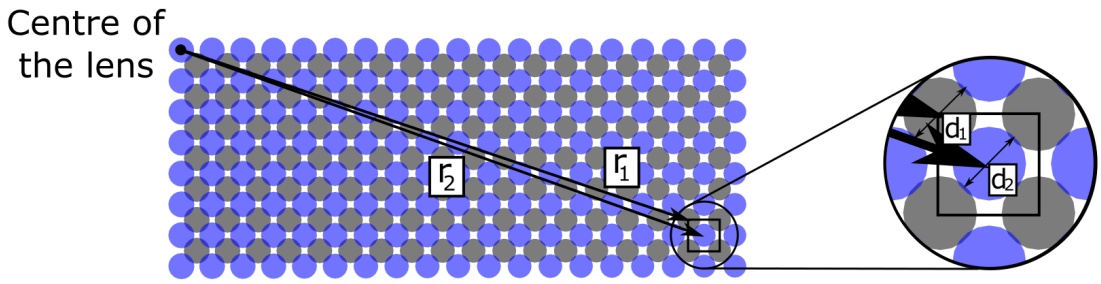

Fig. 4.18 Representation of a portion of a graded index sample featuring the bi-layer metasurface with glide symmetry presented in this chapter. The diameter of each patch is chosen according to its distance to the centre of the lens ($|\vec{r}_1|$). As shown in the close-up, the different patches comprising each unit cell have different position vectors, which yield different diameters. In the figure, the top layer is represented in blue while the bottom layer is coloured grey. The position vectors to the centre of two different patches ($\vec{r}_1$ and $\vec{r}_2$) are shown with black arrows, presenting different lengths. That means that the corresponding patches do not have the same diameter in spite of being part of the same unit cell (as highlighted in the close-up).

The variation of the mode index in the sample compared to its theoretical value is presented in Fig. 4.17. It is presented for a horizontal line that crosses the lens through its centre.

4.5.1 Experimental results

The experimental setup described in section 3.3 was also used to measure the fields propagating across the lens. In this case, the loop antenna acting as a source was placed at the

focus of the Luneburg lens, located on its perimeter, and the probe was used to scan an area of 200 mm by 300 mm on the opposite face of the sample.

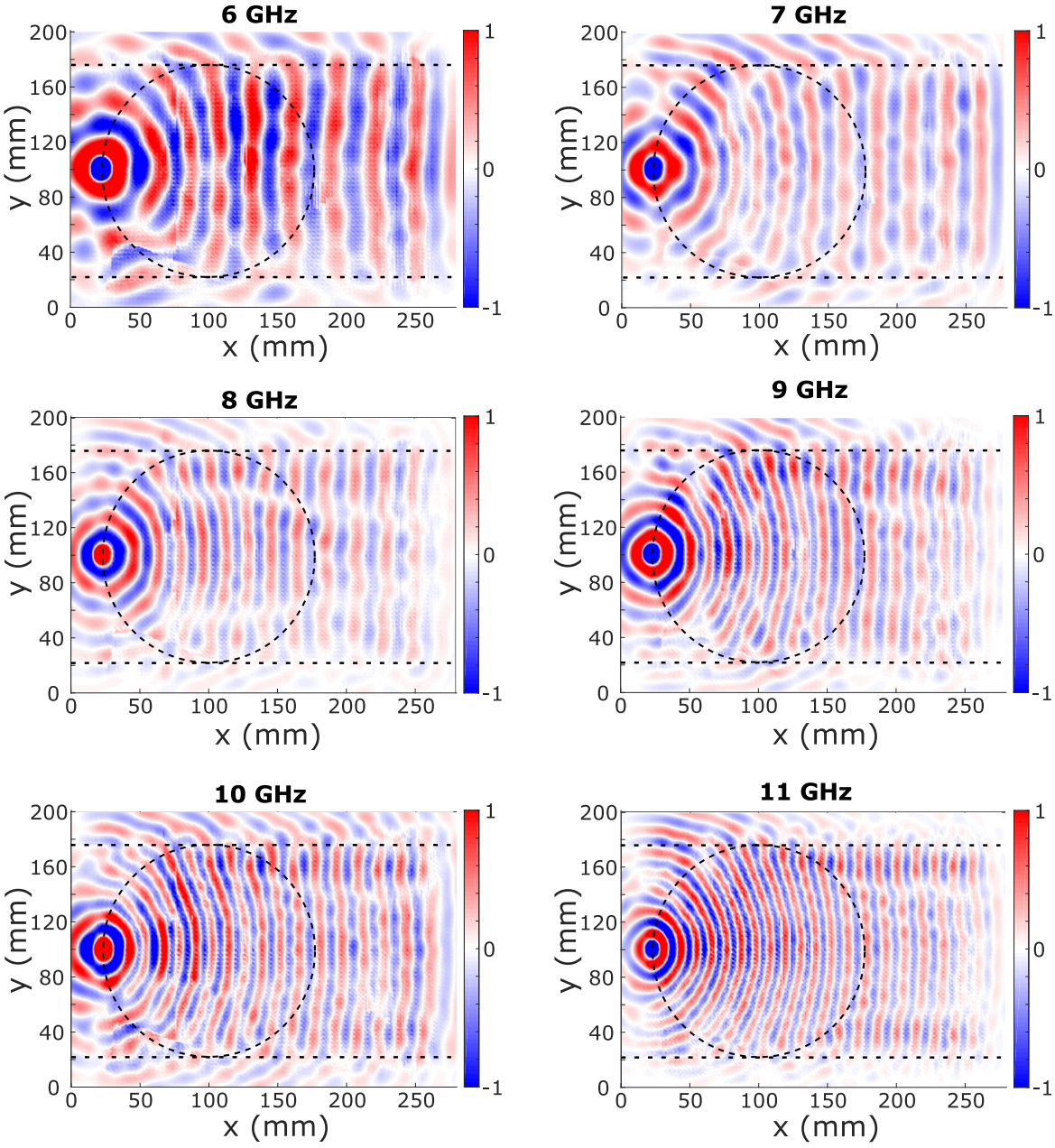

Fig. 4.19 Normalised instantaneous field plot across the surface of the structure containing a Luneburg lens for frequencies between 6 GHz and 11 GHz. The profile of the lens is represented, as a dotted black line. Two horizontal black dashed lines have also been included, delimiting the range of operation of the lens.

The field plots, from which the data corresponding to the radiative modes has been subtracted as explained in section 3.4, are plotted in Fig. 4.19 for frequencies between

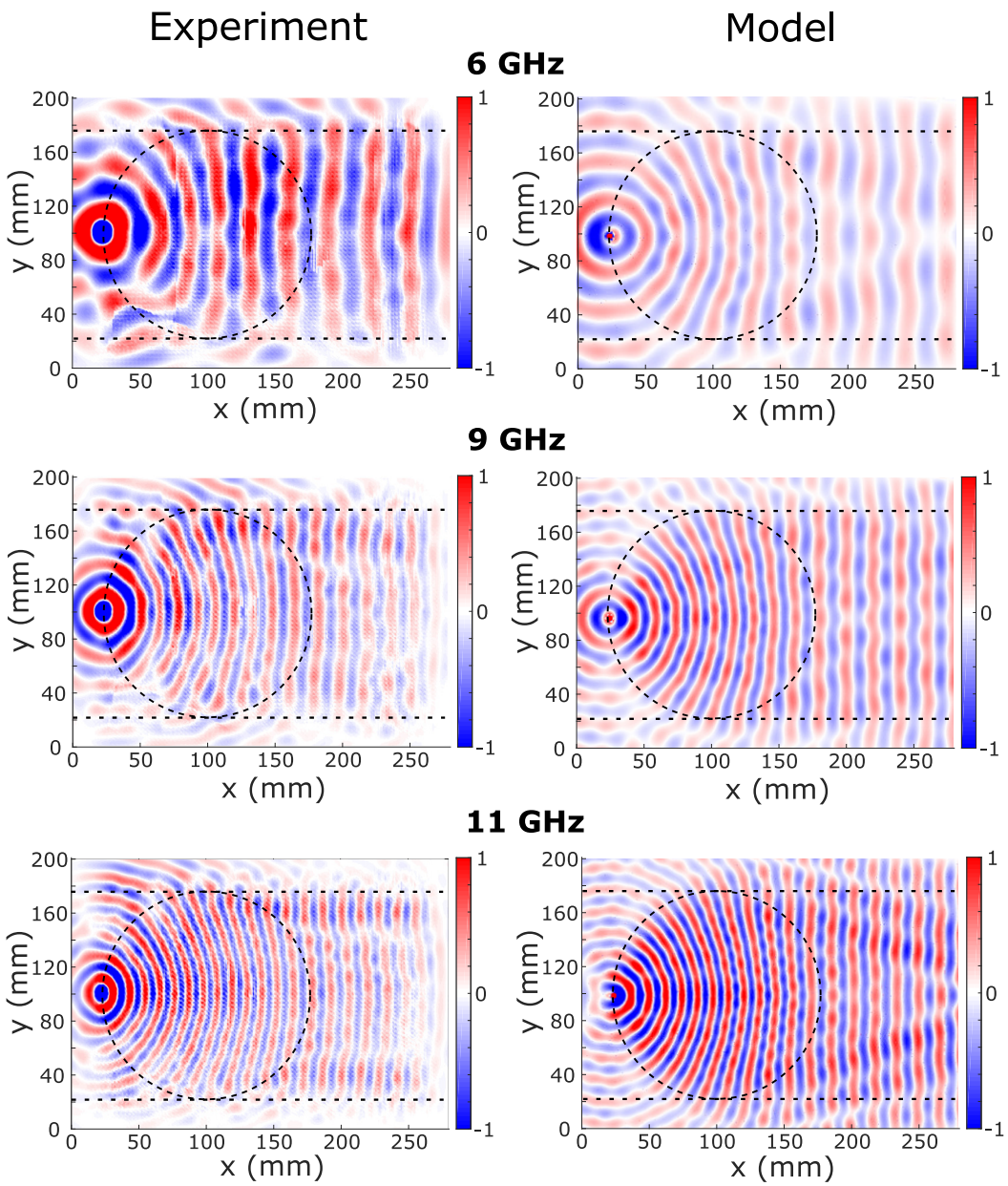

Fig. 4.20 Left column: Measured instantaneous field plot across the surface for 6 GHz, 9 GHz and 11 GHz. The perimeter of the lens is shown with a dashed line. The source is placed at the focus of the lens (located on its perimeter). The surface waves exit the lens to the right with planar wave fronts. The right column corresponds to the fields obtained in the FEM simulation (H_Z).

6 GHz and 11 GHz, which include the limit frequencies of the operational bandwidth. For all these frequencies the circular wave-fronts from the point source are straightened, resembling plane waves, after propagating across the lens, resulting in a fractional operational frequency bandwidth of 53%. This is another way to demonstrate the small frequency dependence

of the mode index presented by the structure: the lens was designed to operate at 10 GHz but because the mode index profile does not vary much in the mentioned frequency band, the structure still presents optimal performance. Another important feature for the optimal performance of some devices like the Luneburg lens is isotropy. As it is an omnidirectional device (focuses plane waves no matter where they come from) it is very important that the metasurface presents the same mode index in all directions. This requirement is also fulfilled by the proposed metasurface, as demonstrated in section 4.4, were circular isofrequency contours were shown.

In Fig 4.20 the field distribution of the surface wave at different frequencies are compared with the results of a FEM simulations where the entire surface has been modelled as a varying impedance sheet.

Both the experiment and the model show similar behaviour: the wavelength of the surface wave is reduced as it gets closer to the centre of the lens due to the increasing mode index. The curvature of the wave fronts is progressively reduced to the point where the wave fronts are planar on exiting the lens. The experimental data is affected by some interference produced by the wave reflection at the edge of the sample, and both the simulation and the experiment show effects caused by diffraction.

In addition, the experiment shows a distortion in the wave fronts as the frequency increases. In contrast, this distortion is not shown in the model, where the wave fronts remain circular. The mentioned distortion is due to a decrease in isotropy of the structure as the frequency increases which was shown in Fig. 4.10.

It needs to be noted that the size of the patches has been selected so that the index profile of the sample is that represented in Fig. 4.16 at 10 GHz. However this is only strictly true at the design frequency. Even though the variation is small, the mode index is not the same at the rest of frequencies. On the contrary, the FEM simulations presented in Fig. 4.20 assume the same index profile (that given in Fig. 4.16) for every frequency. This is the reason why the background wavelength may not be exactly the same in the model and the experiment.

4.5.2 Performance and fractional bandwidth

The performance of the Luneburg lens and its fractional bandwidth can be calculated by comparing the shape of the wave fronts obtained after the wave crosses the lens with a plane wave, representing the theoretical or ideal performance of the lens and with a spherical wave front, representing the shape it would have if the lens was not present. The fractional wavelength is calculated once we determine the range of frequencies for which the plane wave transformation occurs. The expression used to calculate the fractional bandwidth is given in equation 4.9.

$$\text{FBW} = \frac{f\text{max} - f_{\text{min}}}{f_c} \tag{4.9}$$

Here, f_{max} is the upper limit of the frequency band of operation, f_{min} is the lower limit and f_c is the central frequency of the band. It was determined that the range of frequencies at which the performance of the lens does not deviate from its ideal performance more than 10% is between 6.5 GHz and 11 GHz, resulting in a fractional bandwidth of 53%

4.6 Conclusion

In this chapter, a bi-layer metasurface comprised of two square arrays of circular patches with glide symmetry has been studied. In the first place, the effects of adding a second layer to an array of patches was studied. It was concluded that the design with the most desirable characteristics is that where the layers are placed very close together (the separation between the layers is 50 µm while the wavelength of operation is of the order of 10 mm) and are shifted with respect to each other presenting glide symmetry.

The resulting structure shows some advantages with respect to other metasurface designs. One of them is its low profile: it is very thin and lightweight, two desirable characteristics for space and defense applications. Furthermore, glide symmetry reduces the dispersion of the structure, resulting in a more broadband behaviour.

Finally, the variation of the mode index presented by the structure as the diameter of its patches is varied was also studied and a sample containing a graded index device was manufactured and measured. The chosen device was a Luneburg lens whose performance is optimal in the range of frequencies between 6.5 GHz and 11 GHz, translating into a fractional bandwidth of 53%.

In the next chapter, a different design, which increases the bandwidth of operation even further will be presented.

Chapter 5

Glide-Symmetric three-layer metasurface with hexagonal symmetry.

5.1 Introduction

In this chapter, a similar metasurface to that presented in Chapter 4 is introduced. In this case, the structure is comprised of three layers of circular copper patches. Furthermore, instead of arranging the patches in a square lattice, hexagonal symmetry is introduced, which improves the isotropy of the structure. As in the previous case, the layers comprising the structure are also shifted with respect to each other.

Due to the nature of the hexagonal array, there are two symmetric ways of placing a second layer with respect to the first one and a third layer may then be used to either cover all the available positions. Such arrangement in 3D with spheres, yields a face centred cubic structure (ABC) or, if the third layer is aligned with the first layer, a hexagonal close-packed structure (ABA). These arrangements will be discussed in section 5.2.

Finally, it is concluded that the ABC structure presents a very broadband behaviour, with a frequency dependence of the mode index even smaller than that of the structure presented in Chapter 4.

The fabrication technique introduced in section 3.2 was also employed to manufacture the three-layer metasurface, resulting in a flexible and light weight structure. However, the addition of an extra layer complicates the fabrication procedure, and particularly the alignment process.

In this chapter, the design, fabrication and experimental measurement of the metasurface are presented. In the first place, FEM simulations were performed to design and optimise

the structure. These were then followed by experimental measurements accompanied with a comparison of the measured data with modelling results.

Following the characterization of the metasurface, an experimental Luneburg lens device was fabricated and studied experimentally. Its performance is compared with model data from FEM simulations and also with the performance of the Luneburg lens presented in Chapter 4. The improved performance of the presented 3-layer device is confirmed through measurement of the mode propagating across the structure. Finally, the result is a very broadband device which operates between 8 GHz and 19 GHz. This translates into a fractional bandwidth of 73%, larger than that achieved by most metasurface devices including the lens presented in chapter 4, which presents a fractional bandwidth of 53%.

5.2 Background: Hexagonal Symmetry

The hexagonal lattice, also known as a triangular lattice is one of the five 2D lattice types.

In this structure, the lattice points are distributed in a way in which three nearby points form an equilateral triangle. In this way, the lattice vectors have the same length and form a 60° angle. It has a 60° rotation symmetry and three mirror planes.

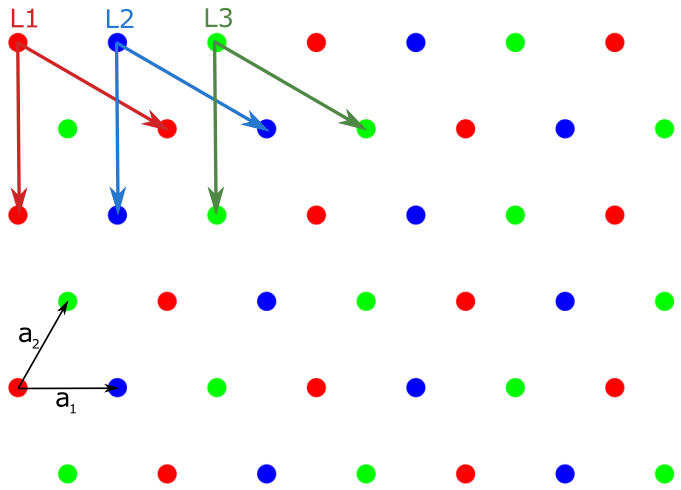

Fig. 5.1 Lattice points of a hexagonal (or triangular) lattice. The three different triangular lattices that comprise the hexagonal lattice are represented with a different colour. The lattice vectors of these three sub-lattices as well as the lattice vectors corresponding to the hexagonal lattice are marked.

Each layer of the structure studied in this chapter forms a hexagonal (or triangular) lattice, which is the combination of three triangular sub-lattices, whose lattice vectors are $\sqrt{3}$ times bigger. Each of these sub-lattices is represented in a different colour in Fig. 5.1. In the same

way, for each color, the centres of the hexagons of that color form a hexagonal lattice with horizontal rows which is in linear scale $\sqrt{3}$ times as large and so on.

If any of the three triangular lattices (red, blue or green in Fig. 5.1) is missing, the resulting structure would be a honeycomb lattice. This is a special lattice as it contains two elements (or lattice points) per unit cell.

As mentioned before, the structure presented in this chapter is a stack (in the out-of-plane direction) of the three hexagonal lattices. The way in which this stacking is made is equivalent to the different ABC layers in a face centered cubic (FCC) structure. This stacking process is represented in Fig. 5.2.

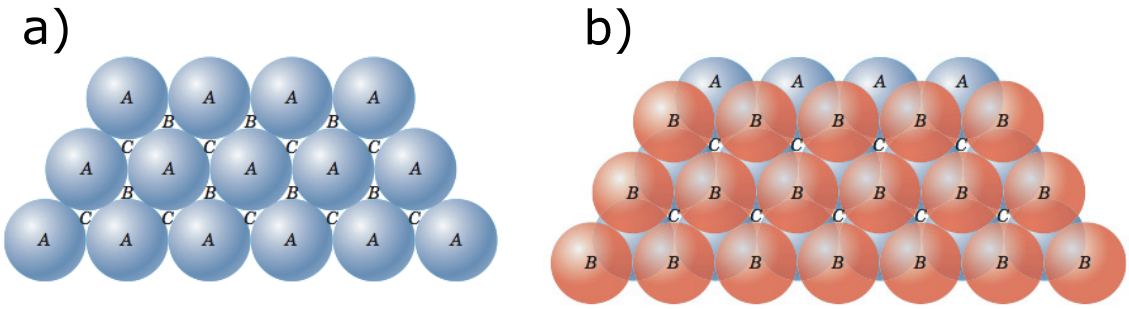

Fig. 5.2 a): Triangular lattice, where the lattice points (elements) are marked with a blue sphere. The two different sets of voids, also in a triangular lattice are marked with B and C respectively. b) Bi-layer structure, where the voids previously marked with a B have been filled with red spheres. There is a third sets of voids marked with C which correspond to the positions of the third layer.

Firstly, we start with a single layer of elements in a triangular lattice. The lattice points (elements) are marked with blue spheres (A) in Fig. 5.2 a). Between adjacent elements, there are two different sets of voids, each of them also arranged in a triangular lattice. These voids are marked with B and C respectively in the figure. In the second image, b), a second hexagonal lattice is added, resulting in a bi-layer structure. The voids previously marked with B have now been occupied by red spheres, representing the second layer of elements. There is a third set of voids marked with C, which corresponds to the positions of the elements which would form the third layer.

A face centered cubic structure is a stack of the three layers previously described following an ABCABC... stack. If there are no elements in the positions described as C (or B alternatively), the structure forms an ABABAB... (or ACACAC...) stack, known as hexagonal close packed structure.

The hexagonal lattice presents a higher number of closest neighbours than the square lattice and therefore presents higher isotropy, which is an important point to consider when designing omnidirectional devices.

One of the most studied structures presenting hexagonal symmetry is graphene. It shows a linear dispersion relation which originates from the symmetry properties of its honeycomb structure [107]. These symmetry arguments can also be extended to systems of bosons (like photons) or general waves, which propagate in a spatially periodic potential with hexagonal structure, for example a photonic crystal [108, 109]. These structures, may present regions in their energy spectra which are effectively described by the Dirac equation for fermions with spin 1/2.

The dispersion (or energy spectra) of graphene and its analogues, presents a very distinctive feature. This is known as the Dirac Point, which is a crossing of two modes at the K-point on the Brillouin zone boundary. It results in the absence of a bandgap, together with a finite group velocity at the Brillouin zone boundary. Symmetry arguments, show that they appear naturally in honeycomb lattices (or, more in general, in lattices with underlying triangular symmetry).

Numerous realizations of artificial graphene have been studied over different frequency ranges [110]. Some systems that can be engineered to present artificial graphene properties are: Two-dimensional electron gases subject to a honeycomb potential lattice [111], molecular assemblies with hexagonal symmetry arranged on a copper surface [112], ultracold atoms in optical lattices [113, 114], photonic crystals [115–117] and microwave systems[118, 119].

At microwave frequencies, a crossing between two modes which does not result in a bandgap, as found when a Dirac point is present, can be interpreted as the lack of coupling between the two modes. This means that they present orthogonal fields which do not interact.

In this chapter, we present a three-layer metasurface with hexagonal symmetry which benefits from the straight dispersion that appears as a consequence of this Dirac-like behaviour.

5.3 Metasurface Design

The metasurface under study is a three-layer structure where each layer constitutes a hexagonal array of circular copper patches. The three layers are identical to each other but shifted so that the patches occupy the different positions of an ABC three-dimensional lattice, like the one described in section 5.2. The layers are fabricated independently according to the procedure described in section 3.2 and then manually stacked together. While aligning the three sheets an oil layer is placed between them to keep the different layers in place via surface tension. The separation between the copper patches is therefore given by the dielectric substrate to which the patches are printed onto plus the oil layer used to bind the

sheets together. As discussed in chapter 3, the minimum separation between the layers is therefore 50 µm (25 µm corresponding to the dielectric substrate and an extra 25 µm of the oil layer). A schematic of the described structure is presented in Fig. 5.3.

In similarity to that presented in the previous chapter, the diameter of the patches can be varied systematically, which results in the potential for variation in the mode index across the surface structure.

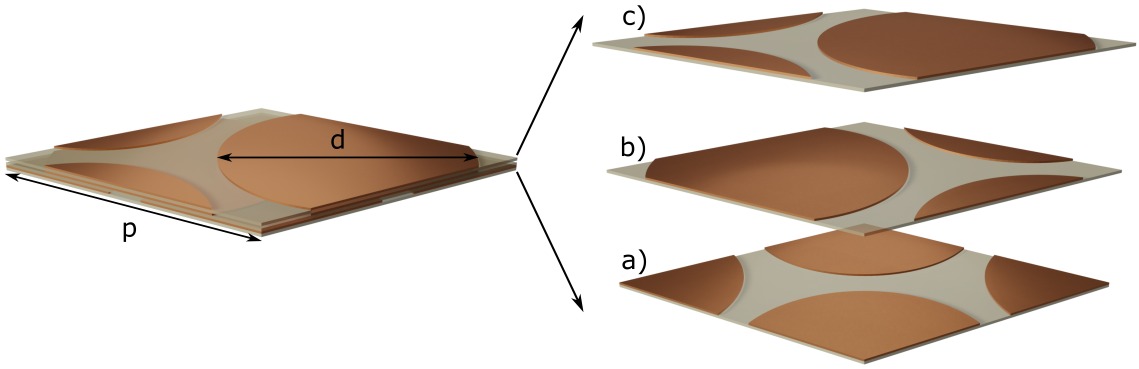

Fig. 5.3 Schematics of a unit cell of a three-layer structure of copper circular patches in a hexagonal array. The different layers are stacked in the configuration of a face centered cubic arrangement (ABC). The diameter of the patches is $d = 2.15$ mm and the periodicity of the structure is $p = 2.4$ mm. Each layer of patches is printed over a dielectric slab of 25 µm as shown on the right hand side.

In this section, numerical eigenmode simulations are performed to obtain the dispersion diagram and field plots of the modes supported by the structure, aiming to give a better understanding of its behaviour in therms of frequency and mode index. The effect of varying the size of the patches comprising the structure is also investigated.

Firstly, a value for the periodicity of the structure (p) is chosen. This determines the scale (and maximum patch diameter) and the frequency of operation of the structures. In this case, a periodicity of $p = 2.4$ mm was used. This sets a range of operation for the metasurface between 15 GHz and 25 GHz. The reasons for using this scale-length are mainly practical as the resolution of the print-and-edge method used is good enough for the chosen patch size and the operational frequency range is optimal for the available experimental setup. However, everything can be scaled so that the operational frequency band matches any particular requirements.

There are two main reasons to choose a hexagonal array over any other lattice. The first one is to benefit from the high symmetry and isotropy of the structure resulting in a similar behaviour for the different directions of propagation of modes across the surface. Also, in

a hexagonal array, the elements are closer together, which maximises the overlap regions between the patches and therefore increases the capacitive coupling between them, which is critical as shown in later discussion.

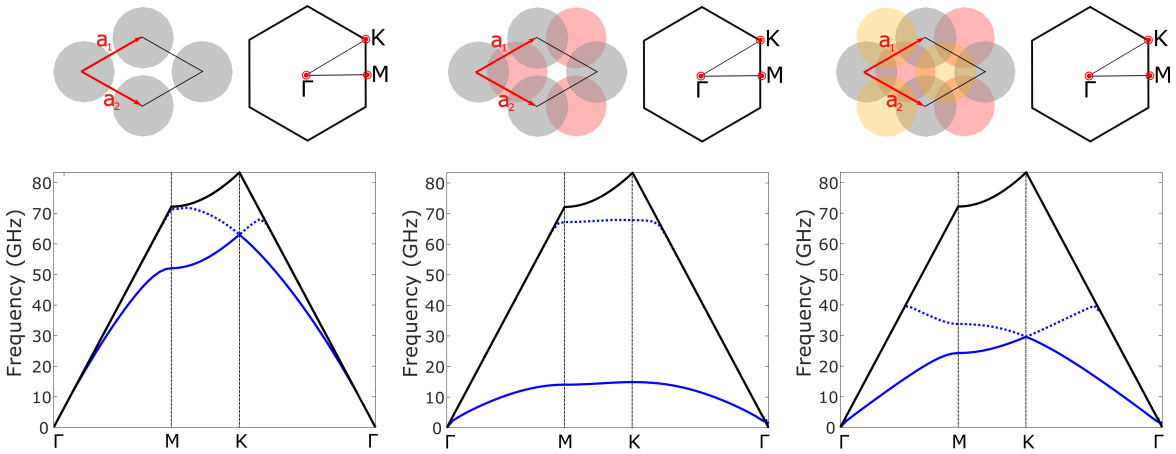

Fig. 5.4 From left to right: dispersion diagrams of the modes supported by structures with one (A), two (AB) and 3 (ABC) layers. In all cases, a hexagonal array of circular metallic patches with a periodicity of 2.40 mm and a patch diameter of 2.15 mm constitutes the different layers. The lowest order mode is represented with a solid blue line and the dotted blue line corresponds to the second mode. The light line is represented in black. The dispersion diagrams have been calculated in the three directions of high symmetry of a hexagonal lattice, between the Γ, M and K points.

In Fig. 5.4 we compare the dispersion diagrams of the modes supported by a single layer (A) and a double layer (AB) with that of the proposed three-layer structure (ABC); all constructed with the same hexagonal array of circular patches with a periodicity of 2.40 mm and a patch diameter of 2.15 mm.

The first structure (mono-layer), supports a very non-linear and dispersive lowest order mode. This mode is very close to the light line for most of the frequency range and then turns quickly to hit the Brillouin zone boundary with zero gradient at its resonant frequency. This resonant frequency is directly related to the resonance frequency of a single patch. This is a clear example of the classic plasmon-like behaviour of most periodic metasurfaces, described in chapter 2. This results in a low mode index for small frequencies followed by a strong variation as the frequency increases towards and asymptotic limit.

In the second dispersion diagram, corresponding to the modes supported by a bi-layer structure (AB), the lowest order mode is pushed down in frequency, away from the light line. This is the same effect that was reported in chapter 4 as a second layer of patches was added. It is due to an increased confinement of the fields, which now propagate primarily inside the

dielectric between the two layers. As a consequence, the mode index increases. However, the structure still shows a resonant, non-linear behaviour with a strong frequency dependence.

In the third graph, corresponding to the structure where all the positions have been filled up (ABC), the typical characteristics of hexagonal lattices are shown. In the first place, a bandgap is found at the M point in the dispersion diagram but is absent at the K point due to the presence of a Dirac Point. This results in a more linear dispersion of the lowest order mode, which now approaches the Brillouin zone boundary with a finite group velocity and therefore it does not have to bend to reach a zero gradient.

This linear dispersion is a very useful feature for microwave engineering, as it increases the bandwidth of operation of prospective devices since $v_p \approx v_g$.

For both multilayer structures, b) and c), there is a big capacitive coupling effect between the overlapping patches. This results in an electric field that is mostly perpendicular to the plane of the structure and confined to the overlap regions. This makes the metasurface present a wave guide-like behaviour, supporting bound surface modes even at low frequencies with a higher mode index than the single-layer structure.

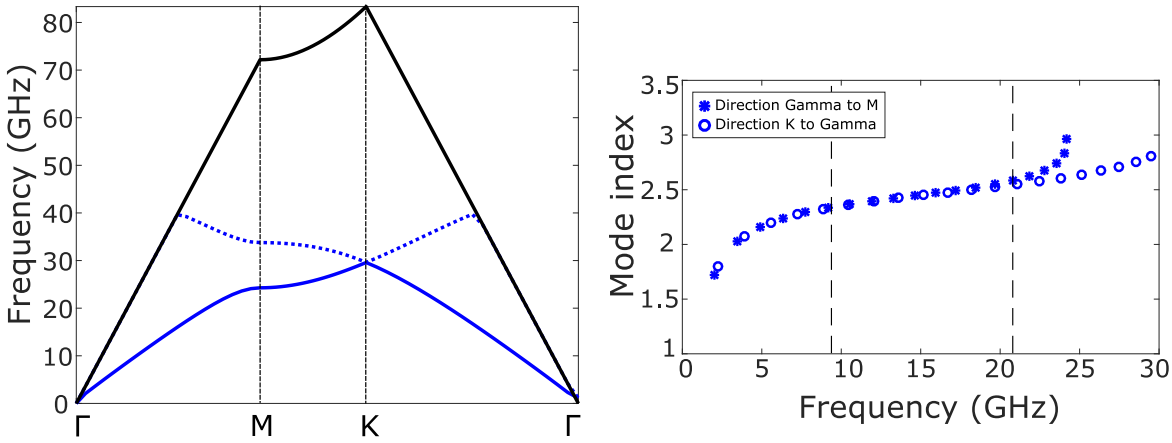

Fig. 5.5 (Left) Dispersion diagram of the modes supported by the three-layer metasurface of circular patches with hexagonal symmetry presented in Fig. 5.3. This structure has a patch diameter of 2.15 mm and a periodicity of 2.4 mm. The first mode is represented with a continuous line and the dotted line corresponds to the second mode. The light line has been represented in black. The dispersion diagram was calculated for the three directions of interest of a hexagonal lattice. On the right hand side, the variation of the mode index with frequency is presented. The mode index was calculated for two different directions (Γ to M (stars) and K to Γ (circles)). The range of frequencies where the variation of the mode index is smaller than 5% with respect to its value at 15 GHz corresponds to the region between the dotted black lines.

The mode index of the lowest order mode supported by the structure shown in Fig. 5.3 is presented in Fig 5.5 (right) as well as its dispersion diagram (left). It is shown

that the behaviour of the structure is isotropic for frequencies up to 21 GHz, as the mode index in both considered directions presents the same tendency. This isotropic behaviour will be also confirmed later by the circular shape of the isofrequency contours. Also, the mode index varies only very slightly with frequency for the range between 9 GHz and 20.5 GHz. Specifically, it only varies by 5% (with respect to its value at 15 GHz) in the range between 9 GHz and 20.5 GHz. This is a clear improvement with respect to most single-layer metasurfaces, and also with respect to the metasurface presented in chapter 4. This small variation of the mode index results in a much more broadband performance of any prospective microwave devices.

5.3.1 Mode index variation

In this section, the variation of the effective mode index presented by the lowest order mode supported by the proposed metasurface when varying the diameter of its patches is studied. In this way, a graded mode index can be defined across the structure.

To study this variation and ultimately, to get the expression which relates the patch diameter to the mode index presented by the structure, several simulations varying the patch diameter were performed. All the simulations performed, keep the same values of the periodicity, dielectric permittivity and thickness for both the dielectric and the oil layer. With the FEM simulations, the dispersion diagram, and from it the mode index of the modes supported by the infinitely periodic metasurfaces are calculated. This study ultimately results in a function that relates the diameter of the patches and the effective mode index for a whole range of frequencies. When the frequency of operation of the prospective device is selected, a direct relation between the diameter and the mode index is well defined.

The effect of varying the diameter of the patches comprising the structure presented in Fig. 5.3 is shown in Fig. 5.6. On the left hand side, the dispersion diagram of the lowest order mode supported by the structure is shown for different values of the diameter of the patches. In this case, only the dispersion diagram in the direction Γ to M is presented. As the patches get smaller, the limiting frequency of the lowest order mode moves up in frequency, towards the light line. This is a consequence of the decrease in the capacitive effect in the metasurface, due to a reduction of the overlap regions between the patches, which also causes a decrease in the confinement of the fields.

On the right hand side of Fig. 5.6, the dependence of the mode index with the patch diameter, obtained from the first plot, is presented. As the behaviour of the structure is isotropic for the studied range of frequencies (as will be shown when the isofrequency contours are presented), one direction is enough to give a clear idea of the behaviour of the structure. The mode index has been normalised to that of the lowest order mode supported

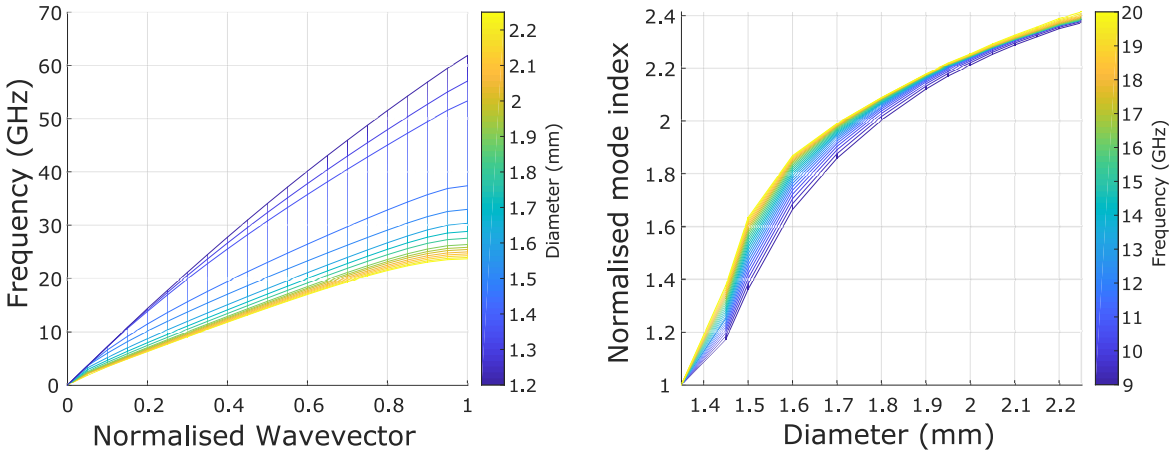

Fig. 5.6 (Left) Dispersion diagram of the lowest order mode supported by the three-layer metasurface of circular patches in a hexagonal array for values of the diameter of the patches between 1.35 mm and 2.25 mm, keeping the periodicity (p = 2.4 mm) constant. As the patches get smaller the dispersion gets closer to the light line. This is a consequence of the reduction of the overlap regions between the patches, which decreases the confinement of the fields and the capacitive effect between the patches. (Right) Normalised mode index presented by the structure as a function of the diameter of the patches for different frequencies. To obtain the normalised mode index it is divided by the mode index presented by the structure with the smallest diameter (1.35 mm).

by the metasurface with the smallest patch diameter, so that the achievable index contrast is highlighted. It is also shown how the mode index varies with frequency. It is important to note that the variation with frequency is within the 5% of the value at 15 GHz as mentioned before.

The frequency of operation of the prospective device (Luneburg lens) was chosen to be 15 GHz. This frequency coincides with the central frequency of the range in which the variation of the mode index is below 5%. The relation that provides the diameter of the patches necessary to obtain a particular mode index is calculated by fitting the data obtained with the FEM software. This relation is shown in Fig. 5.7. The blue dots represent the data obtained with the FEM software, while the red line is an exponential fit, of the form shown in equation 5.1.

$$d = ae^{bn} + ce^{dn} \tag{5.1}$$

For the particular dimensions chosen here, the values of the fitting parameters are: a = 0.002848, b = 2.273, c = 1.379 and d = 0.002241. This functional dependence allows to calculate the patch-size required to achieve any desired mode index (n).

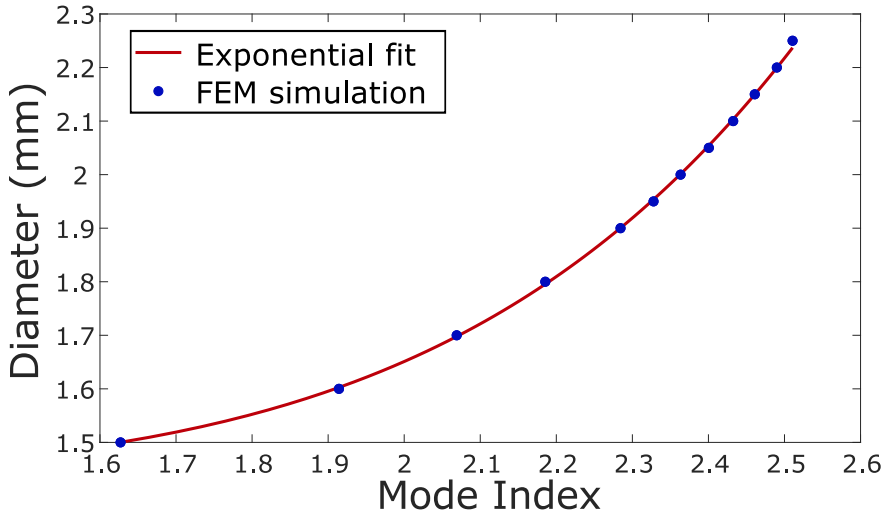

Fig. 5.7 Mode index presented by the lowest order mode supported by the metasurface at 15 GHz as the diameter of the patches that comprise it is varied. The blue dots correspond to the value of the mode index obtained with a FEM simulation and the red line represents an exponential fitting curve.

5.3.2 Two-Dimensional infinitely periodic metasurface: Experimental characterisation

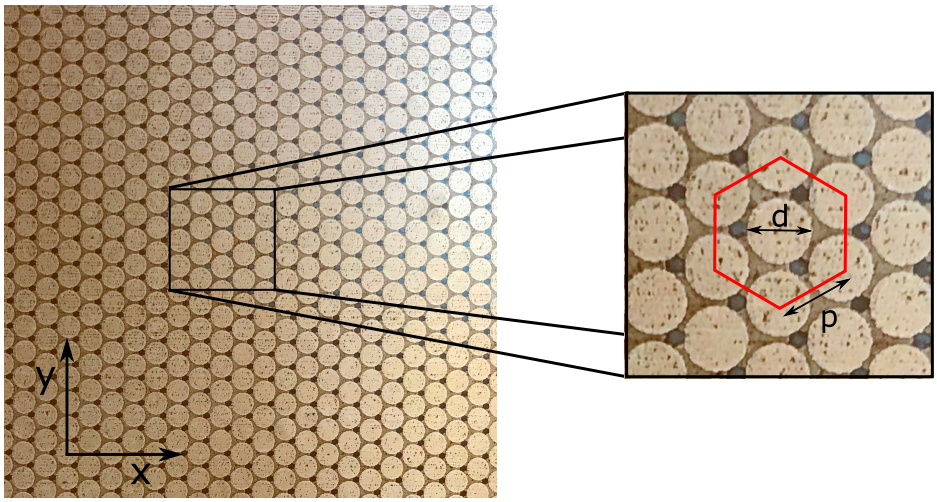

Fig. 5.8 Photograph of the sample used to characterise experimentally the three-layer metasurface presented in this chapter. Each three layers is comprised of circular copper patches with diameter d arranged in a hexagonal lattice of periodicity p.

A two-dimensional sample of the described periodic structure was fabricated and tested as described in chapter 3. A photograph of the sample is shown in Fig. 5.8. In this section, the

experimental results corresponding to the dispersion diagram, mode index and isofrequency contours of such a metasurface are presented.

A surface area of 200 mm × 200 mm was scanned with a near field probe (loop antenna), while the modes in the sample were excited with an identical source. With this, the field profile of the surface waves propagating on the sample was obtained.

The isofrequency contours are the result of taking the two-dimensional Fourier transform of the experimental field data. The normalised Fourier amplitudes of the k_x and k_y components, representing these isofrequency contour plots is presented in Fig. 5.9 for 6 different frequencies between 10 GHz and 35 GHz. The experimental data is represented as a grey-scale to which, the limits of the first Brillouin zone (red solid line) and the light circle (red dashed line) have been added.

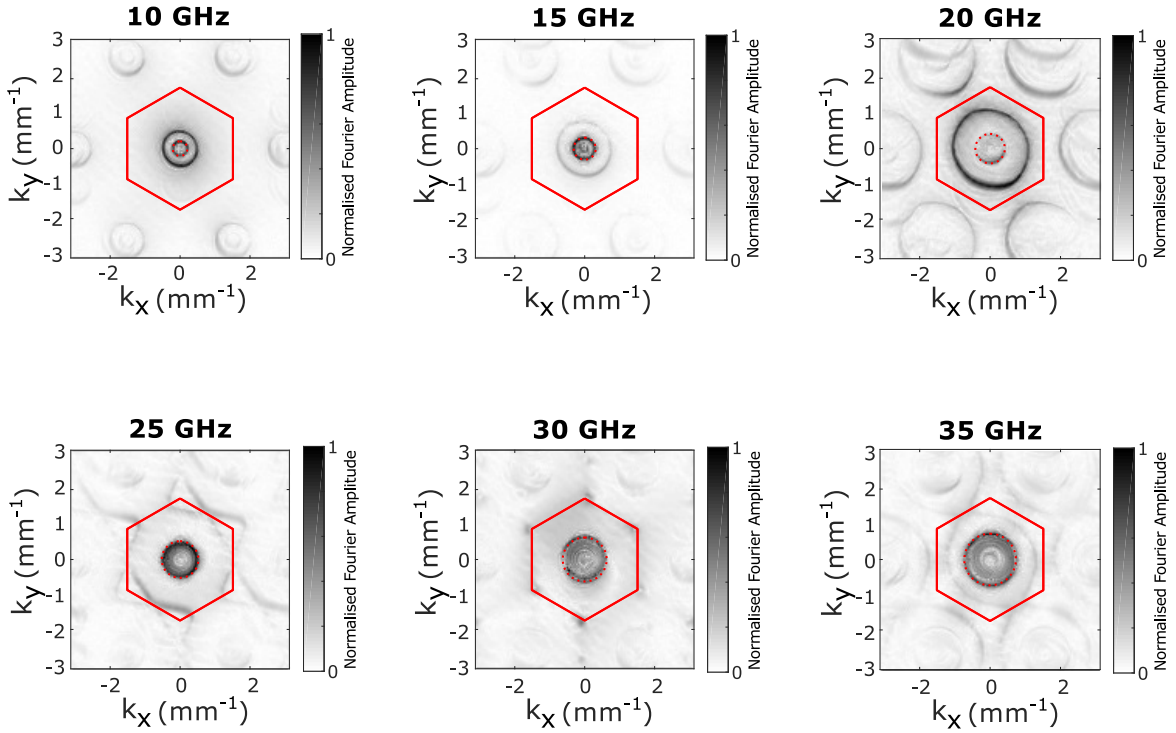

Fig. 5.9 Normalised Fourier amplitude of the experimental field data, representing the isofrequency contours of the modes supported by the presented metasurface structure with hexagonal symmetry for frequencies between 10 GHz and 35 GHz. The first Brillouin zone is represented in red and the light line is also included as a red dotted circle.

There are a some features in these isofrequency contours that need to be highlighted. Firstly, in the center of the plot, we find the light circle (represented with a red dotted line), limiting the area corresponding to the radiative modes. The data inside this circle is of no interest to this study as we are studying the modes bound to the metasurface and therefore

can be removed. The modes propagating on the surface, have a larger in-plane wave vector ($k > k_0$) and are found outside the light circle.

The isofrequency contours presented in Fig. 5.9 show a distortion that is not a consequence of the periodic structure of the metasurface. At low frequencies (10 GHz to 20 GHz), the isofrequency contours should be almost circular since they are not strongly perturbed by the lattice. However, the experimental data shows a distortion in the diagonal direction. This is due to a small misalignment (of the order of 100 µm) of the layers comprising the structure. Such misalignment would increase the overlap regions in one direction (and therefore the capacitance in that direction) while decreasing them in others and therefore causing anisotropy.

As the frequency increases, the isofrequency contours start to deviate from their initial circular shape due to a distortion caused by the array, which adds to the distortion caused by the misalignment. This is visible in Fig. 5.9 at 20 GHz and 25 GHz.

Finally, it is also shown how at 30 GHz the modes reach the Dirac point, as all the radiation is confined to the K points of the structure in reciprocal space.

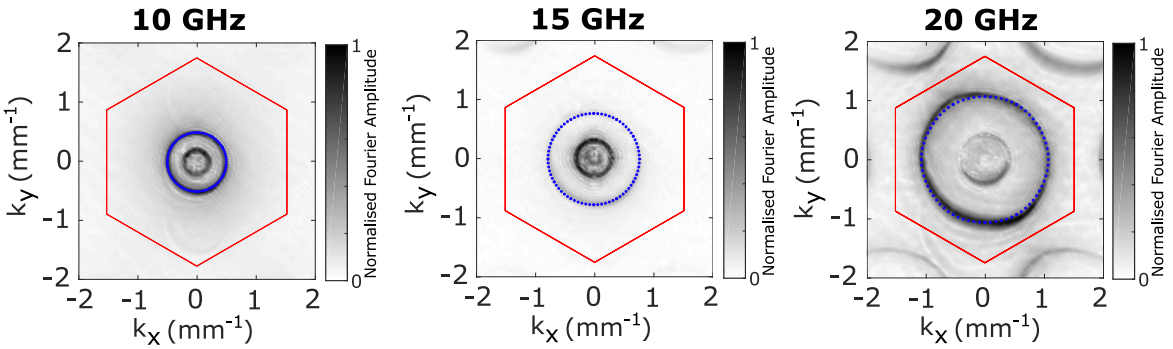

Fig. 5.10 Experimental isofrequency contours at 10 GHz, 15 GHz and 20 GHz (grey scale) compared to the theoretical isofrequency contours, obtained with a FEM software, represented with blue dots. The first Brillouin zone is also represented (solid red line).

In Fig. 5.10, the isofrequency contours at 10 GHz, 15 GHz and 20 GHz are compared with a theoretical calculation obtained with a FEM software. The experimental isofrequency contours are represented as a grey scale while the simulated data has been superposed as red dots. The distortion caused by the misalignment of the layers is clearly evident, particularly at higher frequencies (20 GHz).

This small misalignment is very difficult to eliminate as the layers are aligned manually. However, the alignment technique was improved by adding several alignment marks to reduce it as much as possible. Furthermore, the performance of the device is not much affected as will be shown in section 5.4.

Finally, after determining the Fourier amplitudes at every measured frequency, the dispersion diagram of the modes supported by the structure can be visualised by taking cuts in the directions of interest and then stacking the lines of data obtained for each frequency. In Fig. 5.11 the Fourier amplitudes plotted in frequency and wave vector space, representing the dispersion diagram of the modes supported by the structure are presented. A unit cell of the structure and the directions of high symmetry in reciprocal space are also shown. The experimental measurement is represented as a grey scale while the FEM results are superposed to the experimental data. The dispersion of the first mode is represented with red dots and the second mode with red squares; obtaining very good agreement between the experiment and the simulation.

In the dispersion diagram is easy to appreciate the high linearity of the dispersion of the lowest order mode. The presence of a Dirac point at the K point is also very clear, as the modes cross the Brillouin Zone boundary at the K point with a finite group velocity (non-zero gradient) and without forming a band gap.

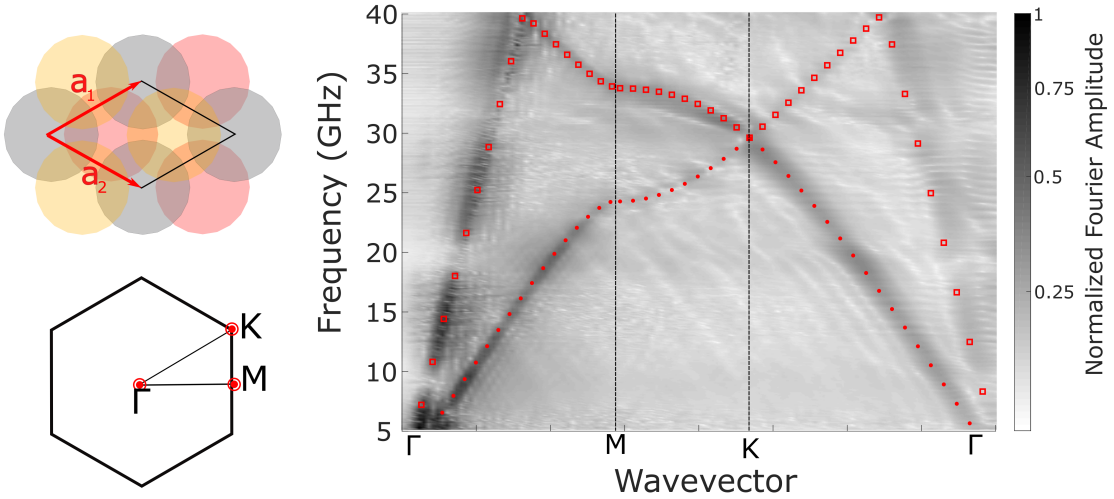

Fig. 5.11 Normalised Fourier amplitude, representing the experimental dispersion diagram of the modes supported by the three-layer structure of circular patches in a hexagonal array. The experimental data is represented as a grey scale and the dispersion diagram obtained with the FEM software is overlaid in red (dots for the first mode and squares for the second). The dispersion diagram has been calculated in the directions of interest for a hexagonal lattice (Γ to M, M to K and K to Γ). Sketches of the unit cell in real space and the First Brillouin zone in reciprocal space are also included.

5.4 Luneburg lens: Design and characterization

As it was done with the 2-layer metasurface presented in Chapter 4, we now proceed to fabricate and test a demonstrator (Luneburg lens) using the three-layer metasurface described in this chapter. The proposed Luneburg lens was designed to operate at 15 GHz, which is the central frequency of the band at which the mode index only varies by 5%.

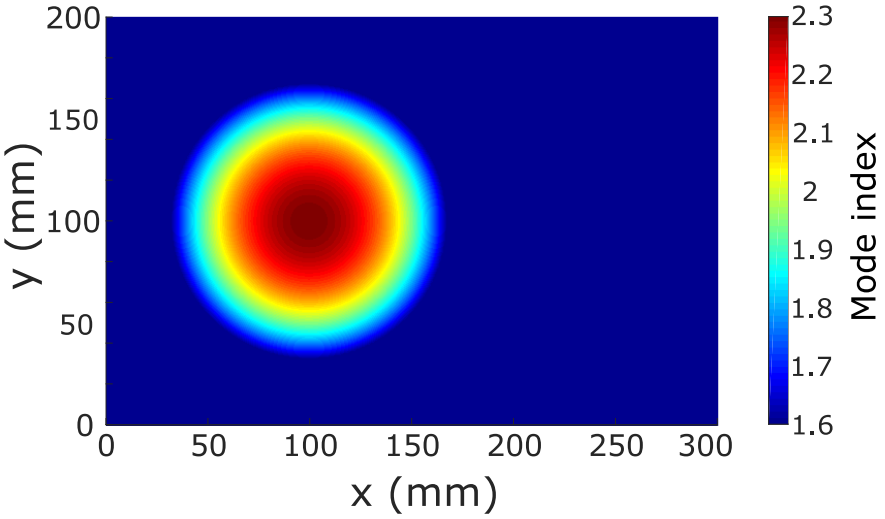

Fig. 5.12 Mode index profile of the experimental metasurface device containing a Luneburg lens. The background metasurface presents a mode index of $n_0 = 1.6$. Inside the lens, the mode index increases radially towards the centre of the lens, where it reaches its maximum value $n = \sqrt{2}n_0$.

A sample with a background index of 1.6, containing a Luneburg lens with a diameter of 135 mm was designed and fabricated. At 15 GHz, the chosen background index yields a wavelength of $\lambda_{bg} = 12.5$ mm. This means that the size of the lens is of the order of ten wavelengths, and therefore the geometrical optics approximation is applicable.

The required index profile was calculated with equation 4.7 and it is represented in Fig. 5.12. In the sample, the background has a constant index of 1.6 and in the lens the index increases radially towards the centre of the lens where it reaches its maximum value ($n_{max} = \sqrt{2} \times 1.6$). In this way, the background contains patches with the smallest diameter.

Finally, the expression relating the patch diameter with the achieved mode index calculated in section 5.3.1, was used to calculate the diameter profile required to achieve such design.

5.4.1 Experimental results

The experimental setup described in section 3.3 was used to measure the fields propagating across the lens. In this case, the loop antenna acting as a source was placed at the focus of the Luneburg lens, located on its perimeter, and the probe was used to scan an area of 200 mm by 300 mm on the opposite face of the sample.

The field plots, from which the data corresponding to the radiative modes (data inside the light circle) has been subtracted, as explained in section 3.4, are plotted in Fig. 5.13 for three different frequencies. These frequencies include the limiting frequencies of the operational bandwidth (8 GHz and 19 GHz).

For the mentioned range of frequencies, the fabricated lens transforms the circular wave-fronts from the point source into plane waves after traversing the lens. The device has therefore a resulting fractional frequency bandwidth of 73%. This broad operational frequency range confirms the small frequency dependence of the mode index presented by the structure.

In Fig 5.13 the field profiles of the surface wave propagating across the metasurface containing a Luneburg lens at different frequencies are also compared with the results of a FEM simulations where the entire surface has been modelled as a sheet with varying isotropic surface impedance. This method, which was explained in chapter 3, does not take into account the internal geometry of the sample or the frequency dependence of the impedance.

Both, experiment and model show a similar behaviour at all frequencies: the wavelength of the surface wave is reduced as it gets closer to the centre of the lens due to the increasing mode index, and the wave fronts are approximately planar on exiting the lens.

The experimental data is affected by some interference produced by the wave reflections at the edge of the sample, and both the simulation and the experiment show effects caused by diffraction due to the finite size of the lens. In this case, the experimental measurements also show a distortion in the fields, which make them slightly asymmetrical. This is again due to a misalignment between the layers that comprise the sample. Such misalignment creates an anisotropic mode index profile which distorts the wave fronts.

The size of the patches was selected so that the index profile of the sample is that represented in Fig. 5.12 at the design frequency (15 GHz). This means that the mode index, although withing the 5% range of variation, is not entirely the same for the rest of frequencies. However, the FEM simulations presented in Fig. 5.13 assume the same index profile (that given in Fig. 5.12) for every frequency which means that the background wavelength may not be exactly the same in the model and the experiment.

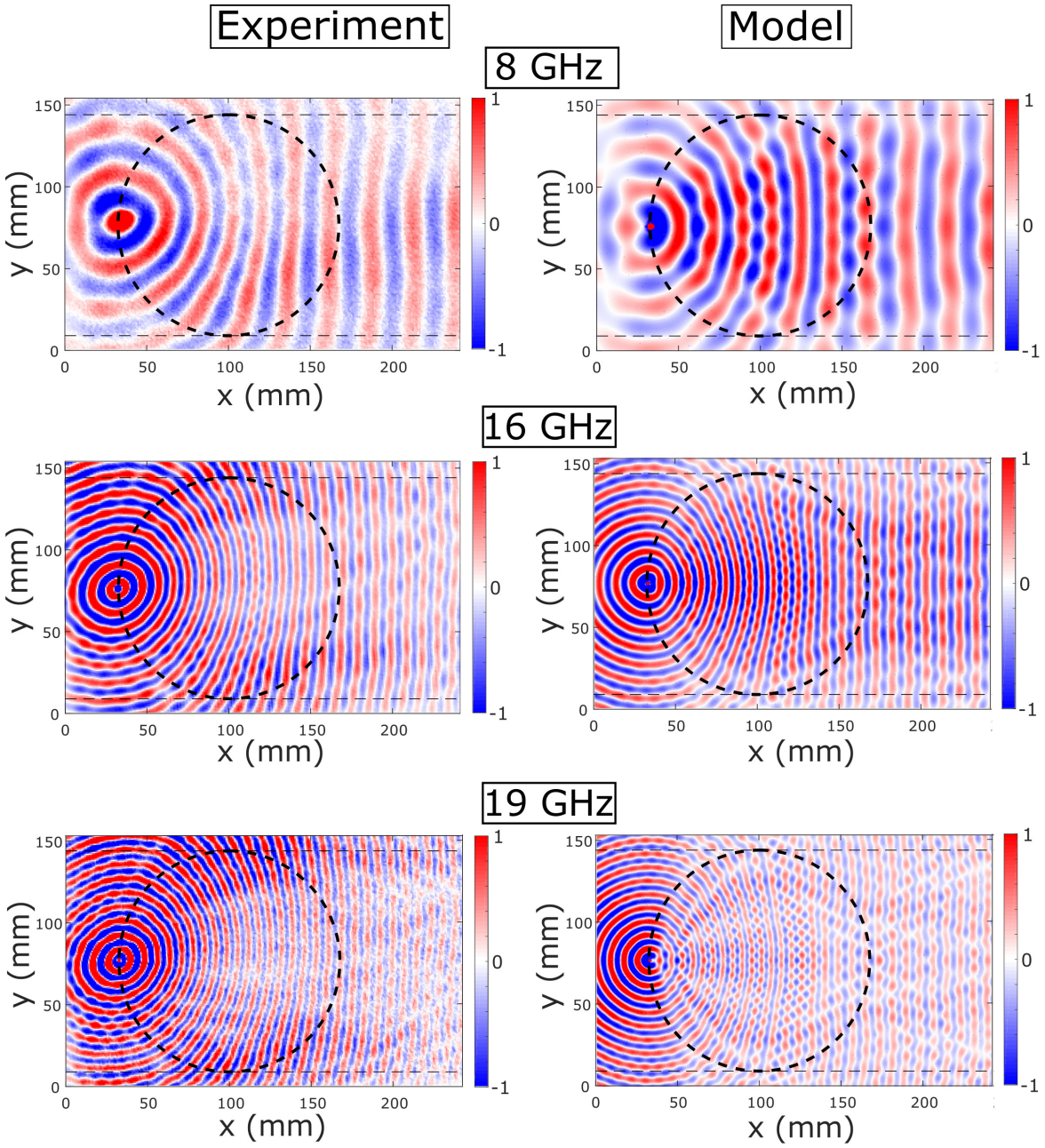

Fig. 5.13 (Left) Normalised instantaneous field plot across the surface of the structure containing a Luneburg lens for frequencies between 8 GHz and 19 GHz. They are compared with the field profile obtained with a FEM software for a structure containing a Luneburg lens modelled as a sheet of varying surface impedance (right). In all cases, the outside edge of the lens is represented, as a dotted black line.

5.4.2 Performance and fractional bandwidth

The performance of the Luneburg lens and its fractional bandwidth can be calculated by comparing the shape of the wave fronts obtained after the wave crosses the lens with a plane wave, representing the theoretical or ideal performance of the lens and with a spherical wave front, representing the shape it would have if the lens was not present. The fractional wavelength is calculated once we determine the range of frequencies for which the plane wave transformation occurs. The expression used to calculate the fractional bandwidth is given in equation 4.9.

In this case, the upper limit of the frequency band of operation is 19 GHz , the lower limit is 8 GHz and the central frequency of the band is 15 GHz. This results in a fractional bandwidth of 78%

5.5 Conclusion

In this chapter, a three-layer metasurface with hexagonal symmetry has been designed and characterised. It presents some of the characteristic features of structures with hexagonal symmetry such as a straight Dirac-like dispersion and a Dirac crossing at the K-point at the Brillouin zone boundary. The structure is also very thin and lightweight, two desirable characteristics for space and defense applications. The linear dispersion presented by the structure together with the improved isotropy given by the hexagonal symmetry make this structure suitable for the manufacturing of broadband and omnidirectional devices. However, the addition of an extra layer of patches (respect to the metasurface presented in Chapter 4) adds some extra difficulty and cost to the manufacturing process of the metasurface. Also, having an extra layer makes the correct alignment of the layers more difficult, resulting sometimes in samples that are more difficult to reproduce and in distortion, due to the misalignment of the layers, as shown in Fig. 5.9 and Fig. 5.13. However, besides these alignment issues, the Fractional bandwidth of a Luneburg lens was proven to increase by 20% when using the three-layer metasurface presented in this chapter.

The results presented in this chapter were published in [9] in 2017.

Chapter 6

Metasurface bilayer for slow microwave surface waves

6.1 Introduction

Slowing down or completely stopping the propagation of an electromagnetic wave across a material may be of value for many areas of physics due to the number of technological applications that would benefit from such control [120].

Slow light was initially studied at optical frequencies, but quickly found applications at other frequencies such as microwaves [121]. Controlling the group velocity of light at microwave frequencies offers a solution to different systems requiring a tunable time delay [122, 123] or phase shift [124, 125]. An example of what can be achieved with the manipulation of the velocity of propagation of electromagnetic waves has already been given in the previous chapters in the form of GRIN devices. These devices are simply structures that slow down the propagation of light in a particular manner to achieve a desired field profile.

In this chapter we explore a novel way of slowing down the propagation of surface waves across a metasurface. For such purpose, a periodic metamaterial structure comprised of elements that extend for more than one unit cell is proposed. With this structure, a mode index up to three times as big as that exhibited by most conventional metasurfaces is achieved. Furthermore, the proposed design is very simple, easy to fabricate and despite its high index the losses are kept very low.

Three different variations of the proposed structure are presented. Firstly, a mono-layer metasurface is studied; this is followed by the addition of a second layer rotated by 90° with respect to the first one. Finally, a third structure is introduced where the top layer has been

shifted with respect to the bottom layer by half of the period of the lattice in both x and y directions; mimicking a glide-symmetric displacement.

For all three cases, the structures have been characterized both numerically and experimentally, obtaining good agreement between both methods.

6.2 Background

Slow light (SL) refers to the possibility of controlling the group velocity of an electromagnetic signal. This control can be achieved by modifying the dispersion characteristics of the medium in which the signal propagates or by engineering a guiding structure. In 1998, Hau led a team that succeeded in slowing a beam of light to about $17\,\mathrm{ms}^{-1}$ in an ultracold atomic gas though electromagnetically induced quantum transparency [126]. Hau and her colleagues later succeeded in stopping light completely, and developed methods by which it can be stopped and later restarted [127]. However, the cryogenic temperatures required to achieve such conditions prevent its direct application in most technological areas. Nevertheless, this study inspired later works where slow light is achieved at room temperature. Some of these systems are: semiconductor waveguides with an applied bias voltage [128], waveguides composed of different insulator-metal combinations [129, 130] or waveguides with a negative–index core clad in dielectric (insulator-negative–index-insulator) [131, 132], optical fibers [133, 134] and coupled cavities [135, 136].

6.2.1 Physical principles of slow light

For a wave-packet travelling in a medium or waveguide, the defining characteristic of slow light is a reduced group velocity in comparison to the speed of light in vacuum. The group velocity is defined as the gradient of the dispersion curve, as shown in equation 6.1;

$$v_{\mathrm{g}} = \frac{dk}{d\omega} = \frac{c_0}{n + \frac{dn}{d\omega}} = \frac{c_0}{n_{\mathrm{g}}} \tag{6.1}$$

where $k(\omega)$ is the wave number, c_0 is the speed of light in vacuum, $n(\omega)$ is the effective refractive index and n_g is the group index.

When the dispersion is normal $dn/d\omega > 0$ then $v_{\mathrm{g}} < c_0/n$ and slow light is achieved. Equally, if the mode index does not vary with frequency ($dn/d\omega \approx 0$) then v_{g}=v_{p}. In this case the propagation of the wave is slowed down with respect to a free-space propagating photon but the propagation characteristics are the same for a broad range of frequencies. This is important for device design.

In order to achieve slow light, the dispersion of the wave needs to be modified, in particular, ensuring it presents large group index (n_g), low distortion and low absorption (low loss).

To modify (n_g), two main approaches can be followed, depending on whether the changes are due to the material itself or to the structural dispersion.

To achieve changes in the material dispersion an artificial manipulation of the resonances in the medium is needed. This is often achieved by other optical effects [137, 138]. Some of these effects are electron-hole recombination in semiconductor optical amplifiers [139, 140] or, in Raman amplifiers, Raman scattering of incoming light with phonons in the lattice of the gain medium, which produces photons coherent with the incoming photons [141, 142]. However, in this thesis, we focus on the engineering of the dispersion by directly modifying the structural properties of the material [143]. In particular, this is realised by the design of different metamaterial structures, containing resonant metallic inclusions with the appropriate shape and periodicity in a dielectric matrix.

Practically, slowing light results in stronger light-matter interactions as the electromagnetic wave has a lower group velocity than that presented by the same mode if it was travelling in free space. The slow light phenomenon can also be discussed in terms of the density of states of a system. The dispersion of a surface wave is defined by the relationship between the propagating wave vector of the mode (k) as a function of frequency (ω). The group velocity can then be studied as a change in the density of states of the system [42], described as $dk/d\omega$.

At frequencies far below the resonance frequency of the surface mode, there is a low density of states as the dispersion of the surface wave resembles that of a free space propagating photon. As the frequency increases towards the resonant frequency, the density of states increases, as there are more k states available per frequency component. The higher k components (k_z, normal to the surface) decay more rapidly into the surrounding medium and there is therefore a higher concentration of energy at the interface of the supported mode, resulting in stronger light-matter interactions [144].

Control of these interactions is possible via the manipulation of the dispersion and band gap structure of a photonic crystal, metamaterial or metasurface. To do so, different arrangements and element designs are introduced.

Applications where a reduced group velocity are advantageous range from the fields of nonlinear optics such as Raman spectroscopy [145] and quantum optics to the fields of optical storage and switching in microwave photonics.

6.3 Metasurface Design

In this chapter, we propose a metasurface comprised of rectangular metallic patches printed over a dielectric slab and arranged in a square lattice. Our design has the peculiarity that the length of the patches is bigger than the periodicity of the structure and therefore they extend across more than one unit cell. To make this possible without intersections with other patches, they need to be rotated with respect to the primitive lattice vectors. Consequently, this angle of rotation determines the maximum permitted length of the patches. A schematic of the proposed structure is represented in Fig. 6.1. In the figure, three unit cells of the structure are outlined in red, green and blue respectively while the patches are represented as grey rectangles. The patches have a length L and a width R and are rotated by an angle ϕ with respect to the horizontal direction of the lattice. There is one rectangular patch per unit cell (marked in a different colour in the figure) and therefore the centres of the rectangles are separated a distance d in both the horizontal and the vertical directions, d being the periodicity of the structure.

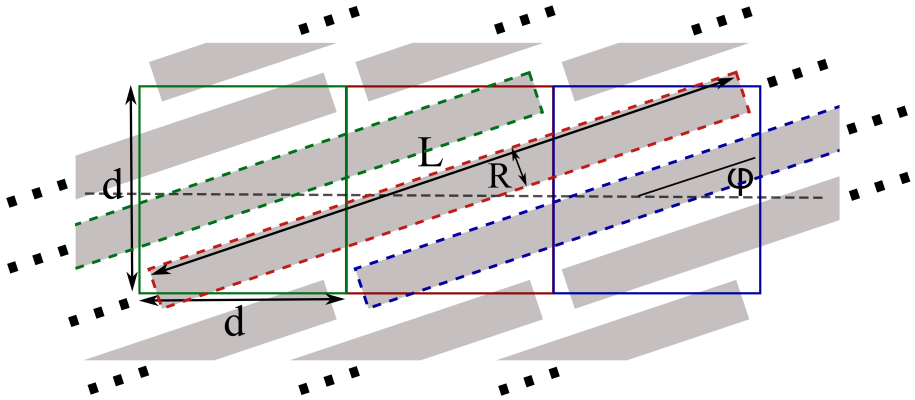

Fig. 6.1 Diagram of a single layer of long rotated rectangular patches in a square array. The rectangular patches have a length L and a width R and are rotated by an angle ϕ with respect to the direction of the horizontal lattice vector. The length of the patches (L) is bigger than the periodicity of the unit cells (d). In this particular case, the wires are three times as long as the unit cell and the angle of rotation is therefore $\phi = \tan^{-1}(\frac{1}{3}) \approx 18.4°$.

The resulting structure has elements that are long compared to the periodicity of the lattice. This means that the resonance of the single elements appears at a lower frequency than that expected for elements the size of the lattice. This results in an increase in the mode

index of the structure, slowing down the propagation of waves bound to its surface [12]. In addition, the Brillouin zone boundary is at high k, and as a result the mode presents high linearity, due to any effects caused by the band gaps introduced by the periodicity of the structure occurring at much higher in-plane wave vector than the one corresponding to half wave resonances of the long strips.

However, a single layer of rectangular patches is a very anisotropic structure, as the waves have a clear preferred direction of propagation. Although this can be a desirable feature for some applications, it is also worth studying different ways of reducing such anisotropy whilst keeping the main point of interest of the structure which is the high mode index presented.

6.4 Mono-Layer

The first structure under study in this chapter is a mono-layer presenting the geometry described in the previous section. The rectangular patches were chosen to be three times as long as the unit cell, resulting in a required angle of rotation of $\phi = \tan^{-1}(\frac{1}{3}) \approx 18.4°$. The periodicity of the structure is d = 2.5 mm, resulting in patches which are L = 7.5 mm long while the width of the patches is R = 0.5 mm. The width of the patches (R) does not have an important effect in the dispersion characteristics of the modes supported by the structure, as found with FEM simulations. As a consequence, its value was chosen to ensure the fabrication tolerances were fulfilled.

The structure was fabricated using the print-and-etch method described in section 3.2, meaning that the copper patches are 18 µm thick and printed over a PET sheet with a thickness of 25 µm and a permittivity $\varepsilon = 2.8$.

After fabricating the structure, it was characterized experimentally, following the procedure explained in chapter 3 and the obtained data compared with the dispersion diagram obtained with a FEM software.

To measure the isofrequency contours and the dispersion diagram of the structure, the setup described in section 3.3 was used. An area of 200 mm by 200 mm was scanned, centred on the position of the excitation source. After performing the scan, a spatial Fourier transform was applied to the instantaneous field, obtained from the measured amplitude and phase data. After this processing, the isofrequency contours are finally obtained.

The normalised Fourier amplitude, showing such isofrequency contours, for frequencies between 10 GHz and 35 GHz is shown in Fig. 6.3. In the figure, the first Brillouin zone boundary and the light circle are also represented in red (solid line for the BZ boundary and dashed line for the light circle).

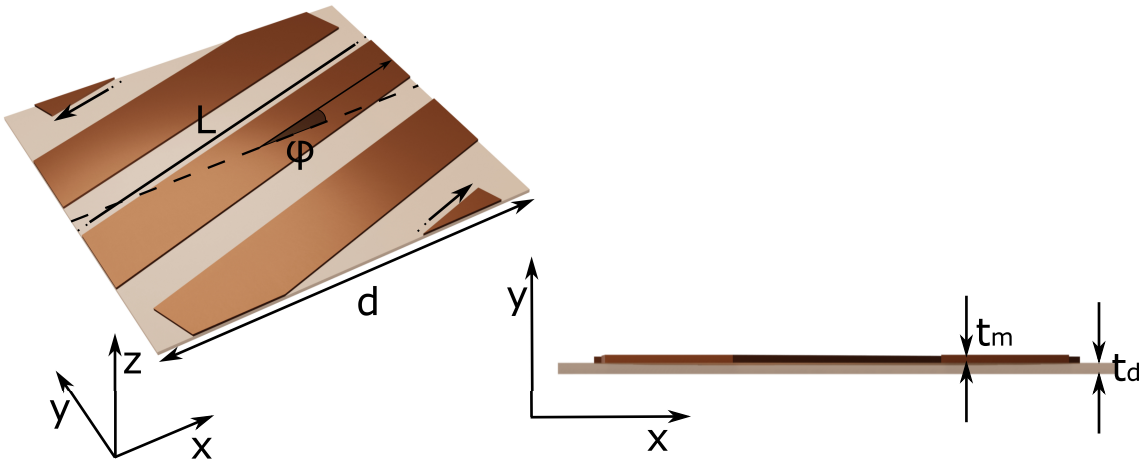

Fig. 6.2 Unit cell of the metasurface comprised of a single layer of copper rectangular patches in a square array. The copper patches ($L = 7.5\,\text{mm}$) are three times longer than the unit cell ($d = 2.5\,\text{mm}$). For this, an angle of rotation of $\phi = \tan^{-1}(\frac{1}{3}) \approx 18.4^\circ$ is required. The thickness of the copper patches is $t_\text{m} = 18\,\mu\text{m}$ and they are printed over a dielectric slab of thickness $t_\text{d} = 25\,\mu\text{m}$ and permittivity $\varepsilon = 2.8$. On the right hand side, a side view of the structure is included.

As predicted, the isofrequency contours show great anisotropy, where the direction of the distortion is related to the angle of rotation of the patches. From the isofrequency contours, it can also be inferred that the structure presents strong beaming in the long direction of the patches. The isofrequency contours at 15 GHz and also at 30 GHz present very straight contours. As the Poynting vector is perpendicular to the isofrequency contours, this means that for a range of wave vectors the Poynting vector points in the same direction and therefore the power transmitted by the surface is channeled in that direction. This direction corresponds to the long direction of the patches (a 18.4° rotation with respect to the horizontal direction).

The instantaneous field plots showing the previously mentioned beaming effect are presented in Fig. 6.4. Both the isofrequency contours and the instantaneous field maps are represented at the two frequencies at which the beaming is strongest (16 GHz and 33 GHz).

The first frequency corresponds to the first mode supported by the surface and the second one to the second order mode. Both isofrequency contours show two very straight sections which translate into energy being channeled in the perpendicular direction, as shown in the instantaneous field maps presented on the right hand side.

The self-collimation or beaming of the electromagnetic fields has been studied as a way of channeling and guiding energy across a structure. This phenomenon has been observed at different ranges of frequencies including optical frequencies [146, 147], terahertz [148] and microwaves [149–151].

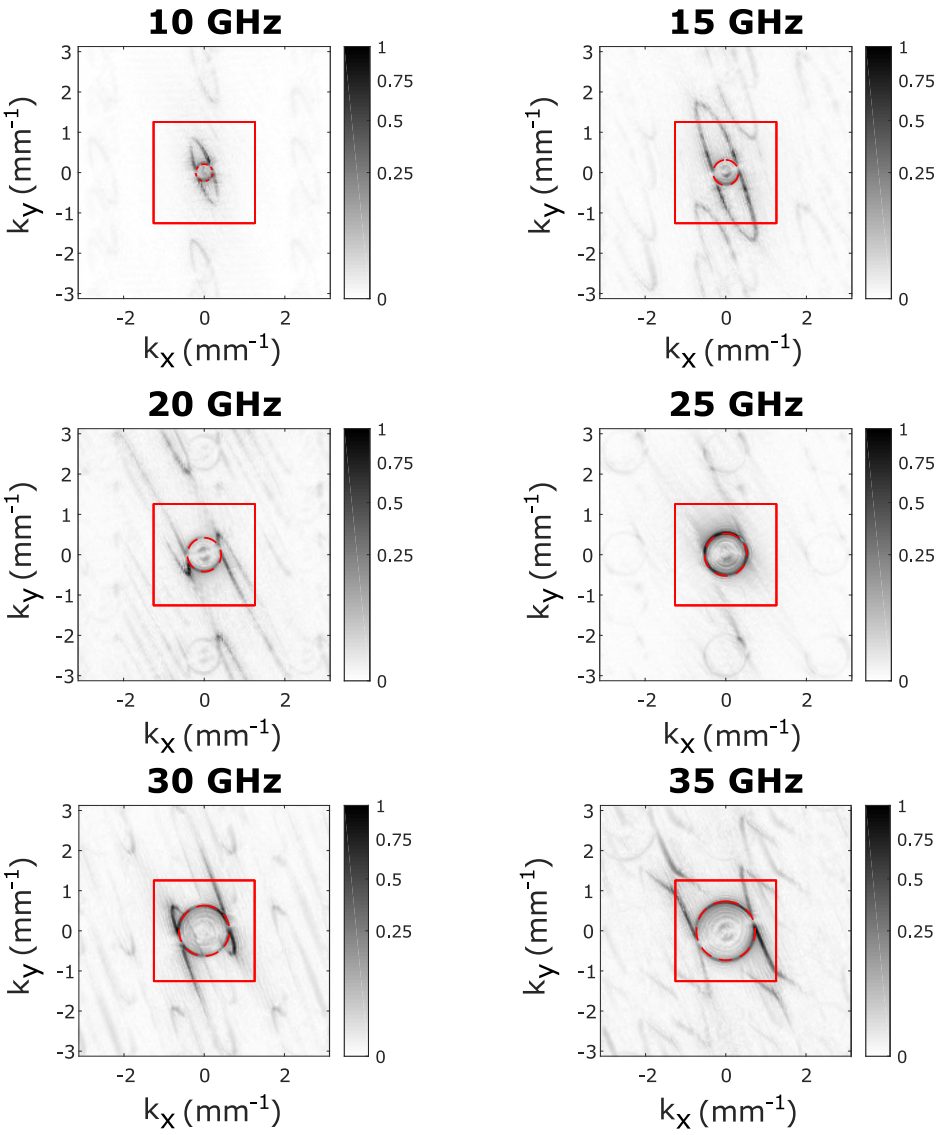

Fig. 6.3 Normalised Fourier amplitude, showing the isofrequency contours of the modes supported by a single layer of rotated long patches in a square array. The length of the patches is $L = 7.5\,\text{mm}$ while the periodicity of the structure is $d = 2.5\,\text{mm}$ and the angle of rotation of the wires is $\phi = 18.4°$. The first Brillouin zone boundary is represented in red, as is the light line, in this case represented with a dashed line.

Finally, from the Fourier-transformed data, the dispersion diagram of the modes supported by the mono-layer metasurface can be inferred (Fig. 6.5). The Fourier spectra obtained from the experimental data is shown as a grey-scale to which the modelled modes have been superposed, showing great agreement.

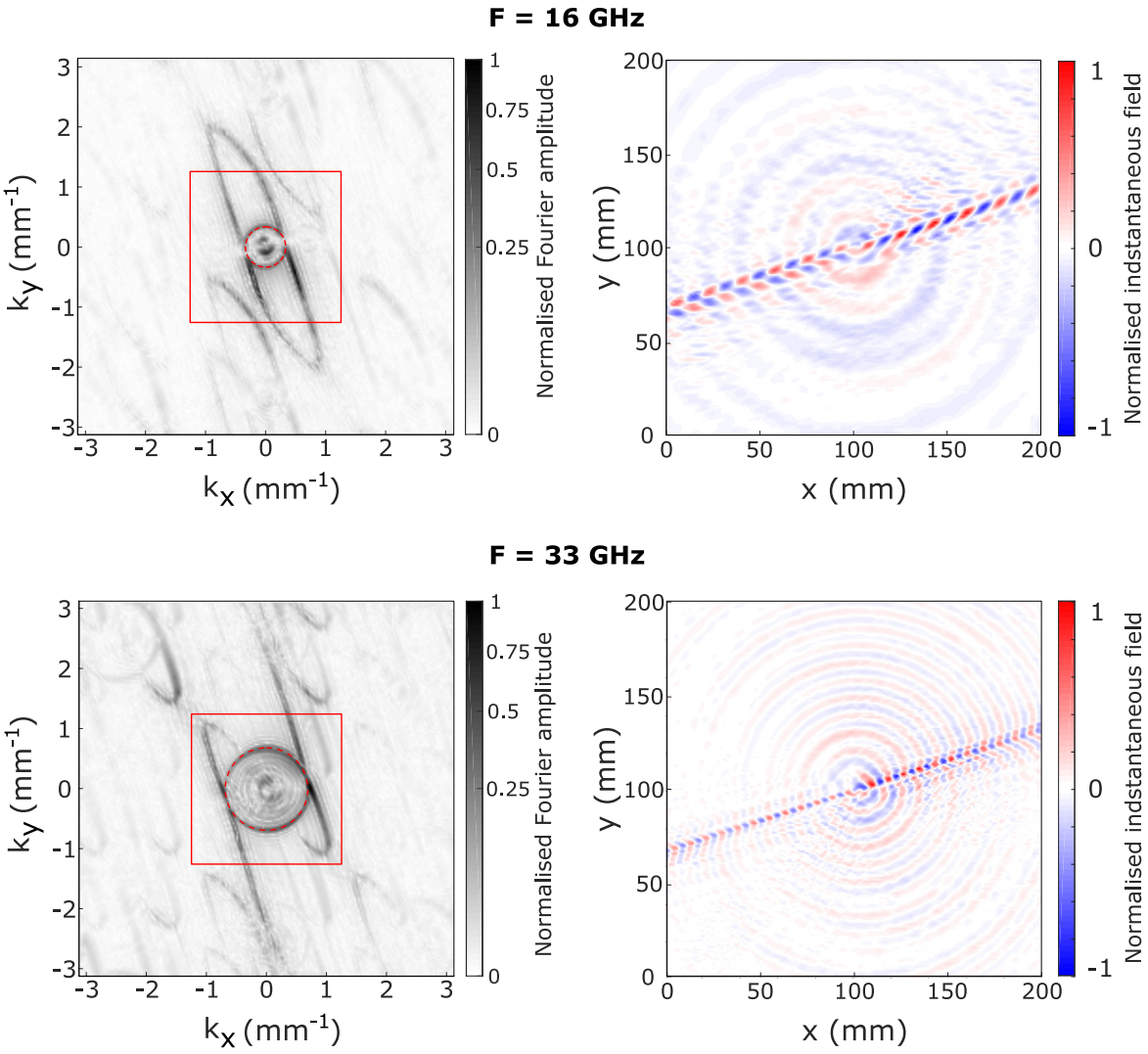

Fig. 6.4 Isofrequency contours (left) and field plots (right) at two different frequencies for a mono-layer of rotated rectangular patches. On the left hand side the isofrequency contours are presented, in both cases showing very straight lines. On the right hand side the normalised instantaneous field plots at those two frequencies are represented, showing very strong beaming.

In this case, unlike for the dispersion diagrams presented in chapters 4 and 5, although the motifs comprising the metasurface are displayed in a square array, the structure does not have four-fold symmetry. This is due to the geometry of the motifs, which are highly asymmetrical, possesing only 180° rotation symmetry. In this way, the overall structure only shows two-fold symmetry and as a consequence, and at least six directions are required to illustrate a complete dispersion diagram. As it is shown in Fig. 6.5, neither the two diagonal directions nor the horizontal-vertical directions are equivalent.

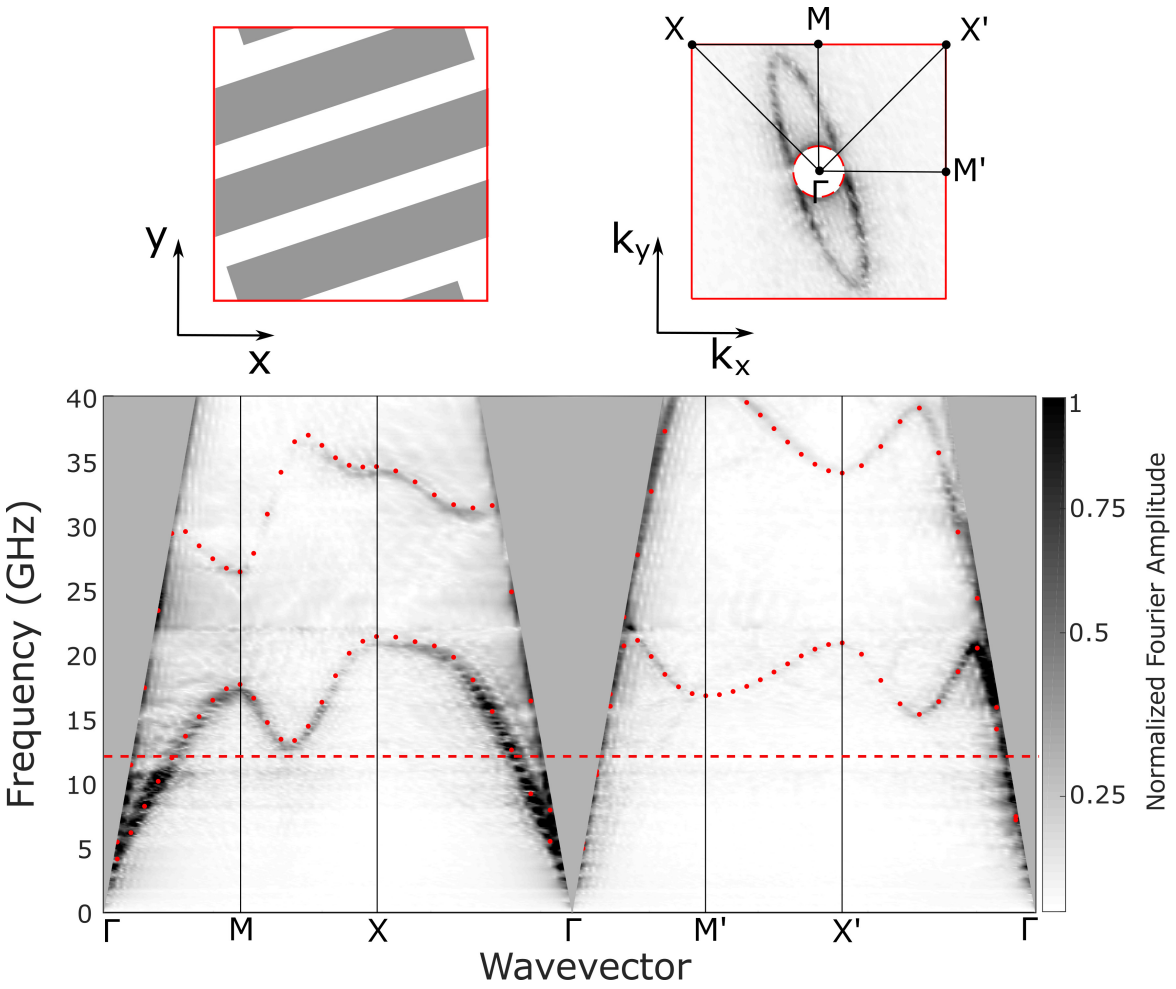

Fig. 6.5 Dispersion diagram of the modes supported by the single-layer array of rotated rectangular patches in a square lattice. Due to the anisotropy of the structure, the dispersion diagram needs to be plotted in two sets of directions. The experimental data is represented in a grey scale on to which the modes obtained with the FEM software have been superimposed (red dots). The area corresponding to the radiative modes (wave vectors smaller than those in the light line) is shaded in grey. On top of the dispersion diagram, a unit cell of the structure and the first Brillouin zone are also included. The different directions in which the dispersion diagram was plotted are marked in in the sketch of the first Brillouin zone. The isofrequency contour at 12 GHz is represented in the first Brillouin zone to clarify the orientation of the structure while a line marking the 12 GHz frequency is also marked in the dispersion diagram.

The dispersion diagram shows two very different behaviours for the different directions of propagation. The first part of the dispersion plot shows a propagating wave bound to the surface, even at low frequencies (Γ-M-X-Γ). This high mode index is caused by the high polarisability of the structure in the direction perpendicular to the patches. Meanwhile, the

second part of the dispersion diagram (Γ-M'-X'-Γ) shows a mode that follows the light line for small values of the wave vector, and for frequencies up to 20 GHz to then present apparent negative dispersion. However, by examining the isofrequency contours, it can be inferred that this apparent negative dispersion is due to an adjacent diffracted mode expanding and penetrating the first Brillouin zone. For negative dispersion to happen, there must exist a propagation of energy in two different directions of the metasurface [152] to allow for the phase velocity to be opposite to the energy flux. Such a situation is not present in this case as the energy is channelled in only one direction.

To sum up, a periodic metasurface exhibiting a high mode index due to its elements being longer than the period of the lattice has been presented. However, it shows high anisotropy as its elements are asymmetric and oriented in a predefined direction. In the next sections, ways of reducing such anisotropy and increasing the mode index even further are investigated.

6.5 Bi-Layer metasurface with a relative 90 degrees rotation

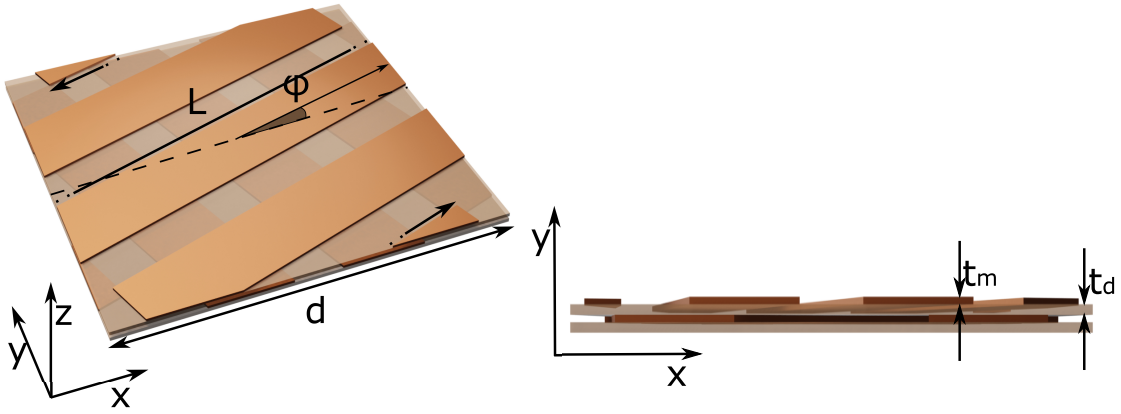

Fig. 6.6 Unit cell of the metasurface comprised of a bi-layer of copper rectangular patches in a square array. These two layers are rotated by 90° with respect to each other. The copper patches ($L = 7.5\,\text{mm}$) are three times longer than the unit cell ($d = 2.5\,\text{mm}$). For this, an angle of rotation of $\phi = \tan^{-1}(\frac{1}{3}) \approx 18.4°$ is required. The thickness of the copper patches is $t_\text{m} = 18\,\mu\text{m}$ and they are printed over a dielectric slab of thickness $t_\text{d} = 25\,\mu\text{m}$ and permittivity $\varepsilon = 2.8$. On the right hand side, a side view of the structure is also included.

The second structure proposed in this chapter combines two identical layers like the one described in the previous section. However, these two layers are rotated by 90° with respect to each other. A unit cell and a side view of this bi-layer structure is represented in Fig. 6.6.

The addition of a second layer creates a capacitive effect between the overlapping regions of the patches and increases the confinement of the electromagnetic fields to the dielectric spacing between the metallic elements. This contributes to a further increase in the mode index of the structure in a similar way as reported for the structures presented in chapters 4 and 5.

In this way, the reduced group velocity found in this structure is a combination of two effects. The long strips lead to a low resonance frequency if they were simply antennas. This will automatically produce a low limit frequency for the lowest mode. However, this does not lead to very slow waves. For this to happen the structure needs to act as a coupled surface waveguide. Beyond the light line, the modes are coupled surface modes. In general, there will be two such modes, a symmetric and an antisymmetric pair. One of these (symmetric in tangential E) will have fields which decay very slowly away from the surface and will sit almost on the light line. This is the long-range mode which is of little interest. The other one has fast decaying fields away from the surface and is the short-range mode, which has the very low velocity. This arises from the large imaginary k_z which in turn leads to very low frequency through $k_0^2 = k_x^2 + k_z^2$. In general, the thinner the structure the larger the imaginary part of k_z and the slower the wave.

The fact that the second layer is rotated by 90° with respect to the first reduces the anisotropy compared to the mono-layer, especially at low frequencies. The bi-layer structure has now near four-fold rotation symmetry (the two layers are not exactly equivalent, because of the substrates there is no mirror symmetry in the perpendicular direction), which makes the horizontal direction almost equivalent to the vertical direction and the same happens to both diagonals. This is clearly shown in the isofrequency contours and dispersion diagram.

Following the same fabrication and measurement procedures as for the previous case, and again adding oil to hold the two layers together, the instantaneous field maps, isofrequency contours and dispersion diagram are obtained for this structure. In the same way, the modes have also been calculated using a FEM software. As in previous chapters, to provide an accurate representation of the experimental sample, an extra dielectric layer needs to be added to the model to account for the oil layer used to bind the two metasurfaces together.

In this case, the bi-layer metasurface supports four different modes. These are represented in the form of isofrequency contours (Fig. 6.7) and in a dispersion diagram (Fig. 6.9).

In Fig. 6.7, the first plot (5 GHz), shows a lowest order mode which presents a fairly isotropic dispersion with an almost circular isofrequency contour. This isotropic propagation is also shown in Fig. 6.8 (Top) at 4 GHz, where the instantaneous field plot, resembling the propagation of a isotropic wave, is represented.

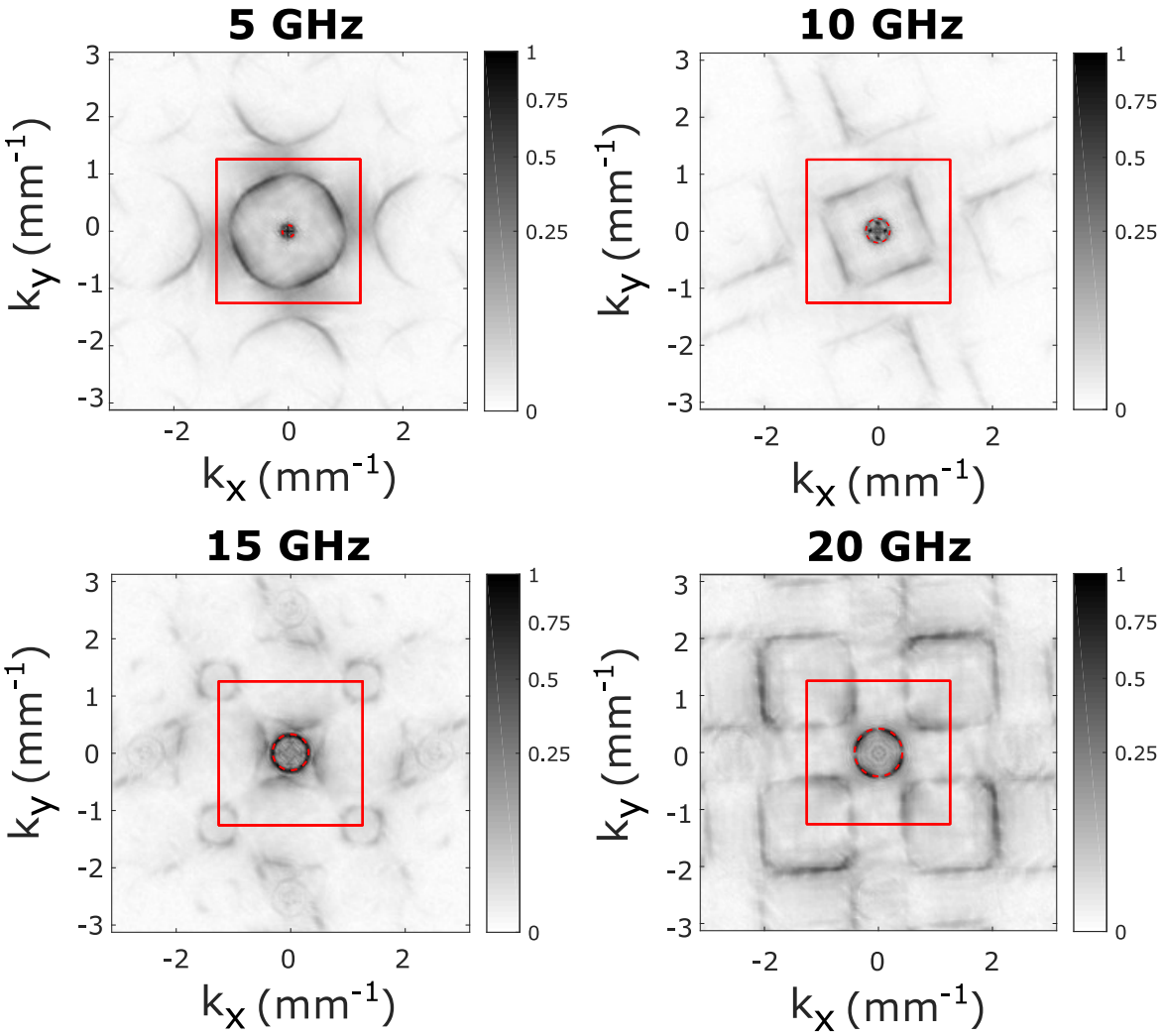

Fig. 6.7 Normalised Fourier amplitude, representing the isofrequency contours of the modes supported by a bi-layer of rotated rectangular patches in a square array when there is a relative rotation of 90° between the layers. The length of the patches is $L = 7.5\,\text{mm}$ while the periodicity of the structure is $d = 2.5\,\text{mm}$ and the patches are rotated $\phi = 18.4°$ with respect to the horizontal lattice vector. The first Brillouin zone boundary is represented in red as is the light circle, in this case represented by a dashed line.

However, the isotropy of the propagating modes supported by the structure is quickly lost as we move up in frequency. Just above 5 GHz, the lowest order mode reaches the Brillouin zone boundary in the [10] direction and a band gap appears, loosing its isotropic behaviour.

At higher frequencies, there are four preferred directions of propagation, which coincide with the directions of the rectangular patches. At 10 GHz, the isofrequency contours adopt a square-like shape, with four very straight sections. This means, that the energy propagates

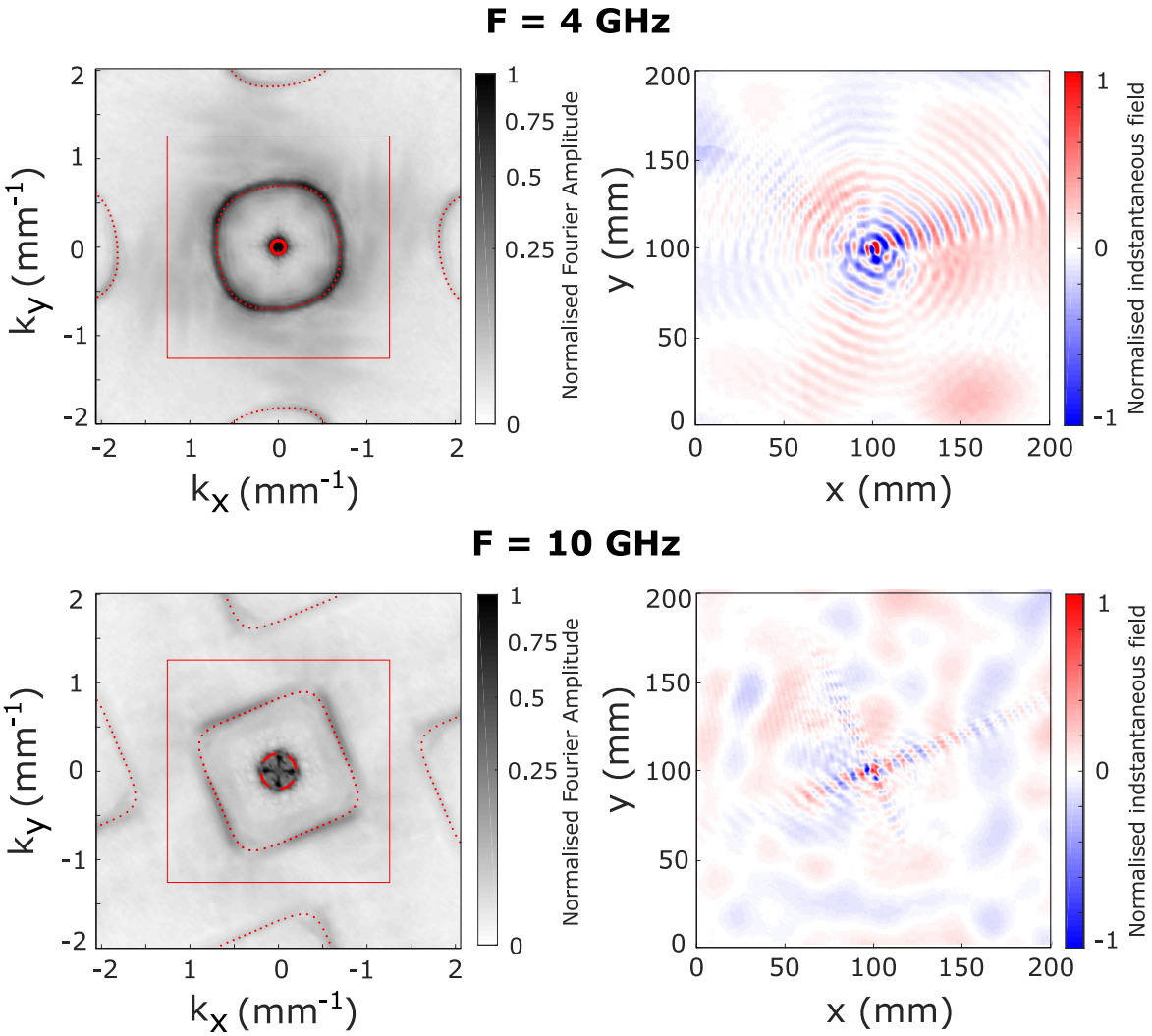

Fig. 6.8 Isofrequency contours of a bi-layer of rotated rectangular patches in a square array for two different frequencies corresponding to the first and second modes respectively. The first Brillouin zone boundary is represented in red and so is the light line, represented by a dashed line. Finally, the modelled isofrequency contours (obtained with FEM software) are also overlaid as red dots. On the right hand side, the normalised instantaneous field plots at the two mentioned frequencies are also included.

mainly in these four directions, perpendicular to the isofrequency contours. The instantaneous field plot showing this effect is also represented in Fig. 6.8 (bottom).

In Fig. 6.8, together with the normalised instantaneous field plots at 4 GHz and 10 GHz, corresponding to the first and second mode respectively, the isofrequency contours at these two frequencies are shown. In these two grey-scale plots, the isofrequency contours are compared with those calculated with a FEM software, showing very good agreement between the experiment and the simulation.

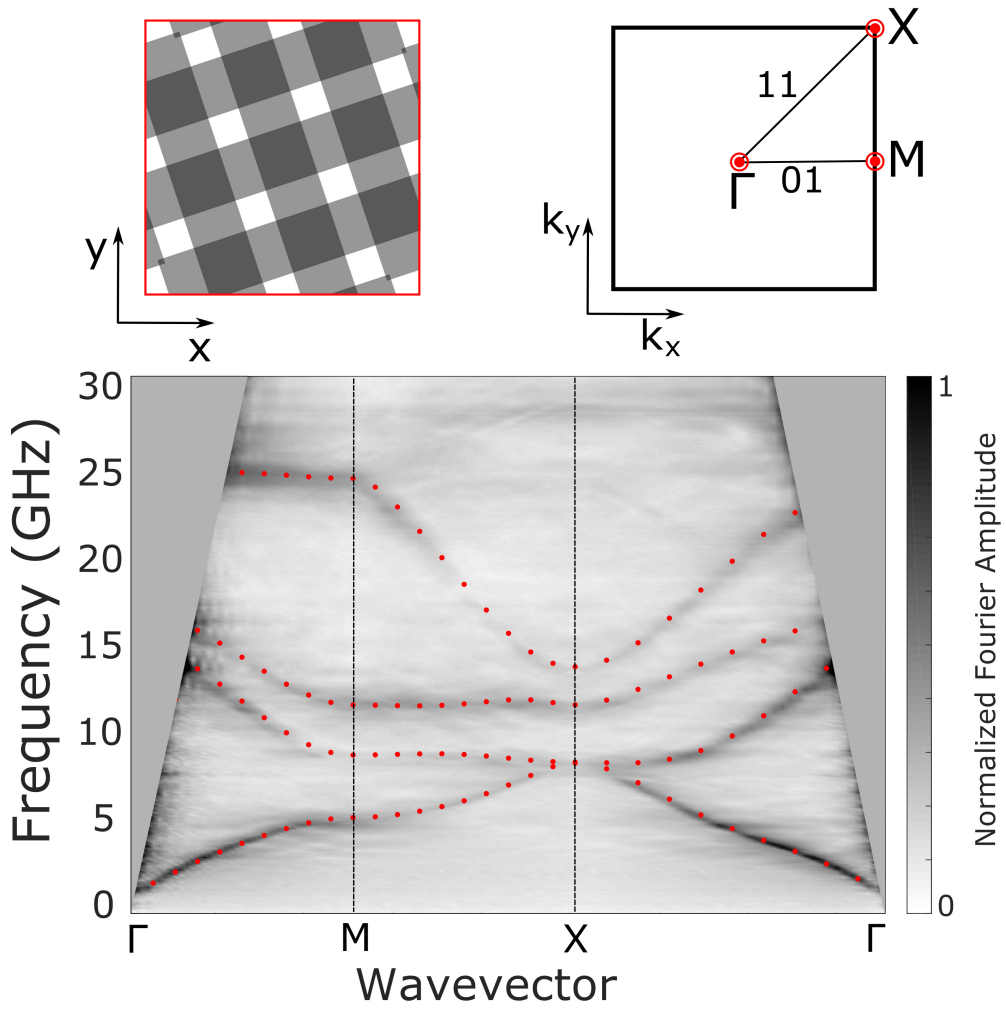

Fig. 6.9 Dispersion diagram of the modes propagating in a metasurface comprised of two layers of rotated rectangular patches in a square array with a relative rotation of 90°. The length of the patches is $L = 7.5\,\text{mm}$ while the periodicity of the structure is $d = 2.5\,\text{mm}$. The experimental data is represented in a grey scale to which the modes obtained with a FEM software have been superimposed (red dots). A unit cell of the structure and a schematic of the first Brillouin zone are also included (Top).

Finally, the dispersion diagram of the modes supported by the structure is represented in Fig. 6.9. In the figure, a unit cell of the structure and the first Brillouin zone with the directions of interest are also included. The experimental data (normalised Fourier amplitude), showing the dispersion of the modes is represented as a grey-scale to which the FEM data has been superimposed as red dots.

The lowest order mode, which appears at a very low frequency propagates with a high mode index. The presented mode index is even higher than that shown by the mono-layer for any of the directions of propagation. This high mode index is due to the combination of two

effects: the first one is the fact that the elements comprising the structure are longer than the unit cell of the structure and therefore, any effects due to the band gaps introduced by the periodicity occur at much higher in-plane wave vector than the one corresponding to half wave resonances of the patches. This, together with the addition of an extra layer, which creates a capacitive effect between the overlapping regions of the patches increases the mode index of the structure.

The second and third modes show negative dispersion since, according to the isofrequency contours, they do not originate from a lattice point (as a diffracted mode would do) and then move towards the light circle as frequency increases.

In this structure, due to the combination of two metasurface layers with orthogonal preferred directions, the power can be channeled in two orthogonal directions (each one on a different layer). This causes at some frequencies a net power flow in the opposite direction to the direction of propagation.

Although negative dispersion is an interesting phenomenon that has widely been studied [153–157] and has found applications in different areas of microwave engineering [158–160], it is not the main focus of this thesis, as we are interested in applications that require an isotropic behaviour. For this purpose, we only focus on the first order mode, which presents positive dispersion with a high mode index that is highly isotropic.

6.5.1 Mode index

The lowest energy mode supported by this structure is very strongly dressed by the surface geometry, reducing its phase (and group) velocity significantly compared to a grazing photon (light-line). As was mentioned before, this is a consequence of the patches being longer than the size of the unit cell, which is the main novelty of this structure.

The variation with frequency of the mode index (i.e., fractional decrease in phase velocity) for the lowest order mode supported by this bi-layer structure is shown in Fig. 6.10. In this figure the mode index calculated from FEM data (blue) is presented alongside the mode index calculated from the experimental data (red) for both the horizontal direction [10] and the diagonal direction [11]. The data from the dispersion diagram plotted in Fig. 6.9 was used to calculate the experimental mode index. For that matter, the values of frequency and wavevector (k) of the points with highest Fourier intensity of the mode were taken. However, the modes have a width and this gives rise to the error bars that are also included in the plot. In spite of this, the mode index calculated experimentally and with the FEM software show very good agreement.

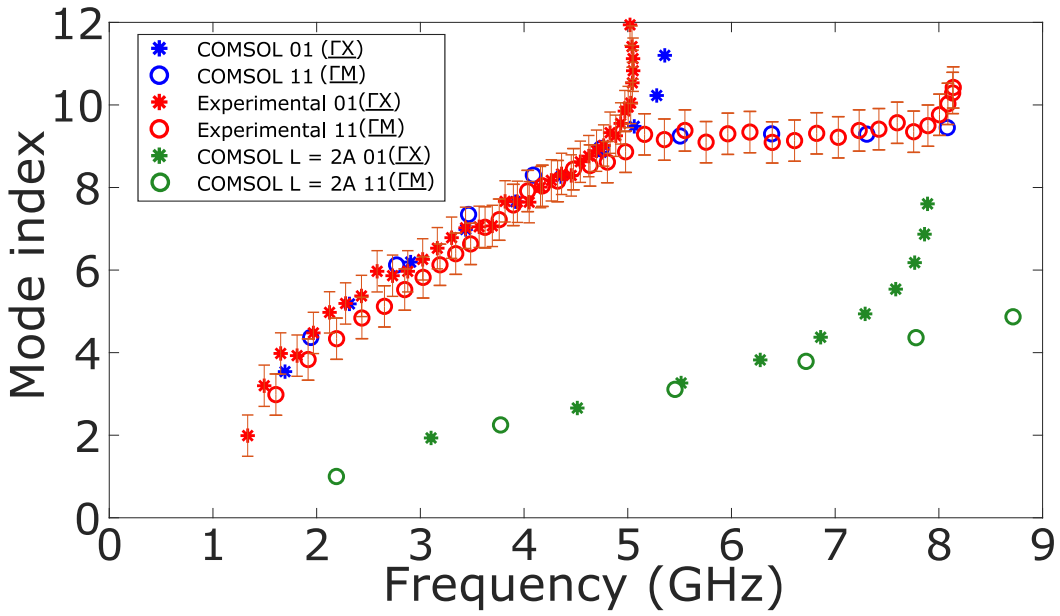

Fig. 6.10 Mode index presented by the lowest order mode supported by the bi-layer structure presented in Fig. 6.6. Both directions of high symmetry are represented; the horizontal direction [10] with stars, and the diagonal direction [11] with circles. The mode index obtained from the experimental dispersion is represented in red with its corresponding error bars while the mode index obtained by FEM modelling is represented in blue. A second set of data (green), representing the mode index for strips that are just twice the length of the unit cell is also shown for the same two directions. In this case the mode index has only been calculated from the simulation data.

For the chosen structural dimensions, the lowest energy mode propagates near-isotropically with a mode index of ≈ 8 at frequencies around 4 GHz. However, this mode index can be tailored by changing the length of the strips.

The patch length chosen for the experimental sample, corresponds to the highest mode index achievable. This is due to fabrication limitations and the resolution of the printer, which make impossible to increase the length of the patches any further. The lower limit of the mode index is that of the dielectric spacer, achieved by shortening the rectangular patches.

In Fig. 6.10, a second set of model data is also shown (green stars and circles). It corresponds to the mode index of a metasurface with the same structure but with shorter rectangular patches, which are in this case only twice the size of the unit cell (5 mm). The metasurface with shorter strips shows a lower mode index, of ≈ 2 at 4 GHz. In this way, varying the length of the rectangular patches, a high contrast graded index profile (of approximately 1:4) can be defined across the surface. This has a potential interest for transformation optics applications and for the design of planar microwave devices. In the

same way, a high mode index can also be useful to reduce the footprint of certain microwave devices.

As was previously mentioned, by reducing the size of the patches, the mode index is clearly reduced whilst the isotropy of the structure is maintained. This enables one to define a permittivity profile across a metasurface, as was done in chapters 4 and 5. However, there is an important difference that needs to be noted in this case. For this structure, as the patches extend to more than one unit cell, the mode index is not a localised property of each individual unit cell. However, as there is only one rectangular patch centered in each unit cell, it would be possible to take this location as the reference point to calculate the appropriate length of the patch, resulting eventually in a unit cell which contains patches of different lengths depending on the positions of their centres.

6.6 Bi-layer with a relative 90 degree rotation and a half pitch displacement

Finally, to conclude this chapter, a third structure was designed to investigate the effects of a glide-symmetric displacement between the layers comprising the metasurface shown in the previous section.

In this way, this third structure is also comprised of two layers of rotated rectangular patches, like the metasurface presented in section 6.5. But in addition to being rotated by 90° with respect to each other, the top layer is displaced by half of the period ($\frac{d}{2}$) in both x and y directions. A unit cell and a side view of the structure are represented in Fig. 6.11.

It needs to be noted that due to the relative 90 degree rotation between the layers, strictly speaking, the resulting metasurface does not have glide symmetry but a combination of glide and twist symmetry.

This bi-layer structure maintains its near four-fold rotation symmetry, as the applied transformation (displacement) is equivalent in both the horizontal direction and the vertical direction and the same happens to both diagonals. This four-fold symmetry is clearly shown later on in the isofrequency contours and dispersion diagram.

Following the fabrication procedure and the measurement techniques described in Chapter 3, the instantaneous field maps, and from them the isofrequency contours and dispersion diagram of the modes supported by the structure were obtained. In the same way, the modes have been calculated with a FEM software. Again, to resemble the experimental results, an extra dielectric layer needs to be added to the model to account for the oil layer used to bind the two metasurfaces together.

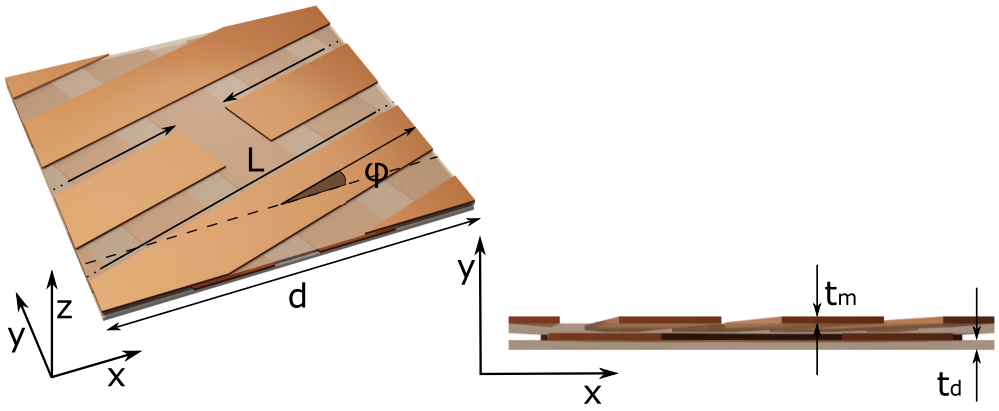

Fig. 6.11 Unit cell of a metasurface comprised of two layers of rotated copper rectangular patches in a square array. These two layers are rotated 90° with respect to each other and displaced by half of the period (d) in both x and y directions. As for the structure presented in Fig. 6.2, the copper patches ($L = 7.5\,\text{mm}$) are three times as long as the unit cell ($d = 2.5\,\text{mm}$). To allow this, the patches are rotated by and angle $\phi = \tan^{-1}(\frac{1}{3}) \approx 18.4°$ with respect to the horizontal direction (x) . The thickness of the copper patches is $t_\text{m} = 18\,\mu\text{m}$ and they are printed over a dielectric slab of thickness $t_\text{d} = 25\,\mu\text{m}$ and permittivity $\varepsilon = 2.8$. On the right hand side, a side view of the structure is also included.

As for the previous case, the displaced bi-layer metasurface also supports four different modes. The corresponding isofrequency contours are represented in (Fig. 6.12) and the dispersion diagram in (Fig. 6.13). In both cases, the experimental data is represented as a grey-scale while the FEM simulation data has been superposed in red. Again a good agreement between the simulation and the experiments was obtained.

The isofrequency contours show a reasonably isotropic lowest order mode, and the dispersion diagram shows that it presents a fairly linear dispersion with a high mode index. Both the isofrequency contour and the dispersion of the lowest order mode are very similar to that of the corresponding mode supported by the bi-layer structure without glide symmetry.

However, the square-shaped isofrequency contours presented by the second mode in the case of no displacement is lost here, as the two lower order modes cross at $\approx 7\,\text{GHz}$, as shown in the dispersion diagram (Fig. 6.13).

As the lowest order mode is very similar for the two bi-layer structures, in terms of the mode index and its dependence with frequency, the glide-symmetric displacement does not offer an improvement, either in terms of linearity (reduced frequency dependence) or in terms of magnitude. The mode index calculated for both structures is shown in Fig. 6.14. The difference in mode index in both the horizontal and diagonal directions is negligible. However, it needs to be pointed out, that the mode index has only been calculated for

frequencies under 6.5 GHz, this is, for frequencies below the crossing between the two lower order modes for the 'glide'-symmetric case.

With this, we can conclude, that in this particular case, a glide-symmetric displacement does not give an improvement in the linearity of the mode and therefore this last proposed structure was not pursued any further. However, this lack of improvement when glide symmetry is introduced is not unexpected. It needs to be kept in mind that the original

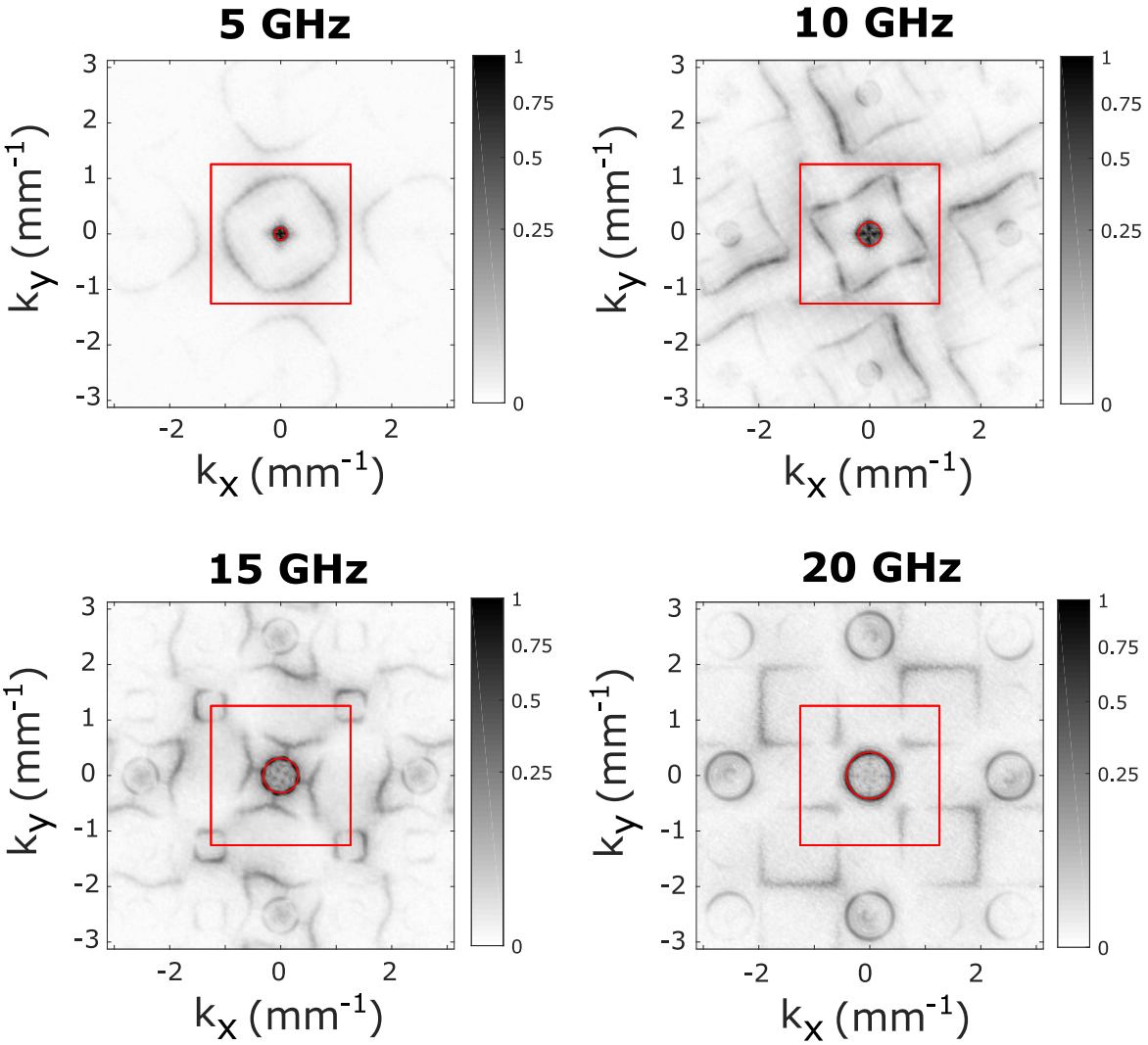

Fig. 6.12 Normalised Fourier amplitude, showing the isofrequency contours of the modes supported by a bi-layer of rotated long patches in a square array when the layers are rotated 90° with respect to each other and displaced by half of the length of the unit cell in x and y. The length of the patches is $L = 7.5$ mm while the periodicity of the structure is $d = 7.5$ mm and the angle of rotation of the wires is $\phi = 18.4°$. The first Brillouin zone boundary is represented in red as is the light circle, represented by a dashed line.

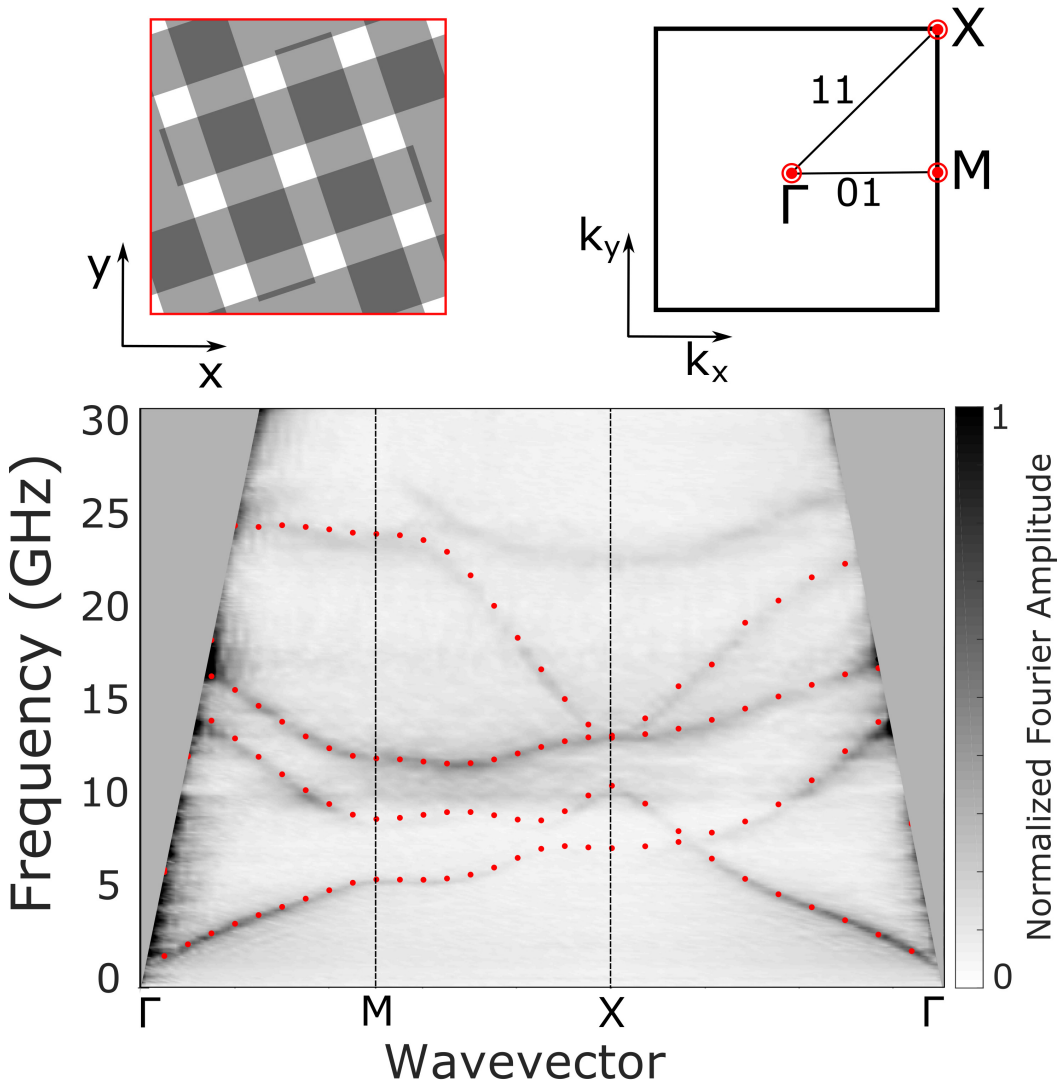

Fig. 6.13 Dispersion diagram obtained for the modes supported by a metasurface comprised of two layers of rotated rectangular patches in a square array. These two layers are rotated by 90° with respect to each other and displaced by half of the period in both x and y directions. The length of the patches is $L = 7.5\,\text{mm}$ while the periodicity of the structure is $d = 2.5\,\text{mm}$. The experimental data is represented in a grey scale to which the modes obtained with a FEM software have been superposed (red dots). In addition to the dispersion diagram, a unit cell of the structure and a schematic of the first Brillouin zone with the directions of interest are also represented (Top).

structure had already two layers and that there was a high symmetry operation between them (rotation symmetry in this case).

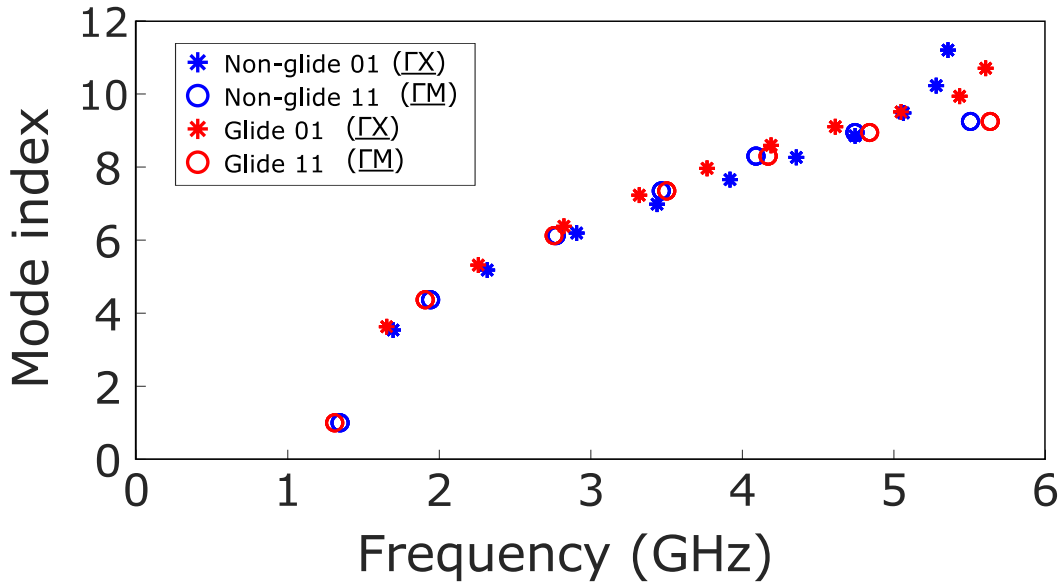

Fig. 6.14 Mode index presented by the structure introduced in section 6.5 (blue) compared to the mode index shown by the same structure but with a glide-symmetric displacement (red). In both cases, the mode index is represented with stars for the horizontal (10) direction and with circles for the diagonal (11) direction.

6.7 Losses

Losses are an important point to consider when designing microwave devices and more generally anything that requires the propagation of an electromagnetic wave. The modes supported by the guiding structure need to be strong enough throughout the entire device to ensure an acceptable performance. This is specially difficult to achieve when the medium supporting the propagation of the fields has a high mode index.

The losses of the second structure presented in this chapter (bi-layer with a 90° rotation) have been quantified for the range of frequencies where the structure supports a near-isotropic propagating mode (between 2 GHz and 5 GHz).

These losses have been quantified in two ways: by an experimental method and a FEM simulation.

To quantify the losses experimentally, the time averaged field magnitude was fitted using a function that includes a term compensating for the radial dependence, assuming the wave propagates isotropically in all directions, and an exponential decay. From the exponential decay, the propagation length can be obtained.

The losses have also been modelled using FEM software, taking into account the conductivity of copper ($\sigma = 5.998 \cdot 10^7$) and the tangent loss of the PET dielectric used as a

substrate ($\tan\delta = 0.0044$). The FEM software is then able to calculate the imaginary part of the supported mode and from it the propagation constant is obtained.

The propagation constant calculated in both ways together with the mode index of the structure are represented in Fig. 6.15. In the figure the mode index obtained experimentally, including error bars is represented in red. As for the decay constant, the values calculated experimentally are represented in blue while the FEM ones are shown in green.

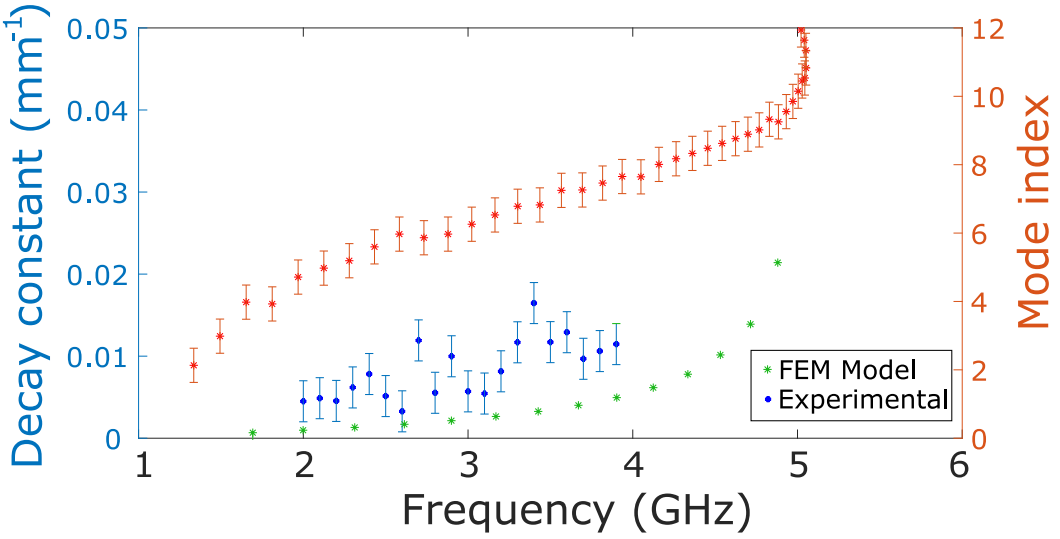

Fig. 6.15 Mode index and decay constant of the lowest order mode supported by a bi-layer metasurface comprised of two square arrays of long rectangular patches with a 90° relative rotation. The decay constant has been obtained in two different ways: The decay constant calculated from the experimental data is represented in blue while the values obtained with a FEM software are represented in green. In both cases, the corresponding error bars are also included.

In both cases, the propagation constant was found to be of the order of $0.01\,\mathrm{mm}^{-1}$, meaning that the fields can propagate between 100 mm and 200 mm before decaying by a factor of e. This is enough for optimal performance of most planar microwave devices. The two methods used to calculate the losses provide only an estimation of the propagation length. However, they give a good estimation of its order of magnitude.

6.8 Conclusion

In this chapter, a novel metasurface design consisting of an array of elements with a length up to three times bigger than the size of the unit cell was presented. The main consequence of this design is an increase in the mode index presented by the structure. This is due to any effects caused by the band gaps introduced by the periodicity of the structure occurring at

much higher in-plane wave vector than the one corresponding to half wave resonances of the long strips.

Also, this ensures that the frequency of operation is far away from the resonant frequency of the constituent metallic elements, hence minimizing the the propagation losses.

Three different metasurface designs featuring the same array of long patches were studied: a mono-layer and two bi-layer structures. The mono-layer shows a very anisotropic behaviour due to the intrinsic anisotropy of the elements comprising the array. This anisotropy, however was corrected by adding a second layer with a 90° rotation with respect to the first one. This also increases the mode index even further as capacitive effects between the overlapping regions of the patches are introduced.

Consequently, due to its high mode index, low loss and isotropy, this metasurface is a good candidate for transformation optics applications and the design of graded index devices.

Finally, the third design, where a displacement of half the periodicity of the structure was introduced in both x and y directions, does not show any major improvements with respect the previous one. As a consequence a further study of its properties was not pursued.

The majority of the results presented in this chapter were published in [11] in 2019.

Chapter 7

Microwave edge modes in a finite metasurface with hexagonal symmetry

7.1 Introduction

In this chapter we study finite planar metasurfaces comprised of two layers of circular metal patches in a hexagonal array. However, to help our understanding, it is first useful to consider the infinite two-dimensionally periodic array. This is characterized in section 7.3, before proceeding to study finite strips of the same metasurface in section 7.4.

In our study, each metasurface is considered infinitely periodic in one direction (y) but only a few periods wide in the orthogonal direction (x). These finite two-layer metasurfaces support an array of bound surface waves that propagate along the long direction of the surface.

Through experiments and modelling we find evidence of a localized edge mode whose characteristics are dependent on the relative alignment of the two layers. In section 7.5, this edge mode is used to guide the propagation of electromagnetic energy around both triangular and hexagonal shapes.

Finally, in section 7.6, the coupling of two of these edge modes is studied. The coupling of edge modes is a well-know phenomenon at optical frequencies, but in this chapter, we demonstrate that it can also be extended to microwave systems. The coupling of the edge modes is studied for two relative configuration of the strips. In the first one, the strips are arranged so that they have mirror symmetry, producing a splitting in frequency of the edge modes as they interact with each other. In the second configuration, the effects of glide symmetry are investigated, resulting in a straightening of the lower order coupled edge mode and a degeneracy at the Brillouin zone boundary (absence of a band-gap).

7.2 Background

Modes that propagate at the interface between two different planar media (surfaces), also known as edge modes, are the subject of interest in many areas of physics due to its broad prospective practical applications.

Edge modes can also be found propagating along the line termination of a structure. They are characterised by a field profile which is highly localised to the interface between the two different surfaces or at the termination of a surface, be these regular or artificial (metamaterials), and decay quickly away from the interface.

Probably, the most well- known structures that support the propagation of edge states are photonic crystals. A photonic crystal (PhC) waveguide is composed of a periodic array of dielectric layers, each with a different associated permittivity. The path of an electromagnetic (EM) mode through a photonic crystal depends on both the arrangement of the layers comprising the crystal and the refractive index experienced by the photon when propagating between the layers.

The spatial positions of the electrons associated with the constituent atoms or molecules in a crystal form periodic potentials with different allowed energy states. Therefore both the conduction properties and the lattice geometry of the crystal dictate the energy at which these states appear. Between the allowed energy states there are ranges of energy where the propagation of the electrons is not allowed, these are known as band gaps. The different bands may be engineered by changing the structure of the crystal, for instance by adding defects.

The path of an electron through such a crystal is dictated by its interactions with the mentioned periodic potentials. In the photonic crystal case, it is the refraction and reflection between the dielectric layers that define the allowed frequencies and directions of propagation of the modes through the system, creating band gaps. In a similar way, this can be replicated in other artificial structures by means of periodic arrangement of resonant elements. These structures are known as metamaterials and metasurfaces.

Since the 1990s, photonic crystals with photonic band gaps have been explored for various device applications [161–163]. Nowadays, the most widely used 2D photonic crystal (PhC) structures are comprised of a high-index thin film with a two-dimensional array of air holes surrounded by air cladding. Their proliferation was due to their intrinsic lossless optical confinement and simple fabrication process. A waveguide can then be created by adding a line defect of missing air holes in the PhC slab [164–166]. Light propagates through the line defect, confined by total internal reflection in the vertical direction and Bragg reflection, due to the photonic band gap, in the lateral direction [167–169].

This kind of structure, however, are not only relevant to the field of photonics. Guiding energy on surfaces, such as steering them around sharp bends and splitting and redirecting energy between channels is of relevance to antenna and communication engineers, and also has fundamental interest to the physics community [170–172].

For those applications, metasurfaces that support the propagation of edge modes have been studied in the past years [173–176].

7.3 Structure design: Infinite layer

The metasurface under study here is comprised of two layers of circular copper patches in a hexagonal array separated by a small dielectric spacing. Both layers are identical but have been displaced with respect to each other in the plane of the structure. In practice, the patches are supported by a dielectric slab that also acts as a spacing between the layers. This structure is similar to the metasurface studied in Chapter 5, with the difference that it only contains two layers of patches.

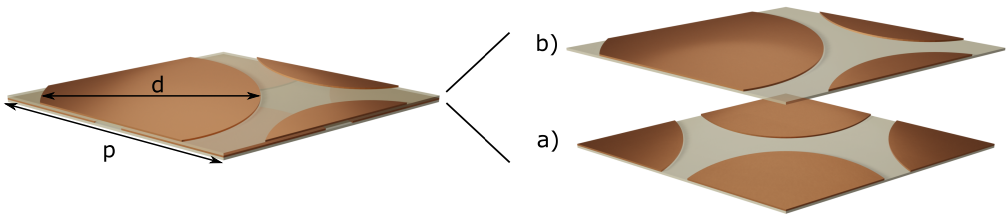

Fig. 7.1 Diagram of a double layer of circular patches in a hexagonal array. The circular patches have a diameter $d = 2.15\,\text{mm}$ and are printed over a dielectric slab of permittivity $\varepsilon = 2.8$ with a thickness of $t = 25\,\mu\text{m}$. The top layer has been displaced by $\frac{p}{\sqrt{3}}$ in the x-direction with respect to the bottom layer, where $p = 2.4\,\text{mm}$ is the lattice spacing of the structure. On the right hand side, the two layers comprising the structure are presented separately.

In Fig. 7.1 a unit cell of the infinite structure is presented. The top layer has been displaced by $\frac{p}{\sqrt{3}}$ in the x-direction with respect to the bottom layer, where $p = 2.4\,\text{mm}$ is the lattice spacing of the structure. The circular metallic patches are made of copper, have a diameter $d = 2.15\,\text{mm}$ and are printed over a dielectric slab of permittivity $\varepsilon = 2.8$ with a thickness $t = 25\,\mu\text{m}$. In the figure, together with the unit cell of the structure, the two layers are presented separately to give a clearer picture of the metasurface.

This metasurface is electrically disconnected, and therefore supports bound surface modes whose fields are predominantly transverse electric (TE) at low frequencies [40]. The lowest energy mode is a hybridization of a grazing plane wave with the resonance supported in the dielectric between the overlapping (upper and lower) regions of metal. In this space, the electric field, shown in Fig. 5.4, is orientated in the z-direction (out-of-plane) and mostly confined to the overlap regions between the layers of patches. Outside the bi-layer, the electric field is primarily in the plane of the surface, but transverse to the propagation direction. Meanwhile, the magnetic field has a component parallel to the direction of propagation and describes loops between adjacent patches.

As was mentioned in chapter 4, for multilayer structures, the subsequent strong confinement of energy associated with the electric fields in the high permittivity dielectric, mainly in the overlap regions, leads to an increase of the mode index (reduction of phase velocity) with respect to the single layer structure.

A prototype of this metasurface was fabricated using the manufacturing technique presented in section 3.2, by carefully stacking and aligning two layers of copper-printed PET. The structure was then characterised using the experimental set-up described in section 3.3. As the modes supported by the structure are TE-like, two loop antennas were used to excite and detect the modes propagating on the metasurface. One of these antennas was used as a magnetic field source and was located in the center of the sample while the other one was used as a probe to scan a 200 mm by 200 mm area on the opposite side of the sample. In this way, the amplitude and phase of the signal associated with the out-of-plane magnetic field on this area was obtained.

After Fourier-transforming the acquired instantaneous field data, the isofrequency contours (represented in Fig. 7.2) were obtained. At low frequencies, below 6 GHz, the mode is indistinguishable from the light line. From that frequency, the effects of the elements comprising the metasurface become evident and the isofrequency contours show the propagation of an almost-isotropic mode for frequencies between 6 GHz and 16 GHz, where it stops propagating and a bandgap begins. However, the isofrequency contours are distorted due to a slight misalignment of the layers, which irregularly deforms its circular shape. This distortion is made more evident as the frequency increases.

Finally, a dispersion diagram, showing this same propagating mode is plotted in Fig. 7.3. In the figure, the Fourier amplitude obtained from the experimental data is shown as a function of the angular frequency (ω) as a grey scale. Meanwhile, the eigenmodes obtained with a FEM software are overlaid as red dots. Good agreement is shown between the experiment and the simulation data.

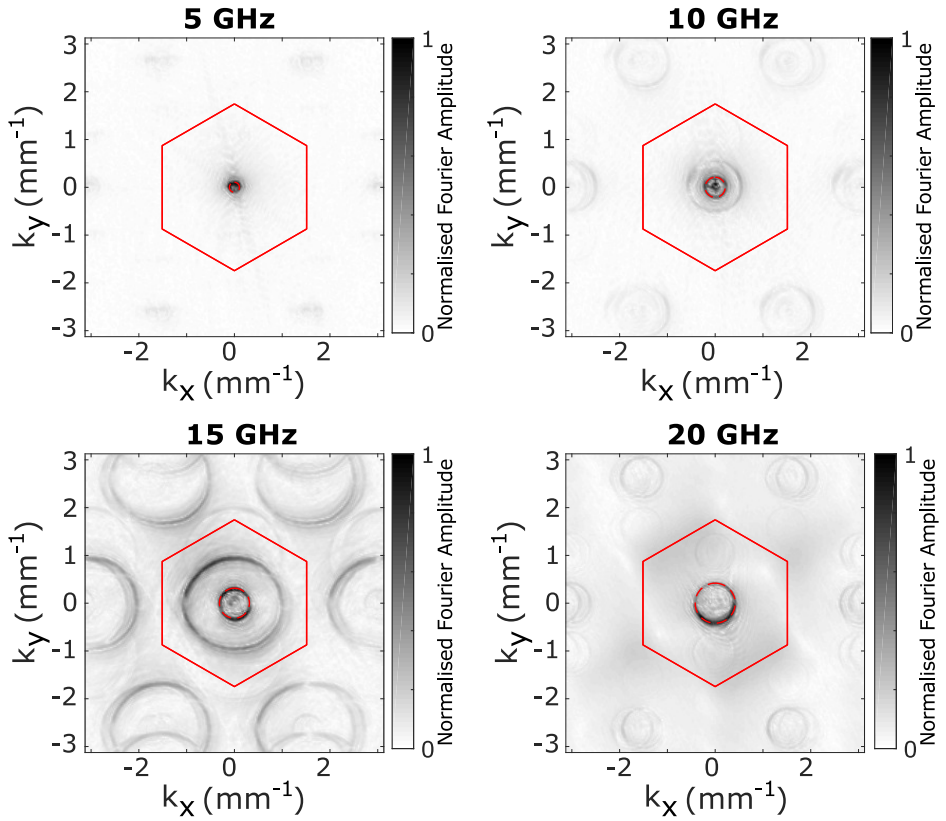

Fig. 7.2 Normalised Fourier amplitude, representing the experimental isofrequency contours of the modes supported by an infinitely periodic tessellation of the unit cell shown in Fig. 7.1. The patches have a diameter $d = 2.15\,\text{mm}$ and a periodicity of $p = 2.4\,\text{mm}$. The dielectric thickness is $t_d = 25\,\mu\text{m}$ and the copper thickness is $t_m = 18\,\mu\text{m}$. The grey-scale represents the normalised amplitude of the Fourier-transformed field-data and the light line and the contour of the first Brillouin zone have been included in red.

The dispersion diagram of this structure was previously modelled in chapter 5 where it was compared with a mono-layer and a three-layer structures featuring the same patch array. In the modelled dispersion diagram a second mode was found but this appears very high up in frequency (around 70 GHz for the chosen dimensions) and is not detected with the current experimental setup.

The lowest order mode, on the contrary appears at a very low frequency, and is bound to the surface even for small values of the wave-vector. This is due to the capacitive coupling between the overlapping regions of metal and the confinement of the fields to the dielectric spacer between the layers of patches.

Despite its high index, this structure was disregarded in chapter 5 as the three-layer structure showed a much more linear dispersion that made it more suitable for broadband graded

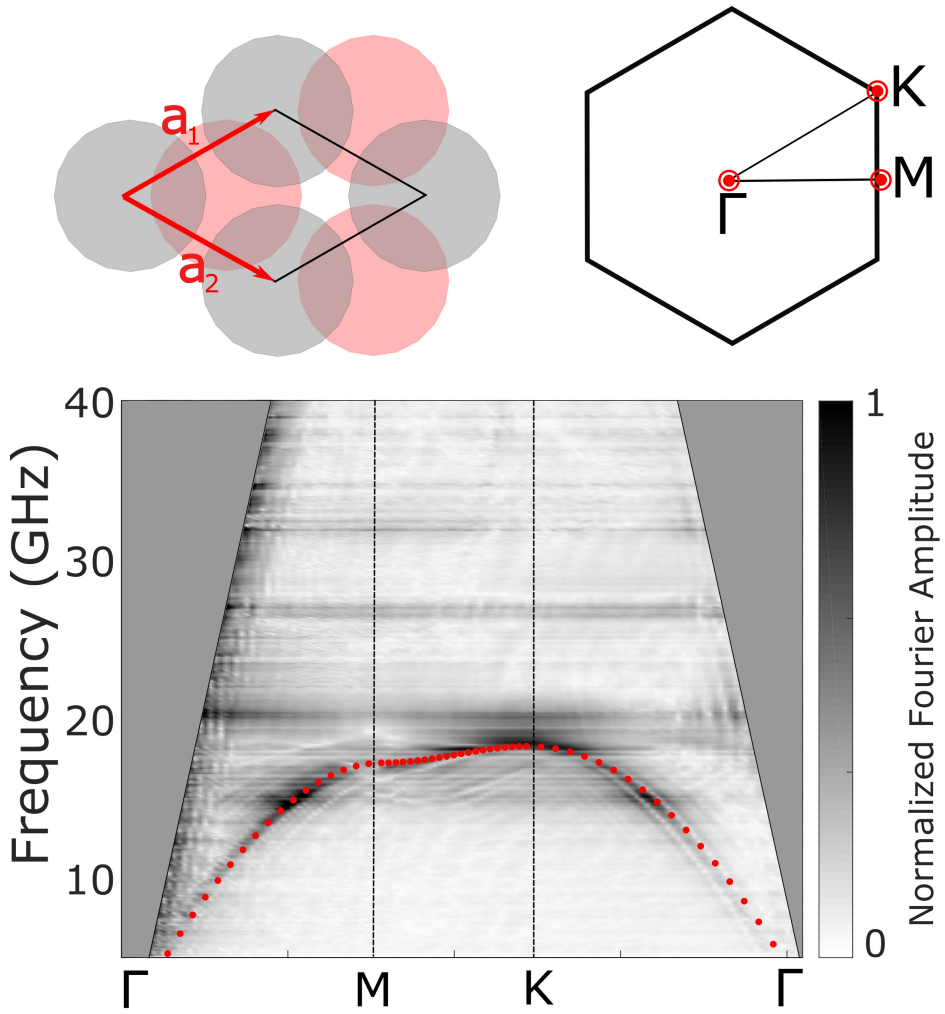

Fig. 7.3 Normalised Fourier amplitude, showing the dispersion diagram of the modes supported by an infinitely periodic tessellation of the unit cell shown in Fig. 7.1. The grey-scale represents the amplitude of the Fourier coefficients of the Fourier-transformed field-data. The red dots are the Eigenmodes predicted by the FEM modelling, using a patch diameter $d = 2.15\,\text{mm}$ and a periodicity of the structure $p = 2.4\,\text{mm}$. The dielectric thickness is $t_d = 25\,\mu\text{m}$ and the copper thickness is $t_m = 18\,\mu\text{m}$. The areas shaded in grey correspond to the radiative modes, which propagate in free space.

index devices. However, in this chapter we study the potential of this bi-layer metasurface to support the propagation of edge modes, when the infinite structure is terminated.

7.4 Edge modes supported by finite periodic strips

As was stated in the background section, the kind of edge modes that are studied in this chapter, are a consequence of the presence of electric charge on the edges (terminations) of the structure.

To study the effect of the termination of the effectively infinite structure, the infinite metasurface was cut into finite-width strips which are 250 mm long in the propagation direction (y), but only a few patches in the transverse direction (x). These strips were fabricated, their dispersion measured and the obtained data was finally compared with FEM simulations.

In the simulations, the finite-width strips are modelled as infinitely periodic in the propagation direction using Floquet boundary conditions and therefore present a rectangular unit cell.

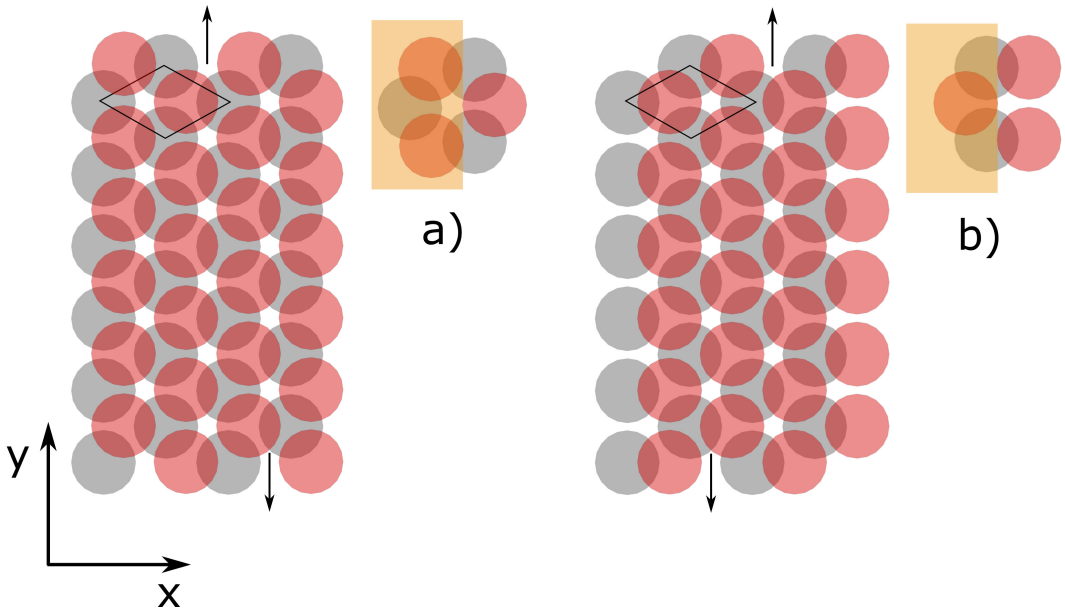

Fig. 7.4 Representation of the two possible arrangements of a 4-patch-wide strips of the 2-layer hexagonal structure. The top layer is represented in red and the bottom layer is represented in grey. A rhombic unit cell of the infinite structure is marked in black. The area highlighted in yellow corresponds to the 'bulk'of the structure. a) shows the structure terminated with two overlap region per edge patch while b) shows the structure terminated with only one overlap regions per edge patch. Both structures have a patch diameter of $d = 2.15\,\text{mm}$ and the periodicity of the structure is $p = 2.4\,\text{mm}$

Our chosen bi-layer metasurface has patches in an hexagonal lattice in each layer, and is 4 patches in width. A single hexagonal lattice geometry presents two sets of voids and therefore there are two available relative positions to place the second layer with respect

to the first one. This, ultimately results in two different possible edge terminations which support different modes. These two different edge-geometries, are shown in Fig. 7.4. In the figure, the top layer is represented in red while the bottom layer is represented in grey. Next to the schematics of the strips there is a close-up of the termination, where the 'bulk' of the structure is shaded in yellow.

Specifically, the first arrangement (a) has two overlap regions per edge patch, while the second one (b), has just one overlap region per edge patch. In both cases, the bulk metasurface remains unchanged. The different arrangements correspond to mode propagation directions 30° apart in the infinitely periodic lattice.

Firstly, the Eigenmodes of both structures were obtained using a FEM software. Their band structure (dispersion) and field distributions are plotted in Fig. 7.5. Since the bulk metasurface is identical for both structures, we associate any differences in the Eigenmodes supported with the edge-geometries.

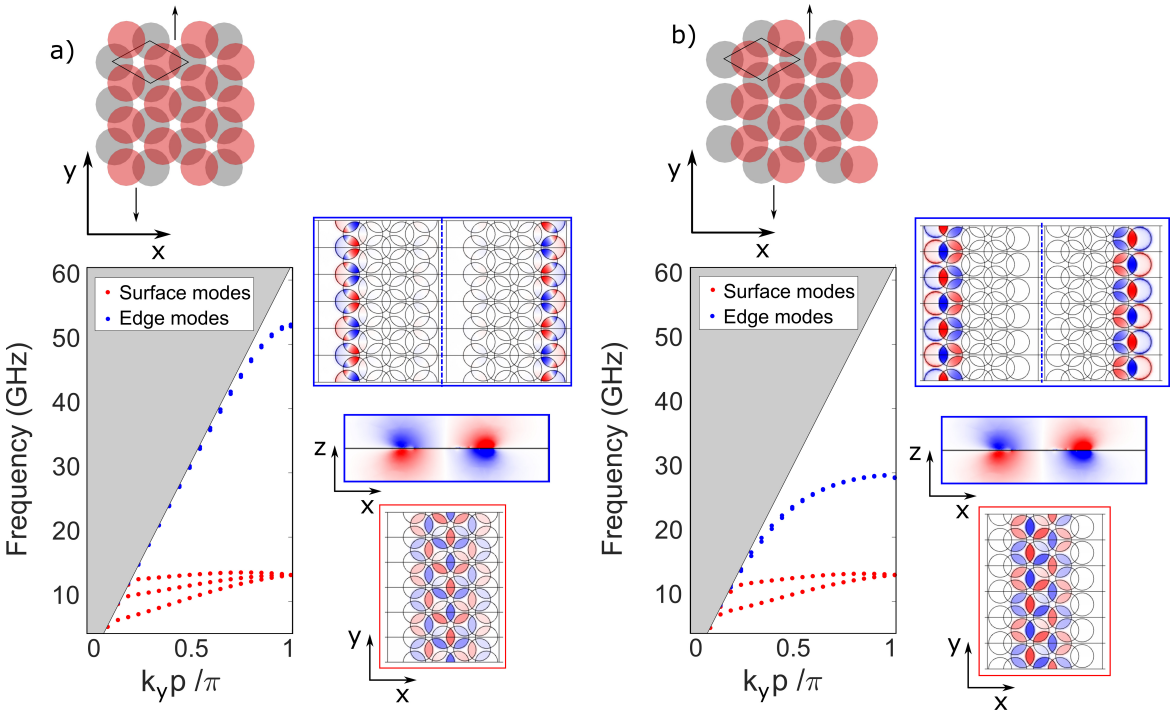

Fig. 7.5 Predictions of the dispersion diagrams of the modes propagating on two strips with different edge terminations and out-of-plane electric field (E_Z) between the layers of patches. They have both been obtained with a FEM software. The first set of plots (a) corresponds to an edge termination with two overlap regions per edge patch while the second one (b) corresponds to a termination with only one overlap region per edge patch. In the dispersion diagrams, the surface modes are represented with red dots and the edge modes with blue dots. The same color-code is used for the outline of the field plots. A side-view of the field for the edge modes is also included.

In the dispersion diagrams, we can identify two families of modes for each structure. The first family of modes, (represented in red in Fig. 7.5), which appears at a lower frequency, corresponds to bulk 'surface' modes according to the field plots. Meanwhile at higher frequencies there is a second set of modes (represented in blue in Fig. 7.5), which correspond to the fields propagating on the edge of the sample.

While for the structure with two overlap regions per edge patch, (a), there is a family of three modes (red dots) that become degenerate at the Brillouin Zone boundary, the geometry with just one overlap region per edge patch, (b), only supports two of these lower energy modes.

A family of 'bulk' modes is observed associated with the quantization in the transverse direction due to the finite size of the sample [177]. As for the number of bulk modes supported in each case; it depends on the number of bulk 'meta-atoms' present in the structure. This number of 'meta-atoms' does not necessarily correspond to the number of patches in each row since the behaviour of the structure is not determined by the resonances of the patches, but the overlaps between them.

Hence the surface's meta-atoms are formed by two patches, one in the top layer and one in the bottom layer and each of them must have three overlap regions. For the unit cell of the first structure (Fig. 7.4 (a)) there are three of these meta-atoms across the strip and hence three surface modes are found, whereas, for the structure in Fig. 7.4 (b) due to the presence of edge patches with a different environment, only two surface modes are found.

The higher energy modes, can be identified as edge modes according to the field plots as they are only allowed to propagate along the interface between the edge of the surface and the surrounding dielectric. In Fig 7.5, a side view of the electric field corresponding to the edge modes is also shown. These plots show a much less confined field, which extends for some wavelengths outside the dielectric spacing between the layers.

The existence of these edge modes is primarily a consequence of the presence of isolated electric charge along the edge of the patches. This presence of isolated electric charge needs to be compatible with an essential condition that needs to be fulfilled by every structure. This is the net neutrality of the whole entity. Because this particular structure is comprised of disconnected patches, every individual patch needs to remain neutral.

For the structure with just one overlap region per edge patch (b), it is very easy to see why some charge on the edge of the patches is required. Since every metal patch must carry zero net charge, the charges on the overlap regions of the lower patches (grey) need to be compensated by a net electric charge of the same magnitude but opposite sign along the edge of the same patch. As there are then charges on the edge of the structure, an edge mode can propagate.

For the structure in Fig. 3 (a), naively, the condition of neutrality is fulfilled with no need for the edges of the patches to be charged as the two different overlap regions in the patch can have opposite sign charges. This is the charge situation that characterises the 'bulk' surface modes, as shown in the field plots in Fig. 7.5. However, it might be the case that both the overlap regions in the same patch have charges of the same sign and therefore a charge of the opposite sign is required on the edge of the patches. This situation results in an edge mode that appears at a much higher frequency and therefore cannot be detected experimentally as being distinct from the light line (our setup measures frequencies up to 40 GHz).

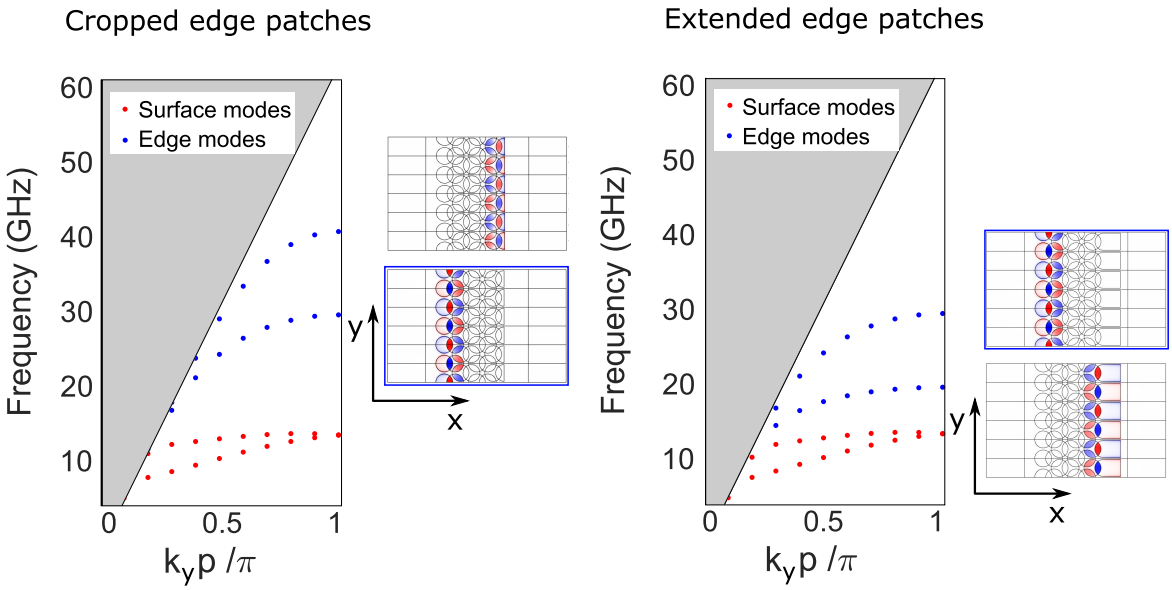

Fig. 7.6 Dispersion diagrams and out-of-plane electric field plots obtained with a FEM software for the modes supported by two strips with shortened (left) and elongated (right) edge terminations. The field profiles have been plotted for a plane between the layers of patches. In both cases, the edges have only one overlap region per edge patch and one of the edges has been kept the same as for the original sample while the bottom patch on the opposite edge has been modified. Again, the surface modes are represented with red dots while the edge modes are represented with blue dots.

Finally, to explain why the edge mode appears at a much higher frequency for the case where there are two overlap regions per edge patch (a), the dispersion diagrams of two more structures were obtained using a FEM software. These two structures are identical as the strip with only one overlap region per edge patch (labelled b) in Fig. 7.4) but the bottom patch on one of its edges has been modified. In the first case, the size of the edge patch was decreased while in the second case this path was elongated. The goal that these modifications have is to either reduce or increase the area where the free charge along the edge can be distributed.

When the patch is elongated, the charge can distribute over a greater area causing the edge mode to lower in frequency. This effect is represented in Fig. 7.6 (right), alongside with an out-of-plane field plot. If on the contrary, the free area of the patch is reduced, the frequency at which the edge mode appears increases (Fig. 7.6, left). This explains the difference between the two edge modes for the two different edge configurations described in this chapter. In the second one (one overlap region per edge patch) the charges are distributed over a greater distance and therefore the edge mode appears at a lower frequency.

7.4.1 Experimental dispersion

A sample containing two finite strips, each of them with one of the different edge termination studied in this chapter was fabricated and measured experimentally. Both strips were printed on the same sample (PET sheet) with enough space between them to ensure there was no interaction between the structures.

To obtain the experimental dispersion, two nominally identical loop-antennas were used, one of them as a source and the other one as a probe. They were each connected to a vector network analyser (VNA) via coaxial cables, and the frequency was swept between 5 GHz and 40 GHz. The source was placed at the mid-width of the strip while the probe was attached to an automated translation stage that scans along the long direction (y) of the strip on the opposite side of the sample. This configuration enables the recording of the amplitude and relative phase of the electromagnetic fields at every point in the frequency and spatial scan.

A 1D Fast Fourier transform was then performed for every measured frequency, resulting in a frequency-wavevector dependence of the Fourier amplitude that illustrates the dispersion of the modes. This dispersion relation is shown in Fig. 7.7. The experimental measurement is presented as a grey-scale plot and the FEM-modelled dispersion as dots. Again, for the simulation data, the surface modes are represented in red while the edge modes are represented in blue. The FEM software calculates the eigenmodes supported by an infinite strip, which resembles the experimental data when the length of the measured strip is several times the wavelength of the propagating mode, as applies in this case.

As shown in Fig. 7.7 there is a good agreement between the measured dispersion and the FEM data. However, to accurately replicate the experimental sample, an extra dielectric layer had to be added between the layers of patches to account for the oil used to bind both layers together. It needs to be pointed out that this oil layer, which increases the separation between the layers of patches, mainly affects the surface modes.

While the surface modes are strongly dependent on the thickness of the sample, moving up in frequency as the separation of the two layers is increased, the edge modes show only weak dependence. This is because the surface modes are determined by the capacitive effect

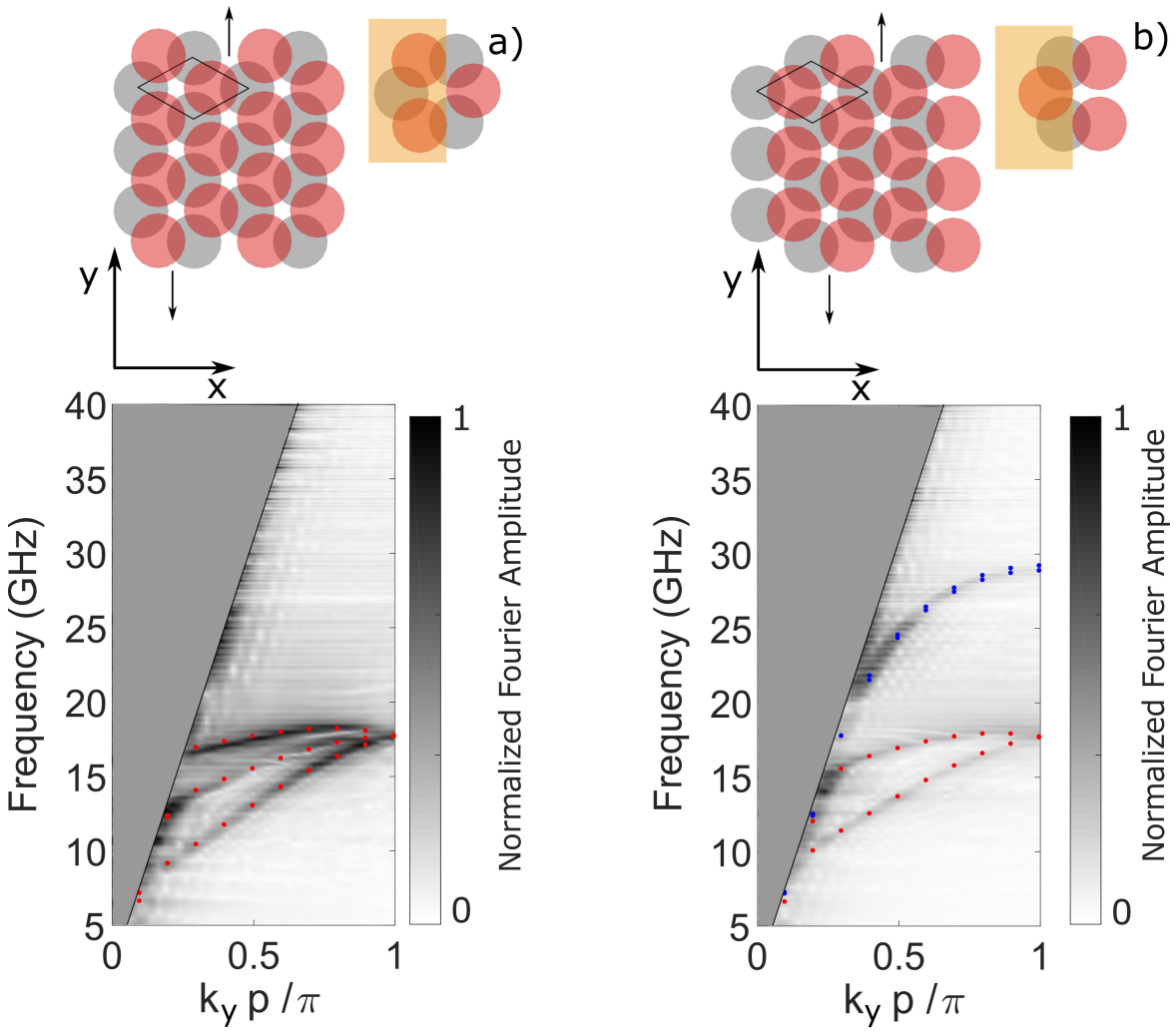

Fig. 7.7 Normalised Fourier amplitude, derived from the the experimental field measurement, showing the dispersion diagrams of the modes supported by the structures presented in Fig. 7.4. The plot on the left corresponds to the structure with two overlap regions at the edge patches, so it does not present an edge mode in the recorded range of frequencies and the plot on the right is for the structure with one overlap region at the edge patches. The FEM-modelled dispersion diagrams are also included (red dots for the surface modes and blue dots for the edge modes), showing excellent agreement with the experimental measurement.

between the patches in both layers whereas the edge modes are determined by the charges accumulated at the edges of the terminating patches. Also, as shown in Fig. 7.5, the fields corresponding to the edge modes are not strongly confined to the dielectric spacing between the layer but extend further into free space.

The changes caused by the addition of this extra dielectric layer can be observed by comparing the plots in Fig. 7.5 (no oil layer added to the model) and Fig. 7.7, where the separation between the layers is increased by adding the oil layer. While the surface modes

move up in frequency when the oil layer is introduced, the edge modes stay in the same position.

Now that the nature and existence of the edge modes have been explained, we proceed to study how they can be used to manipulate the propagation of electromagnetic waves. In the first place, in section 7.5 the edge modes are used to guide the electromagnetic fields around three different shapes, including several corners. Finally, in section 7.6, the coupling of two of the mentioned edge modes is studied.

7.5 Edge modes to guide the electromagnetic fields

A second experiment was carried out in order to further explore the properties of the higher frequency edge modes found for the structure in Fig. 7.4 (b) and to test the capability of such modes to guide the fields around sharp corners. The reason why this termination was chosen is purely because it supports an edge mode which can be differentiated as distinct from the light line even at relatively low frequencies, which can be more easily measured experimentally.

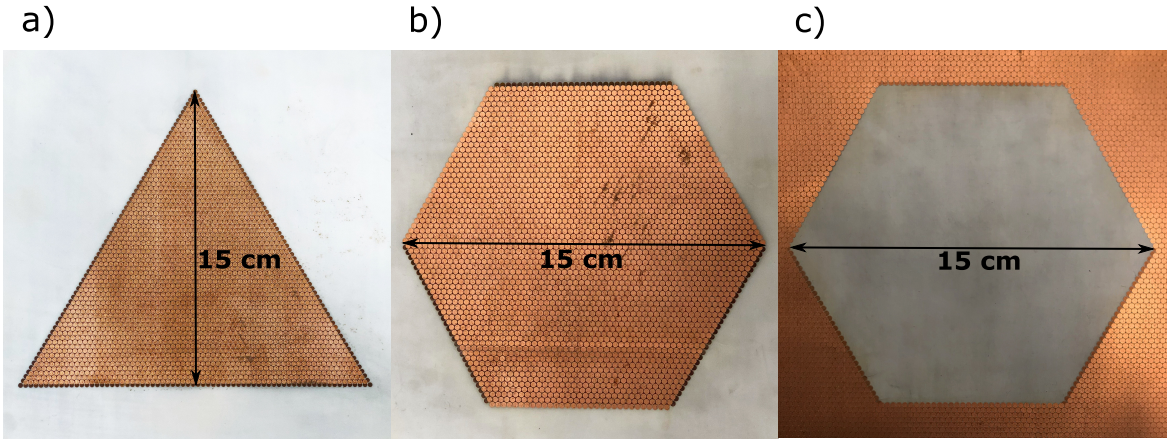

Fig. 7.8 Photographs of the three samples used to study the propagation of the described edge modes around corners. The first one (a)) is a triangular shape with 300° corners, the second one (b)) is a hexagonal shape with 240° corners and the third one (c)) a hollow hexagonal shape with 120° corners. In all three cases, the dimensions of the samples are an order of magnitude bigger than the wavelength.

Firstly, two different samples were studied, one with a hexagonal shape (240° corners) and a second one with a triangular shape (300° corners). Both shapes were etched from metal-coated dielectric sheets, resulting in two bi-layer patch structures surrounded by dielectric. Photographs of these samples are included in Fig. 7.8 (a) and b)).

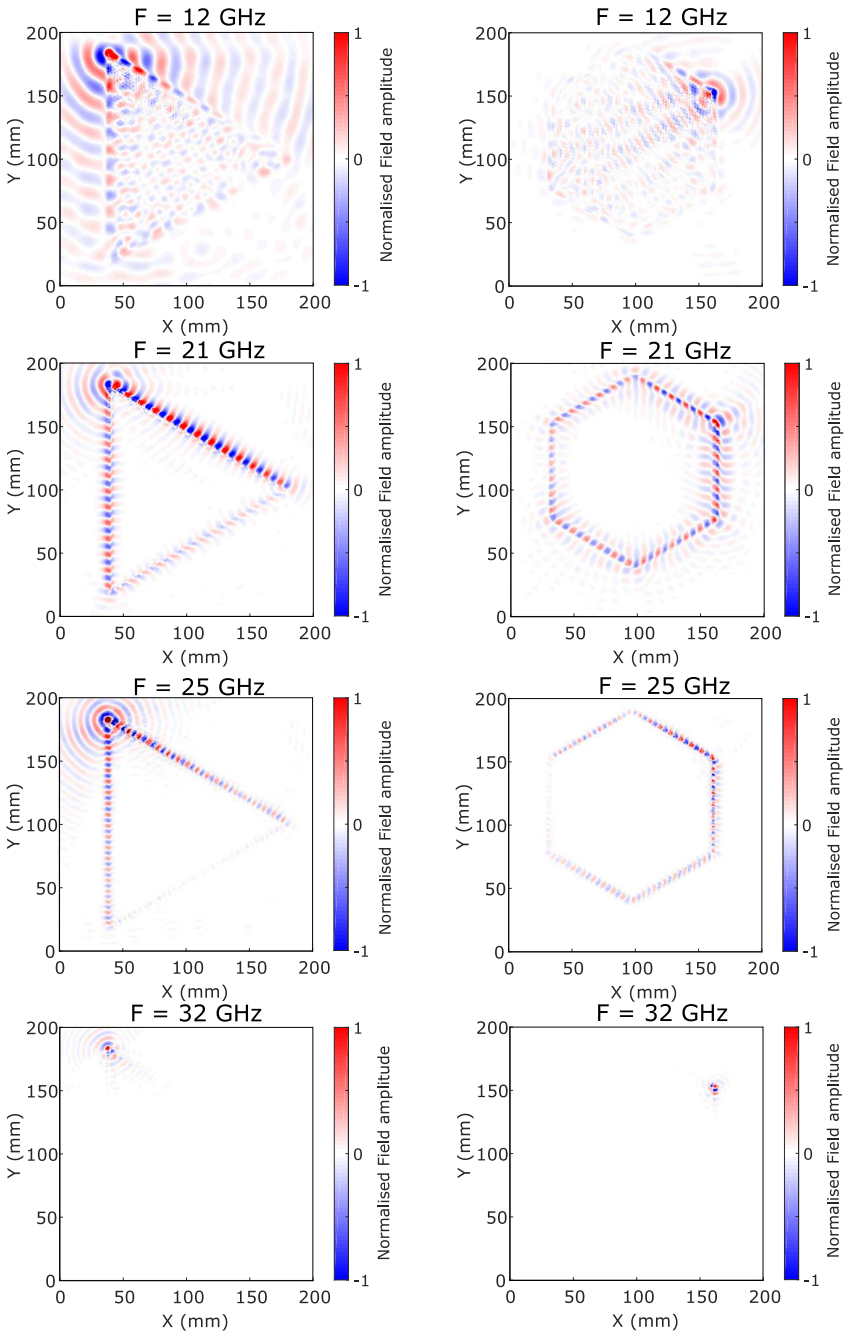

Fig. 7.9 Experimental measurement of the fields on top of the sample with the triangular shape (left) and the hexagonal shape (right). The triangular structure is excited on the top left corner and the hexagonal one on the top right corner. For low frequencies (i.e. 12 GHz) the field penetrates inside the structure. For higher frequencies (i.e. 21 GHz and 25 GHz), where only the edge mode exists, the field propagates around the edges and for frequencies above the cutoff of the modes supported by the structure (i.e. 32 GHz) we do not find any modes bound to the surface.

These samples were designed in a way that all the edges present the geometry that allows the propagation of the edge eigenmode, i.e. all edges have one overlap region per edge patch. While for the triangular shape all three edges have the same orientation, for the hexagonal one the edges alternate between 'up' edges and 'down' edges.

To excite the edge mode, a loop antenna was placed in one corner of the structures and a second loop antenna was used to measure the amplitude and phase of the electromagnetic fields, scanned across the entire opposite face of the sample. The measured fields for four different frequencies are plotted in Fig. 7.9.

For low frequencies (i.e. 12 GHz), where there exists a surface mode, the fields penetrate inside the structure and the mode propagates across the entire metasurface. For higher frequencies, (i.e. 21 GHz and 25 GHz) where only the edge mode exists, the mode propagates around the triangular/hexagonal shape with a rapid evanescent decay of the fields across the surface. Finally, for frequencies above the cutoff of the edge mode (i.e. 32 GHz) we cannot find any mode bound to the edge or surface.

This experiment demonstrates the edge nature of the additional mode supported by the described structure and its capability to guide the electromagnetic fields, even around sharp corners.

Finally an 'inside-edge' sample, complementary to the previously studied hexagonal shape was fabricated and studied. In this case, a hexagonal hole has been etched out from a background infinite 2-layer structure, leaving around the shape an edge-mode-supporting configuration of patches (one overlap region per edge patch). A photograph of this sample can be found in Fig. 7.8, c).

Similarly as for the previous case, the edge mode was excited by placing a loop antenna on the top corner of the hexagonal shape and, using the same experimental setup, the electromagnetic field was measured across the opposite face of the sample.

In Fig. 7.10, a comparison of the field plots for both hexagonal structures is shown for two different frequencies inside the range where the edge mode is supported. It is demonstrated that the edge mode is able to propagate around both configurations even in the presence of sharp corners. For the hexagonal shape, the mode propagates around three corners and for a distance equivalent to more than 20 wavelengths.

The signal radiated as the mode goes around a corner has also been quantified by measuring the amplitude of the field before and after a corner, and is smaller in amplitude than 30% for frequencies between 19 GHz and 22 GHz. A further study of the energy radiated at the corner and the propagation losses is presented in section. 7.7.

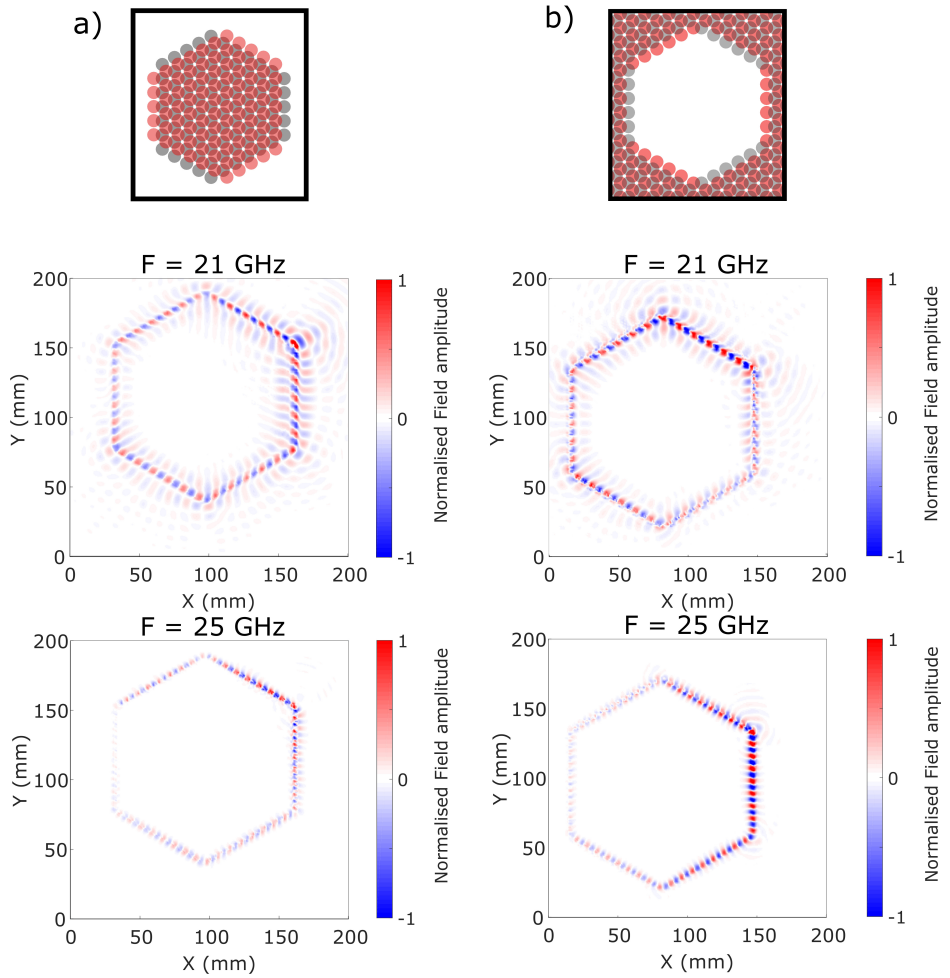

Fig. 7.10 Experimental measurement of the fields on top of the sample with the hexagonal shape (left) and the hexagonal hole (right). Both structures have been excited at the top right corner with a loop antenna. The field plots are shown at 21 GHz and 25 GHz. For both frequencies, only the propagation of the edge mode is supported.

7.6 Coupled edge modes

In this section, we study the interaction between a pair of edge modes. For this purpose, two identical strips (parallel to the y-axis) have been fabricated, as part of the same sample, leaving a small gap between them in the x-direction.

The strips are designed so that they only support the propagation of an edge mode along one of its edges (edge closer to the second strip) for frequencies below 40 GHz.

One of these strips is represented in Fig. 7.11 (right). It is comprised of a bottom layer that is four patches wide and a top layer that is three patches wide. In this way, one of the two edge-arrangements presents one overlap region per edge-patch (edge labelled a) in Fig. 7.11

while the other edge (labelled b) in Fig. 7.11) presents two overlap regions per edge-patch, supporting an edge mode at much higher frequency which cannot be easily observed in the experiments as being distinct from the light line.

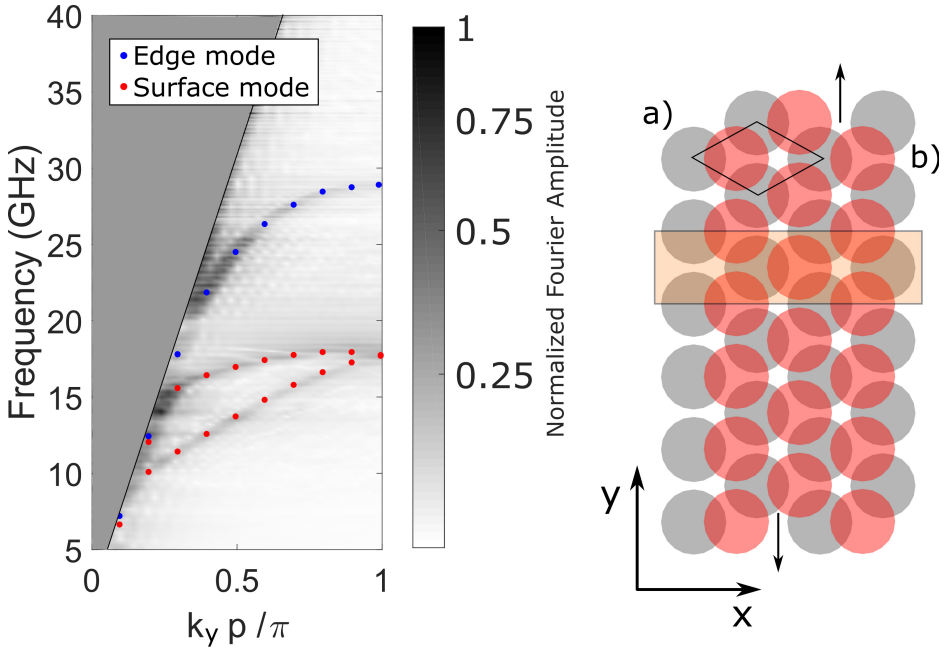

Fig. 7.11 (Right) Sketch of the metasurface designed to study the coupling between two edge modes: The bottom layer (grey) is comprised of 4 rows of patches while the top layer (red) has just three rows. The edge marked a) has just one overlap region and supports an edge mode for frequencies below 40 GHz while the edge marked b) has two overlap regions per edge patch and supports an edge mode that asymtops at frequencies beyond our range of study and hence it follows closely the light line. (Left) Fourier amplitude spectra illustrating the dispersion of the modes supported by the mentioned single strip. The experimental dispersion is plotted as a grey scale and the FEM simulation data has been overlaid as dots. The structure supports the propagation of two surface modes (red) and one edge mode (blue).

The dispersion of the modes supported by this single strip has been determined from experimental data and it has been compared with simulation data from a FEM software. The dispersion diagram is shown in Fig. 7.11 (Left), presenting as predicted two surface modes and only one edge mode at the contemplated range of frequencies.

To study the coupling of the edge modes, two different relative positions of the strips have been studied. In the first case, the edges were aligned to present mirror symmetry while in the second case one of the strips was displaced by half of the period along the vertical direction (y) to explore a glide symmetric configuration. For the glide symmetric case, as the patches are shifted in the vertical direction, the strips can be placed closer together, increasing the coupling strength.

7.6.1 Mirror-Symmetric configuration

A sample with mirror-symmetric edges was built and characterised using the previously described VNA and translation stage setup. The source, a loop antenna, was placed in the gap between the two strips and an identical antenna, acting as a probe was positioned on the opposite side of the sample, used to scan the electromagnetic fields.

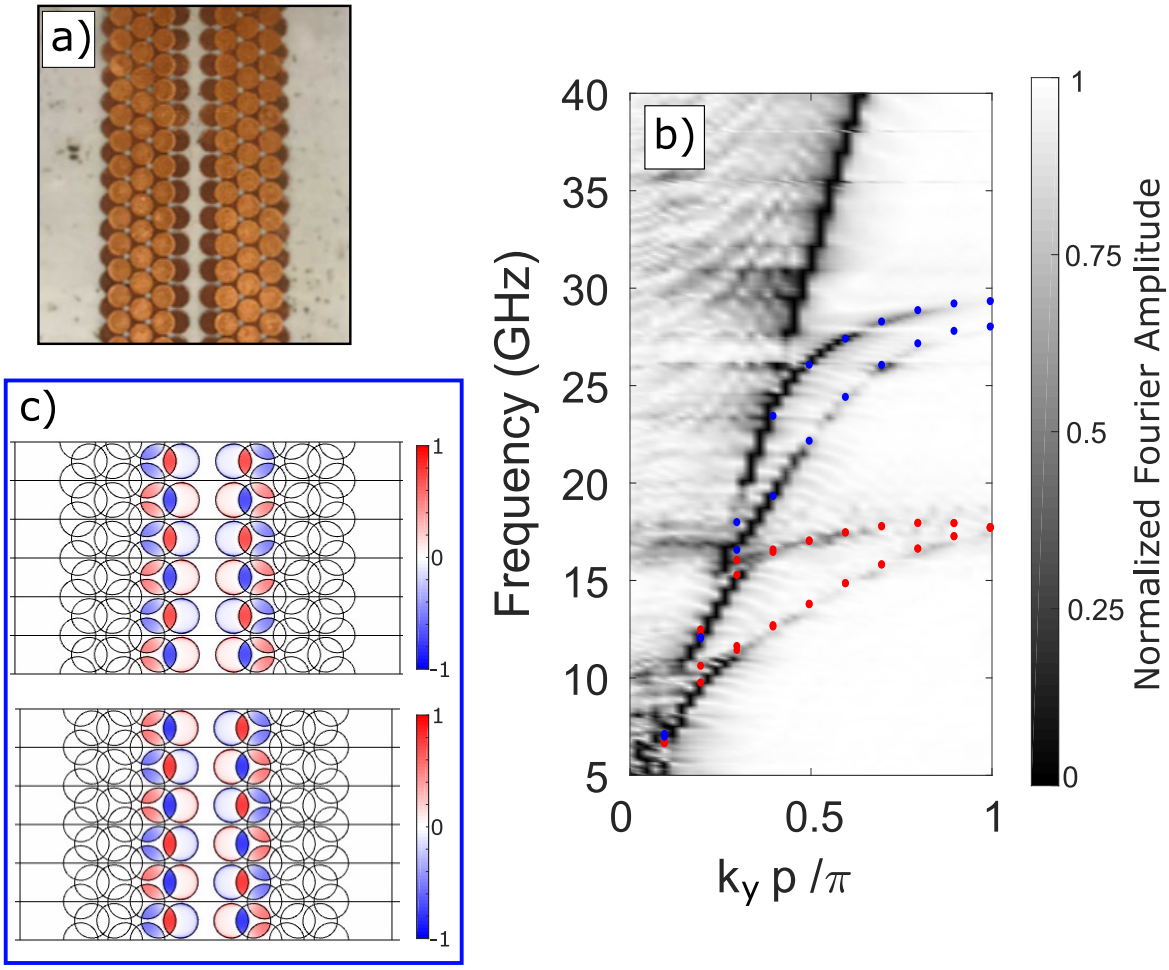

Fig. 7.12 a) Photograph of the sample used to study the coupling between two edge modes with a mirror-symmetric configuration of the strips. Each strip is 3 patches wide on the top layer and 4 patches wide on the bottom layer. b) The grey-scale data is experimental Fourier data illustrating the dispersion diagram of the modes supported. The modelled eigenmodes obtained with the FEM software have been overlaid as dots. The red dots represent the surface modes and the blue dots the edge modes. c) FEM productions of the Out-of-plane electric field distribution for the two coupled edge modes, the higher energy one presents a symmetric field profile while the lower energy one has an anti-symmetric field distribution.

Two different scans were run: a line scan and a surface scan. The first one only scanned the electromagnetic field across one line in the y-direction though the center of the gap

between the strips. By 1D-Fourier transforming this, the dispersion diagram of the coupled edge modes was obtained. It is important to note here that the source had to be placed at the mid-length of the sample to be able to measure the wave vectors in both directions.

The obtained dispersion diagram (experimental and numerical) of the modes supported by the structure as well as the predicted normalised electric field distribution of the coupled edge modes at the Brillouin zone boundary and a photograph of the experimental sample are presented in Fig. 7.12 .

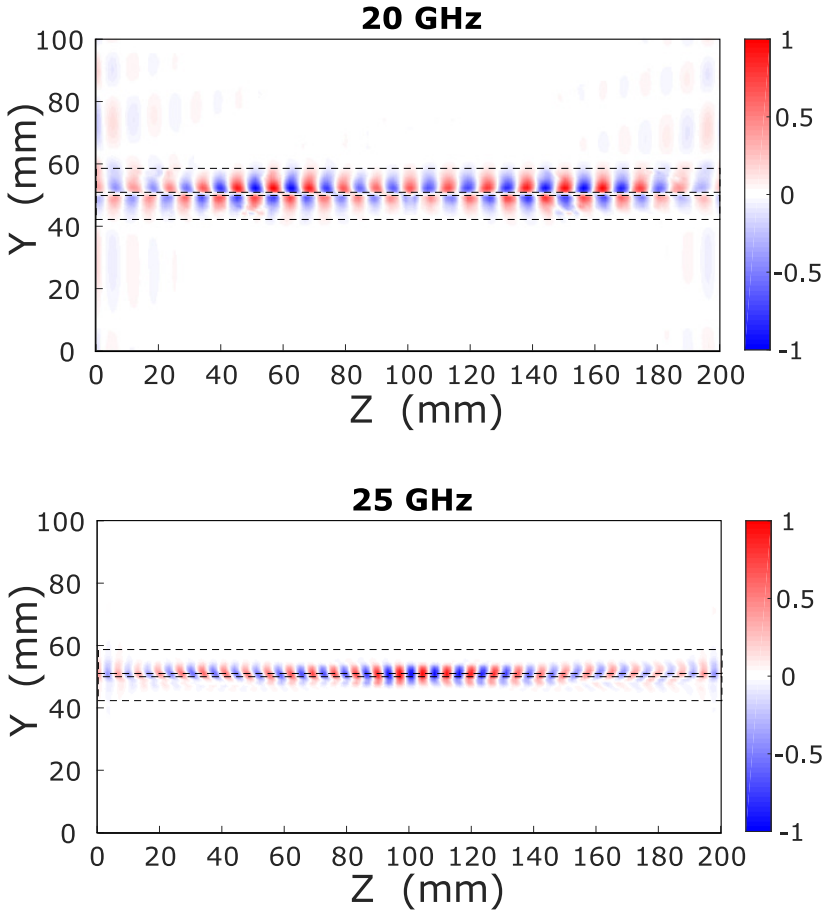

Fig. 7.13 Field plots, recorded experimentally using magnetic loops, corresponding to the symmetric-antisymmetric pair of coupled edge modes. The top one, plotted at 20 GHz corresponds to the lower energy mode, with an antisymmetric field profile while the bottom one, plotted at 25 GHz corresponds to the higher energy symmetric mode. The outline of the sample has been marked with a dotted line. This shows that the lower energy (antisymmetric) mode extends further away from the interface than the symmetric mode.

In the dispersion diagram we find two families of modes. As in the single-strip experiment, at lower frequencies (5 GHz to 20 GHz) we observe two surface modes. Each individual strip supports two surface modes, as there are two full meta-molecules across the width of

the structure. The two strips are identical to one another, and so the modes are degenerate. However, for small wave vectors, both the model and experiment predict a splitting. This is due to the interaction between equivalent modes in the neighbouring strips. This interaction is very weak as the fields of the surface modes are very confined to the dielectric spacing between the layers and only a very small fraction is available to interact with the other mode.

At higher frequencies we observe a second pair of modes that propagate along the inner edges of the structures. One of these modes propagates at a higher frequency than that expected for the edge mode of a single strip and the second one propagates at a lower frequency. This splitting is due to the interaction and coupling between the modes. As the fields of the edge modes are less-well confined than the surface wave fields and extend to the surrounding space, the coupling between them is stronger. This coupling results in a pair of symmetric and anti-symmetric modes. The field plots of the higher energy symmetric mode and lower energy anti-symmetric mode are shown in Fig. 7.12 b).

Finally, the second scan performed was a surface scan, used to probe the fields across a surface area of 200 mm by 100 mm. The field plots obtained from this scan show the two field profiles corresponding to each of the edge modes. These field plots are represented in Fig. 7.13. The first one, plotted at 20 GHz corresponds to the lower energy mode with an anti-symmetric field configuration. The second plot, at 25 GHz shows the higher energy mode, with a symmetric field configuration.

7.6.2 Glide-Symmetric Structure

Following the first study, we investigate the effect of glide symmetry on the interaction of the edge modes. For that purpose, one of the strips was displaced by half of the period in the y-direction (direction of propagation). This symmetry transformation only affects significantly the coupling of the edge modes as it only changes the relative position of the two strips.

A sample with this second configuration was manufactured and characterised experimentally. Again, in the dispersion diagram of the structure, represented in 7.14, we find two families of modes. The surface modes, at lower frequencies, represented in red, and the coupled edge modes, which propagate at higher frequencies (represented in blue). In Fig. 7.14, together with the dispersion diagram of the modes supported by the glide-symmetric structure, a photograph of the sample, and the field plots for the edge modes are represented.

The surface modes for this glide-symmetric structure remain at the same frequency as in the mirror-symmetric case. A small splitting in the surface modes is again observed. However, the edge modes show the effect of glide symmetry. The gap at the Brillouin Zone boundary between the pair of coupled edge modes is closed and the lowest frequency mode

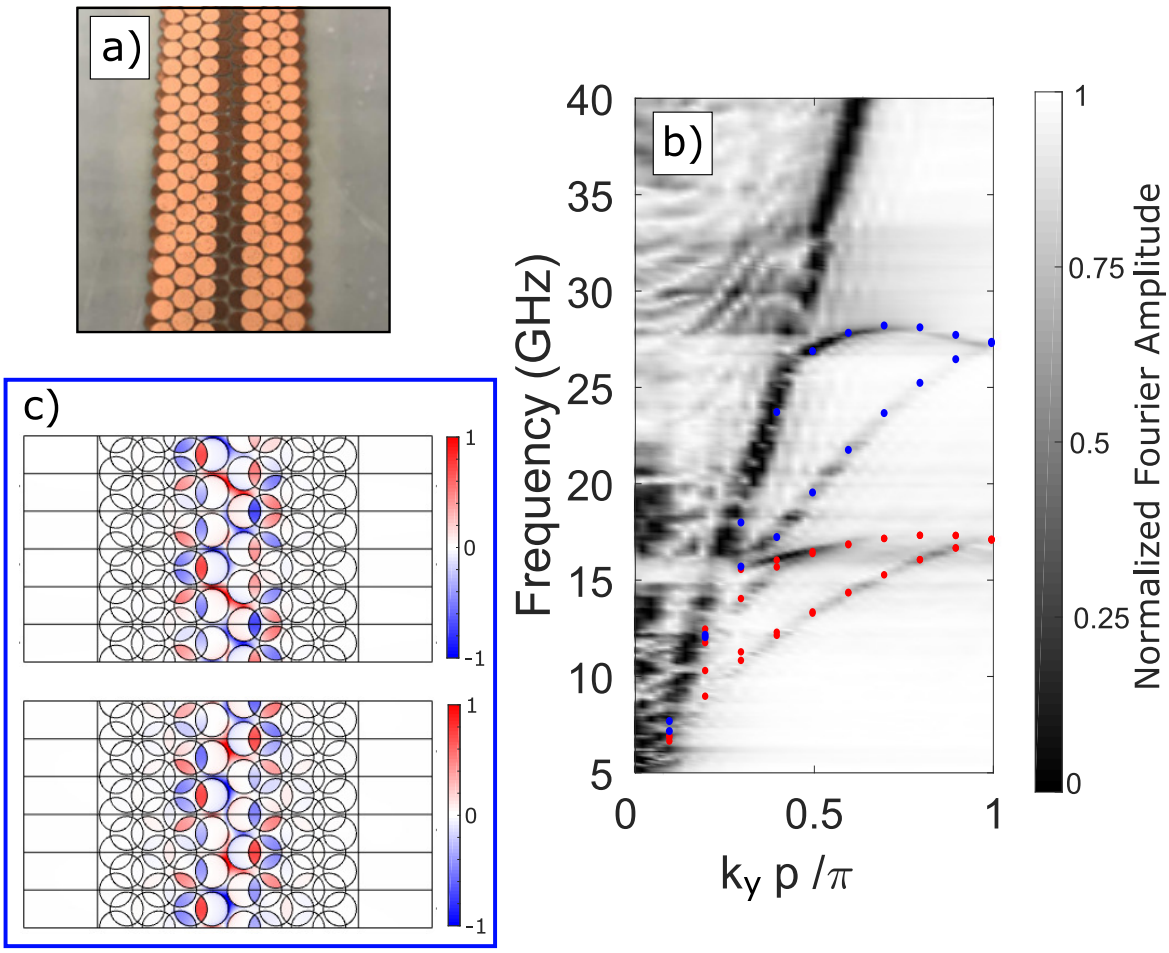

Fig. 7.14 a) Photograph of the sample used to study the coupling between two edge modes with a glide-symmetric configuration. Each strip is 3 patches wide on the top layer and 4 patches wide on the bottom layer. b) Experimental Fourier field data representing the dispersion of the modes supported by the glide-symmetric structure. The eigenmodes obtained with the FEM software have been overlaid as dots. The surface modes are represented by red dots and the edge modes by blue dots. c) FEM predictions of the out-of-plane normalised electric field for the two coupled edge modes for $k_x p/\pi = 0.5$, where the distinction between the symmetric and anti-symmetric modes is clear.

has a more linear dispersion. As for the field distribution, a distinction between a symmetric high frequency mode and and an anti-symmetric mode at a lower frequency is observed (Fig. 7.14 b)). However, this is lost as we move towards the Brillouin zone boundary where the two modes become degenerate. To show the diferentiation between the symmetric and the antisymmetric modes, the out-of-plane field has been plotted for $k_x p/\pi = 0.5$ in Fig. 7.14, c).

7.6.3 Separation Effect

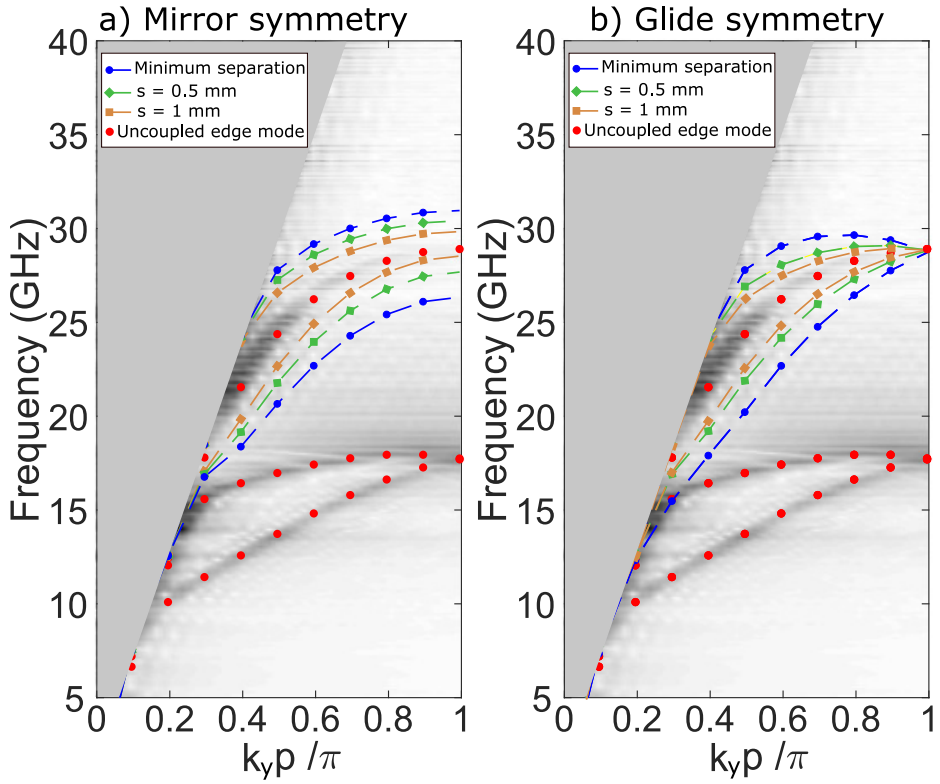

Fig. 7.15 Dispersion diagrams of the modes supported by the coupled-edge-mode structures for three different separations of the strips (1 mm, 0.5 mm and 0.2 mm). They have been plotted on top of the experimental data of a single strip (gray-scale). The single strip also represents the case where there is no coupling between the modes (large separation between the strips). The mirror-symmetric case is represented on the left and the glide symmetry case on the right.

Clearly, the strength of the coupling between two edge modes depends hugely on the separation between them. Although the fields associated with the edge modes extend to free space for longer distances than the surface modes, they decay rapidly as we move away from the interface.

The effect that the separation between the strips has on the coupling of the edge modes was studied by means of FEM modelling. We have run simulations for three different distances between the strips for both configurations. As it was expected, when the strips are placed closer together, the interaction between the edge modes is bigger and therefore the splitting in frequency increases.

For the case where the strips have mirror symmetry the band gap at the Brillouin Zone edge between the coupled edge modes increases to 5 GHz when the strips are only 0.2 mm

away from each other. Meanwhile, for the glide-symmetric case, the coupling weakens as the strips are pulled apart from each other while the degeneracy at the Brillouin zone boundary is maintained.

The cases studied experimentally correspond to the minimum possible separation between the strips in the case of the glide symmetric configuration and to a separation of 1 mm for the mirror-symmetric configuration. In both cases, there is a good agreement between the simulation and experimental results.

7.7 Losses

To conclude this chapter, the propagation losses for the studied edge mode have been estimated experimentally. The range of frequencies over which these losses have been quantified corresponds to the range where the edge mode is exclusively supported and it is clearly distinguishable from the light line.

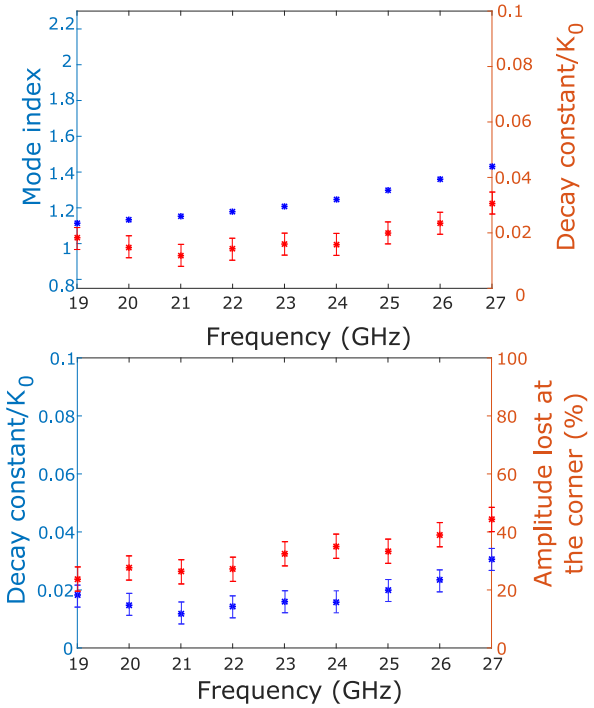

Fig. 7.16 Top: Variation of the mode index and the decay constant of the studied edge mode with frequency. For the range of frequencies where the edge mode is the only mode supported by the structure (19 GHz and 27 GHz), the mode index varies between 1.11 and 1.43 while the decay constant varies between 0.014 and 0.031. Bottom: Decay constant, normalized to the free space wave vector and amplitude lost at the corner for different frequencies in which the edge mode is supported.

We have chosen this range of frequencies because it is where the edge mode can be used for guiding purposes. The decay constant has been quantified from the experimental data in a similar manner to that followed in chapter 6. The field amplitude along the edge was fitted with a function including an exponential decay. From this exponential decay, the propagation length and the decay constant are easily extrapolated.

The decay constant is shown in 7.16 (top) together with the mode index extracted from the experimental data at the same range of frequencies. Between 19 GHz and 27 GHz, the mode index varies between 1.11 and 1.43 while the decay constant of the mode normalized to the free space wave vector varies between 0.014 and 0.031. This means that the wave has to travel for more than 50 wavelengths before its amplitude is reduced by a factor of e.

Finally, the loss due to radiation at the corners has also been quantified over the same range of frequencies. For frequencies between 19 GHz and 22 GHz the losses at the corner are smaller than 30%, however as the frequency increases the percentage of field amplitude lost at the corners also increases. The amplitude loss as the wave propagates around a corner are also shown in Fig. 7.16 (bottom) for the studied range of frequencies.

7.8 Conclusion

In this chapter, a double layered hexagonal metal-patch structure with glide symmetry has been modelled, fabricated and experimentally characterized. Whereas the infinitely periodic structure supports surface modes, localized modes on the edge of a terminated surface are also supported. Two different terminations of the lattice have been identified and studied, one of them presenting an edge mode at much lower frequency than the other. This edge mode has been used to successfully guide the fields around both a triangular and a hexagonal shape. It has been experimentally shown that the structure is capable of supporting the edge mode in two different situations: When a hole is cut out of an infinite sheet and around a shaped metasurface embedded in a dielectric medium.

Finally, the coupling of two microwave edge modes supported by a pair of these metasurfaces has been quantified and the results compared with the predictions from a numerical model. We have also observed coupling between the surface waves supported but this is much weaker than the edge mode coupling because of the strong confinement of the electromagnetic fields.

Further, the effect of glide symmetry on the pair of coupled edge modes has been investigated. The glide symmetry closes the gap between the coupled edge modes at the Brillouin zone boundary and hence yields a more linear dispersion of the lowest order mode.

This study illustrates fully the potential for designer edge states with metasurfaces and thereby novel ways to manipulate microwave energy.

Chapter 8

Conclusions and future work

8.1 Summary of the thesis and conclusions

Throughout this thesis, several metasurfaces with different geometries that support surface modes at microwave frequencies have been presented. Both their structural design and prospective applications differ from each other but they all have some common features. Firstly, they all are multi-layer structures, where each layer is comprised of disconnected elements and with these layers very closely spaced. These general features give the modes supported by the structures a field distribution that is dominated by the capacitive coupling between the overlapping layers of patches. It results in a distribution with an electric field that is mostly confined to the dielectric region between the layers of patches and perpendicular to the plane. Meanwhile, the magnetic field describes loops between adjacent patches. As detailed in previous chapters, such field distributions result in modes which are confined to the surface even at low frequencies, presenting a higher mode index than the equivalent single-layer structures.

For metamaterial structures that support such confined waves, it is a resonance associated with the geometry that acts as an effective surface-plasma-frequency, which subsequently allows for a dispersion analogous to the surface-plasmon-polariton (SPP) dispersion at optical frequencies.

The dispersion of surface waves, is characterised by its mode index. This quantity can be considered analogous to the refractive index for bulk waves. The mode index can be tuned either by varying the dielectric environment in the proximity of a metasurface, or separately, by altering the patterning of that metasurface. The later, is used in this thesis to design two graded index devices, which are characterised and their performance compared to a theoretical model in chapters 4 and 5. In both cases, the geometry of the structure was

chosen to maximise the bandwidth of operation of the devices. That is achieved by reducing the dispersion of the modes supported by the structures.

In chapter 4, a bi-layer design with glide symmetry was presented. It was comprised of two square arrays of circular patches with glide symmetry. Glide symmetry reduces the dispersion of the structure, resulting in a more broadband behaviour.

Different studies were carried out to optimise the performance of the structure, concluding that the design with the most desirable characteristics is that where the layers are placed very close together (the separation between the layers is 50 µm while the wavelength of operation is of the order of 10 mm). The metasurface was finally tested by manufacturing a Luneburg lens whose performance is optimal in the range of frequencies between 6.5 GHz and 11 GHz, translating into a fractional bandwidth of 53%.

In chapter 5 a different metasurface design is presented, whose characteristics in terms of bandwidth and isotropy overperform those of the structure presented in chapter 4. This time, a three-layer metasurface with hexagonal symmetry was designed and characterised. The supported surface waves present some of the characteristic features given by structures with hexagonal symmetry such as a straight Dirac-like dispersion and a Dirac crossing at the K-point at the Brillouin zone boundary. The structure, as the previous one, is also very thin and lightweight, two desirable characteristics for space and defense applications. The straight dispersion presented by the modes supported by the structure together with its improved isotropy, given by the hexagonal symmetry make this structure suitable for the manufacturing of broadband and omnidirectional devices. However, the addition of an extra layer of patches (compared to the metasurface presented in Chapter 4) adds some extra difficulty and cost to the manufacturing process of the metasurface. Besides these issues, the fractional bandwidth of a Luneburg lens was proven to increase by 20% when using the three-layer metasurface presented in this chapter, resulting in a fractional bandwidth of 73%. The results presented in this chapter were published in [9] in 2017.

In chapter 6, the aim was to find a metasurface design that maximised the mode index of the modes it supports. For this purpose, a novel metasurface design consisting of an array of elements with a length up to three times the size of the unit cell was presented. The main consequence of this design is an increase in the mode index presented by the structure, consequence of the patches being longer than the periodicity of the structure. In addition, the mode presents high linearity, due to any effects caused by the band gaps introduced by the periodicity of the structure occurring at much higher in-plane wave vector than the one corresponding to half wave resonances of the long strips.

Also, this ensures that the frequency of operation is far away from the resonant frequency of the constituent metallic elements, hence minimizing the the propagation losses.

Three different metasurface designs featuring the same array of long patches were studied: a mono-layer and two bi-layer structures. The mono-layer shows a very anisotropic behaviour due to the intrinsic anisotropy of the elements comprising the array. This anisotropy, however was corrected by adding a second layer with a 90° rotation with respect to the first one. This also increases the mode index even further as capacitive effects between the overlapping regions of the patches are introduced.

Consequently, due to the high mode index, low loss and isotropy, of the modes it supports, this metasurface is a good candidate for transformation optics applications and the design of graded index devices.

The third design, where a displacement of half the periodicity of the structure was introduced in both x and y directions, does not show any major improvements with respect to the previous one. As a consequence, a further study of its properties was not pursued.

Many of the results presented in chapter 6 were published in [12] in 2019.

Finally, in chapter 7, the propagation of localised edge modes along the termination of a double layered hexagonal metal-patch structure was modelled, fabricated and experimentally characterized. Two different terminations of the lattice have been identified and studied, one of them presenting an edge mode at much lower frequency than the other. This edge mode has been used to successfully guide the fields around both a triangular and a hexagonal shape. It has been experimentally shown that the structure is capable of supporting the edge mode in two different situations: When a 'hole' (region with no patches) is cut out of an infinite metasurface sheet and around a shaped metasurface embedded in a dielectric medium.

Finally, the coupling of two microwave edge modes supported by a pair of these metasurfaces has been measured and the results compared with the predictions from a numerical model. We have also observed coupling between the surface waves supported but this is much weaker than the edge mode coupling because of the strong confinement of the electromagnetic fields.

Further, the effect of glide symmetry on the pair of coupled edge modes has been investigated. The glide symmetry closes the gap between the coupled edge modes at the Brillouin zone boundary and hence yields a more linear dispersion of the lowest order mode. This study illustrates fully the potential for designer edge states with metasurfaces and thereby a novel way to manipulate microwave energy. The studies presented in this chapter were published in [11] and [13] in 2018 and 2020 respectively.

Overall, from the studies carried out as part of this PhD project, four journal articles and four conference papers have been published. However, some other interesting facts and phenomena have also been found that can be further investigated in the future. In the following section, some of the work that could be carried out in the future as a follow up from this thesis is stated.

8.2 Extensions to the work in this thesis

In this section, various ideas for potential future studies, using the concepts presented in this thesis and some new ones are proposed.

The first one, following up from chapter 4, is the development of a Maxwell's Fisheye lens, using the same method proposed for the Luneburg lens. Also, as an extension of chapters 4 and 5, the design of leaky wave antennas by means of a sinusoidally modulated reactance surfaces is proposed.

An additional prospective application of the structures presented in chapters 4, 5 and 6 that was not explored in this thesis is transformation optics. Throughout this thesis, a desirable characteristic of the structures was to maximise isotropy. However, by modifying the shape of the patches, different behaviours in different directions can be achieved as required for transformation optics applications.

With respect to the work started in chapter 7 on edge modes, it can be readily extended, exploring different geometries and different patch shapes.

Finally, some other structures and geometries that have come into consideration during the investigations carried out as part of this thesis are presented.

8.2.1 Maxwell's Fisheye lens

As previously presented in chapter 4, the Maxwell's fisheye lens was the first graded index device ever proposed. It takes the radiation from a point source located on its perimeter and refocuses it creating an identical secondary point image on the opposite side of the lens. The ray tracing and field plot created by a MFE lens are represented in Fig. 8.1.

Despite not having as many applications as the Luneburg lens, some journal articles describing practical applications of the MFE lens have been published over the years [86, 178, 179].

Similarly to the Luneburg lens developed in chapters 4 and 5, the Maxwell's Fisheye (MFE) lens requires a permittivity (and therefore mode index) profile that varies radially

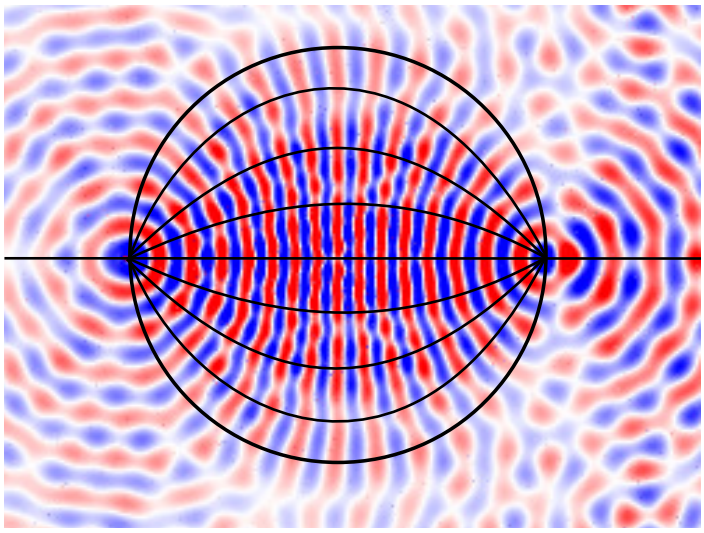

Fig. 8.1 Field profile and ray tracing of a Maxwell's Fisheye lens when a point source is placed on its perimeter. The wave fronts are compressed as they move towards the centre of the lens due to an increase in the mode index. After passing through the lens, the wave fronts are refocused into a secondary point source that is a mirror image of the original one.

with the distance to the centre of the lens, reaching its maximum value at the centre of the lens. The mode index profile required by the MFE lens is shown in equation 8.1.

$$n(r) = \begin{cases} n_0 & \text{if } r > R_0 \\ n_0 \dfrac{2}{1+\left(\frac{r}{R_0}\right)^2} & \text{if } r \leq R_0. \end{cases} \tag{8.1}$$

According to the mode index profile given by such equation, an index variation of 1:2 is required across the sample, as the mode index at the centre of the lens is twice the background index.

A sample containing a MFE lens using the bi-layer metasurface described in chapter 4 was fabricated. A background index of 1.6 was chosen in this case, requiring a mode index of 3.2 at the centre of the lens.

The sample was fabricated following the procedure explained in section 3 and characterised experimentally. In the same way as for the characterization of the Luneburg lens, a loop antenna was used as a source, placed at the perimeter of the lens. An identical loop antenna was used as a probe to scan the electromagnetic fields on the opposite face of the sample. After removing the unwanted radiative part of the data the fields across the surface were plotted. Such field plot is represented in Fig. 8.2 , where it is compared with simulation data for a similar MFE lens obtained with FEM software.

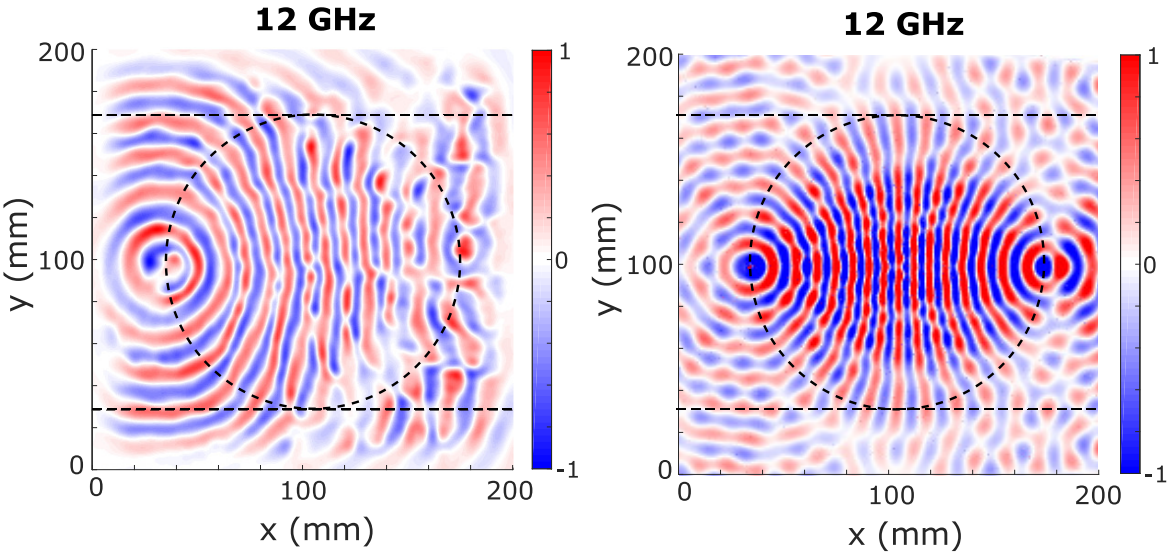

Fig. 8.2 Experimental field profile measured over a sample containing a MFE lens when this is excited with a point source placed on its perimeter (Left). It is compared with the result of a Finite Element model (right).

Although the experimental field plot shows how the wave fronts are compressed as they travel towards the centre of the lens and then they are refocused when approaching the edge of the lens, the focusing is not perfect. As a consequence, a secondary point source is not observed on the opposite side of the lens. Furthermore, the lens fails when we move slightly away from the operational frequency.

One of the reasons why this experiment did not work as well as required is that the 1:2 mode index contrast was not properly fulfilled. In order to have access to a greater mode index contrast, the background mode index needs to be lower than that used for the Luneburg lens sample. This means that the patches need to be smaller and so are the overlap regions between them. As the size of the overlap regions is reduced, any small misalignment or fabrication issue (rough edges or over etching) have a greater influence in the behaviour of the structure. Therefore, we concluded that the realisation of a MFE demonstrator requires an upgrade of the fabrication procedure, probably, moving towards printed circuit board (PCB) techniques.

8.2.2 Leaky wave antennas

Leaky-wave antennas (LWAs) were first proposed in the 1940s by W. W. Hansen. They originally consisted of a one-dimensional slotted rectangular waveguide [180], which allowed the electromagnetic fields to leak out from the guiding structure. In general, a Leaky-wave antenna (LWA), is based on a guiding structure that can be one-dimensional or two-dimensional.

The guiding structure is then manipulated so that the mode bound to the structure leaks [181, 182]. A typical example is a microstrip line that is periodically modulated in order to turn the non-radiating microstrip mode into a radiating leaky mode. Slotted parallel-plate waveguides have also been used extensively as leaky-wave antennas as they are simple to fabricate and feed.

In more recent years, the field of leaky wave antennas has developed extensively since they were first proposed, redirecting towards planar LWAs, which have the advantage of being low profile and easy to manufacture [183]. In addition, the level of interest and the pace of development in the field of planar LWAs has recently accelerated significantly, due to the increase of interest in metamaterials and metasurfaces [52].

Lately, there has been strong interest in high gain, low profile antennas that can be easily integrated into the surfaces of vehicles or other platforms [184–186]. Planar leaky-wave antennas are excellent candidates for this purpose as they leak power from traveling waves propagating along the antenna surface. They are typically characterized by a phase and leakage constant along the antenna. Independent control over these two leaky-wave parameters is highly desired since it allows beam shaping [187–189].

These leaky wave antennas fall into the category of high reactance surfaces, were the reactance is modulated to allow the leakage. This radiation mechanism was first described theoretically by Oliner and Hessel in 1959 [190]. In this paper, a rigorous solution is derived for the propagation characteristics (wave number) and field distributions (field amplitudes) of waves guided by a plane surface that has a surface reactance which has been modulated sinusoidally in the propagation direction. These were obtained numerically, as a continued fraction form, which is rapidly convergent for all values of modulation for both surface wave (modal) and leaky wave (non-modal) solutions.

The reactive plane surface (xy plane), which supports a bound mode propagating in the x-direction, has a proposed surface reactance of the form:

$$\chi(x) = \chi_{\mathrm{S}} \left[1 + M\cos\left(\frac{2\pi}{a}x\right)\right], \tag{8.2}$$

where χ_{S}, is the background surface reactance and M and a are the amplitude and period of the modulation respectively.

The obtained guided-wave solutions are of two types, the (modal) surface waves, for which the wave vector (k) is real, and the (non-modal) leaky waves, for which k is complex. When the modulation spacing a is small, the guided wave is a trapped surface wave. However, when this spacing (M) exceeds a critical value, a leaky wave is created and radiation occurs.

A design procedure and a working leaky wave antenna using this proposed modulated reactance model were presented by Patel and Grbic in 2011 [191]. In this work, a sinusoidally-

modulated reactance surface (SMRS) refers to a surface whose modal surface impedance is modulated sinusoidally.

In the case presented in the 2011 paper, the surface impedance is inductive such that it supports a TM surface wave [192]. However, the same applies to a surface with a capacitive impedance so that the waves supported are TE-like as for the structures described in this thesis.

To design the SMRS leaky wave antenna, the fields of the wave propagating across the structure are expanded in terms of spatial harmonics. The Bloch wave numbers tangential to the surface are given by:

$$k_{\mathrm{x0}} = k, \text{ where } k = \beta - i\alpha, \tag{8.3}$$

$$k_{\mathrm{xn}} = k + \frac{2\pi n}{a}, \tag{8.4}$$

where k_{x0} is the fundamental spatial harmonic and k_{xn} are the higher order ones. The normal wave number is therefore written as:

$$k_{\mathrm{zn}} = \sqrt{k_0^2 - \left(k + \frac{2\pi n}{a}\right)^2}. \tag{8.5}$$

In this way, a dispersion relation can be written in a continued fraction form in terms of M, χ and a.

The result is that for small values of the modulation, M, the solution can be approximated by the solution of k corresponding to no modulation (M=0) [191]. In the case of no modulation, the attenuation constant is zero and the wave number is real. In this way the value of k can be used as an approximation of the propagation constant (β_{approx}).

$$\beta_{\mathrm{approx}} = k_{\mathrm{approx}} = k_0\sqrt{1 + \left(\frac{\chi}{\eta_0}\right)^2}, \tag{8.6}$$

where η_0 is the impedance of free space. This means that there would be a phase delay across the surface but no attenuation and therefore no leakage.

However, in reality, when a modulation is introduced, k is complex and leaky waves are excited but this approximation can be used as a starting point to design a LWA that radiates at a desired angle.

To design the leaky wave antenna, once the frequency of operation and the radiation angle (θ) are chosen, the value of either the period of the modulation (a) or the background impedance (χ) is fixed. Then, the remaining one is calculated using:

$$\sin(\theta) \approx \sqrt{1+\left(\frac{\chi}{\eta_0}\right)^2} - \frac{2\pi}{k_0 a} \tag{8.7}$$

This gives an approximated value of the propagation constant. At this point the modulation (M) is introduced. If M is large, then it might be required to adjust the value of k using the continued fraction form of the dispersion relation.

With this method, the beam direction can be controlled by choosing χ and β appropriately while M controls the attenuation constant and therefore the antenna beam width.

It needs to be noted that when designing a SMRS leaky wave antenna using a metasurface, there are two different periodicities, the periodicity of the lattice (spacing between unit cells) and the period of the modulation.

The downside of this method is the strong variation of the angle of radiation with frequency, which narrows down its application to devices that require a broad frequency of operation. However, as shown in [191] the antenna still radiates when the frequency of operation is varied, only at a different angle, which can be used for scanning purposes.

These types of antenna have been investigated in the recent years, using different metasurfaces for their implementation [193, 194, 68, 195].

The design we propose as an expansion of the work presented in this thesis, is the addition of a modulation following the Luneburg lens design presented in chapter 5. In this way, the planar wave fronts produced by the lens would penetrate a sinusoidally modulated impedance surface which would allow radiation. As the proposed metasurface has a broadband behaviour, the only mechanism that interferes in the variation of the angle of radiation is the described leakage procedure, enabling further control of the later.

8.2.3 Transformation optics

The term transformation optics was first proposed by J. B. Pendry et. al in 2006 [6]. It proposes a way of manipulating electric and magnetic field lines instead of using the ray approximation as geometrical optics does. They showed that this description can provide an intuitive understanding of subwavelength phenomena while also being exact at the level of Maxwell's equations.

Snell's law concerns the refraction of light by transparent media. It gives a picture of the propagation of light in terms of rays, which can be thought of as streams of photons. This simple picture is the basis of the design process of most optical devices. However, this law neglects both reflection at interfaces and diffraction by small features. These features are

only described precisely by the direct application of Maxwell's equations, which is usually a more complicated task.

Transformation optics was developed to give an intuitive picture, similar to that of ray optics, by using instead the elements of Maxwell's equations (the electric and magnetic field lines) and therefore keep the accuracy of such equations. As a result, it gives rules for how these field lines can be manipulated with a high degree of freedom by only a suitable choice of material [196].

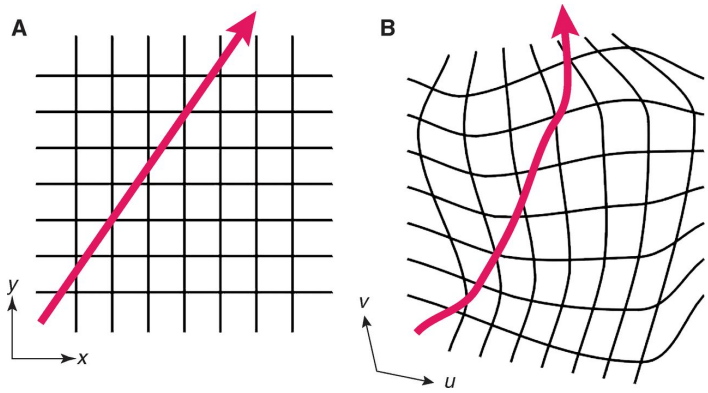

Fig. 8.3 This figure has been taken from [196]. (A) field lines of a uniform displacement field in a Cartesian grid. (B) Same field lines, in this case propagating in a distorted space, which has been bent emulating a rubber sheet. As a result, the field lines take a different trajectory, following the distortion, which is recorded by the new coordinate system.

The idea behind transformation optics, begins with a uniform electric displacement field in free space. The location of the field lines is fixed in a Cartesian system of coordinates, represented in Fig. 8.3 (A). Transformation optics postulates that the field lines are fixed to the coordinate system. This means that when a distortion is applied to the coordinate system, it carries the field lines with it, modifying its trajectory, as shown in Fig. 8.3 (B). The trajectories of the field can therefore simply be modified by distorting the coordinates.

Maxwell's equations can be written in different coordinate systems and this does not change its form but only the values of permittivity and permeability that appear in the equations. These quantities are represented by tensors, that change when the coordinate transformation is applied,

$$\begin{aligned} \varepsilon &\longrightarrow \varepsilon' \\ \mu &\longrightarrow \mu'. \end{aligned} \tag{8.8}$$

The transformed values of ε' and μ' ensure that Maxwell's equations are obeyed by the new configuration of the field lines. This property of adhesion to the coordinate frame applies to any conserved electromagnetic field that can be represented by a field line. Thus, the

Poynting vector also follows this transformation rules. The field lines of the Poynting vector can, in fact, be thought of as a more precise definition of rays of light.

Originally, the early applications of transformation optics involved adapting computer codes from Cartesian to cylindrical geometries [197] by changing the permittivity and permeability profiles instead of the coordinate system. However, with the development of metamaterials and metasurfaces, transformation optics became more than simply a computational tool and was subsequently applied as a way of determining the material properties needed to reshape the electromagnetic field lines.

Some devices that have been realised with the implementation of transformation optics are the perfect lens [159], where a metamaterial with negative refraction is needed, the invisibility cloak [198] and many more [199, 200]. Transformation optics is not a technique unique to the electromagnetic field. It can also be applied to other equations of physics, such as the Helmholtz equation, an approximation to Maxwell's equations [201] and to acoustics [202].

Once the new coordinate system is described in terms of the old coordinates, the necessary transformations to obtain the new values of the permittivity and permeability when the coordinate system is changed as given in [197] are:

$$\begin{aligned} \varepsilon'^{i'j'} &= |\det(\Delta)|^{-1}\Delta_i^{i'}\Delta_j^{j'}\varepsilon^{ij} \\ \mu'^{i'j'} &= |\det(\Delta)|^{-1}\Delta_i^{i'}\Delta_j^{j'}\mu^{ij}, \end{aligned} \tag{8.9}$$

where, the elements of the tensor Δ are given by the first derivatives of the coordinate transformation:

$$\Delta_j^{j'} = \frac{\partial x^{j'}}{\partial x^j} \tag{8.10}$$

As an improvement to the work presented in this thesis, we propose to apply the transformation optics principles to the Luneburg lens presented in chapter 5. In this way, its size can be reduced in the propagation direction, making the sample smaller. This would allow one to introduce a modulation to produce leakage (as explained in the previous section) without a big increase in the overall size of the sample.

The coordinate system transformation required would be:

$$\begin{aligned} x' &= x \\ y' &= \tfrac{y}{\delta} \end{aligned} \tag{8.11}$$

where y is the propagation direction and x is the transverse direction. δ can take any real value, which leads to a 'squeezed' or 'slimmed' Luneburg lens when $\delta > 1$. Following the transformation given by equation 8.9 the new required permittivity and permeability profiles would be:

$$\begin{gathered}\varepsilon' = \varepsilon \begin{pmatrix} \delta & 0 \\ 0 & 1/\delta \end{pmatrix} = 2 - \left(\frac{x'^2+(\delta y')^2}{R^2}\right) \begin{pmatrix} \delta & 0 \\ 0 & 1/\delta \end{pmatrix} \\ \mu' = \mu \begin{pmatrix} \delta & 0 \\ 0 & 1/\delta \end{pmatrix}\end{gathered} \tag{8.12}$$

To simplify these permittivity and permeability profiles, some approximations can be made. The first one regards the permitivitty (ε_{yy}) being smaller than 1. Although an index of less than 1 is achievable using metamaterials, such a structure would be resonant and dispersive, which would limit the bandwidth. To avoid this limitation, (ε_{yy}) can be set to 1. Although this approximation can seem quite crude, since the fields are mainly concentrated to the high refractive index region of permittivity-map, the approximation $\varepsilon_{yy} = 1$ can be taken without severely affecting the performance of the lens [203, 204]. The same applies to the permeability, meaning that it can be asumed that $\mu_{xx} = \mu_{yy} = 1$.

With these approximations, the resulting permittivity profile is realisable with metamaterials but it is also highly anisotropic, requiring elements showing a similar anisotropy. To achieve this, the elements need to be elongated in one direction while reduced in size in the perpendicular direction. A metasurface showing this anisotropic behaviour has already been studied in this thesis. It is the case of the single-layer presented in Chapter 6.

8.2.4 Other ideas and different geometries

Throughout the studies carried out as part of this PhD thesis, many structures and geometries have been considered, however, not all of them have resulted in a finished piece of work.

As an example, similar structures to those presented in chapters 4 and 5 but with different shape elements were also considered. These include an array of circular rings, instead of patches with glide symmetry or an array of hexagonal patches in a hexagonal array.

In the case of the rings, it was concluded that for the requirements pursued in chapter 4, the structure did not provide any improvements with respect to the circular patches. This is due to the important factor being the overlapping metallic regions, which can only be smaller when a void is introduced in the metallic patch. However, when arranged in a bi-layer structure with glide symmetry, rings present a lowest order mode with a straight dispersion

and an absent bandgap at the Brillouin Zone boundary, which can be of interest for a different piece of research.

A different structure that was also studied along with the metasurface presented in chapter 5 consists of a three-layer array of hexagonal patches in a hexagonal array. Using hexagonal patches instead of circular ones increases the metallic overlap regions, increasing the index of the mode supported by the structure. However, the downside is that its isotropy is reduced.

As an additional study, inspired by the work presented in [205], a sinusoidal meandering was added to the edges of the hexagonal patches. This design, however was discarded as the resolution of the print-and-edge method was not good enough to produce an accurate sample. In Fig. 8.4, a unit cell of a single layer of the meandered-patch metasurface is presented.

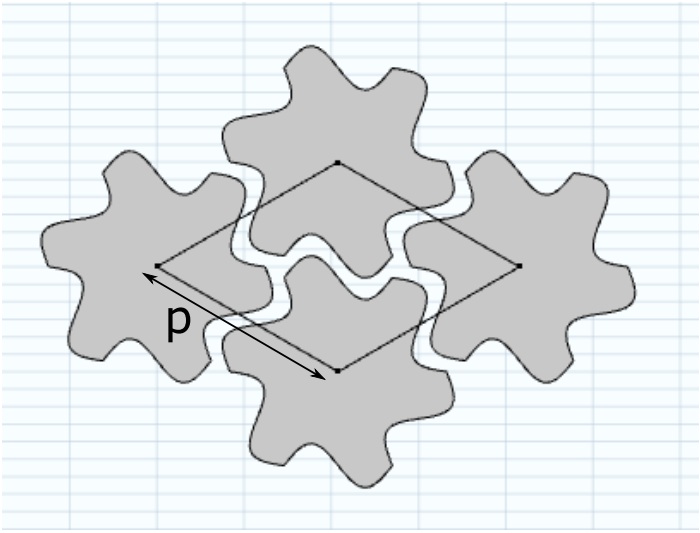

Fig. 8.4 Unit cell of single layer metasurface consisting on meandered hexagonal patches in a hexagonal array with periodicity p.

On a different note, in chapter 6, the long-patch structure, was studied as a way of maximising the index of the mode it supports. However, some other interesting features that could be further pursued were also found. Strong beaming was observed at some higher frequencies in addition to the higher order modes presenting negative dispersion. These two effects would be studied further with longer strips.

In chapter 7, a terminated metasurface comprised of two stacked arrays of patches was presented. The aim of this chapter was to study the edge modes supported by such a structure. It was concluded that the way in which those two layers are aligned modifies the frequency at which the edge modes appear. In order to get a better understanding of the edge modes,

different variations of the terminating patches were proposed. In section 7.4 it is shown how elongating the patches lowers the frequency at which the edge mode appears while shortening the patches does the opposite.

In addition to those modifications, different shapes were also studied and other geometries, such as hexagonal patches were proposed. It would be interesting to study the differences and similarities between the edge modes supported by the different structures. A second interesting point would be to try to infer a method of calculating the asymptotic frequency of the edge modes based on the 'exposed' or 'free' area of the edge patches.

In relation to the work presented in this chapter, the presence of edge modes was also studied when the terminated structure is a bi-layer of circular patches in a square array with glide symmetry. For such a structure, a similar edge mode to that supported by the structure presented in chapter 7 was found. In addition, the effects of glide symmetry are also appreciated in the 'bulk' modes.

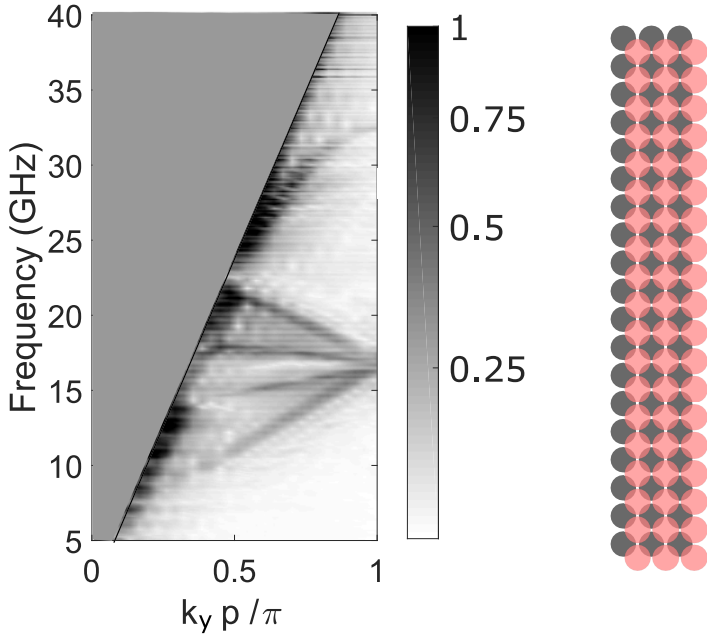

Fig. 8.5 Dispersion diagram of the modes supported by a finite strip of circular patches in a square array with glide symmetry. On the right hand side, a schematic of this strip is shown, the structure is three patches wide in the x direction and can be considered infinitely periodic in the y (vertical) direction.

The dispersion diagram of the modes supported by a finite strip of the bi-layer metasurface with glide symmetry is shown in Fig. 8.5. This experimental dispersion corresponds to the modes supported by a strip that is three patches wide. This means that two surface modes and two degenerate edge modes are expected. In the figure, the two families of modes are clearly distinguishable. At lower frequencies, the surface modes are found, in this case 'folded back'

as consequence of the glide symmetry present in the structure. In addition to this family of modes, a pair of degenerate edge modes is found for higher frequencies, approaching the Brillouin Zone boundary with zero group velocity at approximately 32 GHz. Thus there is much work which would be undertaken with this geometry.

Finally, throughout this entire thesis, only metasurfaces comprised of arrays of disconnected patches have been studied. These structures are known to support TE-like modes however, most of the physics behind the phenomena described in this thesis is also applicable to TM-like modes. It would be interesting to study the complementary structures to those proposed in this thesis. That is, structures formed of continuous metal sheets from which periodic arrays of holes or slots have been removed. Complementary metasurfaces have widely been studied but it would be interesting to see the effect that this has in multilayer structures, as the overlap regions change completely.

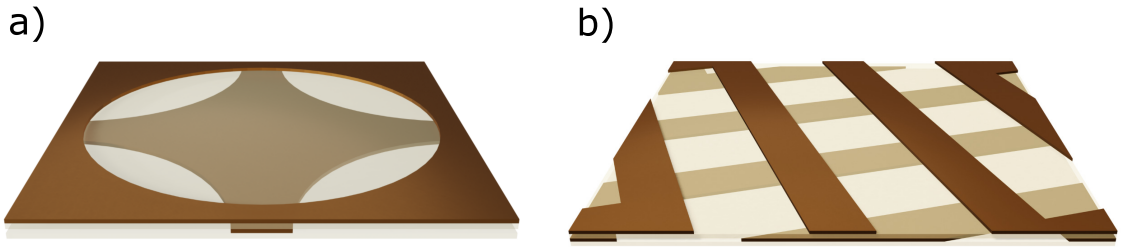

Fig. 8.6 Examples of two holey structures, complementary to those presented in chapters 4 and 6 respectively. The first one (a)) corresponds to an array of circular holes with glide symmetry while b) corresponds to a bi-layer of long slots in a square array.

In Fig. 8.6, two examples of holey structures are shown. The first one, marked a) is bi-layer of circular holes with glide symmetry. This metasurface is complementary to the structure presented in chapter 4. The second structure corresponds to a bi-layer of long slots (three times as long as the unit cell) in a square array. As was done for the structure presented in chapter 6, one layer is rotated by 90° with respect to the first one. This family of complementary structures supporting TM modes would provide a fresh avenue o original research.

8.3 Conclusion: Applications of Metasurfaces

Nowadays, many industries require that communication systems and also shielding structures become lighter and easier to integrate. Among others, this is the case for satellites, aircrafts and unmanned air vehicles (UAVs). For all these applications, where weight needs to be kept very low, being able to transfer power and signal on surfaces is a very desirable feature. In the same way, this can also be implemented in any device where the use of wires wants to be avoided and also for applications where using a wireless network that can be intercepted is not an option. An example of this kind of technology is SurFlow™, a process patented by TWI, which transmits data in the form of electromagnetic waves that travel through composite parts. The system uses no wires or fibre optics and, unlike wireless data transfer, cannot be intercepted remotely. Potential applications for such technology exist throughout industry. In the automotive sector, the technology could significantly reduce the complexity of a vehicle's internal communications network. In robotics, it could be used to enable communication throughout a system without the use of wires. Finally, in consumer electronics, this technology would allow a device to instantly connect to a network simply by making contact with a surface, with no need to plug anything in or detect and connect to a wireless network. Another problem faced by a number of industries is detecting and localising the presence of surface defects and features, which can be the result of accidental damage or deliberate tampering. Examples might include detecting attempts to access a container or tank, sabotage a pipeline, or bullet holes in armour, but could also extend to locating people and machinery on a factory floor. Gekko is a patented technology that sends radiofrequency signals using surface waves. The waves are bound to a specially-treated surface and travel in the air very close to it. These waves tend to remain bound even when the surface is curved or has corners and small gaps. In this technology, specially-designed launchers placed on or close to the surface are used to inject and sense signals, and can be connected to traditional radio transmitters and receivers just like any normal communications or radar system. High-bandwidth data can also be passed between the launchers, for applications that require secure communications. These waves could be used for automated non-destructive inspection of surfaces in a production chain, increasing accuracy and reducing the number of specialised engineers needed.

References

[1] R. H. Ritchie, "Plasma losses by fast electrons in thin films," *Phys. Rev.*, vol. 106, pp. 874–881, Jun 1957.

[2] C. C. Cutler, "Genesis of the corrugated electromagnetic surface," in *Proceedings of IEEE Antennas and Propagation Society International Symposium and URSI National Radio Science Meeting*, vol. 3, pp. 1456–1459, June 1994.

[3] A. A. Oliner and A. Hessel, "Guided Waves on Sinusoidally-Modulated Reactance Surfaces," *IRE Transactions on Antennas and Propagation*, vol. 7, pp. 201–208, 1959.

[4] J. B. Pendry, L. Martín-Moreno, and F. J. Garcia-Vidal, "Mimicking surface plasmons with structured surfaces.," *Science*, vol. 305, no. 5685, pp. 847–8, 2004.

[5] A. Hibbins, B. Evans, and J. Sambles, "Experimental verification of designer surface plasmons," *Science*, vol. 308, pp. 670–672, apr 2005.

[6] J. B. Pendry, D. Schurig, and D. R. Smith, "Controlling Electromagnetic Fields," *Science*, vol. 312, pp. 1780–1782, 2006.

[7] S. Maci, G. Minatti, M. Casaletti, and M. Bosiljevac, "Metasurfing : Addressing Waves on Impenetrable Metasurfaces," *IEEE Antennas and Wireless Propagation Letters*, vol. 10, pp. 1499–1502, 2011.

[8] J. A. Dockrey, M. J. Lockyear, S. J. Berry, S. A. R. Horsley, J. R. Sambles, and A. P. Hibbins, "Thin metamaterial Luneburg lens for surface waves," *Physical Review B*, vol. 87, pp. 1–5, 2013.

[9] J. D. de Pineda, R. C. Mitchell-Thomas, A. P. Hibbins, and J. R. Sambles, "A broadband metasurface luneburg lens for microwave surface waves," *Applied Physics Letters*, vol. 111, no. 21, p. 211603, 2017.

[10] G. Minatti, M. Faenzi, E. Martini, F. Caminita, P. De Vita, D. Gonzalez-Ovejero, M. Sabbadini, and S. Maci, "Modulated Metasurface Antennas for Space: Synthesis, Analysis and Realizations," *IEEE Transactions on Antennas and Propagation*, vol. 63, no. 4, pp. 1288–1300, 2015.

[11] J. D. de Pineda, A. P. Hibbins, and J. R. Sambles, "Microwave edge modes on a metasurface with glide symmetry," *Phys. Rev. B*, vol. 98, p. 205426, Nov 2018.

[12] J. D. de Pineda, G. P. Ward, A. P. Hibbins, and J. R. Sambles, "Metasurface bilayer for slow microwave surface waves," *Phys. Rev. B*, vol. 100, p. 081409, Aug 2019.

[13] J. D. de Pineda, A. P. Hibbins, and J. R. Sambles, "Coupled edge modes supported by a microwave metasurface," *Opt. Lett.*, vol. 45, pp. 1778–1781, Apr 2020.

[14] S. B. Glybovski, S. A. Tretyakov, P. A. Belov, Y. S. Kivshar, and C. R. Simovski, "Metasurfaces: From microwaves to visible," *Physics Reports*, vol. 634, no. Supplement C, pp. 1 – 72, 2016. Metasurfaces: From microwaves to visible.

[15] J. Pendry, "Playing tricks with light," *Science*, vol. 285, no. 5434, pp. 1687–1688, 1999.

[16] B. Hecht, H. Bielefeldt, L. Novotny, Y. Inouye, and D. W. Pohl, "Local excitation, scattering, and interference of surface plasmons," *Phys. Rev. Lett.*, vol. 77, pp. 1889–1892, Aug 1996.

[17] W. L. Barnes, A. Dereux, and T. W. Ebbesen, "Surface plasmon subwavelength optics," *Nature*, vol. 424, pp. 824–830, aug 2003.

[18] F. Capolino, *Theory and Phenomena of Metamaterials, Handbook*. Taylor and Francis, 2009.

[19] S. Walia, C. M. Shah, P. Gutruf, H. Nili, D. R. Chowdhury, W. Withayachumnankul, M. Bhaskaran, and S. Sriram, "Flexible metasurfaces and metamaterials: A review of materials and fabrication processes at micro- and nano-scales," *Applied Physics Reviews*, vol. 2, no. 1, p. 011303, 2015.

[20] C. R. Simovski, "Material parameters of metamaterials (a review)," *Optics and Spectroscopy*, vol. 107, no. 5, pp. 1562–6911, 2009.

[21] Y. Zhao and A. Alù, "Manipulating light polarization with ultrathin plasmonic metasurfaces," *Phys. Rev. B*, vol. 84, p. 205428, Nov 2011.

[22] U. Beaskoetxea, J. C. Iriarte, I. Ederra, I. Maestrojuan, and M. Melara, "Design of multiband conformal antenna for sounding rocket," in *2020 14th European Conference on Antennas and Propagation (EuCAP)*, pp. 1–3, 2020.

[23] N. I. Zheludev and Y. S. Kivshar, "From metamaterials to metadevices," *Nature Materials*, vol. 11, pp. 917–924, Aug 2012.

[24] Q. He, S. Sun, S. Xiao, and L. Zhou, "High-efficiency metasurfaces: Principles, realizations, and applications," *Advanced Optical Materials*, vol. 6, no. 19, p. 1800415, 2018.

[25] B. A. Munk, *Frequency Selective Surfaces: Theory and Design*. Wiley, 2000.

[26] R. Mittra, C. H. Chan, and T. Cwik, "Techniques for analyzing frequency selective surfaces–a review," *Proceedings of the IEEE*, vol. 76, pp. 1593–1615, dec 1988.

[27] F. Costa, A. Monorchio, and G. Manara, "Efficient analysis of frequency-selective surfaces by a simple equivalent-circuit model," *IEEE Antennas Propag. Mag.*, vol. 54, no. 4, pp. 35–48, 2012.

[28] R. Marqués, J. D. Baena, M. Beruete, F. Falcone, T. Lopetegi, M. Sorolla, F. Martín, and J. Garcia, "Ab initioanalysis of frequency selective surfaces based on conventional and complementary split ring resonators," *Journal of Optics A: Pure and Applied Optics*, vol. 7, pp. S38–S43, jan 2005.

[29] M. L and O. A, "Antenna feed system simultaneously operable at two frequencies utilizing polarization independent frequency selective intermediate reflector," Jan. 25 1966. US Patent 3,231,892.

[30] A. Abbaspour-Tamijani, K. Sarabandi, and G. M. Rebeiz, "Antenna-filter-antenna arrays as a class of bandpass frequency-selective surfaces," *IEEE Transactions on Microwave Theory and Techniques*, vol. 52, no. 8, pp. 1781–1789, 2004.

[31] F. Bayatpur and K. Sarabandi, "Multipole spatial filters using metamaterial-based miniaturized-element frequency-selective surfaces," *IEEE Transactions on Microwave Theory and Techniques*, vol. 56, no. 12, pp. 2742–2747, 2008.

[32] S. Yoshida, T. Yamaguchi, and A. Kinbara, "Optical properties of aggregated silver films," *J. Opt. Soc. Am.*, vol. 61, pp. 62–69, Jan 1971.

[33] N. A. Haskell, "The dispersion of surface waves on multilayered media*," *Bulletin of the Seismological Society of America*, vol. 43, pp. 17–34, 01 1953.

[34] *Acoustic surface waves*, vol. 24, Jan. 1978.

[35] G. Goubau, "Surface waves and their application to transmission lines," *Journal of Applied Physics*, vol. 21, no. 11, pp. 1119–1128, 1950.

[36] J. Zenneck, "Über die fortpflanzung ebener elektromagnetischer wellen längs einer ebenen leiterfläche und ihre beziehung zur drahtlosen telegraphie," *Annalen der Physik*, vol. 328, no. 10, pp. 846–866, 1907.

[37] A. Sommerfeld, "The Broadening of the waves and the wireless telegraph," *Annalen der Physik*, no. 28, 1909.

[38] M. Navarro-Cía, M. Beruete, S. Agrafiotis, F. Falcone, M. Sorolla, and S. A. Maier, "Broadband spoof plasmons and subwavelength electromagnetic energy confinement on ultrathin metafilms," *Opt. Express*, vol. 17, pp. 18184–18195, Sep 2009.

[39] D. Sievenpiper, L. Zhang, R. F. J. Broas, and E. Yablonovitch, "High-Impedance Electromagnetic Surfaces with a Forbidden Frequency Band," *IEEE Transactions on Microwave Theory and Techniques*, vol. 47, no. 11, pp. 2059–2074, 1999.

[40] R. Collin, *Field Theory of Guided Waves*. Piscataway, New Jersey: IEEE Press, 1991.

[41] C. Balanis, *, Antenna Theory, Analysis, and Design, 2nd edition*. New York: John Wiley and Sons, 1997.

[42] C. Kittel, *Introduction to Solid State Physics*. ISBN 0-471-11181-3., 2005.

[43] L. Brillouin, *Properties of Materials: Anisotropy, Symmetry, Structure.* Oxford: Oxford University Press, 2005.

[44] L. Dwight and J. Evans, "Coupled Waves and Floquet Approach To Periodic Structures," 1975.

[45] C. Soukoulis, M. Kafesaki, and E. Economou, "Negative-index materials: New frontiers in optics," *Advanced Materials*, vol. 18, no. 15, pp. 1941–1952, 2006.

[46] S.-H. Kim, T.-T. Kim, S. Oh, J.-E. Kim, H. Park, and C.-S. Kee, "Experimental demonstration of self-collimation of spoof surface plasmons," *Phys. Rev. B*, vol. 83, p. 165109, Apr 2011.

[47] N. R. E., *Wave propagation in periodic structures*, vol. 301. ISBN 0486495566., 1953.

[48] J. N. Lalena, "From quartz to quasicrystals: probing nature's geometric patterns in crystalline substances," *Crystallography Reviews*, vol. 12, no. 2, pp. 125–180, 2006.

[49] T. Constant, *Optical Excitation of Surface Plasmon Polaritons on Novel Bigratings*. Ph.D. Thesis, 2013.

[50] J. Dockrey, *Manipulation of Microwave Surface Waves Supported on Metamaterials*. Ph.D. Thesis, 2015.

[51] T. J. Constant, P. Vukusic, A. P. Hibbins, and J. R. Sambles, "Surface plasmons at the Brillouin zone boundary of an oblique lattice," *Applied Physics Letters*, vol. 106, no. 9, 2015.

[52] G. Minatti, F. Caminita, E. Martini, S. Member, and S. Maci, "Flat Optics for Leaky-Waves on Modulated Metasurfaces : Adiabatic Floquet-Wave Analysis," *IEEE Transactions on Antennas and Propagation*, vol. 64, no. 9, pp. 3896–3906, 2016.

[53] J. B. Pendry, D. Schurig, and D. R. Smith, "Controlling electromagnetic fields," *Science*, vol. 312, no. 5781, pp. 1780–1782, 2006.

[54] N. Kundtz and D. R. Smith, "Extreme-angle broadband metamaterial lens," *Nature Materials*, vol. 9, no. 2, pp. 129–132, 2010.

[55] A. Company, *The Essentials of Vector Network Analysis*. 2009.

[56] M. Bosiljevac, M. Casaletti, F. Caminita, Z. Sipus, and S. Maci, "Non-uniform metasurface luneburg lens antenna design," *IEEE Transactions on Antennas and Propagation*, vol. 60, pp. 4065–4073, Sep. 2012.

[57] J. Li, R. Jin, J. Geng, X. Liang, K. Wang, M. Premaratne, and W. Zhu, "Design of a broadband metasurface luneburg lens for full-angle operation," *IEEE Transactions on Antennas and Propagation*, vol. 67, pp. 2442–2451, April 2019.

[58] M. Ebrahimpouri and O. Quevedo-Teruel, "Ultrawideband anisotropic glide-symmetric metasurfaces," *IEEE Antennas and Wireless Propagation Letters*, vol. 18, pp. 1547–1551, Aug 2019.

[59] B. A. Mouris, A. Fernández-Prieto, R. Thobaben, J. Martel, F. Mesa, and O. Quevedo-Teruel, "On the increment of the bandwidth of mushroom-type ebg structures with glide symmetry," *IEEE Transactions on Microwave Theory and Techniques*, pp. 1–11, 2020.

[60] O. Quevedo-Teruel, "Glide symmetries and their application for electromagnetic periodic structures," in *2019 International Symposium on Antennas and Propagation (ISAP)*, pp. 1–3, Oct 2019.

[61] P. J. Crepeau and P. R. McIsaac, "Consequences of symmetry in periodic structures," *Proceedings of the IEEE*, vol. 52, pp. 33–43, Jan 1964.

[62] A. Hessel, A. A. Oliner, M. H. Chen, and R. C. Li, "Propagation in Periodically Loaded Waveguides with Higher Symmetries," *Proceedings of the IEEE*, vol. 61, no. 2, pp. 183–195, 1973.

[63] R. Mittra, C. Chan, and T. Cwik, "Techniques for analyzing frequency selective surfaces-a review," *Proceedings of the IEEE*, vol. 76, pp. 1593–1615, dec 1988.

[64] R. Kieburtz and J. Impagliazzo, "Multimode propagation on radiating traveling-wave structures with glide-symmetric excitation," *IEEE Transactions on Antennas and Propagation*, vol. 18, pp. 3–7, January 1970.

[65] D. R. Jackson and A. A. Oliner, "A leaky-wave analysis of high-gain printed antenna configuration," *IEEE Trans. Antennas Propag*, vol. 36, no. 7, pp. 905–910, 1988.

[66] O. Quevedo-Teruel, J. Miao, M. Mattsson, A. Algaba-Brazalez, M. Johansson, and L. Manholm, "Glide-symmetric fully metallic luneburg lens for 5g communications at ka-band," *IEEE Antennas and Wireless Propagation Letters*, vol. 17, pp. 1588–1592, Sep. 2018.

[67] M. Ebrahimpouri, O. Quevedo-Teruel, and E. Rajo-Iglesias, "Design Guidelines for Gap Waveguide Technology Based on Glide-Symmetric Holey Structures," *IEEE Microwave and Wireless Components Letters*, vol. 27, no. 6, pp. 542–544, 2017.

[68] O. Dahlberg, E. Pucci, L. Wang, and O. Quevedo-Teruel, "Low-dispersive glide-symmetric leaky-wave antenna at 60 ghz," in *13th European Conference on Antennas and Propagation, EuCAP 2019 :*, Proceedings of the European Conference on Antennas and Propagation, 2019. QC 20190902.

[69] E. Rajo-Iglesias, M. Ebrahimpouri, and O. Quevedo-Teruel, "Wideband phase shifter in groove gap waveguide technology implemented with glide-symmetric holey ebg," *IEEE Microwave and Wireless Components Letters*, vol. 28, pp. 476–478, June 2018.

[70] M. Ebrahimpouri, A. Algaba Brazalez, L. Manholm, and O. Quevedo-Teruel, "Using glide-symmetric holes to reduce leakage between waveguide flanges," *IEEE Microwave and Wireless Components Letters*, vol. 28, pp. 473–475, June 2018.

[71] P. Padilla, L. F. Herrán, A. Tamayo-Domínguez, J. F. Valenzuela-Valdés, and O. Quevedo-Teruel, "Glide symmetry to prevent the lowest stopband of printed corrugated transmission lines," *IEEE Microwave and Wireless Components Letters*, vol. 28, pp. 750–752, Sep. 2018.

[72] R. Quesada, D. Martín-Cano, F. J. García-Vidal, and J. Bravo-Abad, "Deep-subwavelength negative-index waveguiding enabled by coupled conformal surface plasmons," *Opt. Lett.*, vol. 39, pp. 2990–2993, May 2014.

[73] E. Rajo-Iglesias, M. Ebrahimpouri, and O. Quevedo-Teruel, "Wideband phase shifter in groove gap waveguide technology implemented with glide-symmetric holey ebg," *IEEE Microwave and Wireless Components Letters*, vol. 28, pp. 476–478, June 2018.

[74] Z. Sipus and M. Bosiljevac, "Modeling of glide-symmetric dielectric structures," *Symmetry*, vol. 11, no. 6, 2019.

[75] T. J. Constant, T. S. Taphouse, H. J. Rance, S. C. Kitson, A. P. Hibbins, and J. R. Sambles, "Surface plasmons on zig-zag gratings," *Opt. Express*, vol. 20, pp. 23921–23926, Oct 2012.

[76] L. Lu, J. D. Joannopoulos, and M. Soljačić, "Topological states in photonic systems," *Nature Physics*, vol. 12, no. 7, pp. 626–629, 2016.

[77] A. G. G. Valerio, Z. Sipus and O. Quevedo-Teruel, "Accurate equivalent-circuit descriptions of thin glide-symmetric corrugated metasurfaces," *IEEE Trans. Antennas Propag*, 2017.

[78] D. T. Moore, "Gradient-index optics: a review," *Appl. Opt.*, vol. 19, pp. 1035–1038, Apr 1980.

[79] G. Minatti, F. Caminita, M. Casaletti, and S. Maci, "Spiral Leaky-Wave Antennas Based on Modulated Surface Impedance," *IEEE Transactions on Antennas and Propagation*, vol. 59, no. 12, pp. 4436–4444, 2011.

[80] B. H. Fong, J. S. Colburn, J. J. Ottusch, J. L. Visher, and D. F. Sievenpiper, "Scalar and tensor holographic artificial impedance surfaces," *IEEE Transactions on Antennas and Propagation*, vol. 58, no. 10, pp. 3212–3221, 2010.

[81] D. A. Atchison and G. Smith, "Continuous gradient index and shell models of the human lens," *Vision Research*, vol. 35, no. 18, pp. 2529 – 2538, 1995.

[82] N. M. Ferrers", *"The Cambridge and Dublin Mathematical Journal"*, vol. 8. "Macmillan", 1953.

[83] N. M. Ferrers", *"The Cambridge and Dublin Mathematical Journal"*, vol. 9. "Macmillan", 1954.

[84] R. Luneburg, *The Mathematical Theory of Optics*. University of California Press, Berkeley: McGraw-Hill Book Company, 1964.

[85] J. C. Maxwell, "Solutions of problems, problem no. 2," *Cambridge and Dublin Mathematical Journal*, vol. 8, p. 188, 1854.

[86] M. A. B. Abbasi and V. F. Fusco, "Maxwell Fisheye Lens Based Retrodirective Array," *Scientific Reports*, vol. 9, no. 1, p. 16244, 2019.

[87] J. Eaton, "On spherically symmetric lenses," *Transactions of the IRE Professional Group on Antennas and Propagation*, vol. PGAP-4, pp. 66–71, December 1952.

[88] N. Wang, Y. Ma, R. Huang, and C. K. Ong, "Far field free-space measurement of three dimensional hole –in –teflon invisibility cloak," *Opt. Express*, vol. 21, pp. 5941–5948, Mar 2013.

[89] B. Orazbayev, N. Mohammadi Estakhri, M. Beruete, and A. Alù, "Terahertz carpet cloak based on a ring resonator metasurface," *Phys. Rev. B*, vol. 91, p. 195444, May 2015.

[90] R. Luneburg, "Mathematical theory of optics, brown univ," *Notes, Providence*, 1944.

[91] C. H. Walter, "Surface-wave Luneberg lens antennas," *IRE Transactions on Antennas Propagation*, vol. AP-8, no. 5, pp. 508–515, 1960.

[92] Y.-j. Park, S. Member, A. Herschlein, and W. Wiesbeck, "A Photonic Bandgap (PBG) Structure for Guiding and Suppressing Surface Waves in Millimeter-Wave Antennas," *Transactions on Microwave Theory and Techniques*, vol. 49, no. 10, pp. 1854–1859, 2001.

[93] Young-Jin Park and W. Wiesbeck, "Angular independency of a parallel-plate luneburg lens with hexagonal lattice and circular metal posts," *IEEE Antennas and Wireless Propagation Letters*, vol. 1, pp. 128–130, 2002.

[94] L. Xue and V. F. Fusco, "Printed Holey Plate Luneburg Lens," *Microwave and Optical Technology Letters*, vol. 50, no. 2, pp. 378–380, 2008.

[95] C. Hua, X. Wu, N. Yang, and W. Wu, "Air-filled parallel-plate cylindrical modified luneberg lens antenna for multiple-beam scanning at millimeter-wave frequencies," *IEEE Transactions on Microwave Theory and Techniques*, vol. 61, pp. 436–443, Jan 2013.

[96] D. Gray, N. Nikolic, and J. Thornton, "Frequency performance of 8 wavelength radius minimal layer number lens antennas," in *2015 IEEE-APS Topical Conference on Antennas and Propagation in Wireless Communications (APWC)*, pp. 1433–1436, Sep. 2015.

[97] K. Gbele, M. Liang, W.-R. Ng, M. E. Gehm, and H. Xin, "Millimeter wave luneburg lens antenna fabricated by polymer jetting rapid prototyping," in *2014 39th International Conference on Infrared, Millimeter, and Terahertz waves (IRMMW-THz)*, pp. 1–1, IEEE, 2014.

[98] L. Xue and V. F. Fusco, "24 ghz automotive radar planar luneburg lens," *IET Microwaves, Antennas Propagation*, vol. 1, pp. 624–628, June 2007.

[99] S. Vinogradov, P. Smith, J. Kot, and N. Nikolic, "Radar cross-section studies of spherical lens reflectors," *Progress in Electromagnetics Research-pier - PROG ELECTROMAGN RES*, vol. 72, pp. 325–337, 01 2007.

[100] B. Arigong, J. Ding, H. Ren, R. Zhou, H. Kim, Y. Lin, and H. Zhang, "Design of wide-angle broadband luneburg lens based optical couplers for plasmonic slot nano-waveguides," *Journal of Applied Physics*, vol. 114, no. 14, p. 144301, 2013.

[101] F. Gaufillet and E. Akmansoy, "Graded photonic crystals for luneburg lens," *IEEE Photonics Journal*, vol. 8, pp. 1 – 11, Feb 2016.

[102] Y. Xie, Y. Fu, Z. Jia, J. Li, C. Shen, Y. Xu, H. Chen, and S. A. Cummer, "Acoustic Imaging with Metamaterial Luneburg Lenses," *Scientific Reports*, vol. 8, no. 1, p. 16188, 2018.

[103] S. . Kim, "Cylindrical acoustic luneburg lens," in *2014 8th International Congress on Advanced Electromagnetic Materials in Microwaves and Optics*, pp. 364–366, Aug 2014.

[104] Q. Cheng, H. F. Ma, and T. J. Cui, "Broadband planar luneburg lens based on complementary metamaterials," *Applied Physics Letters*, vol. 95, no. 18, p. 181901, 2009.

[105] X. Xiong, Y. Liu, Z. Yao, L. Zhang, W. Li, and Q. H. Liu, "Design of a metasurface luneburg lens antenna with flared structure," in *Proceedings of 2014 3rd Asia-Pacific Conference on Antennas and Propagation*, pp. 375–378, IEEE, 2014.

[106] C. Pfeiffer and A. Grbic, "A 2d broadband, printed luneburg lens antenna," in *2009 IEEE Antennas and Propagation Society International Symposium*, pp. 1–4, IEEE, 2009.

[107] J. C. Slonczewski and P. R. Weiss, "Band structure of graphite," *Phys. Rev.*, vol. 109, pp. 272–279, Jan 1958.

[108] P. V. Parimi, W. T. Lu, P. Vodo, J. Sokoloff, J. S. Derov, and S. Sridhar, "Negative refraction and left-handed electromagnetism in microwave photonic crystals," *Phys. Rev. Lett.*, vol. 92, p. 127401, Mar 2004.

[109] T. Ochiai and M. Onoda, "Photonic analog of graphene model and its extension: Dirac cone, symmetry, and edge states," *Phys. Rev. B*, vol. 80, p. 155103, Oct 2009.

[110] M. Polini, F. Guinea, M. Lewenstein, H. C. Manoharan, and V. Pellegrini, "Artificial honeycomb lattices for electrons, atoms and photons," *Nature Nanotechnology*, vol. 8, no. 9, pp. 625–633, 2013.

[111] A. Singha, M. Gibertini, B. Karmakar, S. Yuan, M. Polini, G. Vignale, M. I. Katsnelson, A. Pinczuk, L. N. Pfeiffer, K. W. West, and V. Pellegrini, "Two-dimensional mott-hubbard electrons in an artificial honeycomb lattice," *Science*, vol. 332, no. 6034, pp. 1176–1179, 2011.

[112] K. K. Gomes, W. Mar, W. Ko, F. Guinea, and H. C. Manoharan, "Designer Dirac fermions and topological phases in molecular graphene," *Nature*, vol. 483, no. 7389, pp. 306–310, 2012.

[113] L. Tarruell, D. Greif, T. Uehlinger, G. Jotzu, and T. Esslinger, "Creating, moving and merging Dirac points with a Fermi gas in a tunable honeycomb lattice," *Nature*, vol. 483, no. 7389, pp. 302–305, 2012.

[114] T. Uehlinger, G. Jotzu, M. Messer, D. Greif, W. Hofstetter, U. Bissbort, and T. Esslinger, "Artificial graphene with tunable interactions," *Phys. Rev. Lett.*, vol. 111, p. 185307, Oct 2013.

[115] S. Bittner, B. Dietz, M. Miski-Oglu, and A. Richter, "Extremal transmission through a microwave photonic crystal and the observation of edge states in a rectangular dirac billiard," *Phys. Rev. B*, vol. 85, p. 064301, Feb 2012.

[116] U. Kuhl, S. Barkhofen, T. Tudorovskiy, H.-J. Stöckmann, T. Hossain, L. de Forges de Parny, and F. Mortessagne, "Dirac point and edge states in a microwave realization of tight-binding graphene-like structures," *Phys. Rev. B*, vol. 82, p. 094308, Sep 2010.

[117] M. C. Rechtsman, J. M. Zeuner, A. Tünnermann, S. Nolte, M. Segev, and A. Szameit, "Strain-induced pseudomagnetic field and photonic Landau levels in dielectric structures," *Nature Photonics*, vol. 7, no. 2, pp. 153–158, 2013.

[118] B. Dietz and A. Richter, "From graphene to fullerene: experiments with microwave photonic crystals," *Physica Scripta*, vol. 94, p. 014002, nov 2018.

[119] M. Bellec, U. Kuhl, G. Montambaux, and F. Mortessagne, "Topological transition of dirac points in a microwave experiment," *Phys. Rev. Lett.*, vol. 110, p. 033902, Jan 2013.

[120] T. F. Krauss, "Why do we need slow light?," *Nature Photonics*, vol. 2, no. 8, pp. 448–450, 2008.

[121] M. Santagiustina, G. Eisenstein, L. Thevenaz, J. Capmany, J. Mork, J. Reithmaier, A. De Rossi, S. Sales, K. Yvind, S. Combrie, and J. Bourderionnet, "Slow Light Devices and Their Applications to Microwave and Photonics," *IEEE Photoniccs Society Newsletter*, vol. 26, no. 5, pp. 5–12, 2012.

[122] D. Norton, S. Johns, C. Keefer, and R. Soref, "Tunable microwave filtering using high dispersion fiber time delays," *IEEE Photonics Technology Letters*, vol. 6, pp. 831–832, July 1994.

[123] J. Mora, B. Ortega, A. Díez, J. L. Cruz, M. V. Andrés, J. Capmany, and D. Pastor, "Photonic microwave tunable single-bandpass filter based on a mach-zehnder interferometer," *J. Lightwave Technol.*, vol. 24, p. 2500, Jul 2006.

[124] S. Pan and Y. Zhang, "Tunable and wideband microwave photonic phase shifter based on a single-sideband polarization modulator and a polarizer," *Opt. Lett.*, vol. 37, pp. 4483–4485, Nov 2012.

[125] Y. Zhang and S. Pan, "Generation of phase-coded microwave signals using a polarization-modulator-based photonic microwave phase shifter," *Opt. Lett.*, vol. 38, pp. 766–768, Mar 2013.

[126] L. V. Hau, S. E. Harris, Z. Dutton, and C. H. Behroozi, "Light speed reduction to 17 metres per second in an ultracold atomic gas," *Nature*, vol. 397, no. 6720, pp. 594–598, 1999.

[127] N. S. Ginsberg, S. R. Garner, and L. V. Hau, "Coherent control of optical information with matter wave dynamics," *Nature*, vol. 397, no. 7128, pp. 623–626, 1999.

[128] J. Mørk, R. Kjær, M. van der Poel, and K. Yvind, "Slow light in a semiconductor waveguide at gigahertz frequencies," *Opt. Express*, vol. 13, pp. 8136–8145, Oct 2005.

[129] M. S. Jang and H. Atwater, "Plasmonic rainbow trapping structures for light localization and spectrum splitting," *Phys. Rev. Lett.*, vol. 107, p. 207401, Nov 2011.

[130] J. Park, K.-Y. Kim, I.-M. Lee, H. Na, S.-Y. Lee, and B. Lee, "Trapping light in plasmonic waveguides," *Opt. Express*, vol. 18, pp. 598–623, Jan 2010.

[131] S. Savo, B. D. F. Casse, W. Lu, and S. Sridhar, "Observation of slow-light in a metamaterials waveguide at microwave frequencies," *Applied Physics Letters*, vol. 98, no. 17, p. 171907, 2011.

[132] W. T. Lu, Y. J. Huang, B. D. F. Casse, R. K. Banyal, and S. Sridhar, "Storing light in active optical waveguides with single-negative materials," *Applied Physics Letters*, vol. 96, no. 21, p. 211112, 2010.

[133] K. Y. Song, M. G. Herráez, and L. Thévenaz, "Observation of pulse delaying and advancement in optical fibers using stimulated brillouin scattering," *Opt. Express*, vol. 13, pp. 82–88, Jan 2005.

[134] D. Dahan and G. Eisenstein, "Tunable all optical delay via slow and fast light propagation in a raman assisted fiber optical parametric amplifier: a route to all optical buffering," *Opt. Express*, vol. 13, pp. 6234–6249, Aug 2005.

[135] J. E. Heebner, R. W. Boyd, and Q.-H. Park, "Slow light, induced dispersion, enhanced nonlinearity, and optical solitons in a resonator-array waveguide," *Phys. Rev. E*, vol. 65, p. 036619, Mar 2002.

[136] F. Morichetti, A. Melloni, A. Breda, A. Canciamilla, C. Ferrari, and M. Martinelli, "A reconfigurable architecture for continuously variable optical slow-wave delay lines," *Opt. Express*, vol. 15, pp. 17273–17282, Dec 2007.

[137] J. Heinrichs, "Light amplification and absorption in a random medium," *Phys. Rev. B*, vol. 56, pp. 8674–8682, Oct 1997.

[138] B. Vasić and R. Gajić, "Optical modulation based on tunable light absorption and amplification in metasurfaces coupled with gain medium," *Optics Letters*, vol. 42, p. 2181, 06 2017.

[139] M. Connelly, *Semiconductor Optical Amplifiers*. Boston: MA: Kluwer, 2002.

[140] H. J. S. Dorren, X. Yang, D. Lenstra, H. de Waardt, G. D. Khoe, T. Simoyama, H. Ishikawa, H. Kawashima, and T. Hasama, "Ultrafast refractive-index dynamics in a multiquantum-well semiconductor optical amplifier," *IEEE Photonics Technology Letters*, vol. 15, no. 6, pp. 792–794, 2003.

[141] M. N. Islam, "Raman amplifiers for telecommunications," *IEEE Journal of Selected Topics in Quantum Electronics*, vol. 8, no. 3, pp. 548–559, 2002.

[142] R. H. Stolen and E. P. Ippen, "Raman gain in glass optical waveguides," *Applied Physics Letters*, vol. 22, no. 6, pp. 276–278, 1973.

[143] K. L. Tsakmakidis, A. D. Boardman, and O. Hess, "'Trapped rainbow' storage of light in metamaterials," *Nature*, vol. 450, no. 7168, pp. 397–401, 2007.

[144] . S. T. Jacob and B. Khurgin, *Slow Light: Science and Applications*. aylor and Francis Group, 2009.

[145] R. L. Espinola, J. I. Dadap, R. M. Osgood, S. J. McNab, and Y. A. Vlasov, "Raman amplification in ultrasmall silicon-on-insulator wire waveguides," *Opt. Express*, vol. 12, pp. 3713–3718, Aug 2004.

[146] M. Gumus, I. H. Giden, and H. Kurt, "Broadband self-collimation in c2 symmetric photonic crystals," *Opt. Lett.*, vol. 43, pp. 2555–2558, Jun 2018.

[147] B. Stein, E. Devaux, C. Genet, and T. W. Ebbesen, "Self-collimation of surface plasmon beams," *Opt. Lett.*, vol. 37, pp. 1916–1918, Jun 2012.

[148] C. R. Williams, S. R. Andrews, S. A. Maier, A. I. Fernández-Domínguez, L. Martín-Moreno, and F. J. García-Vidal, "Highly confined guiding of terahertz surface plasmon polaritons on structured metal surfaces," *Nature Photonics*, vol. 2, no. 3, pp. 175–179, 2008.

[149] K.-J. Kim, J.-E. Kim, H. Y. Park, Y.-H. Lee, S.-H. Kim, S.-G. Lee, and C.-S. Kee, "Propagation of spoof surface plasmon on metallic square lattice: bending and splitting of self-collimated beams," *Opt. Express*, vol. 22, pp. 4050–4058, Feb 2014.

[150] S.-H. Kim, T.-T. Kim, S. Oh, J.-E. Kim, H. Park, and C.-S. Kee, "Experimental demonstration of self-collimation of spoof surface plasmons," *Phys. Rev. B*, vol. 83, p. 165109, Apr 2011.

[151] E. Young, J. A. Dockrey, A. P. Hibbins, J. R. Sambles, and C. R. Lawrence, "Strong beaming of microwave surface waves with complementary split-ring-resonator arrays," *Scientific Reports*, vol. 8, no. 1, p. 12102, 2018.

[152] A. Sanada, C. Caloz, and T. Itoh, "Planar distributed structures with negative refractive index," *IEEE Transactions on Microwave Theory and Techniques*, vol. 52, pp. 1252–1263, April 2004.

[153] J. B. Pendry, A. J. Holden, D. J. Robbins, and W. J. Stewart, "Magnetism from conductors and enhanced nonlinear phenomena," *IEEE Transactions on Microwave Theory and Techniques*, vol. 47, pp. 2075–2084, Nov 1999.

[154] J. Zhou, L. Zhang, G. Tuttle, T. Koschny, and C. M. Soukoulis, "Negative index materials using simple short wire pairs," *Phys. Rev. B*, vol. 73, p. 041101, Jan 2006.

[155] D. R. Smith, W. J. Padilla, D. C. Vier, S. C. Nemat-Nasser, and S. Schultz, "Composite medium with simultaneously negative permeability and permittivity," *Phys. Rev. Lett.*, vol. 84, pp. 4184–4187, May 2000.

[156] R. A. Shelby, D. R. Smith, and S. Schultz, "Experimental verification of a negative index of refraction," *Science*, vol. 292, no. 5514, pp. 77–79, 2001.

[157] M. Navarro-Cía, M. Beruete, M. Sorolla, and I. Campillo, "Negative refraction in a prism made of stacked subwavelength hole arrays," *Opt. Express*, vol. 16, pp. 560–566, Jan 2008.

[158] D. Ye, K. Chang, L. Ran, and H. Xin, "Microwave gain medium with negative refractive index," *Nature Communications*, vol. 5, no. 1, p. 5841, 2014.

[159] J. B. Pendry, "Negative refraction makes a perfect lens," *Phys. Rev. Lett.*, vol. 85, pp. 3966–3969, Oct 2000.

[160] F. Falcone, T. Lopetegi, M. A. G. Laso, J. D. Baena, J. Bonache, M. Beruete, R. Marqués, F. Martín, and M. Sorolla, "Babinet principle applied to the design of metasurfaces and metamaterials," *Phys. Rev. Lett.*, vol. 93, p. 197401, Nov 2004.

[161] Y. H. Chen, J. W. Dong, and H. Z. Wang, "Omnidirectional resonance modes in photonic crystal heterostructures containing single-negative materials," *J. Opt. Soc. Am. B*, vol. 23, pp. 2237–2240, Oct 2006.

[162] N. Fukaya, D. Ohsaki, and T. Baba, "Two-Dimensional Photonic Crystal Waveguides with 60° Bends in a Thin Slab Structure," *Japanese Journal of Applied Physics*, vol. 39, pp. 2619–2623, may 2000.

[163] Y. Zhang and B. Li, "Photonic crystal-based bending waveguides for optical interconnections," *Opt. Express*, vol. 14, pp. 5723–5732, Jun 2006.

[164] M. Lončar, D. Nedeljković, T. Doll, J. Vučković, A. Scherer, and T. P. Pearsall, "Waveguiding in planar photonic crystals," *Applied Physics Letters*, vol. 77, no. 13, pp. 1937–1939, 2000.

[165] C. Smith, H. Benisty, S. Olivier, M. Rattier, C. Weisbuch, T. Krauss, R. De La Rue, R. Houdré, and U. Oesterle, "Low-loss channel waveguides with two-dimensional photonic crystal boundaries," *Applied Physics Letters*, vol. 77, 10 2000.

[166] S. Noda, A. Chutinan, and M. Imada, "Trapping and emission of photons by a single defect in a photonic bandgap structure," *Nature*, vol. 407, no. 6804, pp. 608–610, 2000.

[167] M. Notomi, K. Yamada, A. Shinya, J. Takahashi, C. Takahashi, and I. Yokohama, "Extremely large group-velocity dispersion of line-defect waveguides in photonic crystal slabs," *Phys. Rev. Lett.*, vol. 87, p. 253902, Nov 2001.

[168] Y. A. Vlasov, M. O'Boyle, H. F. Hamann, and S. J. McNab, "Active control of slow light on a chip with photonic crystal waveguides," *Nature*, vol. 438, no. 7064, pp. 65–69, 2005.

[169] H. Gersen, T. J. Karle, R. J. P. Engelen, W. Bogaerts, J. P. Korterik, N. F. van Hulst, T. F. Krauss, and L. Kuipers, "Real-space observation of ultraslow light in photonic crystal waveguides," *Phys. Rev. Lett.*, vol. 94, p. 073903, Feb 2005.

[170] T. Ma, A. B. Khanikaev, S. H. Mousavi, and G. Shvets, "Guiding electromagnetic waves around sharp corners: Topologically protected photonic transport in metawaveguides," *Phys. Rev. Lett.*, vol. 114, p. 127401, Mar 2015.

[171] A. Mekis, J. C. Chen, I. Kurland, S. Fan, P. R. Villeneuve, and J. D. Joannopoulos, "High transmission through sharp bends in photonic crystal waveguides," *Phys. Rev. Lett.*, vol. 77, pp. 3787–3790, Oct 1996.

[172] Z. Qiao, J. Jung, C. Lin, Y. Ren, A. H. MacDonald, and Q. Niu, "Current partition at topological channel intersections," *Phys. Rev. Lett.*, vol. 112, p. 206601, May 2014.

[173] R. D. Meade, K. D. Brommer, A. M. Rappe, and J. D. Joannopoulos, "Electromagnetic bloch waves at the surface of a photonic crystal," *Phys. Rev. B*, vol. 44, pp. 10961–10964, Nov 1991.

[174] A. B. Khanikaev, R. Fleury, S. H. Mousavi, and A. Alù, "Topologically robust sound propagation in an angular-momentum-biased graphene-like resonator lattice," *Nature Communications*, vol. 6, p. 8260, oct 2015.

[175] A. B. Khanikaev and G. Shvets, "Two-dimensional topological photonics," *Nature Photonics*, vol. 11, no. 12, pp. 763–773, 2017.

[176] L. Lu, J. D. Joannopoulos, and M. Soljačić, "Topological photonics," *Nature Photonics*, vol. 8, p. 821, oct 2014.

[177] M. Camacho, R. R. Boix, F. Medina, A. P. Hibbins, and J. R. Sambles, "Theoretical and experimental exploration of finite sample size effects on the propagation of surface waves supported by slot arrays," *Phys. Rev. B*, vol. 95, p. 245425, Jun 2017.

[178] O. Bitton, R. Bruch, and U. Leonhardt, "Two-dimensional maxwell fisheye for integrated optics," *Phys. Rev. Applied*, vol. 10, p. 044059, Oct 2018.

[179] M. Gilarlue, S. H. Badri, H. R. Saghai], J. Nourinia, and C. Ghobadi, "Photonic crystal waveguide intersection design based on maxwell's fish-eye lens," *Photonics and Nanostructures - Fundamentals and Applications*, vol. 31, pp. 154 – 159, 2018.

[180] w. W. Hansen, "Radiating electromagnetic waveguide," 1940.

[181] A. A. Oliner, *"Leaky-wave antennas," in Antenna Engineering Handbook*. New York, NY, USA: McGraw-Hill, 1993.

[182] A. A. Oliner and R. Jackson, *"Leaky-wave antennas," in Antenna Engineering Handbook*. New York, NY, USA: McGraw-Hill, 2007.

[183] D. R. Jackson, C. Caloz, and T. Itoh, "Leaky-wave antennas," *Proceedings of the IEEE*, vol. 100, pp. 2194–2206, July 2012.

[184] D. Jackson and N. Alexopoulos, "Gain enhancement methods for printed circuit antennas," *IEEE Transactions on Antennas and Propagation*, vol. 33, no. 9, pp. 976–987, 1985.

[185] A. P. Feresidis and J. C. Vardaxoglou, "High gain planar antenna using optimised partially reflective surfaces," *IEE Proceedings - Microwaves, Antennas and Propagation*, vol. 148, no. 6, pp. 345–350, 2001.

[186] A. P. Feresidis, G. Goussetis, Shenhong Wang, and J. C. Vardaxoglou, "Artificial magnetic conductor surfaces and their application to low-profile high-gain planar antennas," *IEEE Transactions on Antennas and Propagation*, vol. 53, no. 1, pp. 209–215, 2005.

[187] C. Walter, *Traveling Wave Antennas*. New York: McGraw-Hill, 1965.

[188] J. Jacobsen, "Analytical, numerical, and experimental investigation of guided waves on a periodically strip-loaded dielectric slab," *IEEE Transactions on Antennas and Propagation*, vol. 18, no. 3, pp. 379–388, 1970.

[189] Chang-Won Lee and Hyon Son, "Periodically slotted dielectrically filled parallel-plate waveguide as a leaky-wave antenna: E-polarization case," *IEEE Transactions on Antennas and Propagation*, vol. 47, no. 1, pp. 171–178, 1999.

[190] A. Oliner and A. Hessel, "Guided waves on sinusoidally-modulated reactance surfaces," *IRE Transactions on Antennas and Propagation*, vol. 7, no. 5, pp. 201–208, 1959.

[191] S.-m. R. Surface, "A Printed Leaky-Wave Antenna Based on a," vol. 59, no. 6, pp. 2087–2096, 2011.

[192] R. Collin, *Antenna Theory, Part II*. New York: McGraw-Hill, 1969.

[193] B. G. Cai, Y. B. Li, H. F. Ma, W. X. Jiang, Q. Cheng, and T. J. Cui, "Leaky-Wave Radiations by Modulating Surface Impedance on Subwavelength Corrugated Metal Structures," *Nature Publishing Group*, no. 4, pp. 1–7, 2016.

[194] G. Minatti, M. Sabbadini, and S. Maci, "Surface to Leaky Wave Transformation in Polarized Metasurfaces," pp. 298–301, 2013.

[195] U. Beaskoetxea, S. Maci, M. Navarro-Cía, and M. Beruete, "3-d-printed 96 ghz bull's-eye antenna with off-axis beaming," *IEEE Transactions on Antennas and Propagation*, vol. 65, no. 1, pp. 17–25, 2017.

[196] J. B. Pendry, A. Aubry, D. R. Smith, and S. A. Maier, "Transformation optics and subwavelength control of light," *Science*, vol. 337, no. 6094, pp. 549–552, 2012.

[197] A. J. Ward and J. B. Pendry, "Refraction and geometry in maxwell's equations," *Journal of Modern Optics*, vol. 43, no. 4, pp. 773–793, 1996.

[198] X. Zhu, L. Feng, P. Zhang, X. Yin, and X. Zhang, "One-way invisible cloak using parity-time symmetric transformation optics," *Opt. Lett.*, vol. 38, pp. 2821–2824, Aug 2013.

[199] U. Leonhardt and T. G. Philbin, "Chapter 2 transformation optics and the geometry of light," vol. 53 of *Progress in Optics*, pp. 69 – 152, Elsevier, 2009.

[200] N. B. Kundtz, D. R. Smith, and J. B. Pendry, "Electromagnetic design with transformation optics," *Proceedings of the IEEE*, vol. 99, no. 10, pp. 1622–1633, 2011.

[201] U. Leonhardt, "Optical conformal mapping," *Science*, vol. 312, no. 5781, pp. 1777–1780, 2006.

[202] H. Chen and C. T. Chan, "Acoustic cloaking and transformation acoustics," *Journal of Physics D: Applied Physics*, vol. 43, p. 113001, mar 2010.

[203] N. B. Kundtz and D. R. Smith, "Extreme-angle broadband metamaterial lens," *Nature Materials*, vol. 9, no. 2, pp. 129–132, 2010.

[204] A. Demetriadou and Y. Hao, "Slim luneburg lens for antenna applications," *Opt. Express*, vol. 19, pp. 19925–19934, Oct 2011.

[205] C. Pfeiffer and A. Grbic, "A Printed , Broadband Luneburg Lens Antenna," *IEEE Transactions on Antennas and Propagation*, vol. 58, no. 9, pp. 3055–3059, 2010.